UNIVERSITÀ DI TRENTO
Department of Industrial Engineering

Doctoral School in Materials, Mechatronics and Systems Engineering

XXXVIII cycle

# Elastocaloric properties of Natural Rubber for Solid-State Cooling Technologies

**Marica Bianchi**

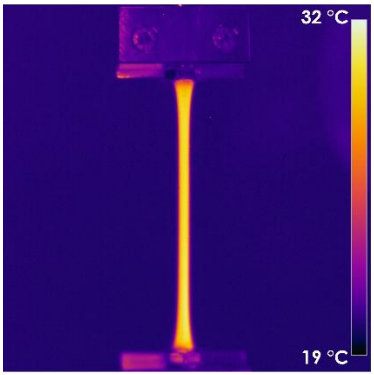


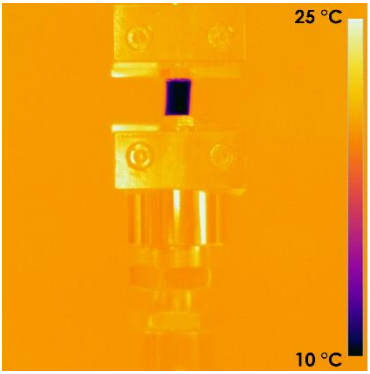


**February 2026**

# ELASTOCALORIC PROPERTIES OF NATURAL RUBBER FOR SOLID-STATE COOLING TECHNOLOGIES

Marica Bianchi

E-mail: marica.bianchi@unitn.it

Approved by:

Prof. Andrea Dorigato, Advisor

Department of Industrial Engineering

*University of Trento, Italy.*

Prof. Luca Fambri, Co-advisor

Department of Industrial Engineering

*University of Trento, Italy.*

Ph.D. Commission:

Prof. Stefano Pandini

Department of Mechanical and Industrial Engineering

*University of Brescia, Italy.*

Prof.ssa Maria Chiara Mistretta,

Department of Engineering

*University of Palermo, Italy.*

University of Trento,

Department of Industrial Engineering

February 2026

**University of Trento - Department of Industrial Engineering**

- - - - - - - - -

**Doctoral Thesis**

**Marica Bianchi - 2026**

# Abstract

In recent years, the need to develop sustainable and energy efficient air-cooling technologies has become increasingly urgent due to the environmental and energy-related disadvantages of conventional vapour-compression air conditioning systems. Solid-state cooling technology, based on caloric effects, represents a promising alternative, with elastocaloric cooling identified as one of the most suitable candidates for replacing conventional air-cooling systems. In this framework, natural rubber (NR), a well-known renewable resource, is attracting increasing attention as an elastocaloric material, owing to its low cost, non-toxicity, long fatigue life, and remarkable elastocaloric properties, which arise from the synergistic contribution of thermoelasticity and strain-induced crystallization. Nevertheless, research on the refrigeration potential of natural rubber is still in its infancy, and not all parameters influencing the elastocaloric behaviour of this material are fully understood. In particular, most studies so far have focused primarily on the influence of testing parameters such as temperature, strain rate and maximum deformation.

This thesis aimed at investigating the influence of rubber network structure and formulation on the elastocaloric properties of NR-based systems. Specifically, the influence of (i) the crosslinking density, and (ii) the addition of nanofillers was systematically analysed.

In the first part, natural rubber samples with varying crosslinking densities (ranging from 2.9 to 5.2 $10^{-4}$·mol/cm$^3$) were prepared and characterized from a structural, thermal and mechanical point of view. Their elastocaloric properties were then thoroughly examined, revealing that crosslinking density is a crucial structural parameter governing cooling performance. The results showed that reducing the crosslinking density enhanced cooling capacity, primarily due to stronger contributions from strain-induced crystallization and thermoelasticity.

In the second part, the effect of adding both natural (MMT) and organo-modified (O-MMT) nanoclays to the most promising

formulation identified in the first part of the work was assessed. Two series of NR-based nanocomposites, containing 1, 3 and 5 phr nanofiller, were prepared and characterized in terms of morphology, thermal, mechanical and elastocaloric properties. The results highlighted that the better dispersion of the organoclays within the rubber matrix promoted not only a better mechanical behaviour (in terms of stiffness and strength), but also a significantly enhanced cooling performance with respect to MMT nanofilled systems. The NR/O-MMT samples demonstrated up to a ~45% increase in heat absorbed per refrigeration cycle compared to the unfilled NR. This improvement was ascribed to a synergistic combination of enhanced strain-induced crystallization, improved macromolecular structural homogeneity, and potential strain amplification effects promoted by the organoclays.

These findings demonstrated that the rubber network structure and formulation represent the fundamental starting point for future research aimed at maximizing the cooling performance of NR-based systems, given their strong influence on the elastocaloric behaviour. This is therefore a fundamental first step towards scaling up solid-state cooling technologies.

# Table of Contents

**1 Introduction ..... 1**

1.1 Motivation and objective ..... 1

1.2 Thesis outline ..... 3

**2 Scientific Background ..... 4**

2.1 Air cooling technology ..... 4

2.1.1 Vapour compression refrigeration systems ..... 5

2.1.2 Environmental impact of vapour compression technology ..... 7

2.1.3 Alternative solutions ..... 10

2.2 Solid state cooling based on caloric effects ..... 11

2.2.1 Magnetocaloric effect ..... 15

2.2.2 Electrocaloric effect ..... 17

2.2.3 Mechanocaloric effect ..... 19

2.2.4 Comparison of caloric effects ..... 25

2.3 Elastomers ..... 26

2.3.1 Market Overview ..... 29

2.3.2 Classifications of elastomers ..... 30

2.3.3 Elastomer processing ..... 31

2.3.4 Vulcanization ..... 34

2.3.5 Rubber elasticity ..... 41

2.3.6 Thermal behaviour of elastomers at high strain rate ..... 48

2.3.7 Strain induced crystallization ..... 51

2.3.8 Mullins effect ..... 56

2.4 Natural Rubber ..... 60

2.4.1 Production of Natural Rubber ..... 64

2.4.2 Properties of Natural Rubber ..... 70

2.5 Elastocaloric effect of Natural Rubber ..... 72

**3 Experimental Part ..... 82**

3.1 Materials ..... 82

3.1.1 Natural Rubber ..... 82

3.1.2 Rubber additives ..... 83

3.1.3 Solvents ..... 84

3.1.4 Nanoclays ..... 84

3.2 Experimental techniques ..... 85

3.2.1 Rheological analysis ..... 85

3.2.2 Density measurements ..... 85

3.2.3 Evaluation of the crosslinking density ..... 86

3.2.4 Morphological analysis ..... 87

3.2.5 X-Ray diffraction (XRD) ..... 87

3.2.6 Differential scanning calorimetry (DSC) ..... 89

3.2.7 Thermogravimetric analysis (TGA) ..... 90

3.2.8 Laser Flash Analysis (LFA) ..... 90

3.2.9 Shore A hardness measurements ..... 91

3.2.10 Quasi-static tensile tests ..... 91

3.2.11 Evaluation of the Mullins effect ..... 92

3.2.12 Evaluation of the elastocaloric effect ..... 92

**4 Effect of crosslinking density on the elastocaloric properties of Natural Rubber ..... 108**

4.1 Introduction ..... 108

4.2 Materials and Methods ..... 109

4.2.1 Materials ..... 109

4.2.2 Sample preparation ..... 109

4.3 Results and Discussion ..... 112

4.3.1 Rheological analysis ..... 112
4.3.2 Density measurements ..... 115
4.3.3 Evaluation of the crosslinking density ..... 116
4.3.4 Differential Scanning Calorimetry (DSC) ..... 117
4.3.5 Thermogravimetric analysis (TGA) ..... 119
4.3.6 Laser Flash Analysis (LFA) ..... 120
4.3.7 Shore A hardness measurements ..... 121
4.3.8 Quasi-static tensile tests ..... 122
4.3.9 Evaluation of strain induced crystallization ..... 125
4.3.10 Evaluation of the Mullins effect ..... 128
4.3.11 Evaluation of the elastocaloric effect ..... 135
4.4 Conclusions ..... 164
**5 Effect of nanoclay addition on the elastocaloric properties of Natural Rubber ..... 166**
5.1 Introduction ..... 166
5.2 Materials and Methods ..... 168
5.2.1 Materials ..... 168
5.2.2 Sample preparation ..... 168
5.3 Results and Discussion ..... 170
5.3.1 Rheological analysis ..... 170
5.3.2 Density measurements ..... 172
5.3.3 Evaluation of the crosslinking density ..... 172
5.3.4 X-Ray diffraction (XRD) ..... 173
5.3.5 Morphological analysis ..... 176
5.3.6 Differential Scanning Calorimetry (DSC) ..... 178
5.3.7 Thermogravimetric analysis (TGA) ..... 179
5.3.8 Laser Flash Analysis (LFA) ..... 181

5.3.9 Shore A hardness measurements ..... 182
5.3.10 Quasi-static tensile tests ..... 183
5.3.11 Evaluation of strain induced crystallization ..... 186
5.3.12 Evaluation of the Mullins effect ..... 188
5.3.13 Evaluation of the elastocaloric effect ..... 193
5.4 Conclusions ..... 202
**6 General conclusions ..... 204**
6.1 Concluding remarks ..... 204
6.2 Future Developments ..... 206
**7 Side activities ..... 211**
7.1 Evaluation of the Physical and Shape Memory Properties of Fully Biodegradable Poly (lactic acid) (PLA)/Poly (butylene adipate terephthalate) (PBAT) Blends ..... 212
7.1.1 Introduction ..... 212
7.1.2 Experimental Part ..... 214
7.1.3 Results and discussion ..... 220
7.1.4 Conclusions ..... 245
**8 References ..... 247**

# List of Figures

Figure 2.1. Evolution of air conditioner demand by country and year [12]. ..... 4

Figure 2.2. Refrigeration cycle of a vapour compression refrigeration system [14]. ..... 5

Figure 2.3. Electricity use for space cooling, which includes fans but is mostly air conditioning [15]. ..... 8

Figure 2.4. History of refrigerant fluid generations [16]. ..... 9

Figure 2.5.Scheme of the magnetocaloric effect [27,28]. ..... 15

Figure 2.6. Scheme of the electrocaloric effect [31]. ..... 17

Figure 2.7. Scheme of the elastocaloric effect [32]. ..... 20

Figure 2.8. Scheme of the barocaloric effect [36]. ..... 24

Figure 2.9. Ashby diagrams of (A) strength vs elongation, (B) Young's modulus vs density and (C) Young's modulus vs strength of different families of materials [49]. ..... 28

Figure 2.10.Global elastomer market [50]. ..... 29

Figure 2.11. End use of elastomers in 2024 [50]. ..... 30

Figure 2.12. Mixing equipment used for rubber compounding. (A) Mix mill and (B) Banbury internal mixer [52]. ..... 33

Figure 2.13. Example of a rheometer curve for vulcanization [62]. . 35

Figure 2.14. Effect of temperature on the vulcanization kinetics of a rubber formulation [64]. ..... 36

Figure 2.15. Effect of accelerator on the vulcanization kinetics [61]. ..... 37

Figure 2.16. Effect of vulcanization on end-use properties [55]. ..... 38

Figure 2.17. Network formation in a sulphur-based curing system [55]. ..... 39

Figure 2.18. Typical stress-strain curve of an elastomeric material [66]. ..... 41

Figure 2.19. General experimental curve of force versus temperature at constant deformation [67]. .....46

Figure 2.20. Total external force and its entropic and energetic components as a function of elongation [67]. .....47

Figure 2.21. Strain induced crystallization in elastomers. The dark dots represent the crosslinking points, the red lines represent the short chains, and the yellow areas represent crystallites [22]. .....51

Figure 2.22. Stress-strain curve and selected WAXD patterns collected during stretching and retraction of natural rubber [70,71]. .....52

Figure 2.23. Structure of a layered silicate nanofiller [74].....54

Figure 2.24. Onset of SIC in (A) unfilled natural rubber and (B) natural rubber filled with 15 phr of organoclay (NR-NC1) [80,81]. 55

Figure 2.25. SIC in unfilled rubber and rubber filled with organoclays [82].....56

Figure 2.26. Natural rubber filled with carbon black and subjected to 6 loading-unloading cycles. (A) Natural rubber filled with 1 phr of CB (B) natural rubber filled with 60 phr of CB [86].....58

Figure 2.27. Theories proposed to interpret the Mullins effect [72].59

Figure 2.28. Chemical structure of natural rubber [92].....60

Figure 2.29. Trend of global rubber production and consumption from 1990 to 2019 [95].....61

Figure 2.30. Applications of NR [98]. .....62

Figure 2.31. Price chart of some grades of natural rubber from 2011 to 2025 [99].....63

Figure 2.32. Plantation of Hevea brasiliensis [105]. .....64

Figure 2.33. Collection of latex from Hevea brasiliensis [91]. .....65

Figure 2.34. The colloidal dispersion of latex [107]. .....66

Figure 2.35. The two categories of creep rubber. (A) Pale Latex Crepe and (B) Estate Brown Crepe [108,109]. .....67

Figure 2.36. Ribbed Smoke Sheets [113].....70

Figure 2.37. Contributions to the elastocaloric effect of NR: thermoelastic effect and SIC. ....72

Figure 2.38. Elastocaloric performance of NR compared to other elastomers [41]. ....74

Figure 2.39. Conversion efficiency parameters at (A) stretching and (B) releasing for NR filled with carbon black [22]. ....75

Figure 2.40. Temperature dependence of adiabatic temperature changes (ΔT) at various strains. The inset shows this behaviour at a strain of 600% [116]. ....76

Figure 2.41. (A)Mechanical energy of deformation and (B) heat absorbed during the releasing phase of NR filled with different amount of ground tire rubber [43]. ....77

Figure 2.42. Scheme of the cooler prototype developed by Sion et al. [118]. ....80

Figure 3.1. Natural rubber TSR SMR 10 supplied by Marangoni Group S.p.a. ....83

Figure 3.2. Crystal structure of Poly(cis-Isoprene) [127]. ....88

Figure 3.3. Procedure followed for the evaluation of the elastocaloric properties using the pendulum testing machine. ....94

Figure 3.4. Mechanism used to actuate the self-locking and unlocking of the pendulum. ....95

Figure 3.5. Positioning of the infrared thermal camera relative to the samples during the experiments. ....97

Figure 3.6. Mechanical energy at stretching (area under the loading curve) and the mechanical energy at retraction (area under the unloading curve) in force-displacement curves of an elastomer. ....99

Figure 3.7. Representation of the temperature variation of one of the tested specimens during the stretching and retraction phase using the high-speed tensile testing machine (maximum deformation applied = 500%). (A) temperature variation as a function of time and (B) corresponding surface temperature images acquired through IR camera. ....101

Figure 3.8. Example of the fitting procedure adopted to determine the characteristic time dampening ($\tau_c$). ....104

Figure 3.9. Example of the integration procedure to determine the heat released and extracted from the environment during the stretching and retraction phase, respectively. .....106

Figure 4.1. Vulcanization curves at 120 °C of the different NR formulations, effect of sulphur and accelerator content. (A-C) Vulcanization curves grouped by accelerator content and (D-F) vulcanization curves grouped by sulphur content. .....114

Figure 4.2. Crosslinking density as a function of density for the vulcanized rubber samples. .....117

Figure 4.3. DSC thermograms of (A) the 1st heating scan and (B) 2nd heating scan of UNR, NR_1.5S, NR_2.5S and NR_3.5S samples. 118

Figure 4.4. (A) TGA curves and (B) DTGA curves of the unvulcanized NR and the crosslinked samples. .....119

Figure 4.5. Representative stress-strain curves from quasi-static tensile tests on NR_1.5S, NR_2.5S and NR_3.5S samples.....123

Figure 4.6. Diffraction patterns of the unvulcanized rubber and crosslinked samples in the unstretched state and at 300%, 400%, and 500% strain. .....125

Figure 4.7. Stress-strain response of the NR samples under cyclic tensile loading. (A) NR_1.5S, (B) NR_2.5S, (C) NR_3.5S. In each graph, the first cycle is highlighted at every deformation level. ....129

Figure 4.8. Peak stress as a function of cycle number and crosslinking density of the prepared NR samples. Maximum deformation level of (A) 200%, (B) 300%, (C) 400%.....131

Figure 4.9. Energy dissipated as a function of cycle number and degree of crosslinking. Maximum strain level of (A) 200%, (B) 300%, (C) 400%. .....132

Figure 4.10. Residual deformation after the 10th cycle as a function of the maximum deformation level and degree of crosslinking of the prepared NR samples. .....133

Figure 4.11. Temperature variation of the surface of the samples as a function of impact velocity. (A) NR_1.5S, (B) NR_2.5S, (C) NR_3.5S samples.....137

Figure 4.12. Trend of deformation of the samples as a function of impact velocity. ..... 137

Figure 4.13. Elastocaloric properties of the NR formulations evaluated using the preliminary set-up. (A) maximum $\Delta T_{heat}$, (B) maximum $\Delta T_{cool}$, (C) $Q_{ab}$ per unit volume of material, (D) $COP_{mat}$. ..... 141

Figure 4.14. Temperature variation on the surface of NR_1.5S sample tested under cyclic condition. (A) NR_1.5S tested at 1.62 m/s and (B) NR_1.5S tested at 1.92 m/s. The temperature variations reported refer to the 1st, 5th and 10th cycles. ..... 143

Figure 4.15. $\Delta T_{cool}$ at different testing speeds for NR_1.5S deformed at 400%. ..... 145

Figure 4.16. (A, C, E) Temperature variation of the surface of the NR samples as a function of time and maximum deformation applied; (B, D, F) Stress in the stretching and subsequent holding step as a function of time and maximum deformation. (A, B) NR_1.5S; (C, D) NR_2.5S and (E, F) NR_3.5S. ..... 147

Figure 4.17. Elastocaloric properties of the produced NR samples as a function of the maximum deformation applied and the crosslinking density. (A) Maximum $\Delta T_{heat}$, (B) maximum $\Delta T_{cool}$ (C) $Q_{re}$, (D) $Q_{ab}$, (E) mechanical energy at stretching per unit volume of material $W_s$, (F) mechanical energy at retraction per unit volume of material $W_r$, (G) $COP_{mat}$. ..... 149

Figure 4.18. Conversion efficiency at (A) stretching and (B) retraction phases of the prepared NR samples. ..... 158

Figure 4.19. Temperature variations of the surface of NR_1.5S deformed at 400% in conditions of natural convection (red curve) and forced convection (blue curve). ..... 160

Figure 4.20. Elastocaloric properties of NR_1.5S deformed at 400% strain under forced convection and in cyclic conditions. (A) maximum $\Delta T_{heat}$, (B) maximum $\Delta T_{cool}$, (C) $Q_{ab}$, (D) $W_s$, (E) $COP_{mat}$ and (F) SR. ..... 163

Figure 5.1. Vulcanization curves of NR and (A) MMT-filled nanocomposites and (B) O-MMT-filled nanocomposites. ..... 170

Figure 5.2. Results of XRD analysis on neat nanoclay and the relative nanocomposites (nanoclay loading = 5 phr). High resolution XRD

patterns of (A) neat MMT and NR_5MMT, (B) neat O-MMT and NR_5O-MMT samples, and (C) experimental fit of the basal peak performed with a Pseudo-Voigt function. .....175

Figure 5.3. FESEM micrographs at different magnifications of the cryofracture surface of the produced NR based nanocomposites. (A, B) NR_5MMT, (C, D) NR_5-OMMT. .....177

Figure 5.4. (A,C) TGA curves and (B, D) DTGA curves of the nanoclays, NR and the produced nanocomposites. (A, B) Refer to MMT-filled nanocomposites, while (C,D) to O-MMT-filled nanocomposites. .....179

Figure 5.5. Representative stress-strain curves from quasi-static tensile tests on (A) NR and NR/MMT nanocomposites, (B) NR and NR/O-MMT nanocomposites.....183

Figure 5.6. Diffraction patterns of neat NR and NR_5MMT and NR_5O-MMT nanocomposites deformed at 400% strain.....186

Figure 5.7. Stress-strain curves of the NR based nanocomposites subjected to uniaxial cyclic tension (maximum strain level = 400%). (A) NR_1MMT, (B) NR_3MMT, (C) NR_5MMT, (D) NR_1O-MMT, (E) NR_3O-MMT, (F) NR_5O-MMT. The first cycle is evidenced in all the graphs. .....189

Figure 5.8. Results from the uniaxial cyclic tension tests on the neat NR and the relative nanocomposites. (A, B) Maximum stress at 400% and (C, D) specific energy dissipated as a function of cycle number. (A, C) refer to NR/MMT samples, while (B, D) to NR/O-MMT samples.....190

Figure 5.9. Residual deformation after ten loading-unloading cycles as a function of type and concentration of nanoclays in the prepared NR nanocomposites. .....191

Figure 5.10. (A, C) Temperature variation of the surface of the samples as a function of time, (B, D) stress variation in the stretching and subsequent holding step as a function of time. (A, B) refer to MMT nanocomposites, (C, D) refer to O-MMT nanocomposites. 194

Figure 5.11. Results of the elastocaloric tests on the neat NR and the relative nanocomposites. (A) Maximum $\Delta T_{heat}$, (B) maximum $\Delta T_{cool}$, (C) $Q_{re}$, (D) $Q_{ab}$, (E) $W_s$ per unit volume of material, (F) $W_r$ per unit volume of material, (G) $COP_{mat}$. .....196

Figure 5.12. Elastocaloric properties of NR_3O-MMT sample under cyclic conditions. (A) $\Delta T_{heat}$, (B) $\Delta T_{cool}$, (C) $Q_{ab}$, (D) $W_s$,(E) $COP_{mat}$ and (F) SR. .....201

Figure 6.1. Scheme of the developed prototype. .....208

Figure 6.2(A-C). 3D printed prototype of the NR-based elastocaloric cooling system. (A) Frontal view, (B) diagonal view and (C) lateral view.....209

Figure 6.3(A,B). Infrared thermal images of the prototype at rest and during operation. (A) Prototype at rest, with rubber bands in thermal equilibrium with the environment. (B) Prototype during operation: half of the rubber bands stretch and heat up while the other half return to the undeformed state and cool down. .....210

Figure 7.1. (A) Graphical representation and (B) schematization of the thermo-mechanical cycle adopted to investigate the shape memory behaviour of the PLA/PBAT blends. .....219

Figure 7.2. Results of the dynamic rheological tests at 180 °C on the neat matrices and on the prepared blends. Trends of (A) storage modulus, (B) loss modulus, (C) complex viscosity as a function of the angular frequency.....221

Figure 7.3. Optical microscope images of the prepared PLA/PBAT blends. (A) PLA_PBAT_15, (B) PLA_PBAT_30, (C) PLA_PBAT_45, (D) PLA_PBAT_60, (E) PLA_PBAT_75. .....223

Figure 7.4. SEM micrographs of the cryofracture surface of neat PLA, neat PBAT and the prepared blends: (A) PLA, (B) PLA_PBAT_15, (C) PLA_PBAT_30, (D) PLA_PBAT_45, (E) PLA_PBAT_60, (F) PLA_PBAT_75, (G) PBAT. .....226

Figure 7.5. TGA tests on neat PLA, neat PBAT and their blends. Trends of (A) residual mass and (B) mass loss derivative as a function of temperature. .....228

Figure 7.6. DSC thermograms of neat PLA, neat PBAT and PLA/PBAT blends. (A) First heating scan, (B) second heating scan. .....230

Figure 7.7. Storage modulus (a) and loss modulus (b) from DMA on neat PLA, neat PBAT and PLA/PBAT blends. .....234

Figure 7.8. Representative stress–strain curves from quasi-static tensile tests on neat PLA, neat PBAT and PLA/PBAT blends. .....236

Figure 7.9. Experimental and theoretical values of the elastic modulus of the produced blends as a function of the PBAT content. .....240

Figure 7.10. Schematization of the proposed mechanism for the shape memory behaviour of the produced blends. Modelization of (a) strain fixity and (b) strain recovery behaviour. The scheme is a simplification as it assumes purely tensile conditions. However, it serves to illustrate the impact of the poor interfacial adhesion between PLA and PBAT on the shape memory properties. .....245

# List of Tables

Table 2.1. External stimulus and conjugated variables for the different caloric effect.....13

Table 2.2.Elastocaloric performance of SMAs and Natural Rubber [34].....22

Table 2.3. Comparison of the cooling performance of representative caloric materials. .....25

Table 2.4. Properties and features of CV, EV and SEV curing systems. .....40

Table 2.5.Properties of NR and other very common elastomers [48,53,98,114,115]. .....71

Table 2.6. Summary of elastocaloric properties of NR and various rubbers. .....79

Table 3.1. Main specifications of the TSR natural rubber, grade SMR 10, used in the PhD thesis. .....82

Table 3.2. Physical properties of the rubber chemicals, data taken from the producers [119]. .....83

Table 3.3. Physical properties of the solvents used, data taken from the producer [120-122].....84

Table 3.4. Nanoclays used in this PhD thesis, data taken from the producer [123].....85

Table 3.5. Impact velocities and impact energies applied for the evaluation of the elastocaloric properties of the prepared NR samples (preliminary set up). .....96

Table 4.1. List of the materials used in this part of the thesis. .....109

Table 4.2. Composition of the NR compounds analysed. .....111

Table 4.3. Procedure used for mixing natural rubber compounds..112

Table 4.4. Minimum torque ($T_{min}$), maximum torque ($T_{max}$) and optimum curing time ($t_{90\%}$) for samples with different sulfur and accelerator content. Selected compositions are highlighted in grey. .....114

Table 4.5. Density values of the samples resulting from the application of Archimedes' principle. .....116

Table 4.6. Experimental crosslinking densities of the prepared NR samples.....116

Table 4.7. Results of the DSC tests on the prepared NR samples..118

Table 4.8. Results of the thermogravimetric analysis on the prepared rubber samples. .....120

Table 4.9. Specific heat capacity, thermal diffusivity and thermal conductivity at 20 °C as a function of crosslinking density obtained from LFA analysis on the prepared NR samples. .....121

Table 4.10. Shore A hardness measurements as a function of crosslinking density for the unvulcanized rubber and the crosslinked samples.....121

Table 4.11. Results of quasi-static tensile tests at 25 °C on NR_1.5S, NR_2.5S and NR_3.5S samples.....123

Table 4.12. Average crystallite size and crystallinity obtained from XRD measurements on NR samples. .....126

Table 4.13. Numerical values of the deformation of the samples as function of impact velocity. .....138

Table 4.14. Characteristic time of temperature dampening calculated in the stretching ($\tau_{c,s}$) and retraction phase ($\tau_{c,r}$), and heat transfer coefficient calculated in the retraction phase ($h_r$) of the samples...140

Table 4.15. Maximum stress values ($\sigma_0$) and percentage of stress relaxation (SR) evaluated in a timescale of 250 s of the stretching phase. .....150

Table 4.16. Temperature decrease assuming that the percentage of crystallinity of the stretched samples is that determined from the XRD analyses (see Table 4.12). .....153

Table 4.17. Characteristics time of temperature dampening ($\tau_c$) and heat transfer coefficient (h) calculated in the stretching and retraction phase of the NR samples. .....154

Table 4.18.Elastocaloric properties of NR_1.5S deformed at 400% strain in forced convection, for an elastocaloric cycle duration of 480 s. .....160

Table 4.19. Elastocaloric properties of NR_1.5S deformed at 400% strain in forced convection, for an elastocaloric cycle duration of 120 s. ..... 161

Table 4.20. Summary of the definitions of the parameters determined in the elastocaloric tests. ..... 162

Table 5.1 List of the materials used in this section of the PhD thesis. ..... 168

Table 5.2. Composition in phr and nomenclature of the produced NR compounds (phr= parts per hundred rubber). ..... 169

Table 5.3. Minimum torque ($T_{min}$), maximum torque ($T_{max}$) and optimum curing time ($t_{90\%}$) of neat NR and the prepared nanocomposites. ..... 171

Table 5.4. Density of the unfilled NR and the relative nanocomposites. ..... 172

Table 5.5. Crosslinking density of the unfilled NR and the relative nanocomposites obtained through swelling tests. ..... 173

Table 5.6. Interlayer spacing for neat nanoclays and the produced nanocomposites calculated using the Bragg's law. ..... 176

Table 5.7. Glass transition temperature of the nanocomposites determined in the 1$^{st}$ and 2$^{nd}$ heating scan. ..... 178

Table 5.8. Results of the thermogravimetric analysis on the nanoclays, neat NR and the relative nanocomposites. ..... 180

Table 5.9. Specific heat capacity, thermal conductivity and thermal diffusivity at 20 °C of neat NR and the relative nanocomposites from LFA. ..... 181

Table 5.10. Shore A hardness measurements for the unfilled rubber and the nanocomposites. ..... 182

Table 5.11. Results of quasi-static tensile tests on the unfilled NR and the prepared nanocomposites. ..... 184

Table 5.12. Average crystallite size and crystallinity obtained from XRD measurements on neat NR, NR_5MMT and NR_5O-MMT, deformed at a strain of 400%. ..... 186

Table 5.13. Percentage of stress relaxation (SR) evaluated over the time scale of the stretching phase from elastocaloric tests on neat NR and the relative nanocomposites. .....194

Table 5.14. Mechanisms involved in the temperature variations of the samples during the stretching and retraction phase. .....197

Table 7.1. List of the prepared samples and their nominal composition. .....215

Table 7.2. Results of the TGA tests on neat PLA, neat PBAT and their blends. .....228

Table 7.3. Results of the DSC tests on neat PLA, neat PBAT and PLA/PBAT blends (first and second heating scan). .....231

Table 7.4. Results of the DMA tests on the prepared blends. .....235

Table 7.5. Results of quasi-static tensile test at 25 °C on neat PLA, neat PBAT and PLA/PBAT blends. .....237

Table 7.6. Strain fixity and strain recovery parameters of neat PLA, neat PBAT and PLA/PBAT blends. .....241

# List of Acronyms

| | |
|---|---|
| ACs | Air Conditioners |
| BR | Butadiene Rubber |
| CAGR | Compound Annual Growth Rate |
| CFCs | Chlorofluorocarbons |
| CNC | Cellulose Nanocrystals |
| COP | Coefficient of Performance |
| CR | Chloroprene Rubber |
| DMA | Dynamic Mechanical Analysis |
| DSC | Differential Scanning Calorimetry |
| EPDM | Ethylene Propylene Diene Monomer |
| GWP | Global Warming Potential |
| HFCs | Hydrochlorofluorocarbons |
| HFOs | Hydrofluoroolefins |
| IEA | International Energy Agency |
| IR | Isoprene Rubber |
| LFA | Laser Flash Analysis |
| MMT | Montmorillonite |
| NBR | Nitrile Butadiene Rubber |
| NR | Natural Rubber |
| OECD | Organisation for Economic Co-operation and Development |
| O-MMT | Organo-Modified Montmorillonite |
| OM | Organo Modified |
| PBAT | Polybutylene Adipate Terephthalate |
| PLA | Polylactic Acid |

| | |
|---|---|
| PVDF | Polyvinylidene fluoride |
| RSS | Ribbed Smoked Sheet |
| SBR | Styrene Butadiene Rubber |
| SBS | Styrene-Butadiene-Styrene |
| SEBS | Styrene-Ethylene-Butylene-Styrene |
| SIC | Strain-Induced Crystallization |
| SMA | Shape Memory Alloy |
| SMR | Standard Malaysian Rubber |
| SR | Percentage of Stress Relaxation |
| TGA | Thermogravimetric Analysis |
| TPE | Thermoplastic Elastomer |
| TPU | Thermoplastic Polyurethane |
| TSR | Technically Specified Rubber |
| XRD | X-ray Diffraction |
| ZDBC | Zinc Dibutyl Dithiocarbamate |

# List of Symbols

| | |
|---|---|
| $A_u$ | Area of the samples in the unstretched state |
| $A_s$ | Area of the samples in the stretched state |
| A | Helmholtz free energy |
| $\alpha$ | Thermal diffusivity |
| B | Magnetic field |
| C | Heat capacity |
| $c_p$ | Specific heat capacity |
| $\Delta T$ | Temperature variation |
| $\Delta T_{cool}$ | Temperature reduction following unloading |
| $\Delta T_{heat}$ | Temperature increase following stretching |
| E | Electric field |
| $E_{100\text{-}200}$ | Elastic modulus evaluated in the strain range 100-200% |
| $\varepsilon$ | Engineering strain |
| $\varepsilon_b$ | Strain at break |
| F | Force |
| h | Heat transfer coefficient |
| $\lambda$ | Thermal conductivity |
| l | Length |
| M | Magnetization |
| m | Weight (mass) |
| $\eta$ | Conversion efficiency from mechanical energy to heat energy |
| p | Hydrostatic pressure |
| P | Polarization |

| | |
|---|---|
| $Q$ | Heat |
| $Q_{ab}$ | Heat absorbed |
| $Q_{re}$ | Heat released |
| $\rho$ | Density |
| $S$ | Entropy |
| $S_m$ | Magnetic entropy |
| $\sigma$ | Engineering stress |
| $\sigma_b$ | Stress at break |
| $\sigma_{200\%}$ | Stress at 200% strain |
| $\sigma_{400\%}$ | Stress at 400% strain |
| $T$ | Temperature |
| $T_{max}$ | Maximum torque |
| $T_{min}$ | Minimum torque |
| $t$ | Time |
| $t_{90\%}$ | Optimum curing time |
| $U$ | Internal energy |
| $W$ | Mechanical energy |
| $W_r$ | Mechanical energy at retraction |
| $W_s$ | Mechanical energy at stretching |

# 1 Introduction

## *1.1 Motivation and objective*

It is widely recognized that the global temperature has increased by 1.1 °C compared to the commencement of the Industrial Revolution. Despite the ostensibly modest nature of this temperature increase, it has engendered a heightened frequency of severe weather phenomena, notably heat waves. The scientific community expects the warming trend to worsen in the future, rendering parts of the world unliveable. In response to the escalating frequency of heat waves, cooling, and particularly air conditioning, has resulted essential for the survival of billions of people around the world as well as for the safeguarding of vital resources such as food and medicine [1-5]. Despite the countless benefits, air conditioners based on vapour-compression technology consume a large amount of electricity (approx. 15% of the total amount) and rely on refrigerant fluids with high Global Warming Potential (GWP) [5-7]. The refrigerant fluids are partially released into the environment during their lifespan, contributing in a significant way to greenhouse gas emissions. These environmental and energy-related challenges underscore the urgent need for more sustainable and efficient cooling technologies.

In recent years, solid-state cooling technology has emerged as a promising alternative to conventional vapour-compression refrigeration [8-10]. The primary distinction lies in the type of refrigerant: while vapour-compression systems employ fluids, solid-state cooling relies on solid materials. By employing solid refrigerants, this new technology eliminates the problem of greenhouse gas emissions and thereby offers a more environmentally sustainable solution. In terms of operation, rather than relying on the compression and expansion of a fluid, solid-state systems exploit caloric effects, i.e., reversible temperature changes exhibited by certain materials when an external field is applied and subsequently removed. Depending on the type of external field, the caloric effect

can be classified as elastocaloric (induced by uniaxial tensile stress), magnetocaloric (magnetic field), electrocaloric (electric field), or barocaloric (hydrostatic pressure). Despite the environmental advantages, the cooling performance of solid-state technologies remains inferior to that of vapour-compression systems, and substantial advancements are still necessary to render them competitive with established cooling technologies [9].

Among solid-state cooling technologies, elastocaloric cooling is particularly noteworthy for its potential to achieve significant energy savings relative to other caloric effects [10]. Indeed, in 2014 the U.S. Department of Energy identified it as the most promising alternative to vapour-compression systems [9]. Within elastocaloric materials, natural rubber (NR) stands out due to its unique combination of nontoxicity, low cost, softness, long fatigue life, and excellent caloric performance, which arises from the synergistic contributions of thermoelasticity and strain-induced crystallization. Nevertheless, research on the refrigeration potential of NR is still in its infancy, and not all parameters influencing the elastocaloric behaviour of this material are fully understood. Only by identifying these key parameters it will be possible to optimize the cooling performance of NR and to advance an elastocaloric cooling technologies capable of competing with existing solutions.

The objective of this thesis was to investigate how the rubber network structure and rubber formulation influence the elastocaloric properties of NR-based systems. In the first part of the study, the effect of crosslinking density on the cooling capacity of NR was evaluated to identify the most promising degree of crosslinking. Subsequently, the potential of nanofillers, specifically nanoclays, to further enhance the cooling capacity of the optimal NR formulation was assessed, focusing on their ability to promote strain-induced crystallisation.

## *1.2 Thesis outline*

This thesis is divided into seven chapters. After the introduction in Chapter 1, Chapter 2 provides an overview on air cooling technologies, highlighting the environmental and energy-related issues associated with conventional vapour-compression systems. The chapter then presents a comprehensive literature review on solid-state cooling as a sustainable alternative, discussing its advantages and limitations, with a particular focus on elastocaloric cooling in elastomeric materials. The properties of elastomers (i.e., elasticity, the Mullins effect, strain-induced crystallization etc), are discussed alongside a thermodynamic explanation of the elastocaloric effect. Natural rubber is examined in detail, with a review of the current state of research on its elastocaloric performance. Chapter 3 presents the materials used in this study (i.e., natural rubber, rubber additives, solvents, nanoclays) and describes the characterization techniques employed, emphasizing the set-ups and the methods used to evaluate the elastocaloric effect. In Chapter 4, natural rubber formulations with different crosslinking densities are prepared and characterized, with a focus on understanding the relationship between crosslinking density and elastocaloric performance. Chapter 5 explores the incorporation of nanoclay fillers into the optimal natural rubber formulation and evaluates their effect on enhancing the cooling capacity. Chapter 6 summarizes the main conclusions of the work and provides recommendations for future research, while Chapter 7 reports the results of an additional activity carried out during the PhD.

# 2 Scientific Background

## *2.1 Air cooling technology*

Air cooling technology refers to conventional cooling systems, such as vapour compression air conditioners and fans, that cool air by mechanical or refrigerant-based means. Air conditioning units (ACs) are specifically designed to regulate the temperature and humidity of indoor spaces, and to preserve vital resources such as food and medicine. With the increase in global average temperatures and increasingly frequent heat waves, the creation of a more comfortable interior environment has become crucial for guaranteeing the survival of billions of people globally [5,11].

Figure 2.1 illustrates how the demand for air conditioners has skyrocketed in recent decades, especially in regions with severe weather, and forecasts the number of air conditioners until 2050.

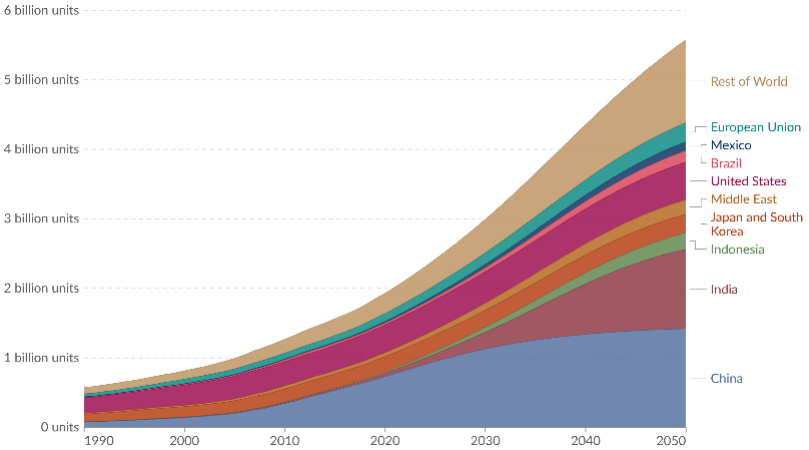


*Figure 2.1. Evolution of air conditioner demand by country and year [12].*

According to the International Energy Agency (IEA), at the end of 2016, 1.7 billion air conditioners were in use worldwide, and by 2050 that number is expected to rise to 5.6 billion, with China, India and

Indonesia accounting for half of the total number [9]. This scenario illustrates how crucial air conditioning is to shield the population from the growing risks associated with climate change.

### 2.1.1 Vapour compression refrigeration systems

Among the commercially available air-cooling technologies, the vapour compression system is the most widely used. This technology is applied in a wide range of devices, from small household refrigerators to large-scale systems that provide many megawatts of cooling capacity for industrial complexes [13].

At the heart of these systems is the working fluid, the refrigerant, which transfers heat through phase changes (boiling and condensation). Specifically, the circulating refrigerant is used as the medium that, through the expense of external work and its phase changes, absorbs and removes heat from the space to be cooled and rejects the heat elsewhere [13]. Vapour compression systems are based on four components: a compressor, a condenser, an expansion device and an evaporator [14]. Figure 2.2 shows a scheme of a vapour compression refrigeration cycle.

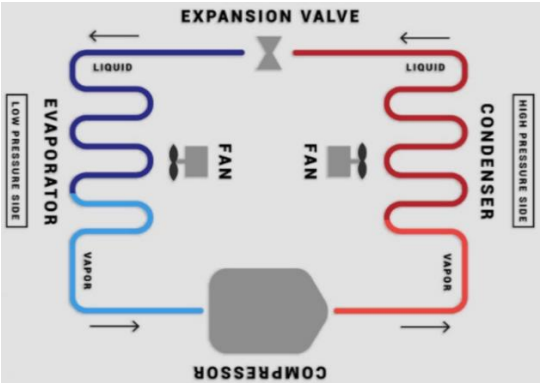


*Figure 2.2. Refrigeration cycle of a vapour compression refrigeration system [14].*

The refrigeration cycle operates as follows:

- In the first stage of the refrigeration cycle, the refrigerant enters a *compressor* as a low-pressure vapour. The compressor raises both the pressure and temperature of the refrigerant and sends it to the *condenser* [14].
- In the *condenser*, the refrigerant flows through a series of S-shaped tubes to which air from the outdoor environment is blown across by a fan. Because the outdoor air is cooler than the refrigerant, heat transfers from the tubing to the cooler air. This heat transfer causes the hot vapour refrigerant to condense back to a liquid. The refrigerant, in a high-pressure liquid state, then leaves the *condenser* and moves on to the metering and expansion stage of the cycle [14].
- The *metering device* maintains high pressure on the inlet side while expanding the liquid refrigerant and lowering the pressure on the outlet side. During expansion, the temperature of the liquid refrigerant decreases [14].
- In a cool, low-pressure liquid state, the refrigerant leaves the metering device and enters coiled tubes in an *evaporator*, across which warm air from the conditioned space is blown by fans. The refrigerant absorbs the heat from the warmer air, reducing the temperature in the conditioned space. Meanwhile, the refrigerant begins to boil and changes to a low-pressure vapour. The low-pressure vapour is then pulled back into the compressor, and the cycle starts over. This cycle continues until the conditioned space reaches the desired temperature [14].

The vapour compression cooling technologies present several strengths:

- Vapour compression enables the implementation of large-scale plants that can manage significant amounts of heat

exchange due to the high latent heat of vaporization of the refrigerant gases used.
- The technology is already widely utilized, standardized, and available.
- A wide range of gases can be used in this process, making it applicable to a broad range of temperatures, even approaching 0 K.
- The manufacturing of compression plants involves relatively inexpensive and easily obtainable materials and chemicals.

However, it is noteworthy that gas compression technology also presents certain energy and environmental issues that need to be taken into account, which will be discussed in the following paragraph.

### 2.1.2 Environmental impact of vapour compression technology

Despite the countless benefits, ACs based on vapour-compression technology consume large amounts of electricity and rely on refrigerant fluids with high Global Warming Potential (GWP) that are partially released into the environment during their lifespan [5,11]. AC systems are indeed prone to refrigerant leaks over time. This can occur for many reasons, including improper installation or maintenance and ageing of the equipment. In addition, if air conditioners at the end of their life are not disposed of properly or are illegally dismantled, refrigerant fluids can flow out during the dismantling. When the coolants are released into the environment, they have a severe environmental impact and contribute significantly to greenhouse gas emissions [5,11]. With respect to electricity consumption, the IEA estimates that “space cooling”- for the most part air conditioners but also fans- consumed around 2100 terawatt-hours (TWh) of power in 2022 [15]. For context, global electricity use in 2022 was around 29000 TWh. That means ACs use around 7% of the world’s electricity, nearly 20% of electricity use in buildings.

Figure 2.3 shows the growth in electricity demand for ACs since 2000 [15].

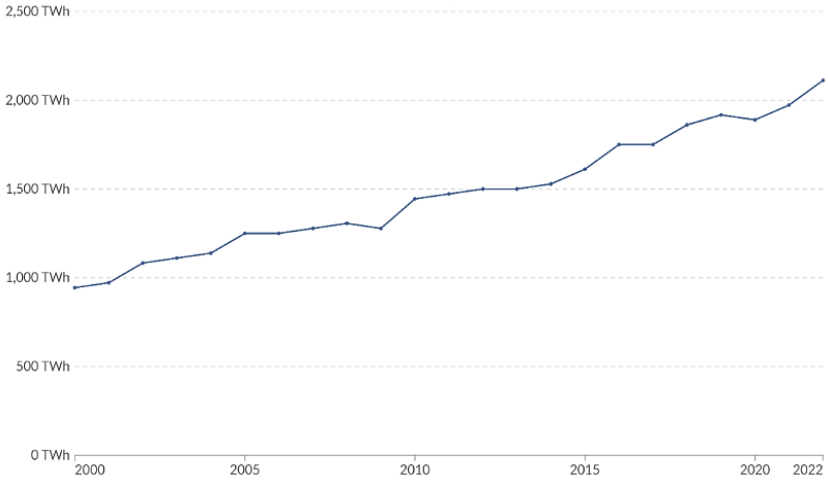


*Figure 2.3. Electricity use for space cooling, which includes fans but is mostly air conditioning [15].*

It is possible to observe that the electricity demand for ACs has doubled in 22 years, with an increase of about 4% per year since 2000.

The refrigerants currently employed in ACs belong to the hydrofluorocarbon (HFCs) family, among which R32, R407c and R134a can be mentioned. These compounds are the result of a series of progressive substitutions that have taken place over the years, starting from the early 20$^{th}$ century. Over time, refrigerants have been gradually replaced due to their environmental impact and the introduction of increasingly strict regulations. As shown in Figure 2.4, four generations of refrigerant fluids can be identified.

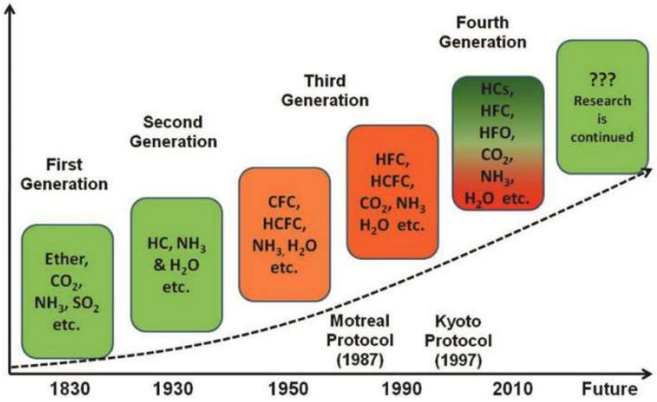


*Figure 2.4. History of refrigerant fluid generations [16].*

The first generation, which covers the period 1830-1930, relied on refrigerants such as ammonia, sulfur dioxide and methyl chloride. Although effective, these refrigerants were flammable or toxic, restricting their use mainly to industrial systems [13]. The demand for safer refrigerants, suitable for use in home and public spaces, prompted the development of chlorofluorocarbons (CFCs) and hydrochlorofluorocarbons (HCFCs), a class of halogenated compounds also known as “freons” [13,16]. These second-generation refrigerants were non-flammable and had low toxicity, making them seemingly perfect refrigerants. However, it was later discovered that these fluids were responsible for damaging the ozone layer and were banned by the Montreal Protocol in 1987. In 1990, the cooling system industry transitioned to third-generation refrigerants, i.e., HFCs. Although the HFCs contain no chlorine and therefore have no ozone depletion potential (ODP), they retained the heat-trapping characteristics of the CFCs and HCFCs [13,16]. By the early 2000s, the potential climate impacts of the HFCs were being considered. A further amendment to the Montreal Protocol, known as the Kigali Amendment, was negotiated in 2016. It phased down the high GWP

HFCs, setting the goal to gradually reduce HFC use by 80–85% by 2036 [13]. As a result, the refrigeration sector is once again seeking alternatives, i.e., the fourth generation of refrigerants. Current research focuses on hydrofluoroolefins (HFOs) and, in some cases, the reconsideration of certain first-generation natural refrigerants, each offering distinct advantages and disadvantages [13,16].

### 2.1.3 Alternative solutions

Although vapour compression cycles have achieved extensive success in air conditioning since their invention, the rising cost of electricity and environmental concerns have increased interest in developing alternative and more sustainable cooling technologies. Solid-state cooling has emerged in recent years as an alternative, greener cooling technology. It refers to cooling technologies that use solid materials and physical effects to transfer heat without involving traditional refrigerants, compressors, or moving mechanical parts [17]. By employing solid refrigerants, this new technology eliminates the problem of greenhouse gas emissions and thereby offers a more environmentally sustainable solution and advantages such as compactness, reliability, and precise temperature control. These alternative technologies include:

- *Thermoacoustic cooling*. This technology converts acoustic energy into cooling by exploiting temperature changes caused by sound wave-induced pressure variations in the gas. Acoustic waves cause the gas to expand and contract. As the gas expands, its pressure and temperature are reduced. Likewise, as the gas contracts, its pressure and temperature are increased [17,18].
- *Thermoelectric cooling*. It operates on the principle of the Peltier effect, where an electric current passing through two different types of semiconductors (p-type and n-type) causes heat to be absorbed at one junction and released at the other. This creates a temperature difference, with one side

becoming cold and the other hot. The cold side can be used for cooling [17].

- *Caloric cooling*. It relies on reversible thermal effects induced in certain materials by the application or removal of external fields. These fields cause large isothermal entropy change or adiabatic temperature changes in the materials, enabling cooling without traditional refrigerants or compressors [17].

Among these solid-state cooling technologies, caloric cooling is developing rapidly and is the most promising refrigeration technology to replace traditional ones. The following paragraph will present this new cooling technology in detail.

## *2.2 Solid state cooling based on caloric effects*

In recent years, solid-state cooling technology has emerged as a promising alternative to conventional vapour-compression refrigeration systems. The primary distinction lies in the type of refrigerant used: while vapour-compression systems employ fluids, solid-state cooling relies on caloric materials. These are solids that undergo reversible and significant entropy changes when an external field, such as electric, magnetic, or mechanical, is applied or removed. When this external field varies adiabatically, the resulting entropy change produces significant temperature variations in the caloric material, which form the basis for solid-state refrigeration [8,19,20]. Specifically, the material heats up when the external field is applied and cools down when it is removed [21].

The temperature difference ($\Delta T$) generated by applying or removing the stimulus quantifies the strength of the caloric effect. A larger entropy change induced by the external field results in a greater temperature change and, consequently, a stronger caloric effect. Typically, entropy changes range from 10 to 100 J/kg·K, while the corresponding temperature variations lie between 3 and 50 °C [19].

By effectively exploiting the temperature variation induced by the external field, an alternative refrigeration cycle to conventional methods can be developed.

Caloric effects are classified as magnetocaloric, electrocaloric, elastocaloric and barocaloric depending on the nature of the caloric material and the external stimulus. The caloric material could be a metal alloy, ceramic, or polymer with unique composition and structural characteristics that enable the expression of the caloric effect.

From a thermodynamic perspective, caloric effects can be generalized using the Maxwell relations derived from the Gibbs free energy [22]. The total entropy of a caloric system S(T, Y) is a function of both temperature (T) and the generalized external field (Y), which represents the magnetic field (B), electric field (E), force (F), or pressure (p).The isothermal entropy change ($\Delta S_{iso}$) resulting from a field variation from $Y_1$ to $Y_2$ can be expressed as reported in Equation (2.1) [22]:

$$\Delta S_{iso}(T, \Delta Y) = \int_{Y1}^{Y2} (\partial X / (\partial T))_Y \, dY \qquad (2.1)$$

where X is the conjugate variable corresponding to the applied field.

The resulting adiabatic temperature change ($\Delta T_{ad}$) is given by Equation (2.2) [22]:

$$\Delta T_{ad}(T, \Delta Y) = -\int_{Y_1}^{Y_2} \frac{T}{C} \left( {}^{\partial X}/_{\partial T} \right)_Y dY \qquad (2.2)$$

Where C is the heat capacity of the material. The specific variables for each caloric effect are summarized in Table 2.1:

*Table 2.1. External stimulus and conjugated variables for the different caloric effect.*

| Effect | External Stimulus (Y) | Conjugate variable (X) |
|---|---|---|
| Magnetocaloric | Magnetic field (B) | Magnetization (M) |
| Elettrocaloric | Electrical field (E) | Polarization (P) |
| Elastocaloric | Uniaxial force (F) | Displacement (l) |
| Barocaloric | Hydrostatic pressure (p) | Volume (V) |

Regardless of the caloric material being used, the steps involved in expressing the caloric effect can be divided into four distinct phases:

1 *Adiabatic application of the external stimulus*. The rapid application of the external field results in an increase in the temperature of the material under adiabatic conditions.
2 *Heat transfer*. While maintaining the application of the external stimulus, the material releases the generated heat to the surrounding environment, reaching thermal equilibrium.
3 *Adiabatic removal of the external stimulus*. The removal of the external stimulus induces the cooling of the material under adiabatic conditions to temperatures lower than the external environment.
4 *Heat transfer*. The material reaches thermal equilibrium with the environment, extracting heat from the surroundings.

By separating the heating (phase 2) and cooling (phase 3), the caloric cycle can be exploited for both heat pumping and cooling applications [21]. Infrared thermography is often used to accurately monitor the temperature variations throughout the cycle. The determination of the temperature variations enables the calculation of the heat extracted/released (for example, by using Newton's law of cooling [23]) and the analysis of the performance of the caloric material.

To identify the most promising caloric materials for the development of solid-state cooling technology, their cooling capacities must be compared. The most accurate comparison between two caloric materials exhibiting the same caloric effect involves evaluating their adiabatic temperature variations and isothermal entropy changes under identical field intensities and environmental conditions. However, such direct comparisons are often unfeasible due to limited available data. Consequently, comparisons are commonly made using $\Delta T$ and $\Delta S$ values normalized by the applied fields [24]. This approach, however, must be applied carefully, as it may lead to erroneous conclusions.

The coefficient of performance ($COP_{mat}$) is another key index to compare the cooling performance of caloric materials. It is generally expressed as reported in Equation (2.3):

$$COP_{mat} = \frac{Q_{ab}}{W} \tag{2.3}$$

where $Q_{ab}$ is the heat removed from the environment, and W is the external work done to vary the intensity of the applied field. The larger the $COP_{mat}$, the better the refrigeration efficiency of the material [9]. However, $COP_{mat}$ is not always calculated uniquely across the literature, with different authors using varying equations, which complicates direct comparison between caloric materials.

In conclusion, solid-state cooling offers several advantages compared to gas compression systems. First, it is environmentally friendly, as it avoids the use of hazardous coolants. Second, since the refrigerant is solid, it enables compact cooling systems. Such systems are both cost- and space-efficient for transportation and storage, and they can be integrated into devices like laptops and batteries through micro-cooling technologies [25]. However, the $COP_{mat}$ of solid-state refrigeration technologies remains relatively low compared to vapour-compression systems, requiring further improvement.

In the following sections, the different caloric effects will be presented and described in detail, along with their advantages and disadvantages.

### 2.2.1 Magnetocaloric effect

Out of the caloric effects, the magnetocaloric effect is the one that has been studied the most. It is defined as the adiabatic and reversible temperature change of a magnetic material caused by the rapid application or removal of a magnetic field (B). The variation in the magnetic field influences the arrangement of electron spins in the material, thereby altering its magnetic entropy ($S_m$) [26]. This change in entropy, which arises primarily from the configurational nature of the electron spins, is responsible for the temperature variation of the material. The scheme of the magnetocaloric effect is shown in Figure 2.5.

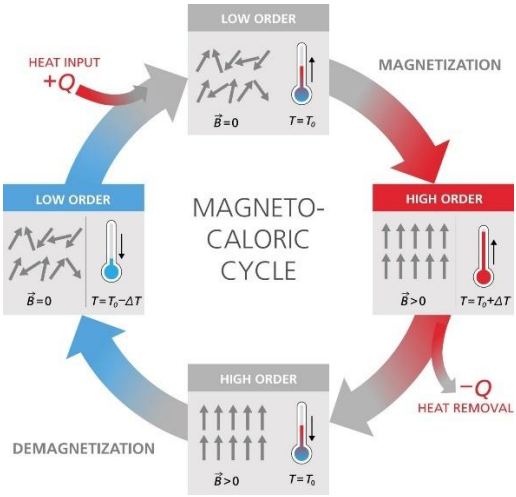


*Figure 2.5.Scheme of the magnetocaloric effect [27,28].*

The magnetocaloric cycle can be explained as follows [22]:

1. When no magnetic field is applied, the magnetic moments in the material are randomly oriented. Instead, when a magnetic field is applied to the magnetocaloric alloy, the magnetic moments align and the material is magnetized. The material experiences a negative entropy variation since the state of the magnetic moments changes from disordered to ordered and, as a consequence, it heats up.
2. The heat of the magnetic material is released to the external environment. In this phase, the magnetic field continues to be applied and is kept constant to avoid a change in entropy of the system.
3. When the magnetic field is removed, the magnetic domains freely reorient and the material is demagnetized. The state of the magnetic domains changes from order to disorder, and the material experiences a positive entropy variation. As a consequence, the magnetic material cools down.
4. The magnetic material absorbs heat from the surroundings. In this phase, the magnetic field is null and the magnetic domains of the material are randomly oriented.

Equation (2.1) and (2.2) evidence that the larger the magnetization variation versus T, the higher is the magnetocaloric effect. Using magnetic materials close to one of their transitions is desired to enhance the cooling effect. Examples of magnetocaloric materials are Gadolinium (Gd) and its alloys, rare earth elements (Dysprosium (Dy), Erbium (Er), Holmium (Ho)), Manganese-based compounds and Heusler alloys. Among these, Gadolinium (Gd) has been widely investigated. It exhibits an adiabatic temperature change of 60 °C under magnetic fields on the order of 60 T [16].

The main advantages of the magnetocaloric effect include the absence of moving parts and the potential for miniaturization, making it particularly attractive for applications such as cooling small electronic components [29]. However, significant drawbacks remain. Achieving a meaningful cooling capacity requires very high magnetic

fields, which are expensive to generate. Furthermore, the material composition poses challenges, as magnetocaloric alloys frequently rely on rare earth elements [29].

### 2.2.2 Electrocaloric effect

The electrocaloric effect refers to the change in entropy and temperature that a polar material experiences when subjected to a variation in electrical field. Typical materials reporting electrocaloric effects are ferroelectric perovskite-like ceramics, such as $PbSc_{0.5}Ta_{0.5}O_3$, $(1-x)Pb(Mg_{1/3}Nb_{2/3})O_{3-x}PbTiO_3$, $PbZr_{0.95}Ti_{0.05}O_3$ or $BaTiO_3$ [30]. The scheme of the electrocaloric effect is shown in Figure 2.6.

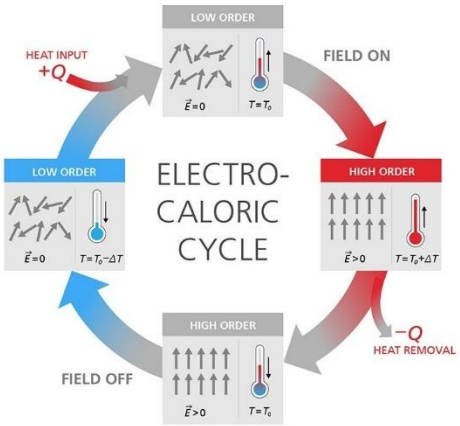


*Figure 2.6. Scheme of the electrocaloric effect [31].*

The electrocaloric cycle can be explained as follows [22]:

1. When an external electrical field is adiabatically applied, the material is polarized due to the alignment of the dipoles. The system's entropy decreases as the state of the dipole changes from disorder to order, and, as a result, the temperature of the polar material rises.

2. The heat of the polar material is released to the external environment. In this phase, the electrical field continues to be applied and is kept constant to avoid a change in entropy of the system.
3. When the electrical field is removed, the material depolarized. The state of dipoles changes from ordered to disordered, and the material experiences a positive entropy variation. As a consequence, the polar material cools down.
4. The material absorbs heat from the surroundings. In this phase, the electrical field is null and the dipoles of the material are randomly oriented.

This effect depends on the change in polarization and is closely related to other electrothermal (pyroelectricity) and electromechanical (piezoelectricity) effects.

It is possible to notice from Equation (2.1) and (2.2) that a large variation of the polarization versus T is necessary to increase the $\Delta T_{ad}$. The optimal point for investigating the electrocaloric effect is in proximity to the Curie temperature, near the paraelectric–ferroelectric phase transition, where entropy is more susceptible to change. However, other phase transitions can be explored, such as the antiferroelectric-ferroelectric phase transition [30].

The main advantage of electrocaloric cooling is the relatively large electrocaloric effect that can be achieved under comparatively low electric fields. Moreover, applying an electric field is technically simple and cost-effective [16]. However, it is important to note that the material's Curie temperature limits the temperature range in which they can operate. Indeed, the electrocaloric effect occurs at temperatures different from ambient temperature and requires complex material synthesis processes to minimize impeding leakage currents, also for modest electrical fields of $10^1$-$10^2$ KV/cm [19]. Additionally, the materials used in this process must be ferroelectric and dielectric, with high breakdown strength, which can be a

limitation. Moreover, many of these materials contain a large amount of lead, which must be considered for environmental and safety reasons. The research is now focusing on lead-free compounds such as $BaTiO_3$ and Polyvinylidene fluoride (PVDF)-based polymers, for example Poly(vinylidene fluoride-trifluoroethylene-chlorofluoroethylene (P(VDF-TrFE-CFE)) [30].

### 2.2.3 Mechanocaloric effect

Mechanocaloric effect refers to the thermal response of a solid induced by changes in its mechanical state. Depending on the nature of the applied mechanical field, mechanocaloric effects are classified into elastocaloric and barocaloric effects. In this section, the elastocaloric effect is introduced first, followed by a discussion on the barocaloric effect.

The elastocaloric effect refers to a change in entropy and temperature that occurs in a solid material when a uniaxial mechanical stress is adiabatically applied or removed. To produce a significant temperature change, the material must experience a large entropy variation during deformation. Depending on the material, this entropy variation may arise from a stress-induced phase transformation or from a transition between amorphous and crystalline states. Elastomers and shape memory alloys (SMAs) are the most researched materials that exhibit the elastocaloric effect. However, in the last few years, families of other materials have been reported to exhibit elastocaloric effect, such as organic-inorganic polymers, multiferroics and fast-ion conductors [19]. In 2014, the U.S. Department of Energy identified elastocaloric refrigeration as the most promising alternative to vapour-compression systems [9]. Figure 2.7 shows the scheme of the elastocaloric effect.

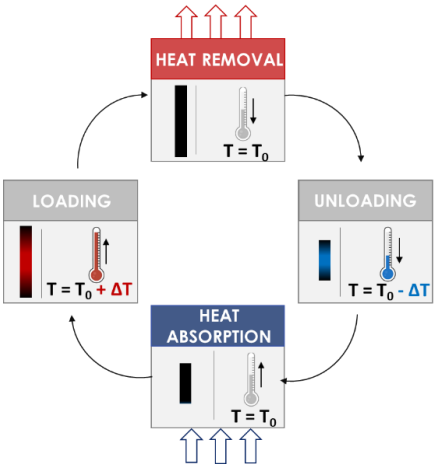


*Figure 2.7. Scheme of the elastocaloric effect [32].*

A standard elastocaloric cycle for SMAs and elastomers involves the following steps:

1. When no external force is applied, elastomers exist in a high-entropy state due to the random configuration of their polymer chains, while SMAs are in their austenitic phase. The application of an external uniaxial stress decreases the entropy and raises the temperature of both materials. In SMAs, this is caused by a stress-induced exothermic transformation from the austenitic to the martensitic phase, accompanied by the release of latent heat. In elastomers, the entropy change arises from the stress-induced orientation of polymeric chains and/or from strain-induced crystallization (SIC), i.e., partial crystallization that occurs as a response to deformation.
2. The heat of the elastocaloric material is released to the external environment. In this phase, the uniaxial stress continues to be applied and is kept constant to avoid a change in entropy of the system.

3. When the external force is removed, the materials restore their original shape, resulting in a positive entropy variation and thus a decrease in temperature. Specifically, SMAs transform back to the austenite phase while elastomers return to their initial high-entropy state. If they are developed, the crystalline domains melt.
4. Finally, the cooled materials are brought into thermal contact with the environment to absorb heat.

Through the cyclical loading and unloading of the materials, a refrigeration cycle could be developed [32]. The elastocaloric effect can be induced with both compressive and tensile stress, but the most commonly used is definitely uniaxial tensile stress. One of the defects of this solid-state cooling is the presence of moving parts, which usually leads to devices that cannot be miniaturized and have potential problems of wear and vibration. Similarly to the magneto- and electrocaloric effect, a large variation of l and F versus T are required to obtain large $\Delta T_{ad}$.

To be considered a good elastocaloric material, certain criteria must be met. These include exhibiting a large latent heat, a significant adiabatic temperature change under the application of moderate uniaxial stresses, good thermal conductivity, a long fatigue life, and affordability. Additionally, such materials must be widely available, have a minimal environmental impact, and generate an elastocaloric effect with low levels of stress [33]. Unfortunately, no current material fully satisfies all these requirements, necessitating trade-offs. SMAs, including Ni-Ti alloys, copper-based alloys, iron-based alloys, and ferroelectric materials, can achieve temperature variations of up to 48°C and have discrete thermal conductivity values [19]. The elastocaloric effect is achieved with minimal material deformations (2-10%) and stresses in the range of 400-900 MPa. However, such high stresses are a significant limiting factor in the applications of the materials. Additionally, the cost of the material itself is another constraint, as the alloys in question necessitate the use of expensive

metals. In the pursuit of a solution to these challenges, elastomers were considered. Natural rubber, silicone rubber and thermoplastic polyurethane (TPU) are among the most studied. These materials can achieve temperature variation up to 10-20 °C, and the tensile stresses required for the expression of the elastocaloric effect are of only several MPa, which is two orders of magnitude lower than for SMAs. Additionally, the cost of elastomers is generally lower than that of SMAs. However, elastomers need to be stretched several times their original length, which is a drawback for the development of a compact cooling device [34]. A comparison between the elastocaloric performances of NR, the most interesting elastocaloric polymer, and SMAs is reported in Table 2.2.

*Table 2.2.Elastocaloric performance of SMAs and Natural Rubber [34].*

| | SMAs | Natural Rubber |
|---|---|---|
| Cost (€/kg) | 100 | 1.5 |
| Fatigue strength up to $10^7$ cycles | strain amplitude 1.5% | strain amplitude 200% |
| Stress, σ (MPa) | Several hundreds of MPa | Several MPa |
| Strain, ε (%) | 2-10% | 300-500% |
| Thermal conductivity (W/mK) | 5.5 | 0.13 |
| $\Delta T_{ad}$ (K) | 20 | 9 |
| $\Delta S$ (kJ/kgm$^3$) | 240 | 54 |
| $\Delta T_{ad}/ \sigma$ (K/GPa) | 13-45 | 5600 |
| $\Delta T_{ad}/ \varepsilon$ (K) | 300 | 1.5 |

SMAs and elastomers have the advantage over magnetocaloric and electrocaloric materials in being less expensive and non-toxic. The

issues that need to be overcome are the heat dissipation during deformation and the generation of heat due to internal friction (specifically in the case of elastomers). In addition, disadvantages associated with the structural stability, mechanical fatigue and phase-transition hysteresis, which lead to irreversibility issues, may negatively affect the cooling performance.

The barocaloric effect is the most recently discovered of the caloric effects. It was first observed during the study of other caloric materials, particularly magnetocaloric ones [35]. It refers to the entropy and temperature change that occurs in a solid material following an adiabatic variation of the applied hydrostatic pressure. To produce a significant temperature change, the material must experience a large entropy variation during the hydrostatic compression, which can sometimes involve phase transitions. Barocaloric materials can be classified into four categories: intermetallic compounds, ionic compounds, organic-inorganic hybrid materials and organic compounds (for example, Natural Rubber and Polydimethylsiloxane). The transitions these materials could undergo upon the application of the hydrostatic pressure could be first-order phase transitions, order-disordered phase transitions, ionic order transitions, ferroelectric or ferromagnetic phase transitions [35]. Figure 2.8 shows the scheme of the barocaloric effect.

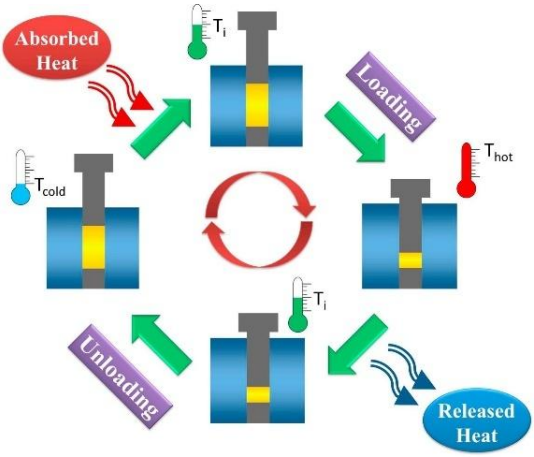


*Figure 2.8. Scheme of the barocaloric effect [36].*

A standard barocaloric cycle involves the following steps:

1. The adiabatic application of a hydrostatic pressure promotes a positive entropy variation in the material, which, as a consequence, heats up.
2. The applied pressure is kept constant, and the heat flows from the material to the environment. The material temperature decreases to the initial temperature.
3. Next, the pressure is adiabatically released. The material experiences a negative entropy variation and cools down.
4. Finally, the material absorbs heat from the surroundings and its temperature gradually increases, reaching thermal equilibrium.

Large barocaloric effects occur near phase transformations that render sizable volume changes.

As well as the elastocaloric effect, all elastomers can act as barocaloric materials due to the contribution of polymer chain rearrangements. One of the main drawbacks of this technology is the

elevated pressure required, reaching values close to 500 MPa for some barocaloric compounds [19].

### 2.2.4 Comparison of caloric effects

In Table 2.3, some representative values of driving fields, adiabatic temperature change at field removing ($\Delta T_{cool}$) and heat absorbed per unit volume of material are reported for each caloric effect. All values referred to calculation performed at room temperature.

*Table 2.3. Comparison of the cooling performance of representative caloric materials.*

| | **Material** | **Field** | **$\Delta T_{cool}$ (°C)** | **$Q_{ab}$ (J/cm$^3$)*** | **Ref.** |
|---|---|---|---|---|---|
| Magnetocaloric effect | Gd | 2-60 T | 5-60 | 9-110 | [16,37] |
| Electrocaloric effect | $BaTiO_3$ (thin film) | 500-800 kV/cm | 2-5 | 6-15 | [38] |
| | P(VDF-TrFE-CFE) | 1000-3000 kV/cm | 2-12 | 5-30 | [34,39] |
| | $PbSc_{0.5}Ta_{0.5}O_3$ (thin film) | 60 kV/cm | 4 | 13 | [40] |
| Elastocaloric effect | Ni-Ti | 600-700 MPa | 17-23 | 55-75 | [19,34] |
| | NR | 1-10 MPa | 3-9 | 5-14 | [34,41-45] |
| Barocaloric effect | $Fe_{49}Rh_{51}$ | 110 MPa | 9 | 26 | [19] |
| | $C_5H_{12}O_2$ | 50-500 MPa | 5-40 | 9-68 | [19] |

* In the majority of the cases, the heat absorbed per unit volume of material has been estimated knowing the $\Delta T_{cool}$, the density and specific heat capacity of the materials

As previously discussed, magnetocaloric, electrocaloric, and barocaloric materials exhibit high cooling performance, in terms of $\Delta T_{cool}$ and $Q_{ab}$, but require very high driving fields, which may limit

their practical implementation in real solid-state cooling devices. A similar consideration applies to SMAs when used as elastocaloric materials. Conversely, elastomers, specifically NR, although exhibiting lower caloric performance, is particularly attractive due to the significantly lower driving fields required to trigger its elastocaloric response.

## *2.3 Elastomers*

Elastomers are a class of natural or synthetic polymeric materials characterized by a glass transition temperature generally between -50 °C and -70 °C [46]. Common example includes natural rubber (NR), polybutadiene (BR), ethylene-propylene rubber (EPR), and ethylene propylene diene rubber (EPDM). From a structural point of view, elastomers are composed of long chain-like molecules held together by a network of crosslinks that prevent the gross mobility of the chains while allowing local mobility of the chain segments. The resulting three-dimensional network can be formed via covalent bonds between the polymeric chains, as in thermoset elastomers, or by physical links, typical of thermoplastics. The process used to introduce covalent bonds between the polymer molecules is known as vulcanization [46]. Conventional vulcanization of the most common rubber types generally involves sulphur-based chemical systems and requires the presence of unsaturation in the polymer chains. Other chemical systems can be used, such as organic peroxides, metal oxides, diamine, etc [47].

Due to their structure, elastomers possess the unique ability to stretch to several times their initial dimensions without rupturing and to recoil rapidly to the original shape when the imposed stress is removed [46]. As highlighted in the Ashby diagrams in Figure 2.9(A-C), this exceptional extensibility, combined with low Young's modulus (0.5-3.0 MPa), distinguishes elastomers from the other class of materials [48]. These mechanical properties make them suitable for

a wide range of applications, including seals, gaskets, tyres, and shock absorbers, where the ability to deform and recover is essential.

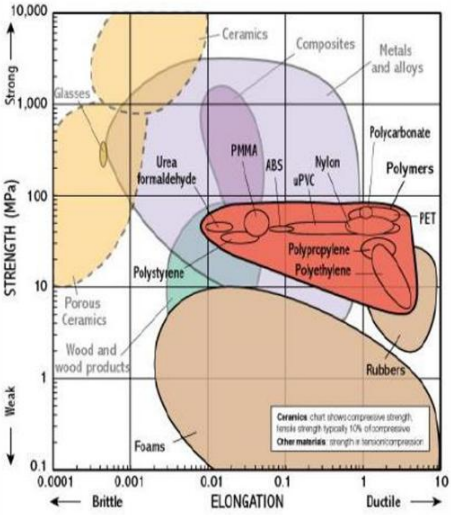


(A)

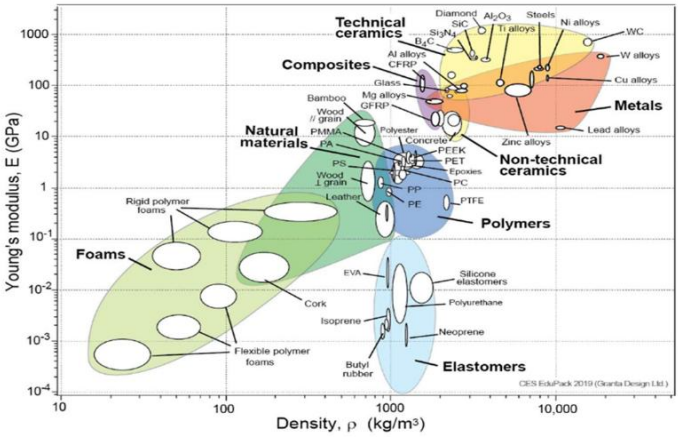


(B)

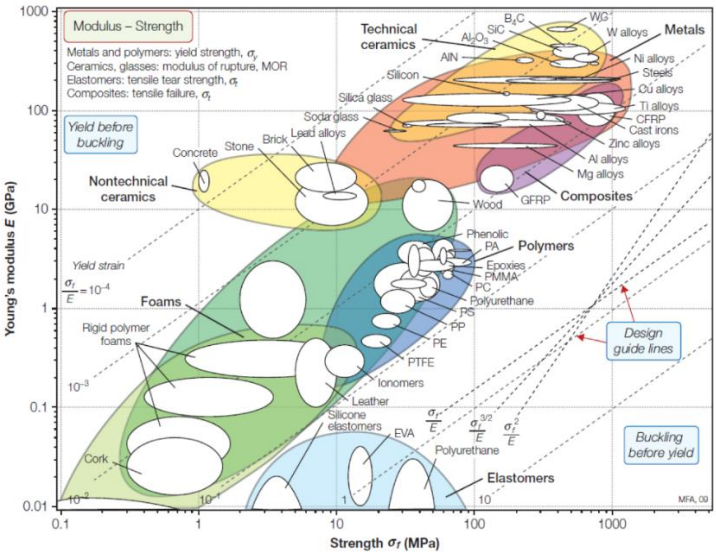


(C)

*Figure 2.9. Ashby diagrams of (A) strength vs elongation, (B) Young's modulus vs density and (C) Young's modulus vs strength of different families of materials [49].*

### 2.3.1 Market Overview

The global elastomers market, primarily led by the Asia Pacific region, is expanding at a healthy clip, driven by innovation, broadening applications, and rising demand across several sectors (Figure 2.10) [50]. In 2024, the global elastomers market size was valued at USD 104.0 billion and is projected to reach USD 141.5 billion by 2030, growing at a compound annual growth rate (CAGR) of 5.3% from 2025 to 2030 [50]. With respect to the applications, elastomers are employed across a wide range of sectors, including automotive, medical, consumer goods, and industrial applications [50]. As depicted in Figure 2.11, which provides an overview of the end use of elastomers in 2024, the automotive segment is definitely the largest user of elastomers. This sector captured the largest revenue share of 41.7% in 2024. The growing use of elastomers in the automotive field is primarily driven by the rising demand for lightweight, durable materials that improve vehicle efficiency and performance.

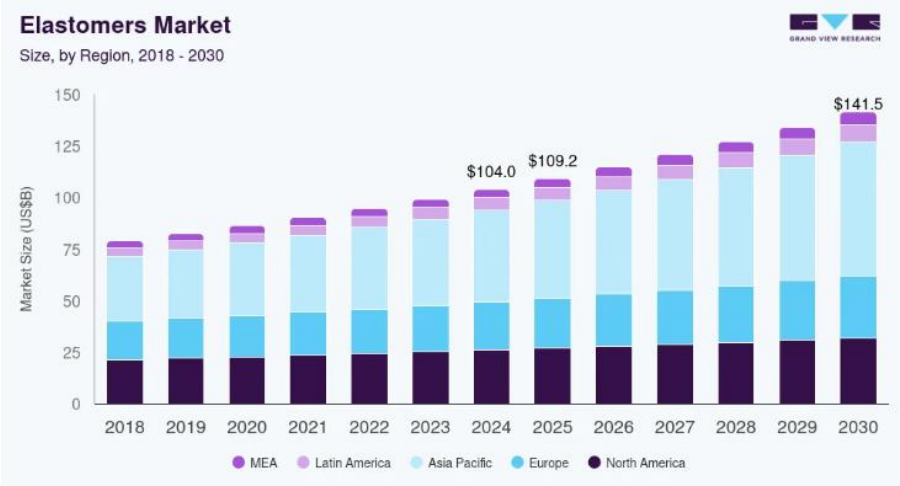


*Figure 2.10.Global elastomer market [50].*

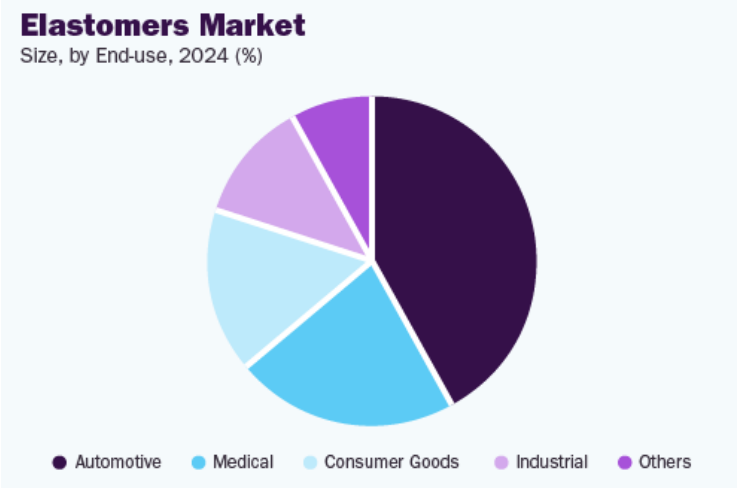


*Figure 2.11. End use of elastomers in 2024 [50].*

### 2.3.2 Classifications of elastomers

Elastomers can be divided into two categories: thermoset elastomers and thermoplastic elastomers (TPEs) [51]. Thermoset elastomers, such as NR, EPDM, and NBR, are characterized by chemical resistance and excellent mechanical and thermal stability that arise from their permanent crosslinked structure. In contrast, thermoplastic elastomers (TPEs), including thermoplastic polyurethane (TPU), styrene-butadiene-styrene (SBS), and styrene-ethylene-butylene-styrene (SEBS), feature physical crosslinking that enables melt reprocessing. TPEs are becoming more and more appealing as sustainable material solutions because, despite their generally poorer performance when compared to thermosets, they have substantial advantages in terms of manufacturing efficiency and recyclability [51]. Although both types are widely used in industry, this PhD thesis will focus on thermoset elastomers, since natural rubber (NR) is the elastomer being researched.

Depending on their performances and properties, thermoset elastomers can be classified into [52]:

- **Elastomers for general purposes**. Diene-based elastomers, such as NR, butadiene rubber (BR), isoprene rubber (IR), styrene-butadiene rubber (SBR), belong to this class [53]. The presence of unsaturation in these polymers makes them susceptible to oxygen and ozone attack, and, in addition, they swell in the presence of hydrocarbon solvents. They are characterized by a low cost and discrete performances at low temperatures. They are widely used for tyres.
- **Elastomers for high-performance applications**. EPDM, chloroprene rubber (CR) and NBR are examples of this class. They have a slightly higher cost with respect to the previous ones but present satisfactory performances and resistance to high temperatures [54]. In particular, EPDM rubber presents excellent resistance to oxygen, ozone and weatherability, while NBR has optimal solvent resistance. They are used to produce O-rings, seals and protective coatings.
- **Special Elastomers**. Silicon rubbers (VMQ, PMQ, PVMQ) and fluorinated rubbers (FPM, FKM) belong to this category. They are characterized by high performance, such as high thermal stability and high resistance to environmental attacks. They are used for pump coatings, oil sealants and textile coatings for equipment exposed to chemical substances [52].

### 2.3.3 Elastomer processing

Elastomers are rarely used in their neat polymeric form. In most cases, to achieve the desired mechanical, thermal, and chemical properties, they are mixed with various additives, shaped into the final product and vulcanized [52,54,55]. The properties of an elastomeric product result from the combination of several factors, including:

- the base rubber
- rubber formulation and additive content
- degree and method of vulcanization
- processing techniques
- final product geometry

Therefore, it is clear that the desired final characteristics of elastomers can only be obtained through careful consideration of all these aspects.

The designation of a specific formulation suitable for the final application of the material is the first step in elastomer processing [54]. The preparation of the formulation is generally carried out at moderate temperatures (40-70 °C) in an operation known as compounding. The elastomer is the principal component, and the amounts of all the other additives are generally expressed in weight per hundred weights of rubber (phr). The most important additives used in rubber production are:

- vulcanizing agents
- accelerators
- antioxidants
- reinforcing agents
- activators
- lubricants and oils

Accelerators are added to the formulation to increase the kinetics of vulcanization and to permit vulcanization to occur at a lower temperature with a greater efficiency. Examples of accelerators are sulphenamides (CBS, TBBS, MBS), thiazoles (MBT), dithiocarbamates, thiurams. Accelerated sulphur systems also required the use of an activator comprising a metal oxide, usually zinc oxide (ZnO), and a fatty acid, commonly stearic acid [56]. Antioxidants are protective agents used to reduce or suppress the deteriorating effect of oxygen, both during the production process and

in the final application. Phenyl betanaphthylamine (PBNA) is an example. Dealing with the reinforcing agents, carbon black is the most used, in particular for tube or tyre production. Finally, oils and lubricants are used to reduce the stiffness of elastomers for processing ease and low cost. All these formulation compounds are mixed in order to obtain a uniform rubber compound in which additives are homogeneously distributed. The mixing equipment used for rubber compounding can be divided into three groups: mills, internal mixers and continuous mixers. An internal mixer and a mix mill are illustrated in Figure 2.12(A, B). Continuous mixers are, in most cases, single or twin extruders [57].

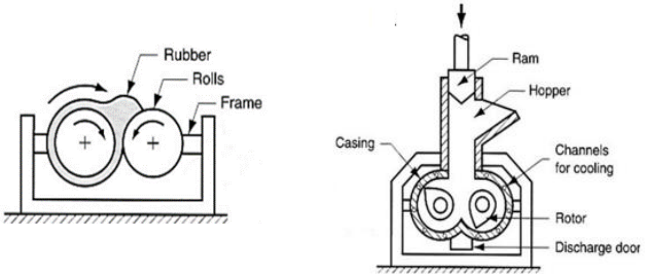


(A) (B)

*Figure 2.12. Mixing equipment used for rubber compounding. (A) Mix mill and (B) Banbury internal mixer [52].*

To prevent premature vulcanization of rubber, mixing generally takes place in two stages. During the first one, additives such as carbon black are mixed with rubber at a temperature around 150 °C. After the rubber has cooled, the additives for vulcanization are introduced and mixed with the rubber [58].

Once the rubber compound is produced, it is shaped into products and heated to a high temperature, usually 150 °C, and high or low pressure to promote the vulcanization. The shaping can occur by [59]:

- extrusion, when a product with a constant cross-section is required, such as pipe, hose, sealing strip and wire covering
- injection moulding is used when a three-dimensional product with a complex shape has to be produced, as a wheel, tyre, sealing ring or shoe sole
- calendering to produce, for example, sheets
- compression moulding
- transfer moulding

Vulcanization temperature and duration strongly depend on the formulation and the desired final properties. This will be discussed in detail in the next paragraph.

### 2.3.4 Vulcanization

Vulcanization is the process by which rubber molecules are chemically crosslinked with an organic or inorganic substance through heat and pressure. Although the crosslinking density, defined as the concentration of chemical crosslinks within a polymer network per unit volume, is low compared to thermoset polymers, the number of crosslinks introduced is sufficient to prevent the irreversible flow of the macromolecules. This reduces the amount of permanent deformation remaining in the material after removal of a deforming force [55,60]. Vulcanization is one of the most crucial procedures in rubber product processing, as the components of the curing system and their proportion affect the vulcanization process and the final mechanical properties of the products [55,61].

The vulcanization characteristics of a rubber compound, i.e., curing time, processability, crosslinking density, etc, are usually determined through rheological analyses, specifically by means of an oscillation disc rheometer. The test is carried out at constant temperature and pressure. The progress of vulcanisation is measured by the increase in the torque required to maintain a given amplitude of oscillation. The increase in torque is proportional to the number of crosslinks

formed per unit volume of rubber, and so to the crosslinking density [55,61]. Figure 2.13 shows an example of a rheometer curve for vulcanization, where the torque is plotted against time.

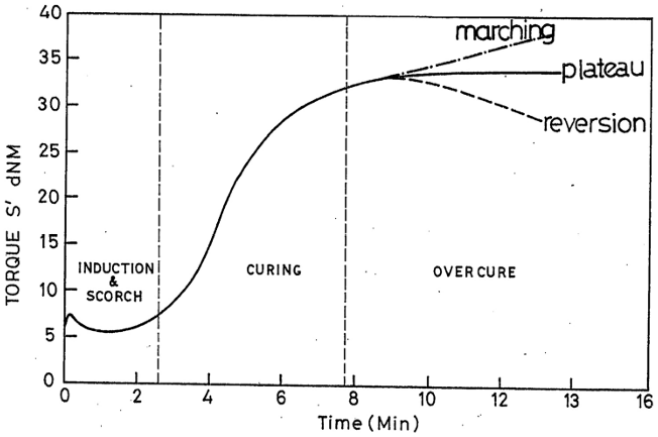


*Figure 2.13. Example of a rheometer curve for vulcanization [62].*

The cure curve gives a complete picture of the kinetics of the vulcanization, which can be divided into three zones: induction and scorch, curing and overcure [63]. The scorch time is measured by the time at a given temperature until the crosslinking reaction starts, and there is a sudden increase in the torque value. All processing and shaping operations of rubber are generally done before this time. In the curing region, permanent crosslinks are formed, which depend on the type and content of the vulcanizing agent, type and content of the accelerator and the temperature. The optimum curing time corresponds to the time at which 90% of the maximum torque is reached. In the overcure region, three scenarios are possible: plateau, reversion (crosslink disappearance) and marching (torque continues to increase with curing time) [55,61].

The parameters that influence the crosslinking density and vulcanization kinetics are:

- temperature
- reactivity of the polymer (microstructure)
- concentrations of crosslinking chemicals (vulcanizing agents, accelerators, etc.)
- type of accelerator

Vulcanization temperature has a significant effect on crosslinking density and structure. Optimum properties are obtained when curing is done at the lowest possible temperature. However, higher temperatures are frequently used to increase productivity [55]. The effect of temperature on the vulcanization kinetics for a certain rubber formulation is shown in Figure 2.14. It is possible to observe that with increasing temperature, the scorch time is reduced, as well as the maximum achievable torque. However, the vulcanization kinetics significantly speed up, and the curing time is reduced.

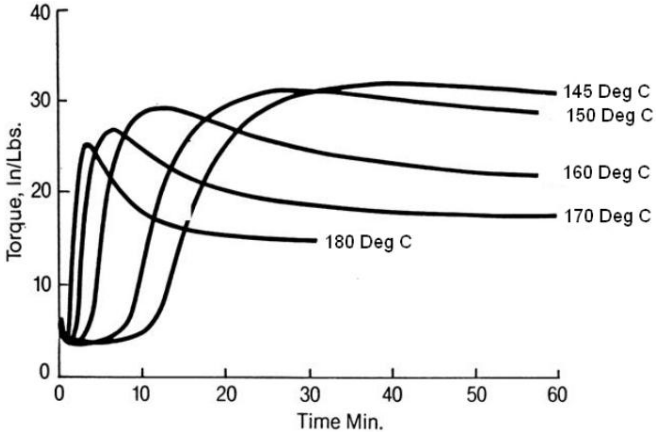


*Figure 2.14. Effect of temperature on the vulcanization kinetics of a rubber formulation [64].*

The type of accelerator selected also plays a pivotal role in the vulcanization kinetics, particularly in the sulphur-based curing systems [55]. In Figure 2.15 the effect of some type of accelerators

on the curing kinetics of NR at 140 °C is shown as an example. For each accelerator, the approximate year of commercial introduction is given in parentheses [61].

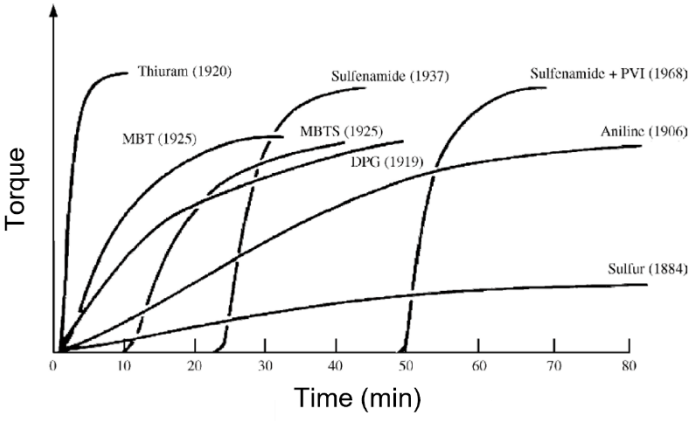


*Figure 2.15. Effect of accelerator on the vulcanization kinetics [61].*

As can be seen, the vulcanisation kinetics change significantly depending on the accelerator used. Generally, dithiocarbamates, such as ZDBC, and thiurams, such as TMTM or TMTD, are ultra-fast accelerators that reduce the scorch time and increase cure rate compared to thiazole accelerator or sulfenamide. Thiurams, in particular, often lead to higher crosslinking density.

The crosslinking density, resulting from rubber formulation and vulcanization parameters, plays a critical role in modulating the final mechanical properties of the elastomeric product, as shown in Figure 2.16. Variations in crosslink density directly affect the rubber network architecture, which in turn governs the mechanical properties.

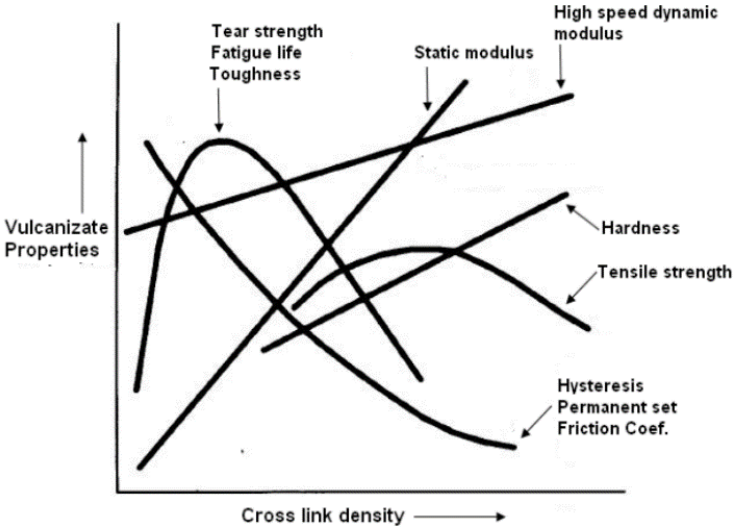


*Figure 2.16. Effect of vulcanization on end-use properties [55].*

Hysteresis, permanent set and friction coefficient are greatly reduced with increasing crosslinking density. Properties like static modulus, high-speed dynamic modulus and hardness increase as the crosslink density increases. The fracture properties, like tensile strength and tear strength, pass through a maximum value as the crosslink density increases and then decrease. These results highlight the crucial role crosslinking density, i.e., vulcanization process and rubber formulation, has on the final properties of the rubber compounds.

Despite the emergence of novel curing systems in recent years, the sulphur-based curing system remains one of the most widely used and economical in the rubber industry (Figure 2.17). In fact, approximately 90% of all rubber products are still manufactured through sulphur vulcanization.

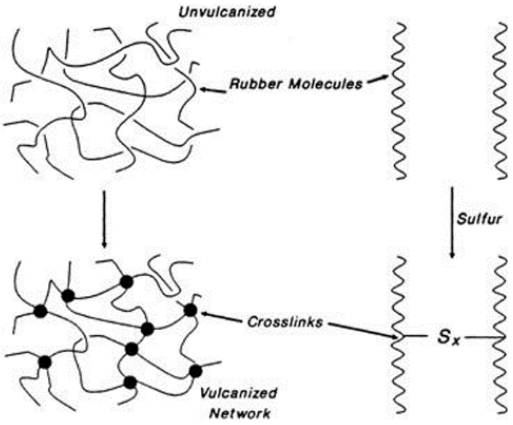


*Figure 2.17. Network formation in a sulphur-based curing system [55].*

Sulphur vulcanization involves a complex reaction mechanism and requires double bonds in the polymer backbone or side groups of the macromolecules. Depending on the sulphur content and the accelerator/sulphur ratio (A/S ratio), three curing systems can be identified [61]:

**Conventional curing systems (CV)**. This curing system is characterized by high sulphur levels (1.5-3.5 phr) and low levels of accelerator (0.4-1.2 phr). The A/S ratio is generally of the order of 0.1-0.6. The vulcanizate mostly presents polysulphidic crosslinks. The CV cure system gives poor reversion, oxidative heat and long-term flex resistance. However, the vulcanizates exhibit good tensile and tear strength, good fatigue and low temperature resistance [61,64,65].

**Efficient curing systems (EV)**. This curing system is distinguished by low sulphur levels (0.4-0.8 phr) and high accelerator contents (2.0-5.0 phr). A/S ratio is generally 2.5-15. The vulcanizate mostly presents monosulphidic crosslinks. The short sulphur crosslinks provide poor tensile and tear strength, poor flex-fatigue life and

abrasion resistance. However, EV cure systems offer good heat ageing and compression set resistance. These cure systems are generally used for rubber products with thick cross-section and for products with static applications [61,64,65].

**Semi-efficient curing systems (SEV)**. This curing system is an intermediate between the EV and CV. The sulphur level is generally 1.0-1.7 phr while the A/S ratio is approx. 0.7-2.5 phr. The vulcanizate presents both monosulphidic and polysulphidic crosslinks. The SEV system has found particular application where compromise between heat ageing and fatigue life is often necessary [61,64,65].

The main properties and features of CV, EV and SEV systems are summarized in Table 2.4.

*Table 2.4. Properties and features of CV, EV and SEV curing systems.*

| **Features** | Curing systems | | |
|---|---|---|---|
| | **CV** | **EV** | **SEV** |
| Poly- and disulphidic crosslinks (%) | 95 | 20 | 50 |
| Monosulphidic crosslinks (%) | 5 | 80 | 50 |
| Heat ageing resistance | low | high | medium |
| Fatigue resistance | high | low | medium |
| Tear resistance | high | low | medium |
| Reversion resistance | low | high | medium |
| Elongation at break | high | low | medium |
| Rubber network homogeneity. | high | low | medium |

As it is possible to observe, the sulphur content and the A/S ratio are crucial parameters that influence the crosslink structure.

### 2.3.5 Rubber elasticity

The most significant property that characterizes elastomers is their elasticity. When subjected to a tensile load above their glass transition temperature, elastomers can be deformed over twice their original length and, once the load is removed, they instantaneously re-acquire the original dimension with no residual deformation. A typical stress-strain curve of elastomeric materials is presented in Figure 2.18.

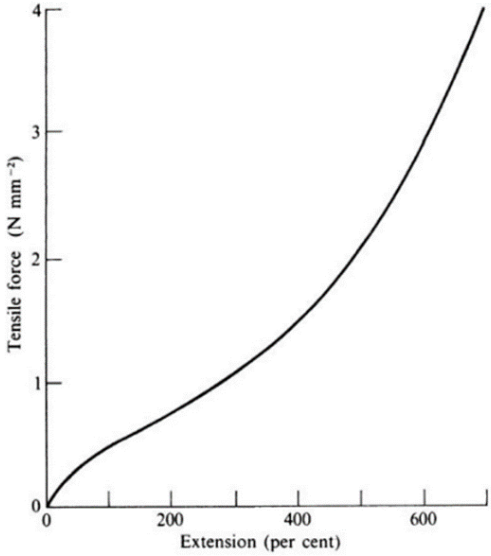


*Figure 2.18. Typical stress-strain curve of an elastomeric material [66].*

As can be seen, elastomers exhibit non-linear elastic behaviour, as the linear elastic region is very limited and does not usually exceed 1% strain. After this initial limited elastic region, a small stress variation leads to significant deformation. Above a certain elongation, an increase in the slope of the stress-strain curve becomes apparent until the material fails [67].

At the origin of these fascinating mechanical properties, there is the entropic nature of rubber elasticity [67]. In the unstretched state, the macromolecules are held together by a network of crosslinks and assume a random-coiled configuration characterized by a high entropy state, which is thermodynamically favourable. Once a tensile load is applied, the molecular chains progressively orient and align in the direction of load application until they are completely stretched. At this point, the load is directly transferred to the covalent bonds of the polymer chain and a strong reduction in configurational entropy is registered. The region in the stress-strain curve where small variations in stress lead to significant deformation is a direct result of the orientation of the polymer chains, while the increase in the material stiffness at a certain elongation value is related to the stretching of the aligned macromolecules.

Moving from the random-coil to the stretched configuration of the polymer chains, the system experiences a strong configurational entropy reduction. As a consequence, to promote the return of the system to its initial lower energy state, retractive forces of entropic nature arise in the network chains. In this way, when the external load is removed, elastomers are able to completely recover their initial dimensions with no residual deformation. In addition, the presence of crosslinks between the macromolecules guarantees the return to the original condition even if the external load is maintained for a prolonged period of time. Because crosslinks prevent an irreversible shift of the polymer chains, the entropy reduction is maintained constant for all the loading time, and the retractive forces do not lose their efficiency to make the macromolecules return to the initial random coil configuration.

The entropic nature of elasticity imparts to rubbers also thermoelastic properties. These properties result in two effects:

- the force at constant extension increases with increasing temperature. This is the opposite behaviour observed for

typical crystalline solids, where the force at constant extension decreases weakly with increasing temperature [68]

- when the elastomers are rapidly stretched, they heat up, while when they are rapidly unloaded, they cool down. This is the fundamental principle behind the elastocaloric effect

The thermodynamics at the base of rubber elasticity is presented in detail below.

To explain how mechanical deformation in elastomers is intrinsically linked to changes in entropy and temperature, relationships between force, length, and temperature on one side, and the thermodynamic variables internal energy and entropy on the other, will be developed and examined. The starting point for developing these relationships is the first and second laws of thermodynamics.

According to the first law of thermodynamics, the change in internal energy of a polymer rubber network (dU) in any process is expressed as reported in Equation (2.4) [67]:

$$dU = dQ + dW \tag{2.4}$$

where dQ is the heat absorbed by the system and dW is the work done by external forces on the system. In a reversible process, the second law of thermodynamics defines the entropy variation (dS) as reported in Equation (2.5):

$$TdS = dQ \tag{2.5}$$

therefore, for a reversible process, Equation (2.4) can be rewritten as reported in Equation (2.6):

$$dU = TdS + dW \tag{2.6}$$

In discussing the equilibrium of a system subjected to reversible changes, as it is elastic deformation, it is convenient to introduce the Helmholtz free energy (A), according to Equation (2.7):

$$A = U - TS \tag{2.7}$$

For a change in A taking place at constant temperature, Equation (2.7) can be expressed according to Equation (2.8):

$$dA = dU - TdS \tag{2.8}$$

Combining this equation with Equation (2.6), the thermodynamic result reported in Equation (2.9) is obtained:

$$dA = dW \tag{2.9}$$

which means that, in a reversible isothermal process, the change in Helmholtz free energy is equal to the work done on the system by the applied forces. When an external tensile force F is applied to the material of length l, the total dW is defined in Equation (2.10):

$$dW = Fdl - pdV \tag{2.10}$$

where p is the pressure and V is the volume. As in rubbers dV is usually very small, the term pdV can be neglected.

By making use of Equations (2.9) and (2.10) the tensile force may be expressed as reported in Equation (2.11):

$$F = \left(\frac{\partial W}{\partial l}\right)_T = \left(\frac{\partial A}{\partial l}\right)_T \tag{2.11}$$

which shows that the tensile force is equal to the change in Helmholtz free energy per unit increase in length of the material.

By making use of Equation (2.8) the tensile force can be expressed also as the sum of two terms, as presented in Equation (2.12):

$$F = \left(\frac{\partial U}{\partial l}\right)_T - T\left(\frac{\partial S}{\partial l}\right)_T \quad (2.12)$$

the two contributions to the force are an energetic term that represents the change in internal energy induced by the external force and an entropic term, which is the product of temperature and the change in entropy, per unit increase in length.

By expressing the Helmholtz free energy in differential form, Equation (2.7) can be rewritten as shown in Equation (2.13):

$$dA = dU - TdS - SdT \quad (2.13)$$

and from Equations (2.6) and (2.10), Equation (2.14) is obtained:

$$dU = Fdl + TdS \quad (2.14)$$

combination of Equation (2.13) and Equation (2.14) gives Equation (2.15):

$$dA = Fdl - SdT \quad (2.15)$$

By partial differentiation of Equation (2.15), Equation (2.16) is obtained:

$$\left(\frac{\partial A}{\partial l}\right)_T = F; \quad \left(\frac{\partial A}{\partial T}\right)_l = -S \quad (2.16)$$

and by exploring a well-known property of partial differentials:

$$\frac{\partial}{\partial l}\left(\frac{\partial A}{\partial T}\right)_l = \frac{\partial}{\partial T}\left(\frac{\partial A}{\partial T}\right)_T$$

Therefore, from Equation (2.16), Equation (2.17) is obtained:

$$\left(\frac{\partial S}{\partial l}\right)_T = \left(\frac{\partial F}{\partial T}\right)_l \quad (2.17)$$

Equation (2.23) gives the entropy change per unit extension in terms of the measurable quantity, $(\partial F/\partial T)_l$, the temperature coefficient of tension at constant length.

Finally, insertion of Equation (2.17) in Equation (2.11) gives Equation (2.18):

$$F = \left(\frac{\partial U}{\partial l}\right)_T + T\left(\frac{\partial F}{\partial T}\right)_l \qquad (2.18)$$

Equation (2.24) is called the thermodynamic equation of state for rubber elasticity. It is of fundamental importance since it provides a direct means of determining experimentally both the internal energy and entropy changes accompanying a deformation. In particular, knowing the force-temperature plot of an elastomer, the internal energy and entropy contributions are given [67]. In Figure 2.19, a general experimental curve (CC') of force versus temperature at constant deformation is illustrated.

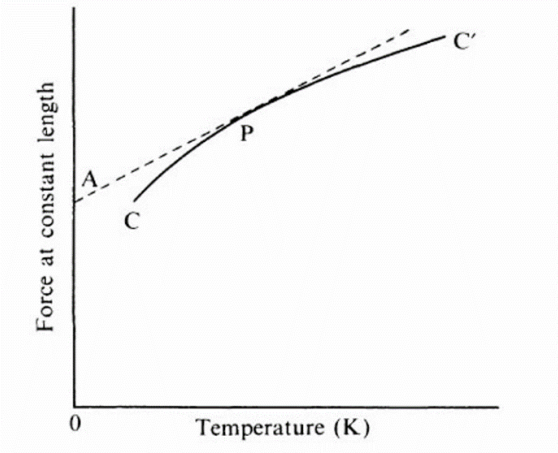


*Figure 2.19. General experimental curve of force versus temperature at constant deformation [67].*

The slope of the curve at a generic point P represents $\left(\frac{\partial F}{\partial T}\right)_l$, which from Equation (2.17) gives the entropy change per unit extension, $\left(\frac{\partial S}{\partial l}\right)_T$, for an isothermal extension at the temperature T. In a similar way, the intercept A of the tangent to the curve at point P on the vertical axis T = 0 K is equal to the change in internal energy per unit extension.

In Figure 2.20, the application of Equation (2.17) and (2.18) to the stress-temperature data at constant extension ratio published by Anthony et al (1942) is shown [67]. It is possible to observe that in elastomers, the dominant component of the force is the entropy component, which accounts for more than 90% of the stress, whereas the energetic component can be considered almost negligible. The reduction of the energetic component above 300% of elongation may be due to strain-induced crystallization [67].

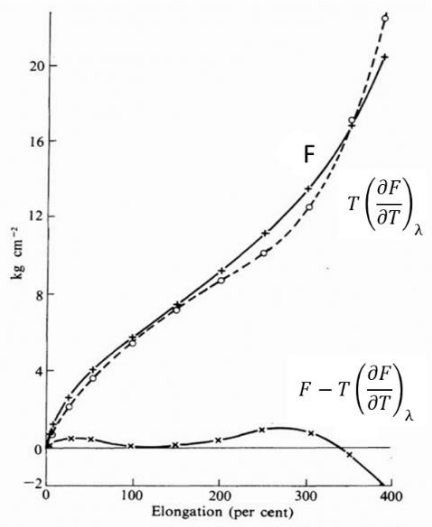


*Figure 2.20. Total external force and its entropic and energetic components as a function of elongation [67].*

### 2.3.6 Thermal behaviour of elastomers at high strain rate

As it was discussed in Paragraph 2.3.5, the thermoelastic effect also implies that elastomers heat up when they are stretched and cool down when they are unloaded. This behaviour is at the basis of the elastocaloric effect and is explained by recalling the basic concepts of thermodynamics of rubber elasticity, namely that the deformation of rubber at constant temperature is associated with a reduction in entropy and a negligible change in internal energy.

Assuming dU = 0, Equation (2.4) becomes Equation (2.19):

$$dW = -dQ \tag{2.19}$$

As the work done by the external force during stretching is positive, it follows that the heat absorbed (dQ) is negative, meaning that heat is evolved during extension. The amount of heat evolved is equal to the work done on the rubber by the external force. This conclusion has the following physical meaning. The internal energy of the rubber is purely kinetic and arises from the thermal agitation of its constituent atoms. This energy depends solely on temperature and is independent of the conformation of the chains (state of strain). As the internal energy remains constant, the work performed by an external force during isothermal deformation must be balanced by the emission of an equivalent amount of heat [67].

If the extension occurs adiabatically, the heat is retained rather than emitted, and the energy supplied by the applied force increases the molecular agitation, producing a rise in the rubber temperature [67]. The temperature rise (ΔT) in an adiabatic extension from the unstrained length $l_0$ to the final length l, can be expressed as reported in Equation (2.20):

$$\Delta T = \frac{\int_{l_0}^{l} f\,dl}{mc_p} \tag{2.20}$$

where $c_p$ is the specific heat capacity of the rubber, which is assumed not to vary when the rubber is deformed and m is the mass of the rubber. If the process is assumed to be reversible, i.e., no internal friction between polymer chains, according to Equation (2.17) and (2.20) ΔT can be expressed as reported in Equation (2.21):

$$\Delta T = -\frac{T}{c_p m}\int_{l_0}^{l}\left(\frac{\partial S}{\partial l}\right)_T dl \qquad (2.21)$$

This equation is very important since it provides a link between the variation in entropy on extension (determined from the stress-temperature variation) and the heat evolved.

If the analysed rubber crystallizes under strain, the thermal effects could be complicated by crystallization, which gives rise to latent heat evolution. In this case an excess temperature rise above that due to the work input can be observed [69]. The temperature rise due to crystallization ($\Delta T_c$) sums up to the contributions related to the conformational entropy changes and can be expressed according to Equation (2.22) [69]:

$$\Delta T_c = \frac{\chi \cdot \Delta H_f}{\rho c_p} \qquad (2.22)$$

where $\chi$ is the fraction of rubber that has crystallized and $\Delta H_f$ is the specific melting enthalpy of the rubber.

If frictional processes are not negligible, the work done during stretching by the external force can be divided into two contributions: the work dissipated due to internal friction between macromolecules and the deformational energy. The contribution of dissipated work ($W_{diss}$) can be estimated according to Trouton's equation reported in Equation (2.23) [69]:

$$W_{diss} = 3\eta tV\left(\frac{dv}{dx}\right)^2 \quad (2.23)$$

where η is the viscosity, dv/dx is the strain rate of deformation and t is the time of application of the deformation. Frictional processes will contribute to heat generation, and thus to the temperature increase of the rubber. This temperature rise due to friction between polymer chains ($\Delta T_f$) is added to the other contributions and can be estimated as reported in Equation (2.24) [69]:

$$\Delta T_f = \frac{3\eta tV}{c_p m}\left(\frac{dv}{dx}\right)^2 \quad (2.24)$$

It has been observed that the importance of frictional processes, and therefore the related temperature increase, declines with temperature.

The amount of deformational energy ($W_{de}$) can be obtained by subtracting to the work done on the system, the amount of work dissipated into friction ($W_{diss}$), according to Equation (2.25) [69]:

$$W_{de} = W - W_{diss} \quad (2.25)$$

The temperature rise resulting from the deformational energy ($\Delta T_{de}$) provides the conformational energy change contribution to the temperature increase and can be expressed as reported in Equation (2.26):

$$\Delta T_{de} = \frac{W_{de}}{mc_p} \quad (2.26)$$

The same thermodynamic analysis also applies when the elastomer is unloaded.

### 2.3.7 Strain induced crystallization

In their unstretched state, most thermoset elastomers are amorphous. However, when these materials are stretched, the extension and orientation of the polymer chains in the direction of loading can induce a partial crystallization of the elastomer. This phenomenon, known as strain induced crystallization (SIC), has been extensively studied in NR, synthetic polyisoprene, polybutadiene, and isoprene-isobutylene rubber [70].

During stretching, the heterogeneous rubber network structure that characterizes elastomers causes the long chains to remain randomly oriented when the short chains reach the fully stretched state. As a result, the fully stretched polymer chains behave as the nucleus of crystallites (Figure 2.21) and, once the SIC threshold is achieved, the crystallinity increases with increasing extension. From a practical point of view, the crystalline domains act as a filler, improving the tensile modulus and tear strength of elastomers. The developed crystalline domains are temporary and, once the load is removed, the polymer chains return to the initial random coil configuration and the crystalline domains melt [70,71].

*Figure 2.21. Strain induced crystallization in elastomers. The dark dots represent the crosslinking points, the red lines represent the short chains, and the yellow areas represent crystallites [22].*

The extent to which an elastomer exhibits SIC is strongly affected by its macromolecular architecture, stereoregularity and steric hindrance, which govern the ability of the polymer chains to align and pack into ordered structures. Although SIC has been observed in different elastomers, NR is the most studied.

To understand how SIC occurs, analysing the stress-strain relationship provides valuable insights. Figure 2.22 reports a stress-strain curve of natural rubber vulcanized by sulphur together with two-dimensional (2D) wide-angle X-ray diffraction (WAXD) patterns corresponding to different stages of stretching and retraction.

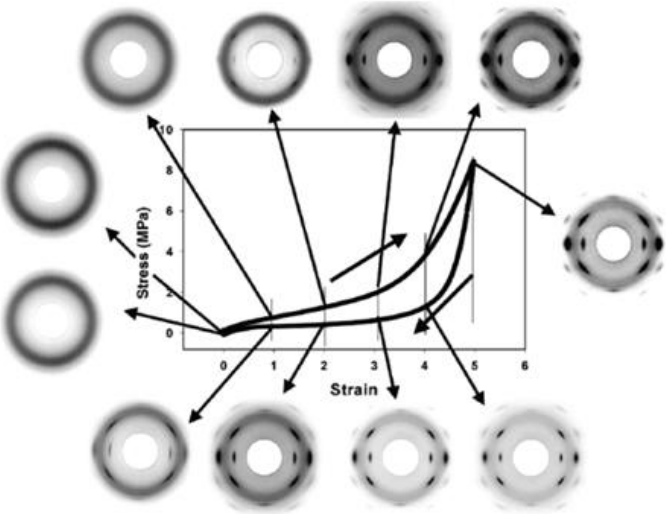


*Figure 2.22. Stress-strain curve and selected WAXD patterns collected during stretching and retraction of natural rubber [70,71].*

In the stretching phase, two well-defined regions can be identified: one at strain $\leq 2$ and the other at strain $\geq 2$. At strain $\leq 2$, WAXD patterns show an amorphous halo [70]. In this region, polymer chains are continuously oriented, although they do not form any crystalline aggregate. At strain $\geq 3$, an oriented crystalline pattern begins to

appear, and crystallinity increases with an increase in strain. Once the critical strain for the onset of SIC is achieved, the stiffness of NR increases drastically. During the unloading phase, crystalline domains melt and, when the strain returns to 0, the crystallinity of NR disappears completely [70]. It is noteworthy that the crystallization kinetics observed during stretching do not align with the melting kinetics during unloading. At a fixed strain level, the crystallinity during unloading is more pronounced than that observed during stretching. The difference between the loading and unloading stress-strain response results also from crystallization and melting and their different kinetics [72].

Several works based on synchrotron studies and performed at 25 °C on NR have revealed that most of the polymer chains remain unoriented, even at large strain (500-600%). Specifically, from WAXD measurements, Toki et al. estimated that 75% of polymer chains remain unoriented, about 20% in the crystalline state and 5% in the oriented amorphous state [70]. These results highlight that the crystalline fraction achievable is limited and generally below 30%. Investigations using molecular simulations revealed that the inhomogeneous rubber network structure, characterized by non-uniform chain length and crosslinking density, is the main origin of the low fraction of oriented amorphous segments at high strains [73].

Several factors influence SIC, including crosslinking density, molecular entanglements, non-rubber components, and the presence of nanofillers. For instance, the onset of SIC in NR with a homogeneous rubber network is primarily dependent on the overall crosslinking density. In contrast, for an inhomogeneous rubber network, it relies on the distribution of the network chains. The incorporation of nanofillers into NR could dramatically improve SIC. Specifically, the role of layered silicates in promoting and increasing the capability of NR to crystallize under strain has been well documented in the literature. Layered silicate nanofillers are characterized by a lamellar crystalline structure, in which every

lamella, 1 nm thick and 200-300 nm long, presents a central octahedral sheet of alumina or magnesia alternated to two external silica tetrahedrons (Figure 2.23).

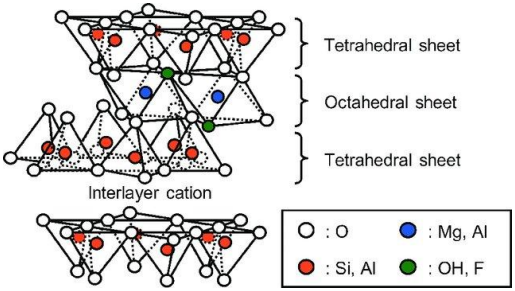


*Figure 2.23. Structure of a layered silicate nanofiller [74].*

These layers are stacked with a regular van der Waals gap between them. Isomorphic substitution within the lamellae generates negative charges that are generally counterbalanced by $Na^+$ or $Ca^{2+}$ cations located in the interlayer region. As the stacks are held together by relatively weak bonds, the intercalation of small molecules between the layers can be performed to obtain a more organophilic clay. The hydrated cations of the interlayer can be exchanged with cationic surfactants such as alkylammonium or alkylphosphonium salts, generating thus organo-modified (OM) clays [75-79].

Carretero-González et al. investigated the effect of OM clays on the structural evolution of NR during deformation [73,80,81]. They found that adding highly anisotropic clay nanoparticles to NR provided a more homogeneously distributed rubber network structure and induced an early onset as well as an enhancement of crystallization under deformation. The onset of SIC moved from 300% strain in the unfilled rubber to 120-140% strain in the filled NR, and the alignment of the clay layers during stretching was revealed to promote a dual crystallization mechanism, as shown in Figure 2.24.

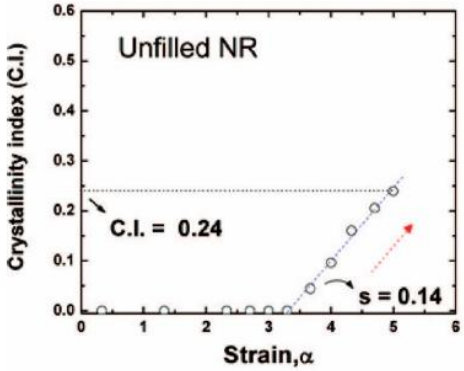


(A)

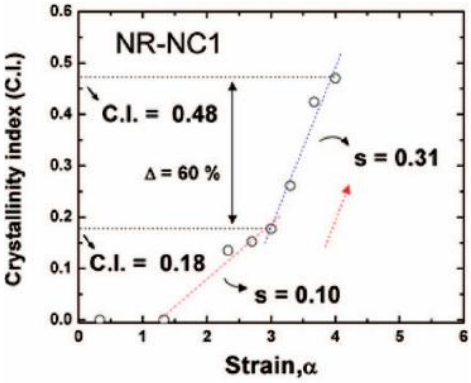


(B)

*Figure 2.24. Onset of SIC in (A) unfilled natural rubber and (B) natural rubber filled with 15 phr of organoclay (NR-NC1) [80,81].*

The neat rubber only exhibits a single crystallization step, whereas the rubber nanocomposites show a first crystallization step at small strains related to the orientation of clay layers during deformation and a second step corresponded to the conventional crystallization mechanism of unfilled NR. The dual crystallization process has also

been observed in NR filled with other highly anisotropic nanofillers, such as carbon nanotubes [73]. Qu et al. demonstrated that increasing in the degree of exfoliation of the clay layers, particularly using OM clays, promotes the SIC of NR (Figure 2.25).

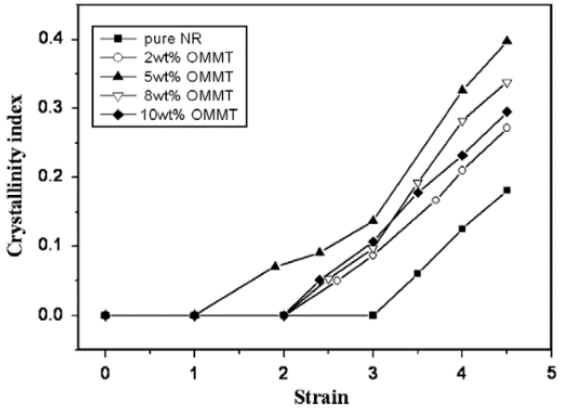


*Figure 2.25. SIC in unfilled rubber and rubber filled with organoclays [82].*

In addition, using real-time mechano-optical behavior, Liang et al. detected that during stretching, the planar structures of the clay layers promote the parallel alignment of the rubber chains, and that the clay orientation increases as the clay content increases, which further promotes the SIC of rubber [82].

### 2.3.8 Mullins effect

Elastomers are often used in applications where they are subjected to cyclic loads or cyclic deformation. Examples include the O-rings and oil seals in dynamic sealing systems, shoe soles subjected to repeated impact during walking or running, rubber buffers in automotive applications, etc.

Under cyclic loading, an appreciable change in the mechanical response of the elastomer occurs after the first extension. Specifically, after the first loading-unloading cycle, a lower stress is required to achieve the same level of deformation [72,83]. This stress softening effect is generally accompanied by a residual strain in the order of 10%. After a short number of cycles, the stress response stabilizes, and the material exhibits a repeatable mechanical behaviour. This phenomenon is referred to as the "Mullins effect", named after the researcher who deeply investigated this behaviour. It is a phenomenon that must be taken into account, as neglecting it can lead to overestimating stiffness and energy dissipation or miscalculating deformation [72,83]. To ensure that the mechanical properties remain consistent during service and to mitigate this effect, the rubber should be pre-stretched up to the desired deformation level several times prior to use, until the mechanical response has stabilized. The Mullins effect is observed both in unfilled and filled rubber, even though it is more pronounced in filled systems [84,85]. Regarding unfilled rubbers, stress softening has been reported in rubbers that initially contain crystallites, as thermoplastic elastomers, or in rubber types that show SIC [83]. Figure 2.26(A,B) shows, as an example of the Mullins effect, the stress-strain curves of NR filled with 1 and 60 phr of carbon black, which were subjected to six loading-unloading cycles.

As can be seen from Figure 2.26, the first loading-unloading cycle differs significantly from the subsequent ones. The maximum stress achieved at the target deformation decreases significantly moving from the first to the subsequent cycles, as does the hysteresis, particularly for the elastomer with a high filler concentration. It should be taken into account that the softened elastomers can recover the mechanical behaviour of the pristine, not stretched material. This recovery occurs slowly at room temperature but can be accelerated by exposing the material to a high temperature or to a solvent. At room temperature, the recovery kinetics are too slow to be noticeable,

making the Mullins effect appear to be irreversible and damaging [72,83].

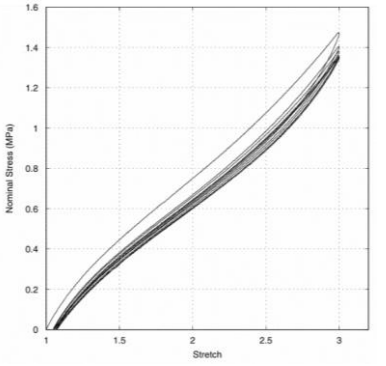


(A)

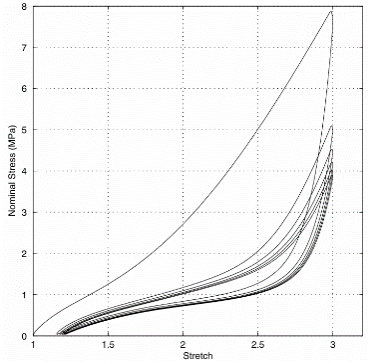


(B)

*Figure 2.26. Natural rubber filled with carbon black and subjected to 6 loading-unloading cycles. (A) Natural rubber filled with 1 phr of CB (B) natural rubber filled with 60 phr of CB [86].*

Sever physical interpretations have been proposed to explain the origin of the Mullins effect. However, the various explanations suggest that up to now there is still no general agreement on the microscopic origin of this effect. The main theories proposed, which include bond raptures, molecule slipping, filler-cluster rapture, chain disentanglement, are shown in Figure 2.27 [72].

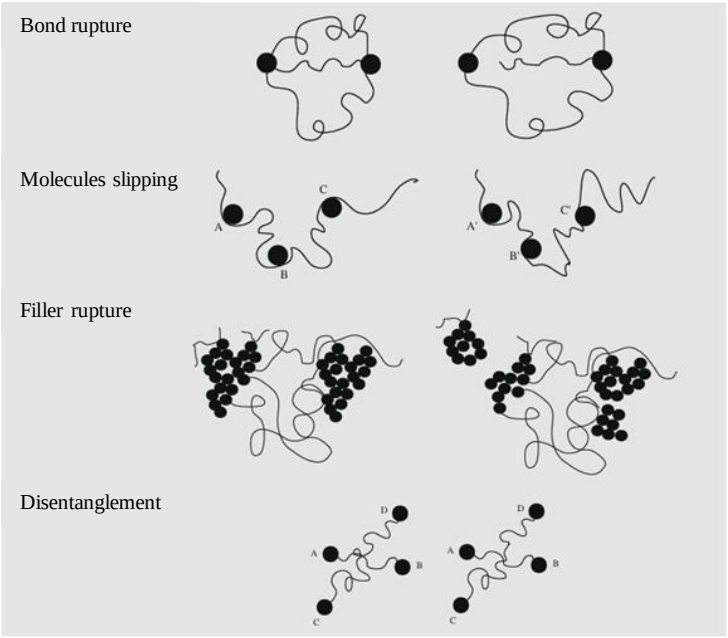


*Figure 2.27. Theories proposed to interpret the Mullins effect [72].*

Blanchard and Parkinson attributed the Mullins effect to bond raptures. According to their theory, the rapture of weaker bonds at the rubber-particle interface occurs during the first extension, resulting in stress softening of the rubber [87]. However, this explanation does not explain the slow recovery of the Mullins effect at room temperature. Houwink proposed that during the first extension, molecules slip over the surface of the fillers and that new bonds are

instantaneously formed along the chains. These new bonds are of the same physical nature as the original ones, but form in different places along the polymer chains. This results in a change of the material entropy, which could be restored by increasing the temperature [88]. However, this hypothesis cannot be applied to unfilled rubbers. Kraus et al, which studied the Mullins effect on NR filled with carbon black, attributed the significant stress softening of these systems to the rupture of the filler structure [89]. However, the rupture of filler structure is irreversible and cannot explain the reversibility nature of this phenomenon. Hanson advanced the hypothesis that, during the first extension, the reduction of entanglements causes an entanglement density change and, as a result, the stress softening. Exposing the material to a higher temperature favours thermal motion of the chains and the production of new entanglements, recovering the initial condition [90].

For the moment, none of these theories is able to completely explain the Mullins effect, and more work is necessary to understand the actual physical source of the Mullins effect.

## *2.4 Natural Rubber*

NR is an indispensable raw material that accounts for approximately 40-48% of total elastomer consumption [91]. It is a high molecular weight polymer, composed primarily by cis-1,4-polyisoprene, whose chemical formula is illustrated in Figure 2.28.

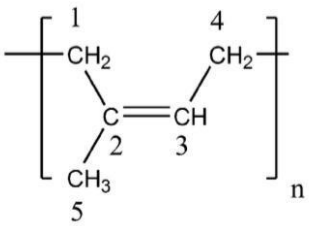


*Figure 2.28. Chemical structure of natural rubber [92].*

Almost 99 % of the world's natural rubber is produced by the Hevea Brasiliensis, commonly called the rubber tree. Originally native to South America, this plant is currently grown in other tropical regions of the globe, namely in Southeast Asia and West Africa, in countries such as Malaysia, Indonesia, Thailand, Vietnam, Cambodia, Ivory Coast, Nigeria, Cameroon, Ghana, and Liberia [93]. In its raw state, NR consists of long, flexible polymer chains with a molecular weight ranging from $10^4$ to $10^7$ g/mol. In this state, it has little practical use but vulcanization converts rubber into a useful and indispensable material [94]. Over the past three decades, the production and consumption of NR have risen significantly (Figure 2.29).

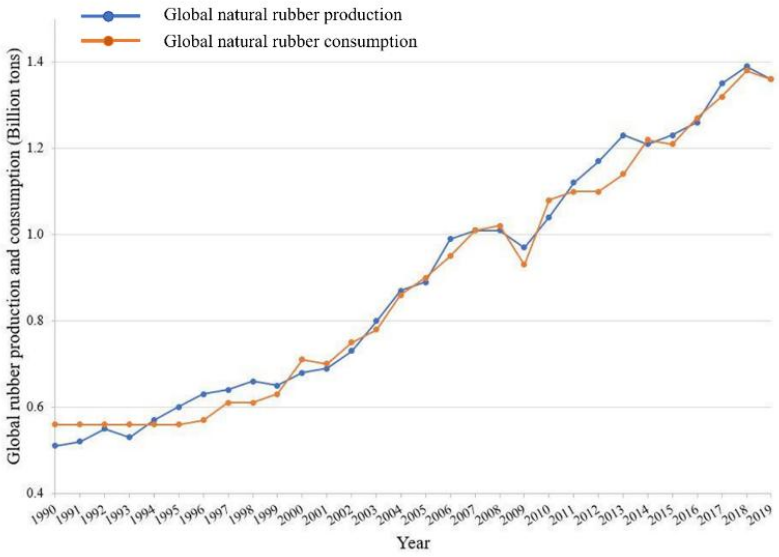


*Figure 2.29. Trend of global rubber production and consumption from 1990 to 2019 [95].*

Although the data reported in Figure 2.29 is current only up to 2019, the Association of Natural Rubber Producing Countries (ANRPC) projects that global NR consumption will reach 1.56 billion tonnes by

the end of 2025 [96]. This growing demand is largely due to the excellent properties this elastomer offers, including high tensile and tear strength, high elasticity, excellent crack growth resistance, and low heat build-up [97]. As a result, it is used in a wide range of applications across various sectors, including engineering, medical, sports, and household products (Figure 2.30). Among all sectors, the automotive industry is by far the largest consumer of natural rubber [93]. It is estimated that over 70% of the natural rubber produced worldwide is used in tyre manufacturing, particularly for automobiles.

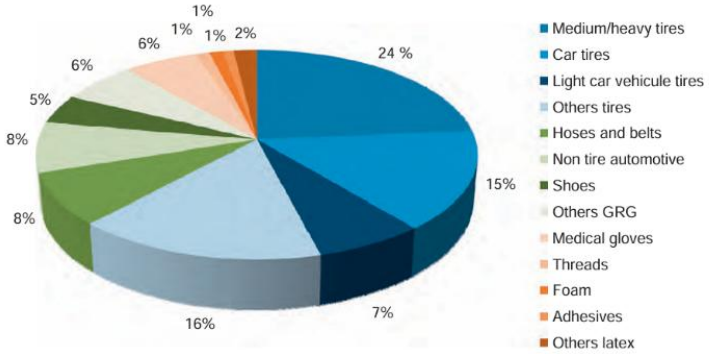


*Figure 2.30. Applications of NR [98].*

From an economic standpoint, the market price of NR is volatile and strongly depends on various factors such as supply and demand, weather and global economic conditions [99]. The price chart of some grades of natural rubber from 2011 to 2025 is shown in Figure 2.31. The grades of natural rubber reported are: Standard Malaysian Rubber Constant Viscosity, Mooney viscosity ML 1+4 at 100°C = 60 ± 5 (SMR CV 60), Standard Malaysian Rubber Latex grade (SMR L), Ribbed Smoked Sheet quality grade 1 (RSS 1), Standard Malaysian

Rubber purity grade 10 (SMR 10) and Standard Indonesian Rubber quality grade 20 (SIR 20).

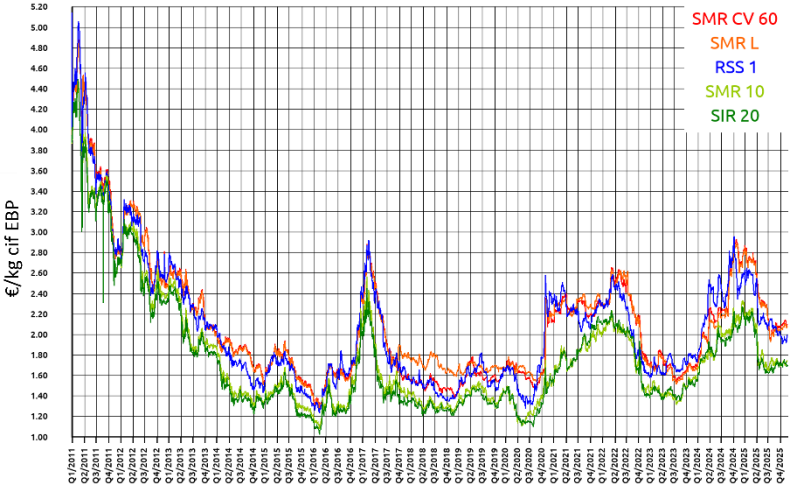


*Figure 2.31. Price chart of some grades of natural rubber from 2011 to 2025 [99].*

In 2011, the price of natural rubber increased due to a combination of strong global demand, limited supply, and adverse weather conditions that disrupted the tapping season. For some rubber grades, prices peaked at € 5/kg. Following the 2011 peak, prices gradually declined, with the benchmark price mostly staying below € 2/kg [100]. In 2020, natural rubber prices crashed due to a loss of demand related to the pandemic. Car factories shut down, slashing demand for tyres and rubber. Prices then rebounded sharply in the second half of 2020 as China recovered, supply remained tight and global demand for rubber gloves and industrial goods surged [101]. Severe weather events in 2024, such as monsoon-related flooding and typhoons, reduced the supply in Thailand and China, causing prices to reach similar levels to those seen in 2011 [102]. In early 2025, output was constrained by

ageing plantations, the effects of El Niño, and a lack of skilled tappers, even though demand was rising [96,103].

### 2.4.1 Production of Natural Rubber

NR occurs in nature as latex, a milky colloidal suspension found beneath the bark or roots of certain trees. The main commercial source is the Hevea brasiliensis species (Figure 2.32). Other potential sources include Guayule (a shrub grown mostly in Mexico), Russian dandelion, Fig trees, Banyan fig and Sunflowers [94]. However, comparative studies have shown that Hevea brasiliensis remains the most suitable candidate due to its high latex production rate [104]. This tropical plant features good bark renewal, a high growth rate after latex harvesting begins, and demonstrates tolerance to severe diseases and strong winds. Additionally, its latex has a higher rubber content, ranging from 30% to 40%, compared to other trees [104].

*Figure 2.32. Plantation of Hevea brasiliensis [105].*

After planting, Hevea brasiliensis trees require about 5–7 years to reach maturity and can remain productive for up to 25 years. Approximately 250–300 plants are planted per hectare, corresponding to a density of 4–5 plants/m². Rubber production begins with the harvesting of latex from the bark of the tree. A skilled worker, known as rubber tapper, makes a precise incision in the bark, allowing the latex to flow out into a collection cup (Figure 2.33). This process is

repeated across multiple trees until a sufficient volume of latex is collected. Each tapping yields about 300 ml of latex, and tapping is usually done once every 2–3 days [98,106]. The plants' peak production period is pre-wintering, which runs from October to January. The wintering period runs from February/March to April/May, during which time the plant loses its leaves and latex production drops dramatically. Each plant produces approximately 10 kg of latex per year, equating to 3 kg of dried rubber.

*Figure 2.33. Collection of latex from Hevea brasiliensis [91].*

The raw latex contains 60% of water and 36% of dry matter. The dry matter is mostly comprised by cis 1,4 polyisoprene and a small percentage (5-6 % w/w) of naturally occurring non-isoprene molecules, such us lipids, proteins, carbohydrates and minerals [98]. As shown in Figure 2.34, the latex is a complex colloidal dispersion, constituted by rubber particles, lutoids and Frey-Wyssling particles dispersed in the cytoplasmic serum (C serum) [107]. Rubber particles are spherical and show a wide range of diameter, from 0.01 to 5 μm, with the majority being 0.1–2 μm diameter. They are constituted by a core of cis 1,4 polyisoprene surrounded by a monolayer of lipids and proteins [98,107].

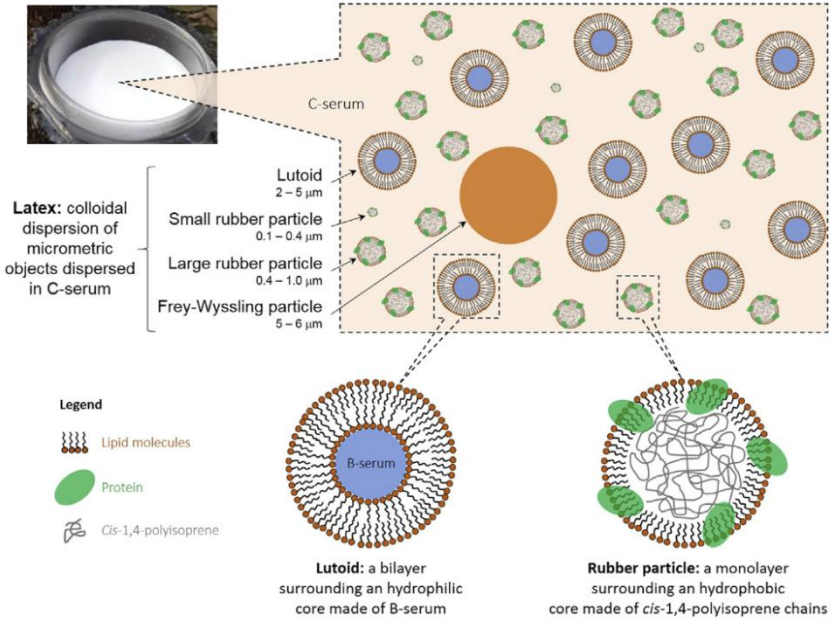


*Figure 2.34. The colloidal dispersion of latex [107].*

Once collected, the latex undergoes a series of processing steps. First, it is sieved to remove impurities such as leaves, twigs and insects. Then, depending on the intended application, it may either be concentrated, usually by centrifuging or evaporation and coagulated, or alternatively directly coagulated and dried. The two approaches lead to two distinct branches of rubber technology, namely latex technology and dry rubber technology [56]. In latex technology, ammonia is added to the latex at a concentration of 0.6-0.7% immediately after tapping to maintain the suspension stability. The latex then undergoes centrifugation, where high-speed spinning separates the rubber particles from the serum. The concentrated latex thus obtained is then shaped by such processes as dipping, coating, moulding and foaming and the resultant shape is set by coagulation.

The coagulation is necessary to neutralize the surface charges of the suspended rubber particles, causing them to agglomerate and precipitate. The major outlets of natural rubber latex are for carpet backing, adhesives, dipped goods such as gloves, balloons, contraceptives and medical tubing [56].

As regards dry rubber technology, a variety of coagulation methods is available. Since the properties of the rubber are affected by trace ingredients and by coagulation agents used, rubbers of different properties are obtained by using different methods [56]. The major types of raw rubber are:

**Crepe rubbers**. Crepe rubbers represent one of the most important forms of processed natural rubber, characterized by a distinctive wrinkled or crinkled appearance [56]. They are used in a variety of applications, including the production of footwear soles, adhesives, sports equipment, consumer and industrial good. In Figure 2.35(A,B), the two categories of creep rubbers, Pale Latex Crepe (PLC) and Estate Brown Crepe (EBC), are shown.

(A) (B)

*Figure 2.35. The two categories of creep rubber. (A) Pale Latex Crepe and (B) Estate Brown Crepe [108,109].*

PLC is the highest grade of crepe rubber. The first step of the manufacturing process consists of mixing the fresh latex with

coagulating agents, mostly organic acids like formic acid or acetic acid, in concentrations of 1-2%. The acid causes the rubber particles to clump together, forming a solid mass that can be processed further. The coagulation process and the processing conditions (temperature, pH levels, and mixing speed) must be carefully controlled to ensure uniform results and a good quality of the final product. Impurities may be trapped if coagulation proceeds too quickly, and undesirable chemical reactions may arise if it proceeds too slowly. The rolling process, which gives crepe rubber its unique texture, can begin once the rubber mass has coagulated. In this step, the material is passed through a sequence of steel rollers, usually placed in pairs with movable spaces between them. To make the rubber sheet thinner and longer, it is folded and run through the rollers several times. The distinctive crinkled texture is produced by the rubber's repeated compression, stretching, and folding during this mechanical operation. After the rolling process, the crepe rubber sheets undergo washing to remove any residual acids, salts, or other water-soluble impurities. Finally, the sheets are hung in well-ventilated drying rooms or chambers [56,110].

The processing of EBC begins with the collection of the field coagulum, which is rubber that has naturally coagulated in collection cups or containers over time. The field coagulum is first cleaned to remove dirt, leaves, and other foreign matter and then passed through rolling mills for further processing. The extended oxidation period, which imparts EBC its brown colour, enhances resilience and aging properties. These qualities make it suitable for industrial applications such as conveyor belts, gaskets, and various moulded rubber products [110].

**Technically Specified Rubber (TSR)**. Technically Specified Rubber (TSR), commonly known as Block Rubber, represents a major advancement in the processing of natural rubber. Unlike traditional grading methods, which relied heavily on visual inspection, TSR is classified based on precise technical parameters measured under

controlled laboratory conditions. This scientific approach ensures that manufacturers worldwide receive rubber with predictable and consistent properties, regardless of its origin [110].

The TSR process begins with the coagulation of liquid latex, typically achieved by adding formic or sulfuric acid. Once coagulated, the solid rubber mass is broken down into smaller, manageable pieces by passing it through rollers or shredders. This size reduction is essential for achieving uniform drying; irregularly sized pieces may dry unevenly, resulting in quality issues such as overdrying or retained moisture [110]. Drying must be gradual and even. Rapid drying can make the rubber brittle and cause cracks, while insufficient drying leaves excess moisture, leading to storage and transport issues. The target is usually a moisture content below 0.8%, which helps prevent mould growth and ensures long-term stability. After drying, the rubber is compressed into standardized bales—typically 33.33 kg or 35 kg each, and wrapped in polyethylene sheets to protect against contamination and moisture absorption [111]. The main exporters of natural rubber, i.e., Malaysia, Thailand, Vietnam, and Indonesia, each produce their national standard TSR grades: SMR (Standard Malaysian Rubber), STR (Standard Thai Rubber), SVR (Standard Vietnamese Rubber), and SIR (Standard Indonesian Rubber). TSR is classified using a systematic scheme: TSR CV (Constant Viscosity), TSR L (Light-colored), and TSR 5, 10, 20 based on dirt content. For example, TSR 5, the highest grade, permits a maximum dirt content of 0.05%, while TSR 20 allows up to 0.20% [110,112].

**Ribbed Smoked Sheet (RSS)**. RSS is a high-quality natural rubber, widely used in the automotive industry, particularly for tyre manufacturing. The production process starts with latex coagulation, using formic acid, which produces a solid rubber mass. This mass is then passed through a series of rollers that squeeze out water and create the characteristic ribbed pattern. These ribs are not just decorative, they increase the surface area, allowing for more efficient drying. The sheets are subsequently hung in smokehouses, where they

are exposed to controlled smoke and heat for several days (Figure 2.36). This smoking process serves multiple purposes: it dries the rubber, provides a natural preservative effect, and imparts the amber colour that indicates quality [110].

*Figure 2.36. Ribbed Smoke Sheets [113].*

Finally, NR can also be produced industrially by synthetic means using Ziegler-Natta catalysts, obtaining isoprene polymer chains with a high cis unit content (96-98%), or with lithium-alkyl catalysts, obtaining chains with a low cis unit content (90-92%) [56,98].

### 2.4.2 Properties of Natural Rubber

Vulcanized NR possesses a unique set of properties that distinguish it from other elastomeric materials. It has a low glass transition temperature ($T_g$) of about -70 °C and a density of 0.92 g/cm³ [48,114]. Its mechanical properties vary depending on the specific formulation and processing method used, with tensile strength ranging from 5 to 30 MPa and an ultimate elongation of up to 1000%. The Young's modulus typically lies between 1.0 and 2.0 MPa, whereas the bulk modulus is significantly higher, in the range of 1–2 GPa [114]. The moduli differ by as much as three orders of magnitude, and this is

primarily attributed to SIC. Shore A hardness lies between 40 and 70. Natural rubber also exhibits excellent fatigue resistance, as well as good tear and abrasion resistance. Its recommended service temperature ranges from -55 °C to 70 °C for continuous exposure, and up to 100 °C for intermittent exposure. Thermally, NR has a relatively low thermal conductivity of about 0.15 W/m·°C and a specific heat capacity between 1.7 and 1.9 J/g·°C [114]. In terms of chemical resistance, NR is resistant to water and steam but is susceptible to degradation when exposed to oils, fuels, ultraviolet (UV) radiation, and certain chemicals, such as chromic and nitric acids [114]. In addition, the exposure to gases such as carbon monoxide, ammonia, ozone and propane is not recommended as it could degrade the material. Finally, NR exhibits optimum elastocaloric properties that are superior to those of other common elastomers. This makes NR an ideal candidate for use in solid-state cooling. The elastocaloric performance of NR will be described in detail in Paragraph 2.5. A summary of the main properties of NR is provided in Table 2.5, together with a comparison with the properties of other very common elastomers.

*Table 2.5.Properties of NR and other very common elastomers [48,53,98,114,115].*

| Properties | NR | SBR | EPDM | CR | NBR |
|---|---|---|---|---|---|
| $T_g$ (°C) | -70 | -60 | -58 | -49 | -24 |
| Service Temp. range (°C) | -50 - +70 | -45 - +70 | -40 - +125 | -35 - +100 | -20 - +100 |
| Shore A | 30-70 | 30-95 | 40-90 | 40-90 | 30-95 |
| Tensile strenght | 5-30 | 10-14 | 2-3 | 10-20 | 10-20 |
| Elongation at break (%) | 1000 | 450-600 | 300-600 | 650-850 | 300-500 |

## 2.5 *Elastocaloric effect of Natural Rubber*

Elastocaloric materials exhibit reversible temperature changes when uniaxial tensile stress is applied and removed under adiabatic conditions (see Paragraph 2.2.3). Among elastocaloric polymers, NR seems to be the most promising one due to its elastocaloric effect being triggered by small stress values (a few MPa) and the significant temperature variations achievable (approx. 12 °C). Furthermore, its non-toxicity, low cost and good fatigue properties have made NR an ideal candidate for use in solid-state cooling [5,11]. The elastocaloric effect of NR was first observed by John Gough, an early nineteenth-century natural philosopher, and later reported by Joule in 1859. However, it is only very recently that the elastocaloric properties of NR have been considered in the development of solid-state cooling technology [5,11]. This research field remains in its infancy, with many aspects yet to be fully understood.

The elastocaloric effect of NR, schematically illustrated in Figure 2.37, is the result of two contributions.

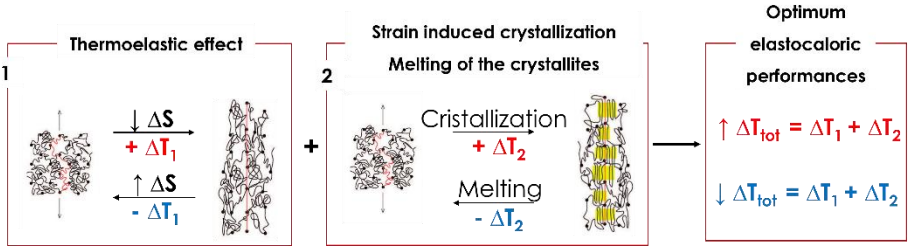


*Figure 2.37. Contributions to the elastocaloric effect of NR: thermoelastic effect and SIC.*

The first is the thermoelastic effect, discussed in Paragraphs 2.3.5 and 2.3.6. Just to recall the concept, during stretching, the orientation of the macromolecules in the stress direction induces a negative entropy variation. As a consequence, the rubber heats up and releases heat to the surrounding environment. When, instead, the material is

unloaded, the return of the polymer chains to the initial high entropy state causes the cooling of the rubber, which absorbs heat from the surroundings, achieving a cooling effect. The second contribution comes from SIC. When NR is stretched at a deformation level higher than 200-300 %, the nucleation and growth of crystalline domains take place, which melt once NR returns to the unstretched state. Since crystallization and melting are exothermic and endothermic phenomena, respectively, the heat developed/released in the stretching/release phase is added to the thermoelastic heat contribution. SIC is more pronounced in NR as compared to other synthetic elastomers due to the stereoregularity and limited steric hindrances of its macromolecular structure, which facilitates the alignment of NR macromolecules upon deformation. The combination of thermoelasticity and significant SIC is the origin of its higher elastocaloric performances with respect to other elastomers that could be considered for this application.

Recent research by Bennacer et al. compared the elastocaloric properties of five common rubbers, including NR, cis-butadiene rubber, chlorosulfonated polyethylene, silicone rubber, and styrene-butadiene rubber, by deforming samples up to 400% elongation at a deformation rate of 600 mm/s [41]. The researchers evaluated the mechanical energy required for deformation, the heat extracted during the releasing phase and the COP. The COP was calculated as the ratio between heat extracted and mechanical energy. They observed that natural rubber exhibited the best cooling performance among the studied elastomers, showing a COP of more than 2 and a corresponding temperature decrease of 3.5 °C. These results are shown in Figure 2.38, where “work” refers to the mechanical energy needed to deform the elastomers and “energy” to the heat extracted from the environment.

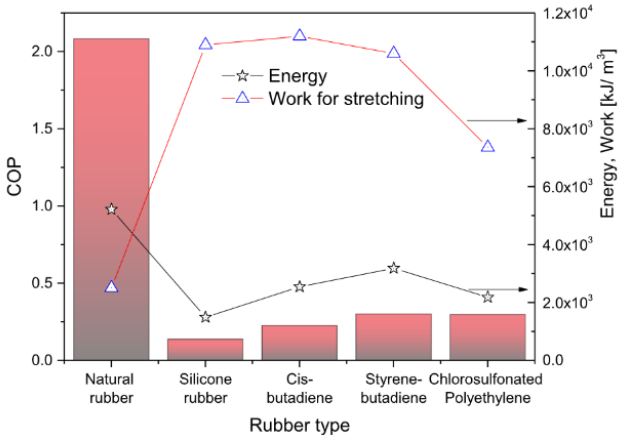


*Figure 2.38. Elastocaloric performance of NR compared to other elastomers [41].*

It is clear that the elastocaloric properties of natural rubber stand out compared to other elastomers. However, they observed that the temperature difference (ΔT) of the material during the stretching phase was higher than that in the recovery stage, meaning that undesired dissipative phenomena occurred.

To maximise the cooling capacity of NR, recent studies have focused on evaluating and understanding the various factors influencing its elastocaloric performance. It has emerged that factors such as deformation level, temperature, strain rate and filler addition affect the cooling capacity. Yukihiro studied the elastocaloric effect of NR filled with carbon black and observed the effect of strain level on the cooling performance [22]. He adiabatically deformed NR samples by 100, 300, 400 and 600%, finding that ΔT increased with the strain level, during both the stretching and releasing phase. At a strain level of 600%, a temperature reduction of 5 °C was registered. Additionally, when he cyclically deformed the samples, he noticed a slight reduction in temperature variation after the initial cycles, which

then stabilised, probably due to mitigation of the Mullins effect. Finally, to evaluate the conversion efficiency from mechanical energy to heat energy during cyclic deformation, Yukihiro calculated a conversion parameter for each cycle at stretching and releasing. This parameter was evaluated as the ratio of heat release/extracted to work of deformation during stretching/releasing, respectively. The results are shown in Figure 2.39(A, B), where $\eta_1$ is the conversion efficiency parameter at stretching, while $\eta_2$ at releasing.

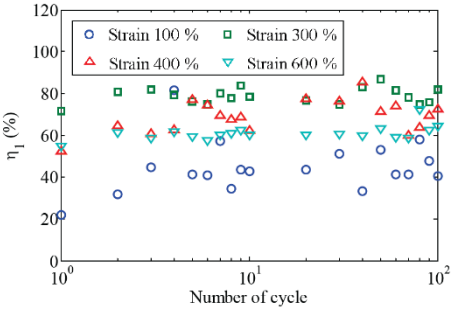


(A)

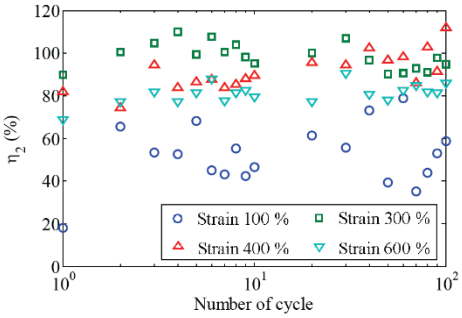


(B)

*Figure 2.39. Conversion efficiency parameters at (A) stretching and (B) releasing for NR filled with carbon black [22].*

Yukihiro found that the conversion efficiency parameters depended on the strain level and that, in all cases, the efficiency parameter $\eta_1$ of the second cycle was larger than those of the first cycle due to the mitigation of the Mullins effect. Indeed, softening caused by the Mullins effect reduced the work of deformation after the first cycle, consequently increasing the conversion efficiency parameter. The highest conversion parameters were obtained for strains of 300 and 400 %. Conversely, lower values were obtained at 600%. This was attributed to an increase in the internal energy variation of NR at the expense of entropy variation, caused by the achievement of a fully stretched state of the polymer chains.

Xie et al. [116] studied the effect of temperature on the elastocaloric properties. They observed that NR exhibited interesting elastocaloric properties over a broad temperature range comprised between 0 and 49 °C. The maximum temperature change at unloading (12 °C) occurred at 10 °C and a strain of 600 %. Within the 10-49 °C temperature range, the ΔT decreased from 12 °C to 5.8 °C, while in the range 10-0 °C it dropped to 4 °C. Figure 2.40 shows the adiabatic temperature changes at release as a function of temperature and strain.

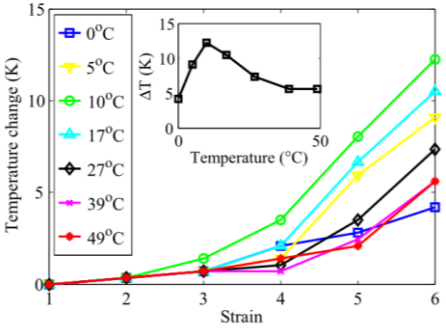


*Figure 2.40. Temperature dependence of adiabatic temperature changes (ΔT) at various strains. The inset shows this behaviour at a strain of 600% [116].*

From a strain of around 3 (onset of SIC), ΔT showed a significant temperature dependence. These results suggest that to take full advantage of the cooling performance of NR, working at a temperature of 10–30 °C and a strain above 300% is needed.

The elastocaloric properties of vulcanized natural rubber filled with ground tire rubber, having dimensions ≤125 μm, were investigated by Candau et. al, who discriminated the contributions of thermoelastic effects and strain-induced crystallization/melting by using a thermodynamic frame [43]. In Figure 2.41, the mechanical energy of deformation and the heat exchange during the releasing phase are reported. The deformation level selected was 500%.

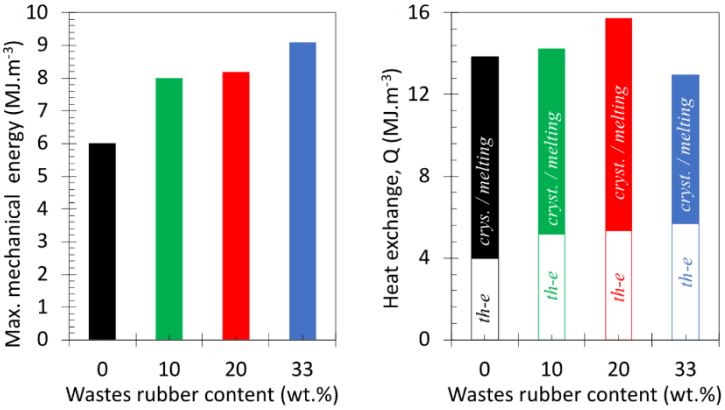


(A) (B)

*Figure 2.41. (A)Mechanical energy of deformation and (B) heat absorbed during the releasing phase of NR filled with different amount of ground tire rubber [43].*

They observed that SIC was the main contribution to the elastocaloric effect and that the elastocaloric properties of the blends increased with a waste rubber content of 20 wt%. In particular, they found an increase in both thermoelastic effects and crystallization abilities and

attributed these observations to a strain amplification effect owing to the presence of non-deformable carbon black aggregates in the waste particles. In subsequent works of Candau et al., the influence of sample thickness on the elastocaloric effect of the same NR/waste rubber blends was investigated [44]. They pointed out that by reducing the sample thickness (up to 0.6 mm), the crosslinking density of the rubber became more homogeneous, leading to an increased SIC ability, which ultimately resulted in an enhancement of the elastocaloric effect.

Candau et al. also explored the elastocaloric properties of vulcanized natural rubber/cellulose nanocrystals (CNC) composites with a CNCs content up to 5 wt% [42]. They observed that, deforming the samples up to 500%, the thermoelastic effect increased in the presence of an increasing amount of CNC due to the strain amplification in the rubbery matrix. Moreover, the ability to crystallize under strain of NR also increased up to a CNC content of 3 wt%. At this content, an improvement of 30% and 15% of the heating and cooling capacity, respectively were observed due to an increase of both the thermoelastic effect and SIC. At 5 wt% the heating/cooling ability of NR/CNC decreases, which was ascribe to a lack of distribution of the CNC due to their aggregation.

A summary of the elastocaloric performance of NR, NR-based systems, and various rubbers is provided in Table 2.6.

*Table 2.6. Summary of elastocaloric properties of NR and various rubbers.*

| **Rubber** | **Strain (%)** | **$\Delta T_{cool}$ (°C)** | **$Q_{ab}$ (J/cm$^3$)** | **COP*** | **Ref.** |
|---|---|---|---|---|---|
| Unfilled NR | 400 | 3.5 | 5.2 | 2.1 | [41] |
| | 400 | 2.5 | 4.3 | - | [116] |
| NR filled with Carbon Black | 600 | 5.0 | 8.4 | - | [22] |
| NR filled with ground tire rubber | 500 | 8.0 | 14.0 | 1.8 | [43, 44] |
| NR filled with cellulose nanocrystals | 480 | 7.0 | - | - | [42] |
| Silicone Rubber | 400 | 1.0 | 1.5 | 0.1 | [41] |
| Cis-butadiene | 400 | 1.7 | 2.5 | 0.2 | [41] |
| Styrene-butadiene | 400 | 2.1 | 3.2 | 0.3 | [41] |
| Chlorosulfonated Polyethylene | 400 | 1.4 | 2.2 | 0.3 | [41] |
| Thermoplastic polyurethane | 400 | 7.7 | 10.0 | - | [117] |

* The COP value was not provided in all the works.

Although some solid-state cooling prototypes utilising the elastocaloric effect of NR have been developed, they are mostly at an experimental or early development stage. For example, Sion et al. developed a solid-state elastocaloric refrigeration device based on NR. The device operates via a cyclic solid-solid heat exchange involving a cyclically stretched NR strip and two heat exchangers: a high-temperature heat exchanger (HHEX) and a low-temperature heat exchanger (CHEX) (Figure 2.42) [118].

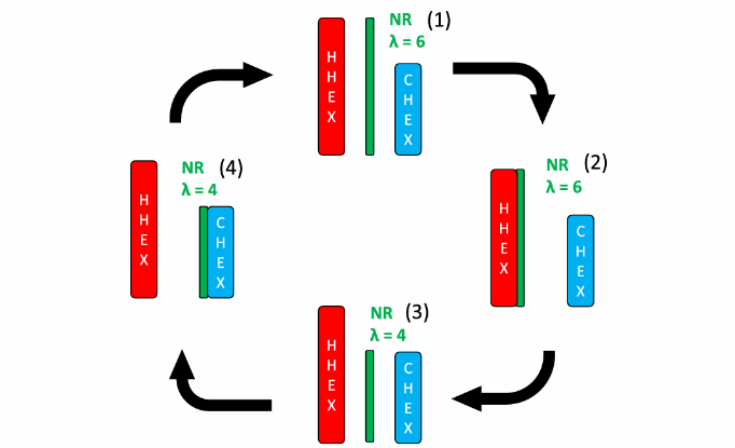


*Figure 2.42. Scheme of the cooler prototype developed by Sion et al.* [118].

During the first step of the cycle (1), the NR is adiabatically stretched to $\lambda = 6$, increasing its temperature. Then, NR is put in contact with HHEX and heat is transferred from the strip to the HHEX (2). After some time, the strip is released at $\lambda=4$, decreasing its temperature (3). The CHEX is put in contact with NR and the heat is transferred from the reservoir to the strip (4). This device provided a cooling power of 390 mW (430 W/kg) [118].

Although the cooling power of current prototypes is still far below that of existing cooling systems, which operate on the order of millions of milliwatts, it is hoped that a deeper understanding of the factors influencing the elastocaloric effect, combined with refinement of the prototypes, will enable performance levels approaching those of conventional cooling technologies.

In summary, the research papers published to date on the elastocaloric effect of NR provide evidence that:

- To maximize the cooling performance, NR must be deformed at strains above the onset of SIC. In most of the

studies, NR shows optimum cooling capability when stretched up to 500-600%. However, the fatigue resistance of NR at such deformations is an aspect never mentioned in the papers

- The rubber network structure seems to play an important role in the elastocaloric effect, even though this aspect has not been investigated in detail
- The addition of fillers to NR seems to increase the cooling capacity, thanks to a strain amplification effect and an enhancement of SIC

However, many aspects of the elastocaloric effect remain poorly understood. For instance, the impact of crosslinking density on the cooling capacity of NR has not yet been investigated. Furthermore, the effect of only certain fillers on the elastocaloric properties of NR is currently known, and it would be valuable to extend this analysis to other filler types. In addition, aspects such as the influence of rubber–filler interactions on elastocaloric performance remain unexplored.

# 3 Experimental Part

## *3.1 Materials*

### 3.1.1 Natural Rubber

The Natural Rubber used in this PhD thesis was a TSR (Technically Specified Rubber) grade SMR 10 (Standard Malaysian Rubber), kindly provided by Marangoni S.p.a (Rovereto (TN), Italy). The main specifications of the rubber are reported in Table 3.1.

*Table 3.1. Main specifications of the TSR natural rubber, grade SMR 10, used in the PhD thesis.*

| Parameter | TSR SMR 10 |
|---|---|
| Ash content (max, %wt) | 0.75 |
| Nitrogen content (max, %wt) | 0.60 |
| Volatile matter (max, %wt) | 0.80 |
| Wallace rapid plasticity (min) | 30 |
| Plasticity retention index (min, %) | 50 |
| Mooney viscosity ML (1'+4') 100 °C | 74 |

The rubber was supplied in a single block weighting approximately 3 kg, and Figure 3.1 shows a representative picture of the received material.


*Figure 3.1. Natural rubber TSR SMR 10 supplied by Marangoni Group S.p.a.*

### 3.1.2 Rubber additives

The chemicals employed in the vulcanization were zinc oxide (curing activator), sulphur (vulcanizing agent), stearic acid (curing activator) and zinc dibutyldithiocarbamate (ZDBC, accelerator). Sulphur, stearic acid and zinc oxide were provided by Rhein Chemie Rheinau GmbH (Cologne, Germany), while ZDBC accelerator was acquired from Vibiplast s.r.l. (Castano Primo (MI), Italy). The main physical properties of the rubber chemicals are reported in Table 3.2. All the chemicals were used as received.

*Table 3.2. Physical properties of the rubber chemicals, data taken from the producers [119].*

| **Vulcanization chemical** | **Appearance** | **Density ($g/cm^3$ at 22 °C)** | **Purity (%)** |
|---|---|---|---|
| Zinc Oxide | white to slightly yellowish powder | 5.68 | ≥ 93% |
| Sulphur | Yellow, light yellow | 1.64 | - |
| Stearic acid | White solid flakes | 0.87 | ≥98% |
| ZDBC | White granules | 1.00-1.20 | ≥80% |

### 3.1.3 Solvents

Toluene, acetone and methanol were acquired from Carlo Erba Reagents S.r.l., (Cornaredo MI, Italy) and were used for the determination of the crosslinking density of the produced NR samples. The main physical properties of these solvents are reported in Table 3.3. All the solvents were used as received

*Table 3.3. Physical properties of the solvents used, data taken from the producer [120-122].*

| Solvent | Description | Molecular Weight (g/mol) | Density ($g/cm^3$) | Boiling point (°C) | Purity (%) |
|---|---|---|---|---|---|
| Toluene | Clear, colourless liquid | 92.1 | 0.862-0.872 | 109.9-111.4 | ≥ 99.5 |
| Acetone | Clear liquid | 58.0 | 0.790-0.792 | 55.8-56.3 | ≥ 99.8 |
| Methanol | Clear liquid | 32.0 | 0.791-0.793 | 63.6-65.6 | ≥ 99.9 |

### 3.1.4 Nanoclays

Natural montmorillonite (Cloisite® Na+) was provided by Southern Clay Products, Inc. (Gonzales, Texas), while organomodified montmorillonite (Cloisite® 20A) was obtained from BYK-Chemie GmbH (Wersel, Germany). The main characteristics of the selected clays are summarized in Table 3.4. The organic modifier of Cloisite® 20A was dimethyl dihydrogenated tallow ammonium cations, at a loading of 95 meq/100 g clay, where tallow (T) is ~65% $C_{18}H_{37}$; ~30% $C_{16}$ $H_{33}$ and ~5% $C_{14}H_{29}$.

*Table 3.4. Nanoclays used in this PhD thesis, data taken from the producer [123].*

| Trade name | Code | Organic modifier | Density (g/cm$^3$) | Lamellar spacing, $d_{001}$ (nm) |
|---|---|---|---|---|
| Cloisite® Na+ | MMT | None | 2.86 | 1.17 |
| Cloisite® 20A | O-MMT | 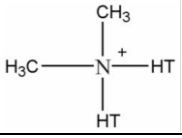 | 1.80 | 2.70 |

## *3.2 Experimental techniques*

### 3.2.1 Rheological analysis

The vulcanization characteristics of the NR formulations were investigated through rheological measurements, using a DHR-2Rheometer (TA Instrument Waters L.L.C., New Castle, DE, USA) in plate-plate configuration. The tests were performed under isothermal conditions at 120 °C with a constant strain amplitude of 1 % and frequency of 1.7 Hz, in accordance with ASTM D5289 [124], with a gap distance set to 1 mm. Disc samples (diameter 25 mm, thickness 1 mm) were selected for the measurements. The maximum torque ($T_{max}$), the minimum torque ($T_{min}$) and the time required to reach 90% of the maximum torque ($t_{90\%}$) were evaluated. The vulcanization was monitored over a maximum period of 60 minutes. One specimen was tested for each formulation.

### 3.2.2 Density measurements

In accordance with the standard ASTM D792 [125], the density of the samples was measured by Archimede's principle. The tests were performed at ambient temperature and employing Mettler kit ME-33340. The specimens were weighed in air and immersed in methanol. The density was calculated using Equation (3.1):

$$\rho = \frac{a}{a-b} \times P \qquad (3.1)$$

where a is the weight of the sample in air, b is the weight of the material submerged in methanol, and P is the density of methanol at the testing temperature (0.791 g/cm$^3$ determined by using the Mettler kit ME-33340). For each NR formulation, three specimens were tested.

### 3.2.3 Evaluation of the crosslinking density

In accordance with the standard ASTM D6814 [126], the determination of the crosslinking density (υ) of the NR samples was conducted through equilibrium swelling measurements in toluene. NR specimens, weighing approximately 0.10 g each, were first immersed in acetone for three days to remove the acetone-soluble fraction. The rubbers were then dried for 24 hours in a ventilated oven and cooled to room temperature. After that, the specimens were immersed in toluene for 4 days until equilibrium state was achieved. Subsequently, the specimens were taken out, the swollen mass were weighted ($w_s$) and subjected to drying to eliminate excess solvent in a ventilated oven at 60 °C until constant weight (i.e., approx. 24 h). Finally, the dried masses were recorded ($w_d$). Then, the crosslinked density ($\upsilon$) was determined through Equation (3.2) developed by Flory-Rehner:

$$\upsilon = \frac{-\ln(1-V_r)+V_r+XxV_r^2)}{V_1 x(V_r^{\frac{1}{3}}-V_r)/2} \qquad (3.2)$$

where $X$ is the polymer-solvent interaction parameter, $V_1$ is the molecular volume of solvent, and $V_r$ is volume fraction of polymer in a swollen network in equilibrium with pure solvent, calculated according to ASTM D6814 standard, as reported in Equation (3.3):

$$V_r = \frac{\frac{w_d}{\rho_d}}{\frac{w_d}{\rho_d}+\frac{w_{so}}{\rho_s}} \quad (3.3)$$

where $w_d$ is the weight of dry rubber, $\rho_d$ is the density of dry rubber, $w_{so}$ is the solvent absorbed by the sample, evaluated as difference between $w_s$ and $w_d$, and $\rho s$ is the density of the solvent.

The values used for the molar volume of toluene ($V_1$), for the Flory-Huggins interaction parameter ($X$) and the toluene density were 106.288 $cm^3$/mol, 0.391 and 0.867 $g/cm^3$, respectively [114]. The density of dry natural rubber was determined by Archimede's principle in methanol according to Equation (3.1). For each NR formulation, six specimens were tested.

### 3.2.4 Morphological analysis

The nanoclays dispersion in the NR matrix was investigated using a field emission scanning electron microscope (FESEM) AG-SUPRA40 (Carl Zeiss AG, Oberkochen, Germany), operating at an acceleration voltage of 2.5 kV. The samples were soaked in liquid nitrogen for 1 hour and then cryofractured. The fracture surface was analyzed after Pd-Pt sputtering to provide enhanced electrical conductivity.

### 3.2.5 X-Ray diffraction (XRD)

X-Ray diffraction analyses were performed with the aim of investigating (i) the extent of SIC of the stretched NR samples and (ii) to evaluate the dispersion of the nanofiller within the NR matrix.

To evaluate the extent of SIC in the samples, diffraction data were collected in transmission geometry by means of the UniTN Textris texture goniometer. This operated with a Cu-anode source coupled with 2D-collimating optics. The stretched samples (0%, 300%, 400% and 500%) were fixed to a custom-made sample holder and positioned on the X-Ray beamline. Two-dimensional diffraction

images were collected over an acquisition time of 120 s using a Dectris Eiger 1M hybrid pixel detector. The diffraction images were then azimuthally integrated over 5-degrees intervals for a total of 72 spectra for each sample. Integrated data analysis was performed through the Maud software, starting from the literature structure model of Poly(cis-Isoprene) [127]. The proposed model was based on a monoclinic symmetry with lattice constants a = 12.46 Å, b = 8.89 Å, c = 8.10 Å, β = 92°, with polymer chains aligned along the c crystallographic axis (Figure 3.2).

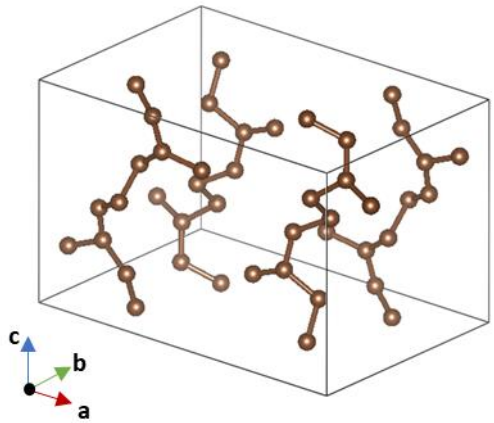


*Figure 3.2. Crystal structure of Poly(cis-Isoprene) [127].*

In the first refinement step, only background and scale parameters were optimized. Then, the average crystallite size was manually set to a reasonable starting value (10 nm) and the preferred orientation modelling was introduced by means of the Entropy-modified Williams-Imhof-Matthies-Vinel (EWIMV) algorithm. Later, lattice parameters were also refined. Average crystallite size was evaluated by means of the Scherrer's formula applied to the main (2 0 1) reflection, as reported in Equation (3.4):

$$D_{201} = \frac{K\lambda}{\beta cos\theta} \quad (3.4)$$

where *D* is the average crystallite size, *K* is the shape factor, $\lambda$ is the X-ray wavelength (Cu-ka = 1.5419 Å), $\beta$ is the full width at half maximum (FWHM) of the peak and $\theta$ is the Bragg angle. Crystallinity content was evaluated in a semi-quantitative way by computing the ratio between the sum of the intensities of visible Bragg contributions (coherently scattered signals) and the total integrated intensity of the diffraction pattern, obtained from averaged integrated patterns. XRD measurements were performed on specimens having dimensions 25x25x1mm$^3$, and only one specimen was tested for each formulation.

To evaluate the dispersion of the nanofiller in the NR matrix, the data was taken with a Rigaku D/Max-B X-Ray diffractometer in Bragg--Brentano parafocusing geometry, a diffracted beam monochromator, and a conventional Cu target X-ray tube set to 40 kV and 30 mA. Acquisition range (expressed in terms of 2Θ angle) was set from 1° up to 60°, with a with a 2Θ step of 0.02° and an acquisition time of 2 s per step. To determine the basal spacing of the nanofiller, the Bragg's equation was used, as reported in Equation (3.5):

$$2d_{001}\sin\theta = n\lambda \quad (3.5)$$

Where $d_{001}$ is the basal spacing, θ is the Bragg angle, n is the diffraction order, and λ is the X-ray wavelength ((Cu-ka = 1.5419 Å). XRD measurements were performed on specimens having dimensions 25x25x1mm$^3$, and only one specimen was tested for each composition.

### 3.2.6 Differential scanning calorimetry (DSC)

Differential scanning calorimetry (DSC) tests were performed on the NR samples by means of a Mettler DSC30 calorimeter (Mettler

Toledo, Switzerland). One specimen was tested for each composition, with a mass of approximately 10 mg. The specimens were subjected to the following thermal sequence: (I) first heating scan from -100 °C to 150 °C at 10 °C/min, (II) cooling scan from 150 °C to -100 °C at -10 °C/min, (III) final heating scan from -100 °C to 150 °C at 10 °C/min. Nitrogen was used as the purge gas at a flow rate of 100 ml/min. DSC analysis allowed the determination of the glass transition temperature of the samples and to study the effect of filler addition (if present) on the thermal properties of the NR samples.

### 3.2.7 Thermogravimetric analysis (TGA)

Thermogravimetric analysis was performed by using TGA Q5000 IR thermo balance (TA Instrument) to investigate the influence of natural rubber formulation on the degradation resistance of the materials. Samples, weighting approx. 30 mg, were tested at a heating rate of 10 °C/min from 30 °C to 700 °C under a nitrogen flow of 10 mL/min. One sample for each rubber formulation was tested. The temperature associated to a mass loss of 5 % ($T_{5\%}$) and the mass loss at 700 °C ($m_{700}$) was evaluated. In addition, from the first derivative of the thermogravimetric curve (DTGA), the temperatures corresponding to the maximum rate of mass loss were identified ($T_{peak}$).

### 3.2.8 Laser Flash Analysis (LFA)

The material capability to release/absorb heat to the environment and the kinetics of such heat exchanges depend on the thermal properties of the material. For this reason, the specific heat capacity ($c_p$), thermal conductivity ($\lambda$) and thermal diffusivity ($\alpha$) of the NR samples were measured through Laser Flash Analysis (LFA) with a Netzsch LFA 447 instrument. Cylindrical samples (diameter 12.7 mm, thickness 1 mm) were die-cut from the produced NR sheets. The tests were carried out at 20 °C and for each specimen five pulses were performed. To compute the thermal diffusivity ($\alpha$), the Cowan method with numerical pulse correction was employed. For the

determination of the heat capacity, the reference material Pyroceram 9606 was employed, according to the standard ASTM-E 1461 [128]. The thermal conductivity was calculated according to Equation (3.6):

$$\lambda = \alpha \rho c_P \qquad (3.6)$$

where $\rho$ is the density of the sample (g/cm$^3$) determined by Archimede's method, while $\alpha$ and $c_p$ are the data provided by the LFA measurements. For each NR formulation, three specimens were tested.

### 3.2.9 Shore A hardness measurements

According to the ASTM D2240 standard [129], Shore A hardness was measured at 25 °C using a Hilderbrand Durometer (Prüf-und Meßtechnik GmbH, Wendlingen am Neckar, Germany). Square specimens 15 mm wide and 3 mm thick were tested, after pressing an indenter against the specimen for a time equal to 10 s. The load level was set at 488 g. Ten specimens were tested for each formulation.

### 3.2.10 Quasi-static tensile tests

Room temperature uniaxial tensile tests were performed on a universal testing machine Instron 5969 equipped with a load cell of 10 kN and operating at a crosshead speed of 500 mm/min. The strain was measured with a resistance extensometer Instron 2603 with a gauge length of 25 mm. The tests were carried out on ASTM D412 specimens [130]. From the tests, the stress corresponding to strain levels of 200 % and 400 % was determined ($\sigma_{200}$, $\sigma_{400}$), together with the stress at break ($\sigma_b$), the corresponding strain ($\varepsilon_b$) and the specific tensile energy to break ($E_b$), calculated as the integration of the stress-strain curve from zero-strain to rupture. The elastic modulus ($E_{100\text{-}200}$) was measured as the slope of the stress-strain curve in the strain region 100-200%. Five specimens were tested for each composition.

### 3.2.11 Evaluation of the Mullins effect

To investigate the Mullins effect, NR samples were subjected to uniaxial cyclic tensile tests ten times by using a testing machine Instron 5969 equipped with a load cell of 10 kN and operating at a crosshead speed of 125 mm/min. The strain was measured with a resistance extensometer Instron 2603 (gauge length of 25 mm). Specimens having dimensions of 25x10x3 $mm^3$ were used. The samples were cyclically stretched up to the desired deformation level (200 %, 300 % or 400 % defined depending on the samples) and one specimen was tested for each formulation and strain level. The energy dissipated and the stress corresponding to the maximum strain applied ($\sigma_{M200}$, $\sigma_{M300}$, $\sigma_{M400}$) were determined for each cycle. To accurately assess the residual deformation of the samples, two lines spaced 1 cm apart were marked on the surface of the specimens. Following the completion of 10 cycles, the distance between the lines was measured immediately after the sample dismounting from the instrument, and the residual deformation was then calculated.

### 3.2.12 Evaluation of the elastocaloric effect

#### *3.2.12.1 Set up description*

To assess the elastocaloric effect of the samples, a preliminary experimental set up was initially employed, as no tensile testing machine available at the University of Trento could satisfy the required specifications, namely, crosshead speeds on the order of meters per second (to guarantee an adiabatic deformation process) and a stroke of at least 20 cm. Subsequently, collaboration was established with Step Lab S.r.l. (Resana, TV, Italy), a company specialized in the production of electrically actuated machines for mechanical testing, which provided a high-speed tensile testing system meeting the requirements. The elastocaloric tests were carried out on-site at their facilities. The evaluation of the effect of crosslinking density on the elastocaloric performance of the NR sample (described in Chapter 4) was performed by using both setups.

Conversely, the elastocaloric properties of the NR nanocomposites (described in Chapter 5) were determined only by using the high-speed tensile testing machine. Below, the preliminary experimental set-up and the high-speed tensile testing machine are described, along with the data processing procedure, which was identical in both cases.

With the preliminary experimental set-up, a pendulum testing machine was used, and tensile impact tests (setup ISO 8256 method B) were performed. The tests were carried out at room temperature, and specimens of 1 mm thickness and 15 mm wide were used. The gauge length was set at 27 mm. The procedure adopted for investigating the elastocaloric performance is shown schematically in Figure 3.3 and described in detail below.

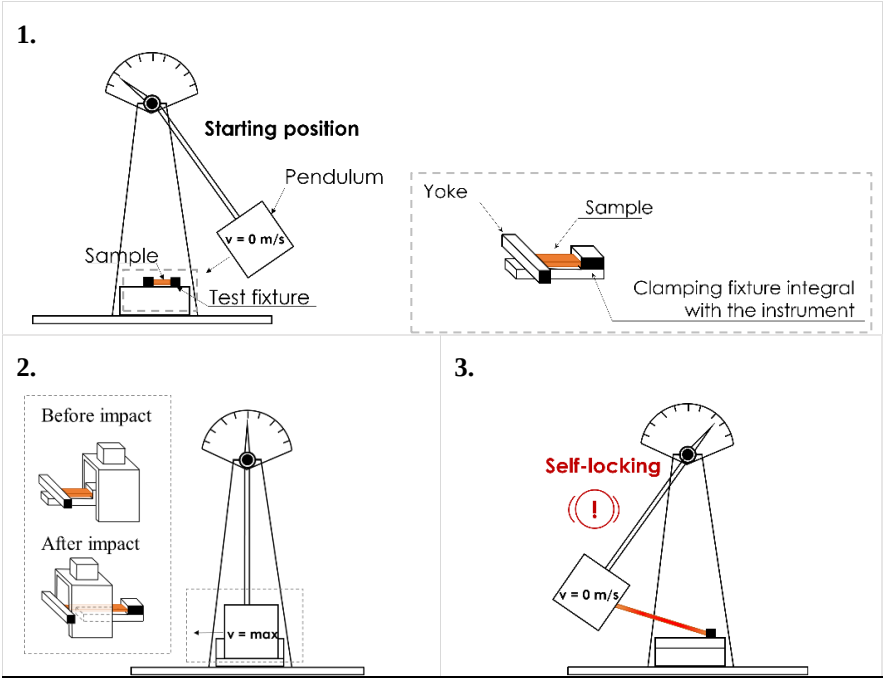

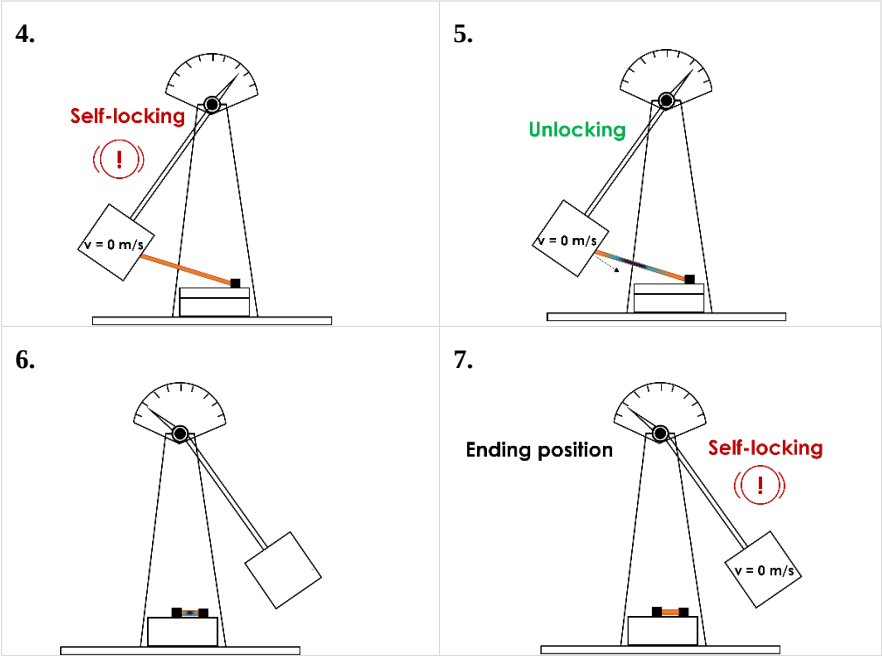


*Figure 3.3. Procedure followed for the evaluation of the elastocaloric properties using the pendulum testing machine.*

**1.** The specimen was fixed to a clamping fixture integral to the instrument on one side, while a rigid yoke was attached to the other side of the specimen. The distance between the yoke and the clamping fixture was 27 mm. The pendulum was lifted at the starting position (corresponding to a specific impact energy and impact velocity) and subsequently released downward.

**2.-3.** When the pendulum hammer struck the yoke, the yoke remained attached to the pendulum and the specimen was rapidly stretched, heating up. When the pendulum reached the maximum height (kinetic energy null), it self-locked, maintaining the sample in traction. By measuring the length of the stretched specimens, the deformation of the material was determined.

**4.** Sufficient time was allowed for the specimen to return to room temperature. The specimen was cooled by natural convection.

**5.-6.** After that, the system was unlocked, and the pendulum was released downward. The specimen recovered the deformation and cooled down, absorbing heat from the environment.

**7.** The pendulum was self-locked at the starting position.

The mechanism used to actuate the self-locking and unlocking of the pendulum is illustrated in more detail in Figure 3.4.

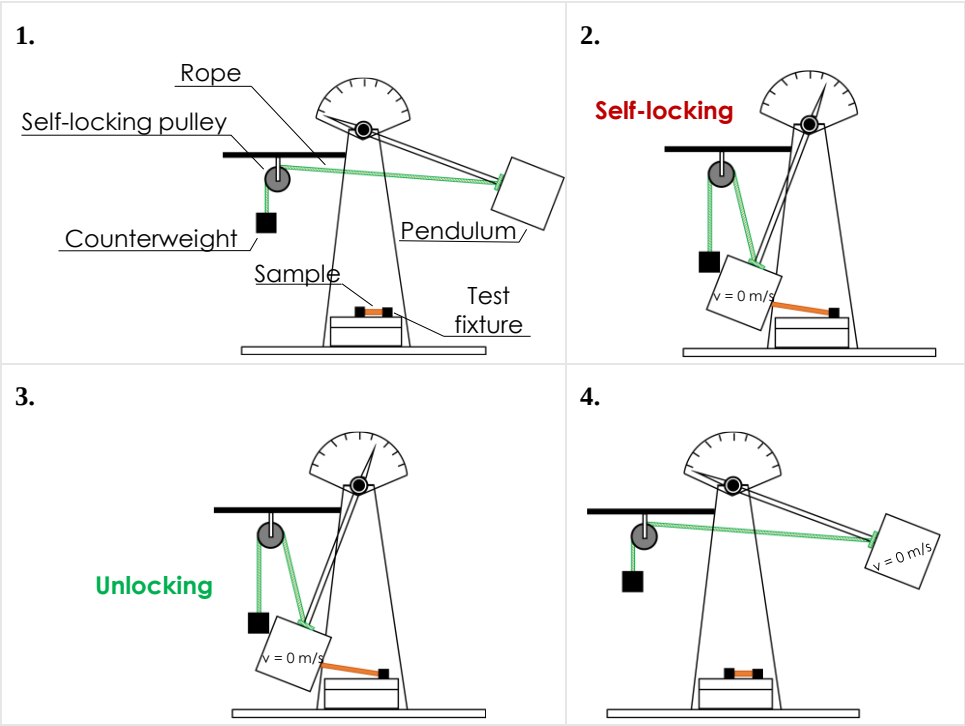


*Figure 3.4. Mechanism used to actuate the self-locking and unlocking of the pendulum.*

A self-locking pulley (Petzl, Micro Traxion) was mounted on a rigid support perpendicular to the plane of motion of the pendulum apparatus, and a rope was routed through it. One end of the rope was attached to the pendulum, while the other end was connected to a counterweight (Figure 3.4(1)). The counterweight was used to provide sufficient tension to ensure the rope slid smoothly through the pulley while the pendulum was moving. After the pendulum stretched the specimen and reached its maximum height, the onset of the backswing triggered the pulley to lock the rope, thereby arresting the pendulum's motion (Figure 3.4(2)). Conversely, the unlocking procedure was carried out by manually releasing the pulley and fixing the pendulum in the starting position (Figure 3.4(3,4)).

To eliminate the Mullins effect, the samples were pre-stretched three times in the manner described in Paragraph 3.2.12.1, and then re-fixed at both ends to remove the influence of residual strain. For each NR sample, four starting positions of the hammer were considered and, consequently, four impact velocities and impact energies. The values are reported in Table 3.5.

*Table 3.5. Impact velocities and impact energies applied for the evaluation of the elastocaloric properties of the prepared NR samples (preliminary set up).*

| | **Impact velocity (m/s)** | **Impact energy (J)** |
|---|---|---|
| Starting position 1 | 0.99 | 1.07 |
| Starting position 2 | 1.31 | 1.87 |
| Starting position 3 | 1.62 | 2.86 |
| Starting position 4 | 1.92 | 4.01 |

The temperature variation of the surface of the specimens was recorded by using an infrared thermal imaging camera FLIR E60

(FLIR Systems, Inc., Wilsonville, OR), placed at a fixed distance of 25 cm from the surface of the NR strips. The IR thermal camera resolution was 0.1 °C, the acquisition frequency of the IR image was set at 16 fps and the emissivity parameter employed was 0.9. The FLIR software (Version 5.13.18031.2002) was used to measure punctual temperature values in the central part of the specimens. Figure 3.5 shows the positioning of the infrared thermal camera relative to the samples during the experiments.

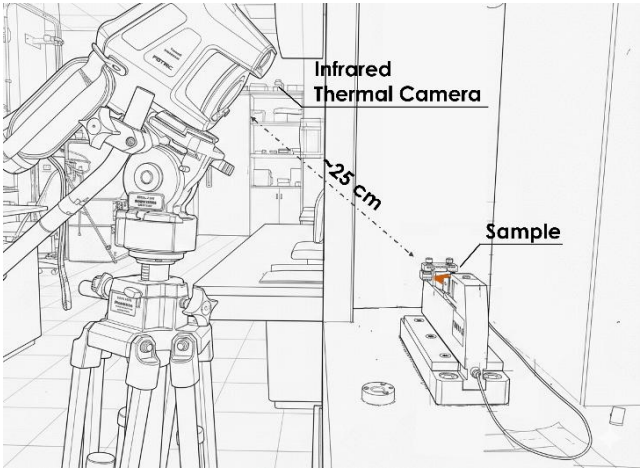


*Figure 3.5. Positioning of the infrared thermal camera relative to the samples during the experiments.*

This preliminary set-up presented several limitations. First, it was not possible to control the deformation level of the samples. Second, the deformation rate was not constant during the deformation as it decreased from the selected impact velocity to 0 m/s. Furthermore, with this experimental setup, it was not possible to verify whether the selected impact velocities ensured adiabatic deformation of the samples. Given the high impact velocities, it is likely that the deformation occurred under adiabatic conditions, although this has not been conclusively demonstrated. The performance of the samples

was compared by fixing the impact velocity. However, this comparison was not precise and only partial, as the deformation level varied depending on the stiffness of the formulations.

The high-speed tensile testing machine used at STEP Lab was a STEP Lab XUD05 equipped with a 1 kN load cell. The tests were carried out at room temperature (approx. 22 °C) and rectangular specimens 1 mm thick and 15 mm wide were used. The distance between the specimen grips was set at 25 mm (tested volume of the specimens of about 0.4 $cm^3$). The following procedure was adopted to evaluate the elastocaloric performance: at first, the specimens were rapidly stretched up to the desired deformation level, setting the crosshead speed at 0.5 m/s (strain rate 20 $s^{-1}$). This testing speed was selected as it ensured adiabatic conditions. After that, they were maintained in traction for a fixed amount of time, to allow the materials to return to room temperature. The cooling of natural rubber occurred both by natural convection and forced convection. The NR samples were then unloaded, at the same crosshead speed of the stretching phase, followed by a relaxation step. The strain levels explored ranged between 300% and 500% and two specimens were tested per each strain level. The surface temperature variation of the samples during the elastocaloric tests was recorded by using an infrared thermal imaging camera IRtech Fotric 348A (E Instrument Group s.r.l., Lesmo MB, Italy), placed at a fixed distance of 50 cm from the surface of the NR strips, having a thermal sensitivity of 0.04 °C. The acquisition frequency was set at 16 fps and the emissivity parameter employed was 0.9. The AnalyzIR software (Version 5.0.7.117) was used to measure punctual temperature values in the centra part of the specimens.

For each test, the mechanical energy at stretching ($W_s$) and the mechanical energy at retraction ($W_r$), illustrated as an example in Figure 3.6, were calculated integrating the force by the displacement.

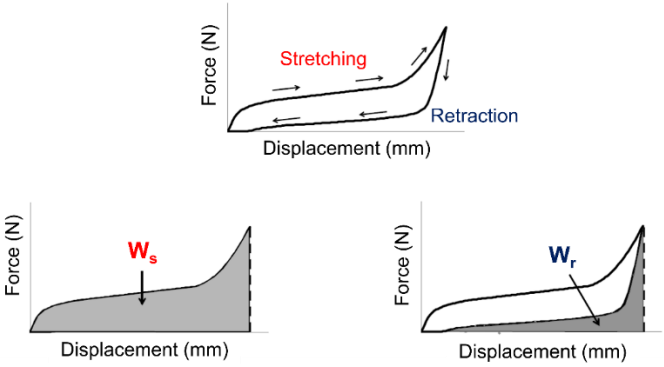


*Figure 3.6. Mechanical energy at stretching (area under the loading curve) and the mechanical energy at retraction (area under the unloading curve) in force-displacement curves of an elastomer.*

The stress relaxation of the samples in the relaxation step after stretching was also evaluated. In particular, the stress sustained by the sample was plotted as a function of time and the percentage of stress relaxation (SR) was calculated according to Equation (3.7):

$$SR\ (\%) = \frac{\sigma_0 - \sigma_x}{\sigma_0} \cdot 100 \qquad (3.7)$$

where $\sigma_0$ is the maximum stress, attained when the selected deformation is achieved, and $\sigma_x$ is the stress at the end of the relaxation phase.

### *3.2.12.2 Calculation of the elastocaloric properties*

The data processing procedure followed to determine the elastocaloric properties of the samples was identical for both the set-up.

As the thickness of the tested samples was 1 mm and Biot number (i.e., the ratio between the thermal resistance for conduction inside

the body and the resistance for convection at the surface of the body [23]) was found to be less than 0.1, temperature difference between the surface and the core of the specimens could be considered negligible. Thus, the temperature could be deemed uniform throughout the material. Both during the stretching and retraction phase, the temperature of the samples, determined by using the infrared thermal camera, was represented as a function of time. The temperature variation of one of the tested specimens, deformed during the test at 500 %, is reported as an example in Figure 3.7(A,B).

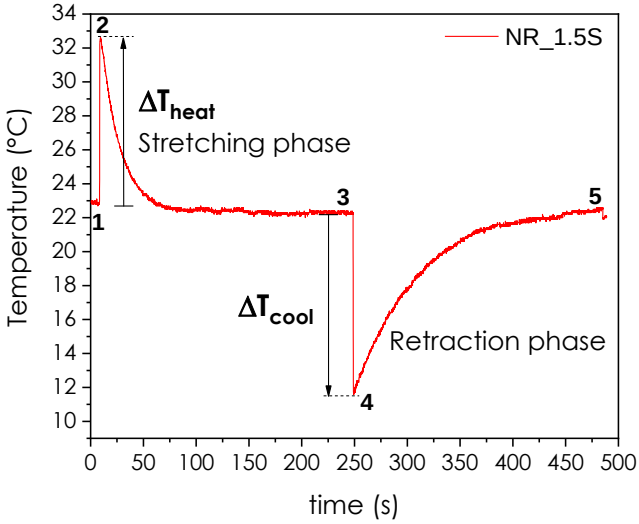


(A)

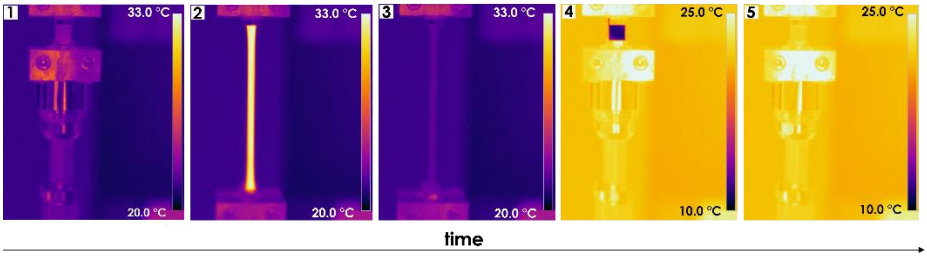


(B)

*Figure 3.7. Representation of the temperature variation of one of the tested specimens during the stretching and retraction phase using the high-speed tensile testing machine (maximum deformation applied = 500%). (A) temperature variation as a function of time and (B) corresponding surface temperature images acquired through IR camera.*

For each specimen and strain level explored, the temperature increase during the stretching phase ($\Delta T_{heat}$) and the temperature reduction during the retraction phase ($\Delta T_{cool}$) were registered. In addition, the characteristic time of temperature dampening ($\tau_c$), the heat released to the environment per unit volume during the stretching phase ($Q_{re}$) and the heat absorbed from the environment per unit volume during the retraction phase ($Q_{ab}$) were calculated. The $\Delta T_{heat}$ and $\Delta T_{cool}$, represented in Figure 3.7, were respectively evaluated as the difference between the temperature of the NR samples just after the stretching and releasing phase (points 2 and 4 in Figure 3.7) and the temperature assumed by the material before the mechanical action (points 1 and 3 in Figure 3.7), assuming the material to be in thermal equilibrium with the environment). The characteristics time of temperature dampening, i.e., the time in which the temperature difference between the NR samples and the air drops, in absolute value, at a fraction equal to 1/e (≈ 37%) of the initial value, was calculated both for the stretching and retraction phases. This parameter is of fundamental importance since provides information about the kinetics of the heat exchange process [23]. The thermal

analysis adopted to determine $\tau_c$, and to describe how the temperature of the NR samples evolved over time due to the convective heat transfer with the surrounding fluid, is described below.

Immediately after stretching or retraction, the NR samples were assumed to be at a uniform temperature $T_0$ (i.e., points 2 and 4 in Figure 3.7) and immersed in a fluid at constant temperature $T_f$. Because $T_0 \neq T_f$, the material subsequently underwent either cooling (after stretching) or heating (after retraction) as heat was exchanged with the surrounding fluid. Heat transfer within the solid occurred by conduction, whereas heat exchange between the solid and the surrounding fluid occurred by convection. Since the temperature variation between the sample and the environment remained small [45], the radiative heat transfer phenomena were considered negligible.

Although heat transfer within the NR samples is governed by Fourier's law, the internal thermal resistance was much smaller than the convective resistance at the sample–fluid interface, as indicated by a low Biot number. Consequently, any temperature gradients that arose inside the material after stretching or retraction were rapidly eliminated by thermal conduction, and the samples remained in quasi-thermal equilibrium at all times. Under these conditions, the temperature of the NR samples was considered spatially uniform and dependent only on time, and the heat-transfer process was controlled primarily by convection at the surface.

Under these assumptions, the transient energy balance of the NR samples reduced to a lumped heat-capacity equation, where the rate of change of the internal energy of the sample equals the heat exchanged with the surrounding fluid, as reported in Equation (3.8):

$$-hA\left(T - T_f\right) = \rho V c_p \frac{dT}{dt} \qquad (3.8)$$

where A is the area of heat exchange ($m^2$), T is the temperature of the sample assumed at time t, V is the volume of the material ($m^3$), ρ is the density ($g/m^3$) and $c_p$ is the specific heat capacity of the material ($J/(g \cdot K)$). The material properties (ρ, $c_p$) were assumed to be independent on strain and temperature, and the convective heat-transfer coefficient was assumed to be constant.

Solving the equation by separation of variables and integrating then, from the initial conditions (t= 0, T= $T_0$) to the generic conditions t and T, Equation (3.9) is obtained:

$$\frac{T - T_f}{T_0 - T_f} = e^{\left(-\frac{hA}{\rho V c_p}\right)t} \tag{3.9}$$

From which it follows Equation (3.10):

$$T(t) = T_f + \left(T_0 - T_f\right)e^{-hA/\rho V c_p t} = T_f + \left(T_0 - T_f\right)e^{-t/\tau_c} \tag{3.10}$$

All the influencing quantities (A, $c_p$, h, V, ρ) can be combined into the characteristic time of temperature dampening, $\tau_c$, as reported in Equation (3.11):

$$\tau_c = \rho V c_p / hA \tag{3.11}$$

Equation (3.11) can be rewritten as the product of a lumped thermal capacitance and a convection thermal resistance, as reported in Equation (3.12):

$$\tau_c = \left(\rho V c_p\right)\left(\frac{1}{hA}\right) \tag{3.12}$$

The higher the lumped thermal capacitance and the convection thermal resistance, the slower is the heat transfer process.

To quantify the time required for the material to return to the environmental temperature $T_f$, the time to reach 98% of the initial temperature difference can be calculated as shown in Equation (3.13):

$$t_{98\%} = \tau_c \ln\left(\frac{T_0 - T_f}{T - T_f}\right) = \tau_c \ln\left(\frac{T_0 - T_f}{0.02(T_0 - T_f)}\right) = \tau_c \cdot 3.9 \qquad (3.13)$$

This equation highlights that the time required for the material to return to $T_f$ can be estimated as four times the characteristic time of temperature dampening.

The characteristic time of heat exchange was determined by fitting the experimental temperature variation curves, related to the stretching and retraction phase, by using Equation (3.10). Figure 3.8 shows an example of the fitting procedure.

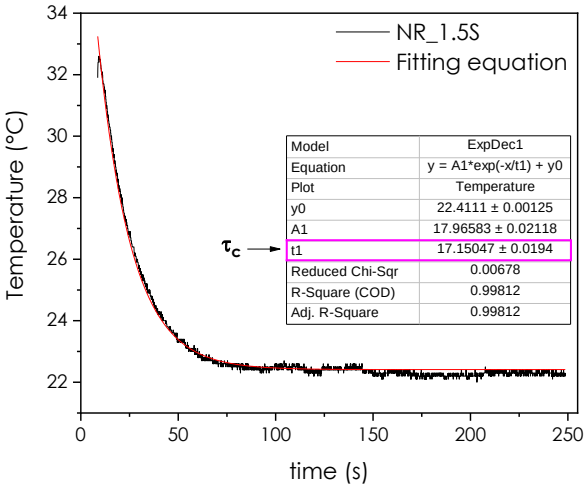


*Figure 3.8. Example of the fitting procedure adopted to determine the characteristic time dampening ($\tau_c$).*

Once determined the characteristic time of temperature dampening ($\tau_c$), the heat transfer coefficient (h) was evaluated by using a reverse

procedure. From Equation (3.11), as all the other parameters are known, the heat transfer coefficient could be determined via Equation (3.14) as:

$$h = {}^{\rho V c_p}/_{A\tau} \qquad (3.14)$$

The heat-transfer coefficient determined using this procedure is valid only for the specific experimental arrangement adopted. The orientation of the material and the manner in which it is deformed influence the surrounding flow field and, consequently, the convective heat-transfer conditions.

The heat released ($Q_{re}$) and extracted ($Q_{ab}$) from the environment per unit volume of material was calculated, respectively, via Equations (3.15) and (3.16) as:

$$Q_{re} = h_s \cdot A_s \cdot \int_{t1}^{t2} T(t)dt \,/V \qquad (3.15)$$

$$Q_{ab} = h_r \cdot A \cdot \int_{t3}^{t4} T(t)dt \,/V \qquad (3.16)$$

where $h_s$ and $h_r$ are the heat transfer coefficients determined experimentally in the stretching and retraction phases, as previously explained, $A_s$ is the surface of the sample between the specimen grips during stretching, A is the area of the unstretched sample between the specimen grips, $t_1$, $t_2$, $t_3$ and $t_4$ define the time interval in which the heat release/absorption from the environment occurred (see Figure 3.9), while T(t) is the experimental temperature variation within the samples during the tests.

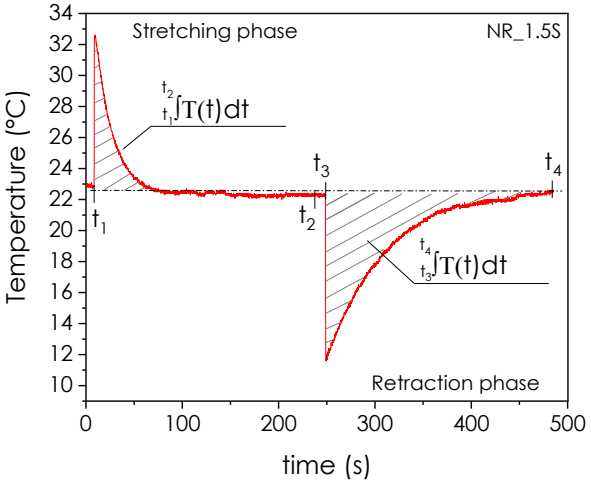


*Figure 3.9. Example of the integration procedure to determine the heat released and extracted from the environment during the stretching and retraction phase, respectively.*

Finally, the Coefficient of Performance ($COP_{mat}$) value was calculated based on the set-up used. In particular, for the preliminary set-up, the $COP_{mat}$ was evaluated as the ratio between the heat absorbed during retraction phase ($Q_{ab}$) and the impact energy per unit volume of material (I), as reported in Equation (3.17):

$$COP_{mat} = \frac{Q_{ab}}{I} \tag{3.17}$$

while, for the high-speed tensile testing machine, as the ratio between $Q_{ab}$ and the mechanical energy at stretching employed to deform the samples during the elastocaloric tests, per unit volume of material ($W_s/V$), as reported in Equation (3.18):

$$COP_{mat} = \frac{Q_{ab}}{\left(\frac{W_s}{V}\right)} \tag{3.18}$$

The $COP_{mat}$ parameter was qualitative (i.e., it refers to the material rather than a prototype) and was introduced solely to compare the performance of the produced samples and to identify the most promising formulation.

# 4 Effect of crosslinking density on the elastocaloric properties of Natural Rubber

***Part of this chapter has been published in:***

M. Bianchi, L. Fambri, G. Fredi, A. Pegoretti and A. Dorigato

**"Elastocaloric Performance of Natural Rubber in Solid State Cooling: Evaluation of the Effect of Crosslinking Density"**

*Applied Sciences 2024, 14, 10525*
*https://doi.org/10.3390/app142210525*

## *4.1 Introduction*

As already explained in Chapter 2, global temperatures have risen by approximately 1.1 °C since the Industrial Revolution, leading to more frequent extreme weather events such as heat waves and floods [6,13]. To cope with rising temperatures, air conditioning has become essential for billions of people worldwide. However, conventional vapour-compression systems consume large amounts of electricity and use refrigerants with high global warming potential, creating a feedback loop that exacerbates climate change [13].

Elastocaloric cooling has emerged as a sustainable and efficient alternative to conventional refrigeration technologies [9]. Among elastomers exhibiting the elastocaloric effect, NR stands out due to its unique combination of nontoxicity, low cost, softness, long fatigue life, and excellent caloric performance, which arises from the synergistic contributions of thermoelasticity and strain-induced crystallization [41,43]. Nevertheless, research on the refrigeration potential of NR is still in its infancy, and not all parameters influencing the elastocaloric behaviour of this material are fully understood. Only by identifying these key parameters it will be possible to optimize the cooling performance of natural rubber and to

advance solid-state cooling technologies capable of competing with existing solutions. Recent works have mainly explored the effect of testing parameters such as temperature, strain rate and maximum deformation on the elastocaloric properties of NR [22,116]. However, the relationship between rubber network structure, specifically the crosslinking density, and the elastocaloric effect has never been systematically addressed. Hence, the focus of Chapter 4 is to examine the potential impact of crosslinking density on the elastocaloric performance of NR and elucidate the nature of this influence.

## *4.2 Materials and Methods*

### 4.2.1 Materials

The materials used in this Section are listed in Table 4.1, along with the reference Section that provides their detailed description.

*Table 4.1. List of the materials used in this part of the thesis.*

| Material | Section |
|---|---|
| Natural Rubber | 3.1.1 |
| Zinc Oxide | 3.1.2 |
| Sulphur | 3.1.2 |
| ZDBC | 3.1.2 |
| Stearic Acid | 3.1.2 |
| Toluene | 3.1.3 |
| Methanol | 3.1.3 |
| Acetone | 3.1.3 |

### 4.2.2 Sample preparation

With the aim of producing NR samples with different degrees of crosslinking density, nine NR compounds were prepared, each with a different combination of sulphur and accelerator. The selected

sulphur contents were 1.5, 2.5 and 3.5 phr, while the accelerator contents were 0.4, 0.7 and 1.0 phr. Among the NR compounds produced, the three that led to distinct crosslinking densities were selected for the study. A conventional curing system, i.e., rubber formulations characterized by a sulfur-to-accelerator ratio ranging between 0.1 and 0.6, was chosen for the NR formulations. This choice was dictated by the fact that, according to the literature [61,64,65], physical properties such as tensile strength, fatigue resistance and elongation at break are superior in this type of system. When the application of NR in a solid-state cooler is considered, good fatigue resistance is of fundamental importance, as the rubber in this working condition should be subjected to several loading and unloading cycles. The composition in parts per hundred rubber (phr) of the prepared NR compounds, along with their codes, is reported in Table 4.2. The code of the natural rubber samples consists of the term NR, followed by a number indicating the sulfur content (in phr) and the letter S for sulfur, and a number indicating the accelerator content (in phr), followed by the letter A for the accelerator. The code UNR refers to the uncrosslinked rubber.

The vulcanization characteristics of the produced NR compounds were investigated through rheological analysis. As it will be discussed in Section 4.3.1, the results evidenced that the compounds characterized by an accelerator content of 0.7 phr and different sulphur concentrations (NR_1.5S_A0.7, NR_2.5S_A0.7 and NR_3.5S_A0.7) were those leading to distinct crosslinking densities. From that point in the study, the accelerator concentration will be omitted in the code.

*Table 4.2. Composition of the NR compounds analysed.*

| Sample | NR (phr) | Sulphur (phr) | ZnO (phr) | Stearic acid (phr) | ZDBC (phr) |
|---|---|---|---|---|---|
| **UNR** | 100.0 | 0.0 | 0.0 | 0.0 | 0.0 |
| **NR_1.5S_0.4A** | 100.0 | 1.5 | 5.0 | 2.0 | 0.4 |
| **NR_1.5S_0.7A** | 100.0 | 1.5 | 5.0 | 2.0 | 0.7 |
| **NR_1.5S_1A** | 100.0 | 1.5 | 5.0 | 2.0 | 1.0 |
| **NR_2.5S_0.4A** | 100.0 | 2.5 | 5.0 | 2.0 | 0.4 |
| **NR_2.5S_0.7A** | 100.0 | 2.5 | 5.0 | 2.0 | 0.7 |
| **NR_2.5S_1A** | 100.0 | 2.5 | 5.0 | 2.0 | 1.0 |
| **NR_3.5S_0.4A** | 100.0 | 3.5 | 5.0 | 2.0 | 0.4 |
| **NR_3.5S_0.7A** | 100.0 | 3.5 | 5.0 | 2.0 | 0.7 |
| **NR_3.5S_1A** | 100.0 | 3.5 | 5.0 | 2.0 | 1.0 |

The rubber compound production process referred to ASTM 3182 standard, with the mixing stages summarized in Table 4.3. The setting of all the parameters was based on optimisation resulting from preliminary tests. First, NR underwent a mastication process lasting five minutes in an internal mixer (Thermo Haake Rheomix 600, Thermo Fisher Scientific, Waltham, MA, USA), equipped with counter-rotating rotors, operating at a temperature of 50 °C and a rotation speed of 60 rpm. Subsequently, the rubber chemicals were added to NR. The order of addition was as follows: ZnO, stearic acid, ZDBC and, lastly, sulphur. Upon the introduction of the rubber compound chemicals, the mixture was blended and homogenized for two minutes.

*Table 4.3. Procedure used for mixing natural rubber compounds.*

| Stage | Process/Ingredients | Time (min) |
|---|---|---|
| I | Mastication of NR | 5 |
| II | ZnO | 1 |
| III | Stearic Acid | 1 |
| IV | ZDBC | 1 |
| V | Sulphur | 1 |
| VI | Mixing for homogenization | 2 |

The resulting NR compounds were then subjected to vulcanization using a Carver hydraulic hot press (Carver, Wabash, IN, USA). The vulcanization process was performed at a temperature of 120 °C and a pressure of 5 bar. Depending on the formulations, the curing time varied between 16 and 19 minutes. The optimal curing time was selected based on the result of the rheological analysis described in Section 4.3.1. The vulcanization occurred in molds having dimensions 110x110x1 $mm^3$ and 110x110x3 $mm^3$. Samples with a thickness of 1 mm were used for the evaluation of the elastocaloric properties and for the determination of thermal properties by means of LFA analysis, while the 3 mm-thick samples were produced to conduct the mechanical characterization.

## *4.3 Results and Discussion*

### 4.3.1 Rheological analysis

Rheological analysis was performed to study the vulcanization characteristics of the produced NR compounds and to identify three formulations leading to distinct and quite equally separated crosslinking densities. The tests were carried out at 120 °C, a temperature selected on the basis of preliminary trials. The selection of the three NR formulations was based on the maximum torque value measured at the end of the vulcanization process, which was used as

an indicative parameter of the crosslinking degree. The vulcanization curves of the investigated rubber compositions, expressed as torque as a function of time, are shown in Figure 4.1(A-F). To better understand the results, Figure 4.1 (A-C) presents the vulcanization curves grouped by fixed accelerator content, while Figure 4.1(D-F) shows the curves grouped by fixed sulphur content. In Table 4.4, the main vulcanization characteristics are reported.

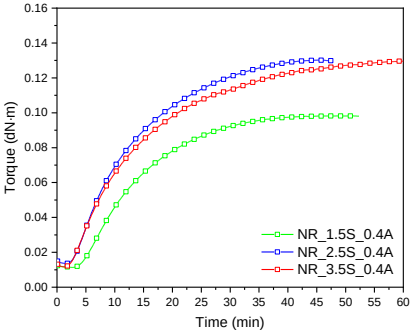


(A)

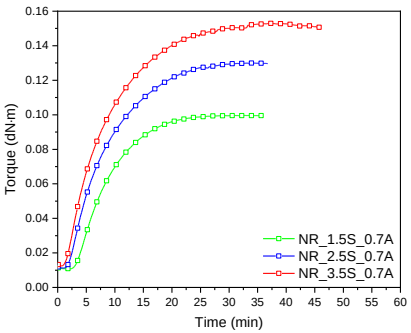


(B)

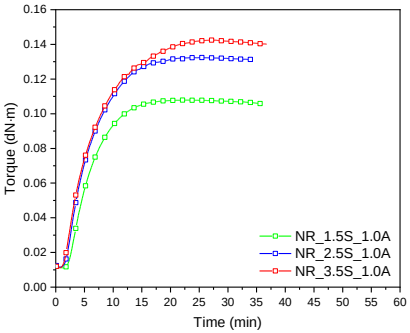


(C)

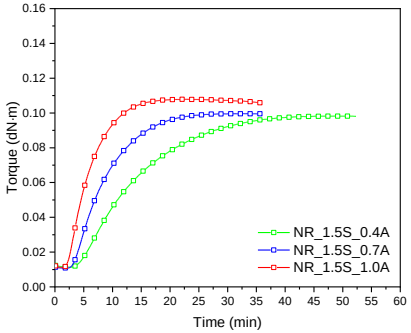


(D)

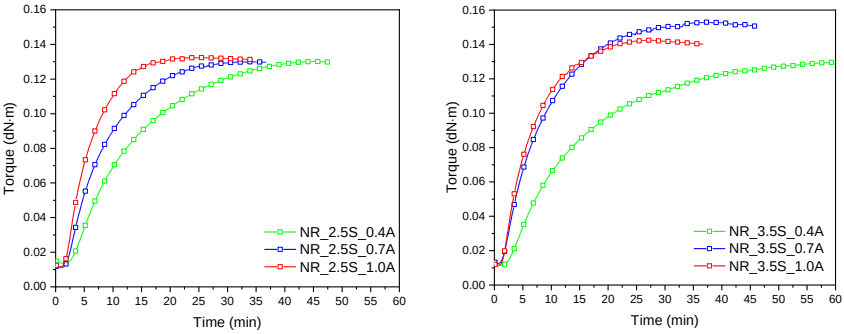


(E) (F)

*Figure 4.1. Vulcanization curves at 120 °C of the different NR formulations, effect of sulphur and accelerator content. (A-C) Vulcanization curves grouped by accelerator content and (D-F) vulcanization curves grouped by sulphur content.*

*Table 4.4. Minimum torque ($T_{min}$), maximum torque ($T_{max}$) and optimum curing time ($t_{90\%}$) for samples with different sulfur and accelerator content. Selected compositions are highlighted in grey.*

| Sample | $T_{min}$ (dN·m) | $T_{max}$ (dN·m) | $t_{90\%}$ (min) |
|---|---|---|---|
| **NR_1.5S_0.4A** | 0.0113 | 0.0982 | 27 |
| **NR_2.5S_0.4A** | 0.0136 | 0.1302 | 28 |
| **NR_3.5S_0.4A** | 0.0117 | 0.1297 | 34 |
| **NR_1.5S_0.7A** | 0.0108 | 0.0996 | 16 |
| **NR_2.5S_0.7A** | 0.0112 | 0.1300 | 18 |
| **NR_3.5S_0.7A** | 0.0125 | 0.1531 | 19 |
| **NR_1.5S_1.0A** | 0.0112 | 0.1078 | 11 |
| **NR_2.5S_1.0A** | 0.0116 | 0.1324 | 12 |
| **NR_3.5S_1.0A** | 0.0111 | 0.1425 | 15 |

As might be expected, increasing the accelerator content speeds up the vulcanization kinetics, leading to the attainment of complete crosslinking within a shorter time. This is clearly visible by analysing the vulcanization curves in Figure 4.1(A-F) and the $t_{90\%}$ reported in Table 4.4. The vulcanization process can be considered nearly complete when the measured torque value stabilizes and reaches a plateau value. The accelerator concentration does not significantly affect the maximum torque achievable, and thus the crosslinking density. Indeed, keeping the sulphur content constant and increasing the accelerator concentration, the maximum torque remains mostly unchanged, with the exception of the tern NR_3.5S_0.4A, NR_3.5S_0.7A and NR_3.5S_1.0A shown in Figure 4.1F. The NR_3.5S_0.4A formulation does not achieve a plateau, the torque continues to slightly increase with time, suggesting that high sulphur level and low accelerant concentration leads to incomplete crosslinking at 120 °C within the time frame considered. In contrast, the sulphur concentration is a parameter that greatly affects the $T_{max}$ achievable, as can be observed in Table 4.4. Increasing the sulphur concentration while keeping the accelerator content constant leads to a higher degree of crosslinking. From a comparison of all the formulations produced, it is possible to notice that the three compounds constituted by an accelerator content of 0.7 phr (Figure 4.1B) exhibit distinct and quite equally separated $T_{max}$ and, consequently, a distinct degree of crosslinking. Moreover, since the accelerator concentration is kept constant, the formulations differ exclusively in their sulphur content. These three formulations were therefore selected for further investigation and from this point onwards, the accelerator concentration will not be reported in the samples code.

### 4.3.2 Density measurements

The density values of the unvulcanized rubber and the different crosslinked samples, resulting from the application of Archimedes' principle, are reported in Table 4.5.

*Table 4.5. Density values of the samples resulting from the application of Archimedes' principle.*

| Sample | Density (g/cm$^3$) |
|---|---|
| UNR | 0.847 ± 0.009 |
| NR_1.5S | 0.958 ±0.006 |
| NR_2.5S | 0.968 ± 0.005 |
| NR_3.5S | 0.981 ± 0.007 |

The vulcanization of NR results in an increase in material density as the formation of chemical bonds holds polymer chains more tightly and restricts their movement, leading to a more compact structure. For example, the formulation NR_1.5S exhibits a 13% higher density compared to UNR, while the NR_3.5S sample shows a 15% increase. For the crosslinked samples, the density increases progressively with increasing sulphur content and hence the crosslinking degree, as it will be further discussed in Paragraph 4.3.3. The experimental results are in good agreement with the values reported in the literature for similar systems [114].

### 4.3.3 Evaluation of the crosslinking density

The crosslinking densities of the produced samples, obtained by the swelling method, are reported in Table 4.6.

*Table 4.6. Experimental crosslinking densities of the prepared NR samples.*

| Sample | Crosslinking density ($10^{-4}$·mol/cm$^3$) |
|---|---|
| NR_1.5S | 2.94 ± 0.21 |
| NR_2.5S | 4.04 ± 0.22 |
| NR_3.5S | 5.24 ± 0.51 |

The results confirm that the selected rubber formulations lead to three distinct degrees of crosslinking. As expected, with increasing sulphur content and keeping the other additives constant, the crosslinking density of NR increases. The data dispersion seems to depend on sulphur content: the crosslinking density distribution observed in NR_3.5S is wider with respect to NR_2.5S and NR_1.5S. This experimental evidence suggests a lower material homogeneity and could be related to difficulties in obtaining a good dispersion of the vulcanizing agent when increasing the sulphur content in the NR formulations. Figure 4.2 shows the trend of the crosslinking degree as a function of density. It clearly evidences that both these physical properties increase linearly with increasing sulphur content in the formulation.

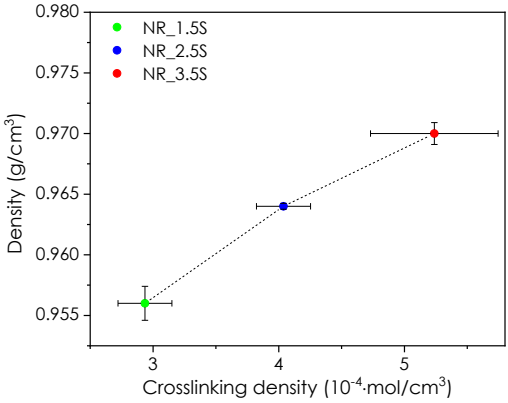


*Figure 4.2. Crosslinking density as a function of density for the vulcanized rubber samples.*

### 4.3.4 Differential Scanning Calorimetry (DSC)

To investigate the thermal properties of the produced samples, DSC analyses have been carried out. Figure 4.3(A,B) shows the thermograms of the 1st heating scan and 2nd heating scan of UNR,

NR_1.5S, NR_2.5S and NR_3.5S samples, while in Table 4.7 the glass transition temperature ($T_g$) values are reported.

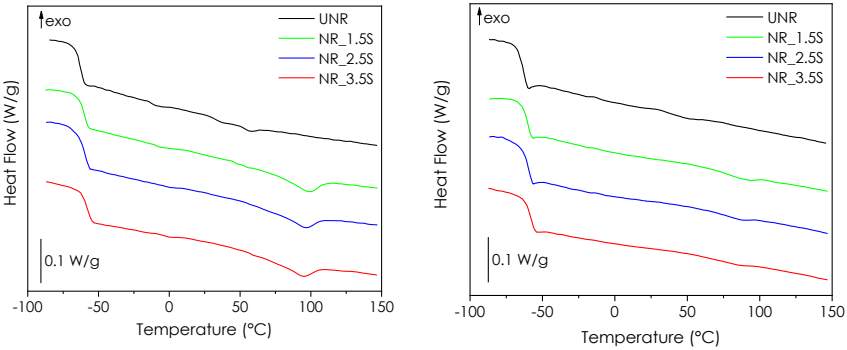


*Figure 4.3. DSC thermograms of (A) the 1st heating scan and (B) 2nd heating scan of UNR, NR_1.5S, NR_2.5S and NR_3.5S samples.*

*Table 4.7. Results of the DSC tests on the prepared NR samples.*

| | **1st heating scan** | **2nd heating scan** |
|---|---|---|
| **Sample** | $T_g$ (°C) | $T_g$ (°C) |
| UNR | -63.8 | -63.2 |
| NR_1.5S | -61.0 | -60.5 |
| NR_2.5S | -60.3 | -60.5 |
| NR_3.5S | -59.0 | -59.0 |

As it can be seen in Table 4.7, the $T_g$ remains essentially unchanged for all rubber formulations between the first and the second heating scan, indicating that the vulcanization process was completed for all the samples. A slight increase in $T_g$ is registered when moving from UNR (-63.8 °C) to the least crosslinked sample NR_1.5S (-61.0 °C). This is reasonable, considering that NR_1.5S underwent melt

compounding and vulcanization, which may have increased macromolecular packing and reduced the polymer chain mobility. Among the vulcanized samples, $T_g$ further increases slightly from NR_1.5S (−61.0 °C) to NR_3.5S (−59.0 °C), confirming that different crosslinked samples were produced and the degree of crosslinking increases with increasing sulphur content.

In the crosslinked samples, an endothermic peak is visible at 70 °C, which disappears in the second heating scan. This signal could be attributed to the evaporation of absorbed moisture. As this endothermic peak is not observed in the unvulcanized sample, the moisture absorption is probably a consequence of the rubber chemicals introduced in the formulations.

### 4.3.5 Thermogravimetric analysis (TGA)

TGA analysis were performed to study the thermal degradation of the produced NR samples. The thermogravimetric curves of UNR and the crosslinked samples, along with the first derivative curves, are shown in Figure 4.4(A,B) while Table 4.8 presents the most important results.

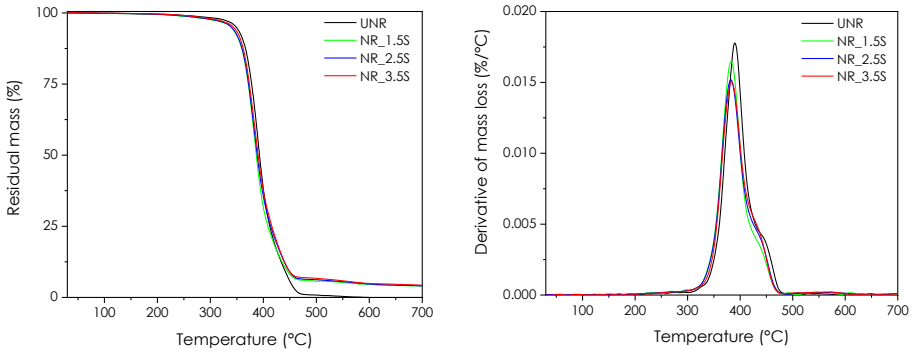


(A) (B)

*Figure 4.4. (A) TGA curves and (B) DTGA curves of the unvulcanized NR and the crosslinked samples.*

*Table 4.8. Results of the thermogravimetric analysis on the prepared rubber samples.*

| Sample | $T_{5\%}$ (°C) | $T_{peak}$ (°C) | $m_{700}$ (%) |
|---|---|---|---|
| UNR | 348.7 | 398.8 | 0.0 |
| NR_1.5S | 339.0 | 382.8 | 4.0 |
| NR_2.5S | 343.3 | 383.3 | 4.3 |
| NR_3.5S | 339.5 | 382.6 | 4.0 |

The results reveal that all samples are thermally stable up to a temperature of approx. 250 °C and then undergo a single major degradation step between 300 and 500 °C. The thermogravimetric curves overlap, suggesting that rubber vulcanization does not enhance the thermal stability. As shown in Figure 4.4A, the non-vulcanized rubber exhibits complete degradation, leaving no residual mass. In contrast, crosslinked samples present a $m_{700}$ of approximately 4.0–4.3%, which can be attributed to the presence of zinc oxide in the rubber formulation. The maximum degradation rate of UNR occurs at slightly higher temperatures compared to the crosslinked samples. Nevertheless, within the range of crosslinking examined, the degree of crosslinking does not affect the temperature at which the maximum degradation rate occurs, which remains at approximately 383 °C. The presence of a shoulder on the main peak of the DTGA of all the samples suggests that the degradation is not a uniform process and may occur in two overlapping steps.

### 4.3.6 Laser Flash Analysis (LFA)

The material capability to release/absorb heat to the environment and the kinetics of such heat exchanges depend on the thermal properties of the material. For this reason, the values of specific heat, thermal diffusivity and thermal conductivity were measured by LFA analysis. The values obtained are reported as a function of the crosslinking density in Table 4.9.

*Table 4.9. Specific heat capacity, thermal diffusivity and thermal conductivity at 20 °C as a function of crosslinking density obtained from LFA analysis on the prepared NR samples.*

| Sample | Crosslinking density ($10^{-4}$·mol/cm$^3$) | $c_p$ (J/g·K) | α (mm$^2$/s) | λ (W/m·K) |
|---|---|---|---|---|
| NR_1.5S | 2.94 ± 0.21 | 1.704 ± 0.049 | 0.081 ± 0.001 | 0.132 ± 0.003 |
| NR_2.5S | 4.04 ± 0.22 | 1.822 ± 0.063 | 0.081 ± 0.002 | 0.143 ± 0.006 |
| NR_3.5S | 5.24 ± 0.51 | 1.775 ± 0.044 | 0.082 ± 0.001 | 0.143 ± 0.004 |

The values of thermal diffusivity, thermal conductivity and specific heat capacity obtained are in agreement with those reported in the literature [114]. No significant differences are observed within the prepared samples, leading to the conclusion that the crosslinking density, in the range studied, does not influence the thermal properties of the samples. Consequently, the origin of any difference in the elastocaloric performance of the NR samples is not attributable to differences in the heat transfer behaviour of the materials.

### 4.3.7 Shore A hardness measurements

In Table 4.10 the results of the Shore A hardness test are reported as a function of crosslinking density.

*Table 4.10. Shore A hardness measurements as a function of crosslinking density for the unvulcanized rubber and the crosslinked samples.*

| Sample | Crosslinking density ($10^{-4}$·mol/cm$^3$) | Shore A hardness |
|---|---|---|
| UNR | - | 25.6 ± 2.2 |
| NR_1.5S | 2.94 ± 0.21 | 38.0 ± 0.8 |
| NR_2.5S | 4.04 ± 0.22 | 41.3 ± 0.7 |
| NR_3.5S | 5.24 ± 0.51 | 43.9 ± 1.3 |

As it could be expected, the Shore A hardness of NR significantly increases following vulcanization. For instance, the least crosslinked sample exhibits a hardness value that is 48% higher than that of UNR sample. Among the vulcanized samples, the hardness value increases with increasing crosslinking density. A higher number of bonds between the rubber chains makes the material stiffer and more resistant to penetration. A trend similar to that observed for hardness is also expected for the stiffness of the materials, as hardness is an indirect measure of Young's modulus of an elastomer [131]. Both properties reflect the strength of the bonds between the polymer macromolecules and, consequently, the material's resistance to deformation.

### 4.3.8 Quasi-static tensile tests

According to the literature [34], NR should be deformed at strain levels close to or higher than 300% to enhance its cooling capacity, as the best elastocaloric performance is achieved when NR crystallizes under strain. Knowing the mechanical behaviour of the samples, and, specifically, the strain at break, is crucial for selecting the strain range to be explored in the elastocaloric tests. The deformation level must, in fact, remain sufficiently far from the strain at break to avoid premature failure during elastocaloric testing. Therefore, quasi-static tensile tests were performed on the samples. The representative stress–strain curves obtained are shown in Figure 4.5, while the main results are summarized in Table 4.11.

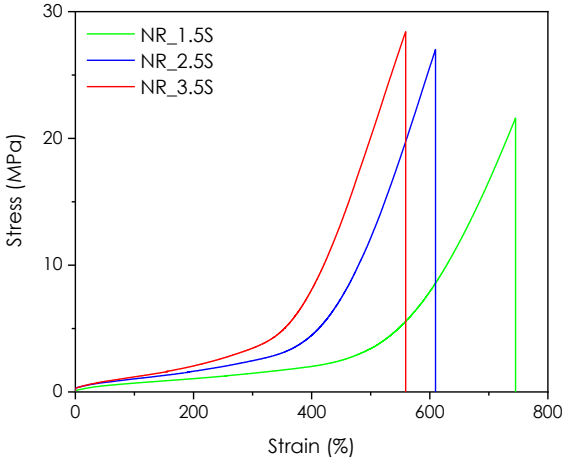


*Figure 4.5. Representative stress-strain curves from quasi-static tensile tests on NR_1.5S, NR_2.5S and NR_3.5S samples.*

*Table 4.11. Results of quasi-static tensile tests at 25 °C on NR_1.5S, NR_2.5S and NR_3.5S samples.*

| Sample | $E_{100\text{-}200}$ (MPa) | $\sigma_{200}$ (MPa) | $\sigma_{400}$ (MPa) | $\sigma_b$ (MPa) | $\varepsilon_b$ (%) | $E_b$ (J/cm$^3$) |
|---|---|---|---|---|---|---|
| NR_1.5S | 0.39 ± 0.08 | 1.08 ± 0.13 | 2.10 ± 0.24 | 21.3 ± 3.7 | 730 ± 14 | 36.0 ± 4.7 |
| NR_2.5S | 0.55 ± 0.06 | 1.71 ± 0.52 | 3.70 ± 0.84 | 23.1 ± 6.3 | 573 ± 79 | 34.6 ± 2.1 |
| NR_3.5S | 0.88 ± 0.07 | 2.07 ± 0.12 | 8.02 ± 1.16 | 22.9 ± 7.1 | 523 ± 47 | 37.5 ± 1.3 |

The stress–strain curves shown in Figure 4.5 present the typical hyperelastic behavior, characterized by an initial “toe region” in which small deformation results in a linear increase in stress, followed by a “plateau region”, where stress remains relatively constant despite further increases in strain, and, finally, a stiffening region in which the material experiences a significant increase in stress as a result of material stiffening. According to the literature [132], rubber stiffening can be attributed to two phenomena: the first

is related to the achievement of the maximum extensibility of the polymeric chains during stretching, while the second mechanism regards the occurrence of strain-induced crystallization. As the crosslinking density of natural rubber increases, the stress–strain curves in Figure 4.5 show a progressive stiffening of the samples. This can also be noted when comparing the stress required to deform the materials by 200% and 400% (see Table 4.11), the values of which increase, moving from NR_1.5S to NR_3.5S. For example, $\sigma_{400\%}$ is equal to 2.1 MPa in NR_1.5S and 8.0 MPa in NR_3.5S. This is a reasonable result considering that the chain length between crosslinks is reduced as the degree of crosslinking increases and, consequently, the limit of chain extensibility is reached earlier [133,134]. Focusing on the stress and strain at break, it is possible to observe that while $\sigma_b$ is comparable among the samples, $\varepsilon_b$ undergoes a reduction, even if not dramatic, with an increasing degree of crosslinking. Finally, the $E_b$ appears to be independent on the degree of crosslinking, with values of approx. 35-36 J/cm$^3$ for all the samples. This arises because the increase in stiffness with increasing crosslinking density is counterbalances by a reduction in the strain at break.

The results demonstrate that the samples could be safely deformed up to 500% strain for the evaluation of the elastocaloric effect, as this strain level remains sufficiently below the $\varepsilon_b$ of all samples. It should be emphasized that the stress required to achieve 500% of deformation ranges between 3 MPa (NR_1.5S) and 15 MPa (NR_3.5S), and is close to the pressure required to compress a refrigerant fluid in the current air conditioning systems, i.e., approx. 1-8 MPa [135]. This is a positive aspect that must be underlined since other caloric materials under study for developing solid-state refrigeration systems, such as shape memory alloys or ferroelectric materials, require stress levels of at least one or two orders of magnitude higher. For example, for shape memory alloys, several hundreds of MPa are required to exhibit elastocaloric performance

[34]. This makes the behaviour of NR interesting and of great potential for solid-state cooling applications.

### 4.3.9 Evaluation of strain induced crystallization

To evaluate the extent of SIC of the samples in the deformation range of 300-500%, XRD analyses were performed on the samples in the stretched state. The diffraction patterns obtained for the crosslinked samples in the unstretched state and at 300%, 400%, and 500% strain are shown in Figure 4.6, while the crystallinity and the average crystallite size values are reported in Table 4.12.

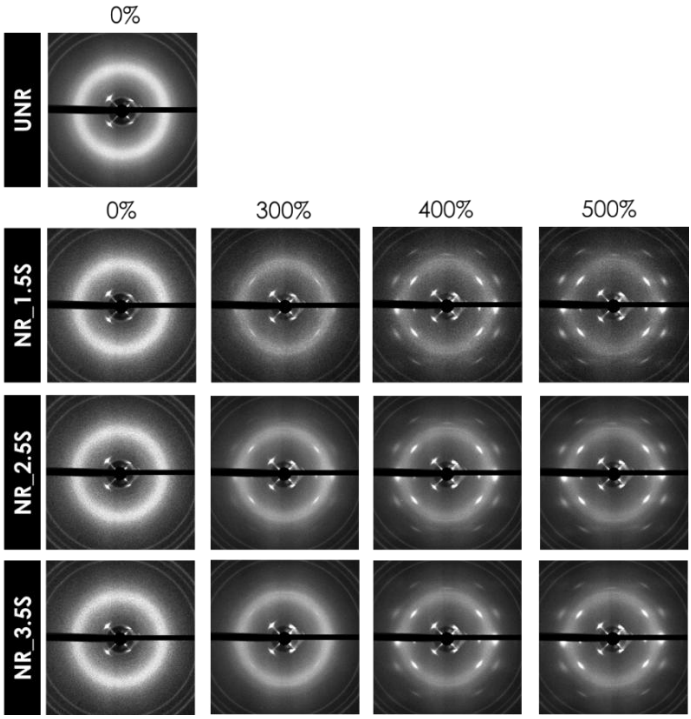


*Figure 4.6. Diffraction patterns of the unvulcanized rubber and crosslinked samples in the unstretched state and at 300%, 400%, and 500% strain.*

*Table 4.12. Average crystallite size and crystallinity obtained from XRD measurements on NR samples.*

| Sample | Deformation (%) | Average Crystallite Size (Å) | Crystallinity (%) |
|---|---|---|---|
| UNR | 0 | - | - |
| NR_1.5S | 0 | N/A | 0.0 |
| | 300 | < 50.0 | 10.5 |
| | 400 | 91.6 | 11.8 |
| | 500 | 108.6 | 12.6 |
| NR_2.5S | 0 | N/A | 0.0 |
| | 300 | < 50.0 | 8.7 |
| | 400 | 59.8 | 10.7 |
| | 500 | 75.1 | 12.5 |
| NR_3.5S | 0 | N/A | 0.0 |
| | 300 | < 50.0 | 8.4 |
| | 400 | 53.0 | 10.0 |
| | 500 | 57.0 | 10.7 |

In the undeformed state, the diffraction patterns of all samples display a diffuse amorphous halo along with reflection rings attributable to the presence of ZnO in the rubber formulations. The amorphous halo indicates that vulcanized NR is completely amorphous and the polymer chains do not show preferred orientation. At 300% strain, highly oriented crystalline reflection peaks begin to appear in the diffraction patterns of all samples, with their intensity increasing as the strain level rises. The most intense reflection arcs correspond to the crystallographic planes (2 0 0), (2 0 1), and (1 2 0), while the less

intense ones correspond to the planes (1 2 1), (2 0 2) and (0 0 2) [136]. These results confirm the deformation range of 300-500% is suitable for the evaluation of the elastocaloric effect, as it combines the contribution of thermoelasticity and strain-induced crystallization. The calculated crystallinity factor evidences that the capability of NR to crystallize under strain is promoted, not only by increasing the strain, but also by reducing crosslinking density. Indeed, for a given deformation level, the crystallinity increases by reducing the degree of crosslinking. The crystallinity is thus higher in NR_1.5S and ranges from 10.5 % at 300% strain to 12.6% at 500% strain. As regards the average crystallite size, it depends on both crosslinking density and strain. In all samples, crystallite size increases with increasing strain, and, at a fixed deformation level, it increases as crosslinking density decreases. For instance, at 500%, the average crystallite size determined for NR_1.5S is 108.6 Å, while for NR_3.5 is 57.0 Å, i.e., almost half. As suggested by Huneau [132], the maximum crystallite size is probably governed by chain length between crosslinks, and thus decreases as crosslinking density increases. The observed trend in crystallinity and average crystal size as a function of degree of crosslinking are consistent with previous observations by Trabelsi et al. [136] and Tosaka et al. [137], who studied the influence of crosslinking density on SIC.

To conclude, the observed dependence of the extent of SIC on the degree of crosslinking suggests that the crosslinking density could affect the elastocaloric response. Given the higher crystallinity content, a more pronounced elastocaloric effect is expected in NR_1.5S. However, SIC is only one of the two contributors to the elastocaloric effect.

By analysing the crystallinity content together with the stress–strain curves in Figure 4.5, it appears that the primary physical origin of the strain-stiffening regime is the progressive approach to the finite extensibility of the polymer chains, i.e., the rubber network structure controls the strain-stiffening mechanism. Although SIC is known to

contribute to the stress increase, the crystallinity data indicate that it does not control the onset of strain stiffening. In particular, NR_1.5S at 500% strain exhibits a higher crystallinity than NR_2.5S and NR_3.5S, despite still being close to the plateau region, whereas the latter samples are already in the strain-stiffening regime. This suggest that SIC is not the physical origin of strain stiffening, but rather a secondary effect that reinforces the material.

### 4.3.10 Evaluation of the Mullins effect

An elastocaloric cooling device requires the repetitive stretching and releasing of rubber. Consequently, it becomes crucial to thoroughly examine the mechanical response of the samples under cyclic loading conditions, particularly considering the susceptibility of NR to the Mullins effect. The quasi-static tensile tests evidence that the samples could be deformed up to 500% for the evaluation of the elastocaloric effect. Therefore, the evaluation of the Mullis effect was performed cyclically stretching the materials up to 200, 300 and 400%. An analysis at a strain level of 500% was also intended; however, due to problems encountered with the extensometer at high elongations during cyclic tensile tests, this could not be performed. Figure 4.7(A-C) shows the stress–strain response of the NR samples under cyclic tensile loading for the different strain levels.

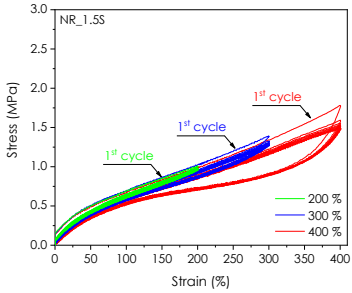


(A)

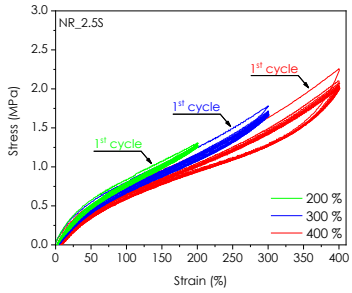


(B)

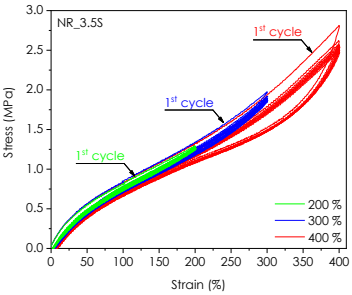


(C)

*Figure 4.7. Stress-strain response of the NR samples under cyclic tensile loading. (A) NR_1.5S, (B) NR_2.5S, (C) NR_3.5S. In each graph, the first cycle is highlighted at every deformation level.*

Analyzing Figure 4.7(A-C), the Mullins effect can be observed in all the samples, particularly in those subjected to a deformation of 300% and 400%. Progressing from the first to subsequent cycles, a noteworthy stress-softening phenomenon becomes evident, together with a reduction in the hysteresis loop, which is representative of the dissipated energy. As the deformation level increases, the Mullins effect becomes increasingly evident. This empirical observation aligns with existing literature on the subject [72]. However, to obtain a more precise comparison of the cyclic tensile behaviour of the samples, the stress at the maximum deformation per each cycle (peak stress) and the energy dissipated in the 1st, 2nd, 5th and 10th cycles have been determined, with the results shown in Figure 4.8(A-C) and Figure 4.9(A-C), respectively, while the residual deformation at the end of the 10th cycle is reported in Figure 4.10.

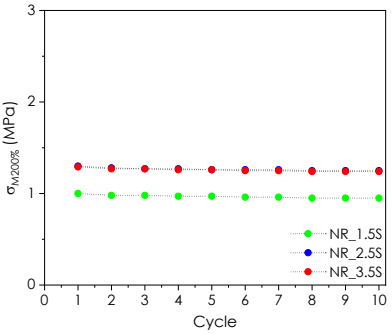


(A)

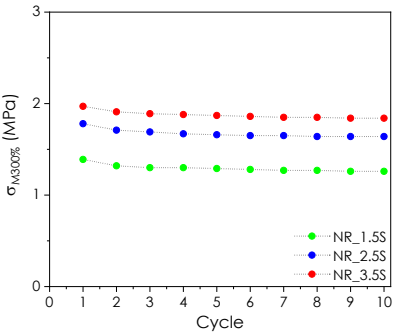


(B)

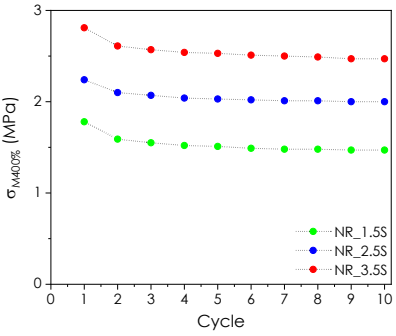


(C)

*Figure 4.8. Peak stress as a function of cycle number and crosslinking density of the prepared NR samples. Maximum deformation level of (A) 200%, (B) 300%, (C) 400%.*

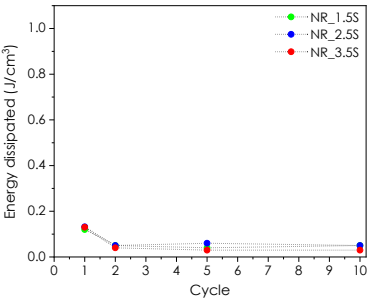


(A)

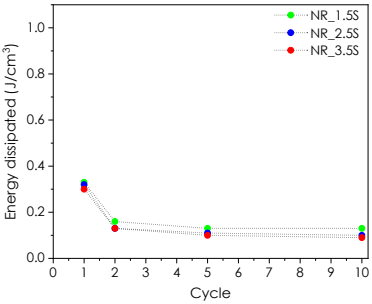


(B)

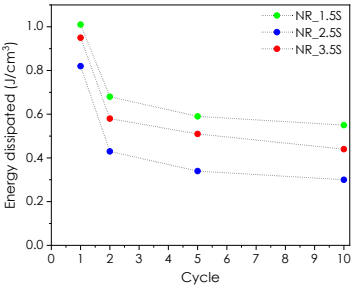


(C)

*Figure 4.9. Energy dissipated as a function of cycle number and degree of crosslinking. Maximum strain level of (A) 200%, (B) 300%, (C) 400%.*

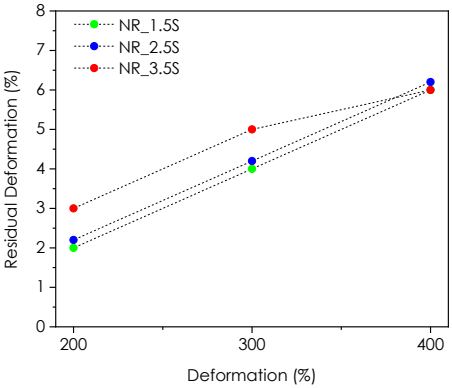


*Figure 4.10. Residual deformation after the 10th cycle as a function of the maximum deformation level and degree of crosslinking of the prepared NR samples.*

Several considerations can be made. As it can be appreciated in Figure 4.8(A-C), the stress softening is more pronounced moving from the 1st to the 2nd cycle. After the 2nd cycle, the maximum stress only slightly decreases, suggesting the mechanical response of the material is stabilized. With increasing strain level, the difference between the peak stress of the 1st and 2nd cycle increases as well. The same consideration can be made also for the energy dissipated (Figure 4.9(A-C)). The variation of the hysteresis loop from the 1st and subsequent cycles is even more pronounced than the stress softening. For example, NR_2.5S experiences a reduction of dissipated energy at 400% strain from 0.8 J/cm$^3$ to 0.4 J/cm$^3$ moving from the 1st to the 2nd cycle. For maximum deformation levels of 200% and 300%, the samples show quite similar dissipated energy values. In contrast, even after the first cycles, significant differences are observed at 400%, where NR_1.5S exhibits the highest hysteresis, followed by NR_3.5S and NR_2.5S. According to Le Cam [138], once the Mullins effect is mitigated, the hysteresis loop in NR reflects changes in the material's microstructure, i.e., significant changes in internal energy associated with SIC. The mechanical energy applied to deform the material is

elastically stored in the amorphous phase and released with different kinetics during crystallite melting upon unloading, generating the hysteresis loop. Therefore, following Le Cam's reasoning, the higher crystallinity content observed in NR_1.5S at 400% strain compared to the other formulations (see Section 4.3.9) could account for the larger hysteresis determined for this sample. However, despite NR_2.5 shows a higher crystallinity than NR_3.5, its hysteresis loop is the least extended. Probably, there are other factors (such as number of dangling chains, trapped entanglements, etc.) that govern the dissipated energy together with SIC. In the future, it will be essential to conduct further analysis to validate this hypothesis.

Finally, the residual deformation values at the end of the $10^{th}$ cycle are shown in Figure 4.10. The values range from 2% to 6% depending on crosslinking degree and applied strain. When holding the degree of crosslinking constant, there is a rise in residual deformation with increasing strain level. Conversely, maintaining a constant strain level, the residual deformation increases with the crosslinking density, specifically at 200% and 300% strain levels, while at 400% the values are close to each other. Since the residual deformation was evaluated at the end of the $10^{th}$ cycle, its trend as a function of cycle number is not known. However, since both dissipated energy and peak stress show the same behaviour, it could be reasonable to assume that the residual deformation so does as well. Therefore, it may be hypothesized that most of the residual deformation results from the $1^{st}$ cycle.

In conclusion, these results highlight the need to pre-stretch the rubber just before its application, especially when its use involves deformation of more than 200%. It is evident that the extent of strain plays a pivotal role in the Mullins effect, whereas the impact of crosslinking density remains not entirely understood. Investigation at a strain level of 500% was not possible; however, based on the results obtained, the Mullins effect is expected to be even more pronounced than that observed at 400%.

In the assessment of the elastocaloric effect, the NR samples underwent a pre-stretching procedure immediately before testing. This pre-stretching procedure was adopted to mitigate the influence of the Mullins effect, which could otherwise compromise the accurate assessment of the elastocaloric performance. However, the Mullins effect is a reversible process and, if the rubber is left to rest for prolonged periods, a partial recovery of this effect may occur. This aspect should be taken into account from a practical point of view, since if a solid-state AC device is not used for a long period of time, the Mullins effect of NR should be removed before its use. Future works will need to determine how long it takes for the material at rest to fully recover the Mullins effect.

### 4.3.11 Evaluation of the elastocaloric effect

Two different testing configurations were used to assess the elastocaloric effect of the samples. Initially, a preliminary experimental set-up was employed, as no tensile testing machine available at the University of Trento could satisfy the required specifications (see Section 3.2.12.1). These preliminary tests provided a first qualitative evaluation of the elastocaloric performance of the materials. Subsequently, collaboration was established with Step Lab S.r.l. (Resana, TV, Italy), which provided a high-speed tensile testing system that met the requirements, enabling precise evaluation and comparison of the elastocaloric performance of the samples. The elastocaloric tests were carried out on-site at their facilities.

#### *4.3.11.1 Evaluation of the elastocaloric effect using a preliminary set-up*

The preliminary evaluation of the elastocaloric properties of the samples was performed using an impact testing machine, following the procedure described in Section 3.2.12. Figure 4.11(A-C) shows the temperature variation of the surface of the NR samples during the stretching and retraction phase as a function of time and impact

velocity. With increasing impact velocity, the materials exhibited increased deformation, and at the same impact velocity, the NR samples showed different strain levels. The resulting deformation as a function of impact velocity are presented in Figure 4.12 and Table 4.13. Numerical values of the deformation of the samples as function of impact velocity.. Before testing, the samples were cyclically deformed twice to mitigate the impact of the Mullins effect.

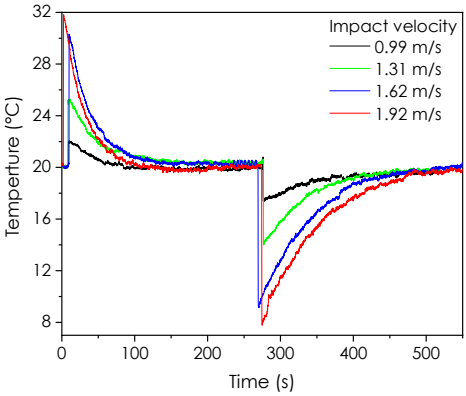


(A)

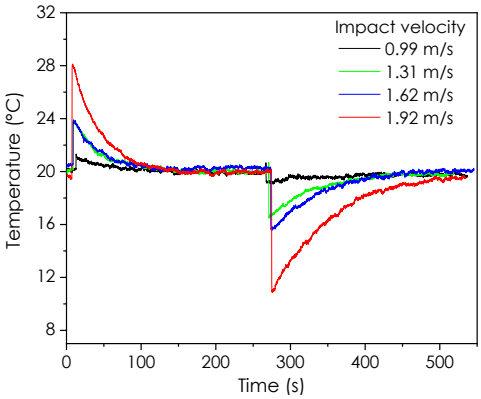


(B)

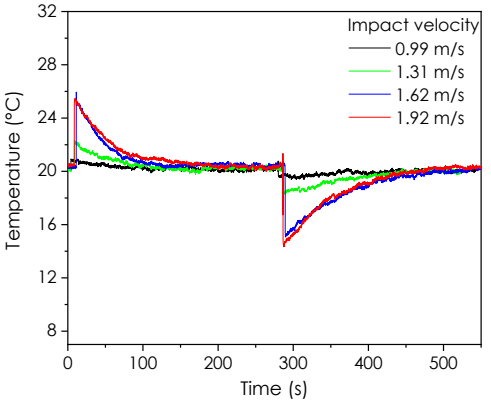


(C)

*Figure 4.11. Temperature variation of the surface of the samples as a function of impact velocity. (A) NR_1.5S, (B) NR_2.5S, (C) NR_3.5S samples.*

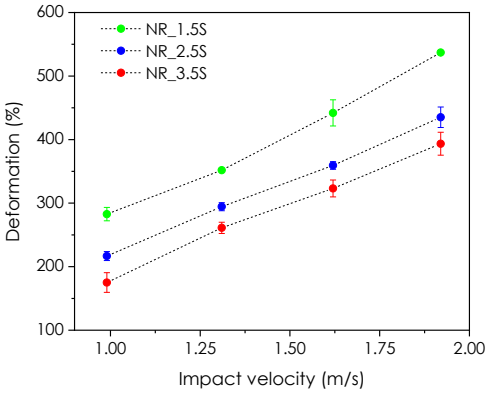


*Figure 4.12. Trend of deformation of the samples as a function of impact velocity.*

*Table 4.13. Numerical values of the deformation of the samples as function of impact velocity.*

| | | Impact velocity (m/s) | | | |
|---|---|---|---|---|---|
| | **Sample** | **0.99** | **1.31** | **1.62** | **1.92** |
| **Deformation (%)** | NR_1.5S | 282.7 ± 10.5 | 351.9 ± 0.1 | 442.0 ± 20.6 | 537.0 ± 0.1 |
| | NR_2.5S | 216.7 ± 7.1. | 294.4 ± 6.4 | 359.3 ± 6.0 | 435.2 ± 16.1 |
| | NR_3.5S | 175.0 ± 15.5 | 261.1 ± 8.8 | 323.1 ± 13.3 | 393.5 ± 18.0 |

For all the samples and testing conditions, the elastocaloric effect is clearly observed. The fast stretching of the materials induces a positive temperature variation caused by the thermoelastic effect and, for samples reaching sufficiently high deformation (≥ 200-300 %), by SIC. When the pendulum self-locks, maintaining the samples in traction, the temperature progressively decreases until reaching ambient temperature and thermal equilibrium. In the retraction phase, the return of the materials to the undeformed, high entropy state and the melting of the crystallites (if developed during the stretching phase) causes the rubbers to cool down.

The impact velocity is the first parameter affecting the temperature variations of the samples. In all the cases, an increase in impact velocity results in greater temperature variations, both during stretching and retraction. The observed dependence could be explained by analysing Figure 4.12 and Table 4.13, where the deformation of all the samples, ranging between 200-550%, is shown to increase almost linearly with impact velocity (i.e., impact energy). In agreement with the results reported in the literature [22], the elastocaloric effect increases with deformation as the entropy variation experienced by the elastomer increases with strain. Moreover, the higher orientation of the macromolecules achieved with increasing strain levels favours strain-induced crystallization

phenomena, which further contributes to the effect. The combined increase of thermoelastic and SIC contribution with strain is likely at the basis of the observed experimental outcome. However, the data obtained do not allow for determining whether impact velocity has an additional effect on the temperature variations, beyond that directly associated with deformation. As highlighted in the literature [22], for the same imposed strain, any deformation rate that ensures adiabatic conditions should not influence the observed temperature variations. This suggests that deformation itself plays the most significant role.

By further analysis, it can be noted that the width of the temperature peaks in Figure 4.11(A-C) (i.e., the time required for the sample to return to ambient temperature) is wider in the retraction phase with respect to the stretching stage. The characteristic time of temperature dampening, determined both during heating (stretching phase) and cooling (retraction phase), reported in Table 4.14, confirms this observation.

For a given degree of crosslinking and impact velocity, the $\tau_{c,r}$ is always higher than $\tau_{c,s}$. During stretching, the specimen becomes thinner and the area of heat exchange increases, favouring a more rapid heat transfer. The heat transfer coefficient, determined only in the retraction phase, are very similar and ranges from 8.4 W/m$^2$K to 14.5 W/m$^2$K, falling within the typical values for natural convection conditions (3-20 W/(m$^2$K)) [139].

*Table 4.14. Characteristic time of temperature dampening calculated in the stretching ($\tau_{c,s}$) and retraction phase ($\tau_{c,r}$), and heat transfer coefficient calculated in the retraction phase ($h_r$) of the samples.*

| | | Impact velocity (m/s) | | | |
|---|---|---|---|---|---|
| | **Sample** | **0.99** | **1.31** | **1.62** | **1.92** |
| **Stretching phase $\tau_{c,s}$ (s)** | NR_1.5S | 33.8 | 37.3 | 30.9 | 28.2 |
| | NR_2.5S | 54.6. | 36.3 | 31.6 | 37.3. |
| | NR_3.5S | 57.5 | 48.1 | 32.4 | 46.4. |
| **Retraction phase $\tau_{c,r}$ (s)** | NR_1.5S | 61.8. | 61.1. | 73.7 | 80.8 |
| | NR_2.5S | 61.6. | 60.7 | 69.2 | 80.7 |
| | NR_3.5S | 95.6 | 105.1 | 82.9 | 72.4 |
| **Retraction phase $h_r$ (W/m$^2$K))** | NR_1.5S | 13.2 | 13.4 | 11.1 | 10.1 |
| | NR_2.5S | 14.4 | 14.5 | 12.7 | 10.9 |
| | NR_3.5S | 9.2 | 8.4 | 10.6 | 12.2 |

According to the procedure described in Section 3.2.12., the temperature increase during the stretching phase ($\Delta T_{heat}$), the temperature reduction during the retraction phase ($\Delta T_{cool}$), the heat extracted from the environment during the retraction phase per unit volume of material ($Q_{ab}$) and the coefficient of performance ($COP_{mat}$) were evaluated. The dependence of these parameters on crosslinking density and impact velocity has been investigated, keeping in mind the relationship between impact velocity and deformation. Figure 4.13(A-D) shows the obtained results.

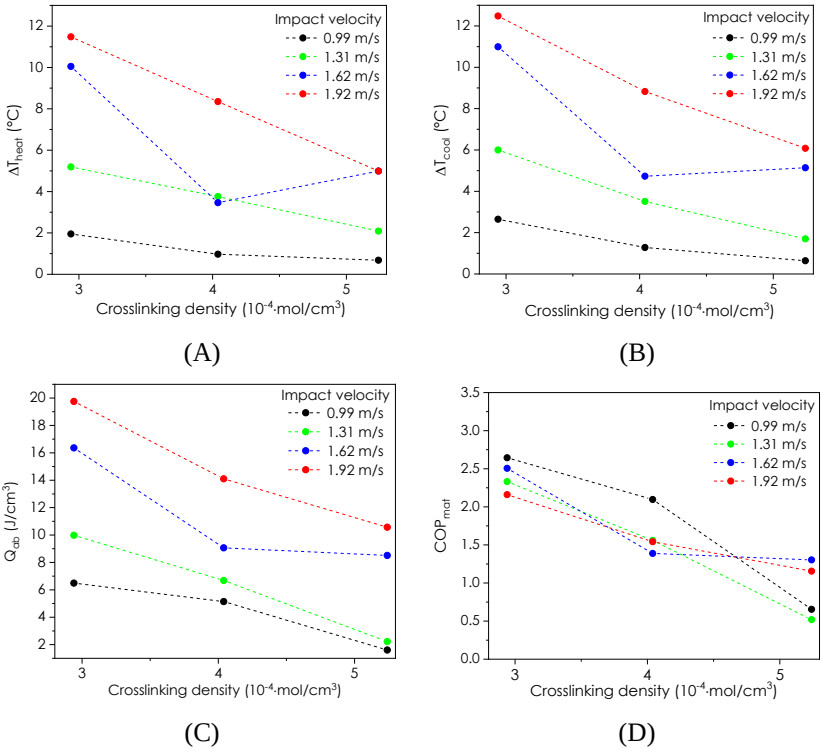


*Figure 4.13. Elastocaloric properties of the NR formulations evaluated using the preliminary set-up. (A) maximum $\Delta T_{heat}$, (B) maximum $\Delta T_{cool}$, (C) $Q_{ab}$ per unit volume of material, (D) $COP_{mat}$.*

For a given impact velocity and crosslinking density, the values of $\Delta T_{heat}$ and $\Delta T_{cool}$ are very similar, indicating that dissipative phenomena, such as internal friction between macromolecules, could be considered negligible. Figure 4.13(A-D) evidences that the crosslinking density could be another parameter influencing the thermal response of natural rubber. Indeed, for any given impact velocity, an almost linear increase in $\Delta T_{heat}$, $\Delta T_{cool}$, $Q_{ab}$ and COP is observed with reducing crosslinking density. Such a linear increase is not clearly visible considering that data obtained for an impact

velocity of 1.62 m/s. Under this testing condition, the parameters measured for NR_2.5 deviate from the general trend, which may be attributed to sample slippage between the grips and the limited reliability of the testing setup.

Among the tested samples, NR_1.5S exhibits the best cooling performance and appears to be the most promising candidate for application in a solid-state cooling device. When tested at an impact velocity of 1.92 m/s, it shows a $\Delta T_{cool}$ of 12.3 °C and a heat absorption capacity of 19.5 J/cm$^3$. By way of comparison, the highest reported $\Delta T_{cool}$ in the literature for NR is approx. 13 °C when deformed by 550% [45]. The most significant cooling capacity in terms of $Q_{ab}$ is achieved at an impact velocity equal to or higher than 1.31 m/s, which corresponds to a deformation greater than 300%. As regards the COP of NR_1.5S, it ranges between 2.2 and 2.6, with the maximum value achieved for an impact velocity of 0.99 m/s.

However, a direct comparison of the elastocaloric performance between the prepared samples should be made with caution, since at the same impact velocity the samples experience different deformation levels. Figure 4.12 shows that, for any given impact velocity, NR_1.5S sample deforms more, followed by NR_2.5 and NR_3.5. For instance, NR_1.5S deforms by 440% at 1.62 m/s, while NR_2.5S and NR_3.5S deforms by 360% and 320%, respectively. This trend is consistent with the results of quasi-static tensile tests. These findings suggest that elastocaloric performance improves as crosslinking density decreases. However, to confirm this trend, the samples should be tested under identical deformation and testing conditions. This would enable an understanding of whether the superior cooling capacity of NR_1.5 is due to its lower crosslinking density or the higher deformation level it achieved.

From these preliminary analyses, since the least crosslinked sample appeared to be the most promising, its elastocaloric performance was also evaluated under cycling conditions. The aim was to assess

whether the elastocaloric properties remained stable when the material was subjected to repeated deformation, as cyclic stability is crucial for long-term service of elastocaloric refrigeration systems [9]. The NR_1.5S sample was therefore tested for up to ten cycles at impact velocities of 1.62 and 1.92 m/s. Only the two highest impact velocities were selected, since if the properties remain stable at these velocities, they can be expected to be stable also at lower ones. Figure 4.14(A,B) shows the temperature variation of the NR_1.5S sample corresponding to the 1st, 5th and 10th cycles.

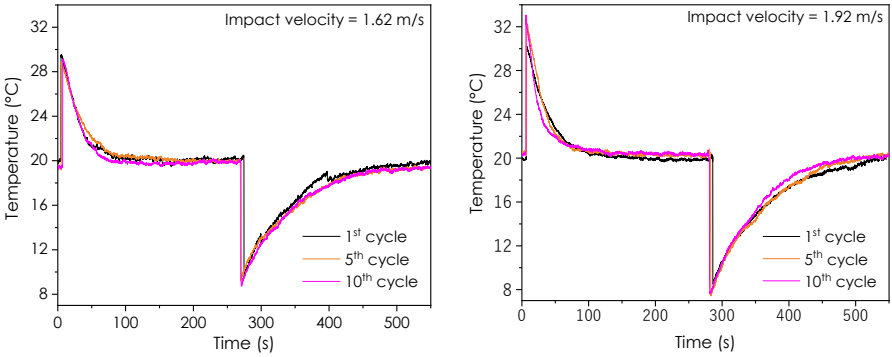


(A) (B)

*Figure 4.14. Temperature variation on the surface of NR_1.5S sample tested under cyclic condition. (A) NR_1.5S tested at 1.62 m/s and (B) NR_1.5S tested at 1.92 m/s. The temperature variations reported refer to the 1st, 5th and 10th cycles.*

The results clearly show that the elastocaloric effect of the least crosslinked sample remains stable up to the 10th cycle. For both impact velocities, the temperature variations overlap, and no significant differences can be observed.

In summary, the preliminary investigation of the elastocaloric response of NR samples has led to the following conclusions:

- The elastocaloric effect is consistently observed in all samples and under all experimental conditions.
- Higher impact velocity results in larger temperature variation and cooling capacity, which can be primarily attributed to the greater deformation achieved.
- Crosslinking density appears to be a parameter affecting the elastocaloric properties: for a given impact velocity, $\Delta T_{heat}$, $\Delta T_{cool}$, $Q_{ab}$, and COP increase with decreasing crosslinking density.
- The least crosslinked sample, NR_1.5S, exhibits the most promising performance, and its elastocaloric response is stable over at least ten consecutive cycles.

Nonetheless, a performance comparison between samples must be interpreted with care, since at the same impact velocity the degree of deformation differs significantly with the crosslinking density.

#### *4.3.11.2 Evaluation of the elastocaloric properties using a high-speed tensile testing machine*

Thanks to the collaboration with Step Lab S.r.l. (Resana, TV, Italy), a company specialized in electrically actuated machines for mechanical testing, it was possible to investigate the elastocaloric properties of the samples using a high-speed tensile testing system. This setup enabled precise comparison of the elastocaloric performance of the samples, as the materials could be deformed at the same strain level and deformation rate, minimizing variables that were uncontrolled in the preliminary setup and that did not allow for an accurate comparison. All tests were conducted on-site at their facilities.

To select the testing speed that ensured adiabatic conditions, some preliminary elastocaloric tests were conducted, following the procedure described in Section 4.3.11. The NR_1.5S sample, chosen for this evaluation, was stretched at 400 % and unloaded at different testing speeds, ranging between 0.025 m/s (strain rate of 1 $s^{-1}$) and 1

m/s (strain rate of 40 $s^{-1}$). The $\Delta T_{cool}$ measured in the unloading is reported as a function of testing speed in Figure 4.15.

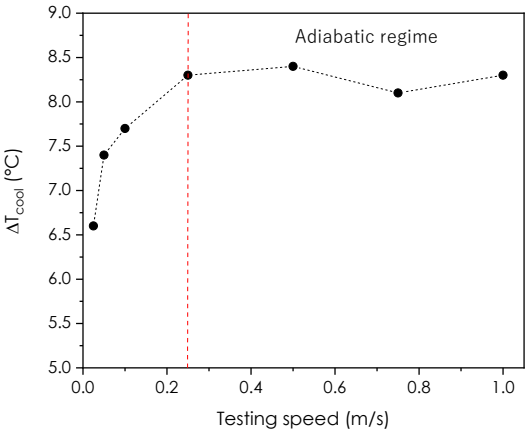


*Figure 4.15. $\Delta T_{cool}$ at different testing speeds for NR_1.5S deformed at 400%.*

The results show that for testing speeds above 0.25 m/s, $\Delta T_{cool}$ remains almost constant at approx. 8.3 °C, indicating that unloading occurs under adiabatic conditions. Once the testing speed is lowered, the material exchanges heat with the environment, causing $\Delta T_{cool}$ to gradually decrease until reaching 6.6 °C at a testing speed of 0.025 m/s. Based on these results, a testing speed of 0.5 m/s (strain rate of 20 $s^{-1}$) was selected for conducting the elastocaloric tests. It should be noted that this testing speed is lower than the impact velocities used in the preliminary setup. In the elastocaloric tests performed with the pendulum testing machine, however, the testing speed was not constant and decreased until reaching 0 m/s. In contrast, in the tests performed with the high-speed tensile testing machine, the testing speed remained constant throughout the stretching and retraction stages.

In the preliminary investigation conducted using the pendulum testing machine, the most significant cooling capacities were observed when the samples reached deformations of more than 250%. Therefore, for the evaluation and comparison of the elastocaloric properties using the high-speed tensile testing machine, the selected strain levels were 300%, 400%, and 500%. Before testing, the samples were cyclically deformed twice to mitigate the impact of the Mullins effect. The parameters that were determined in the tests are $\Delta T_{heat}$, $\Delta T_{cool}$, $Q_{ab}$, $Q_{re}$, $W_s$ and $W_r$ per unit volume of material and the $COP_{mat.}$ The procedure used to calculate these parameters is described in Section 4.3.11.

Figure 4.16A, 4.16C, and 4.16E show the temperature variation of the surface of the NR samples during the stretching and retraction phases as a function of time and deformation, while Figure 4.16B, 4.16D and 4.16F report the stress sustained by the samples as a function of time in the stretching and subsequent holding phase. The calculated parameters are reported in Figure 4.17(A-G).

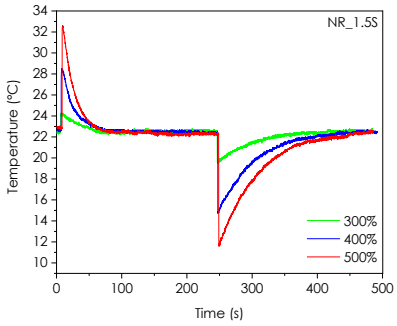


(A)

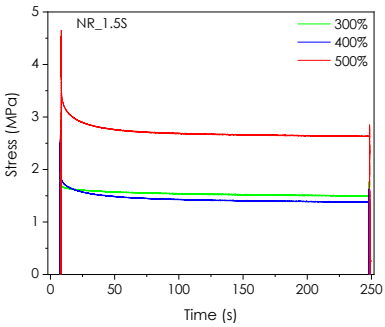


(B)

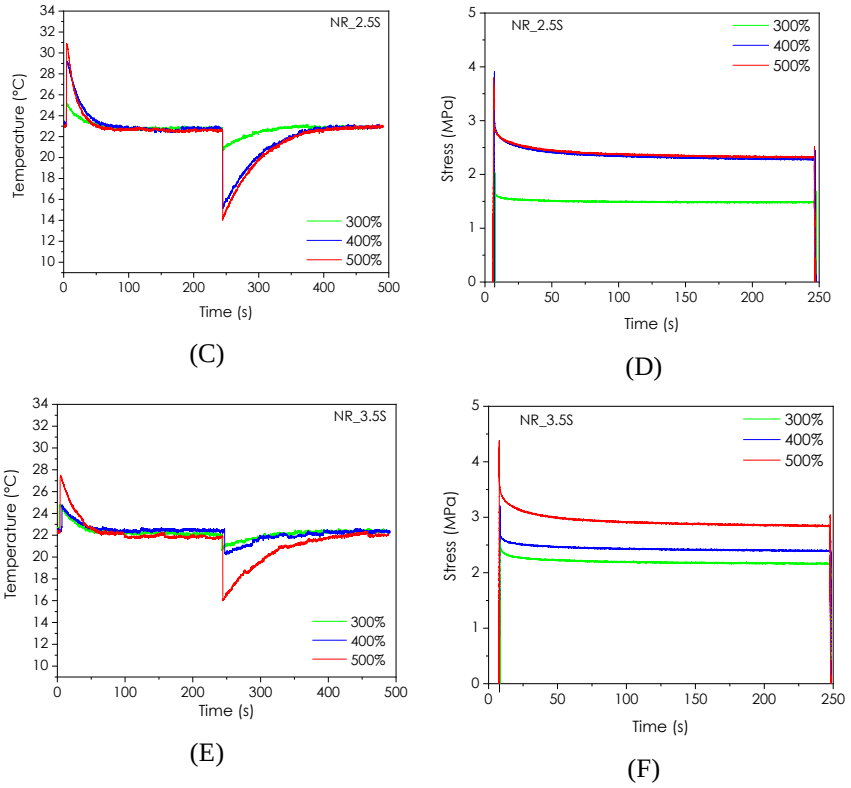


*Figure 4.16. (A, C, E) Temperature variation of the surface of the NR samples as a function of time and maximum deformation applied; (B, D, F) Stress in the stretching and subsequent holding step as a function of time and maximum deformation. (A, B) NR_1.5S; (C, D) NR_2.5S and (E, F) NR_3.5S.*

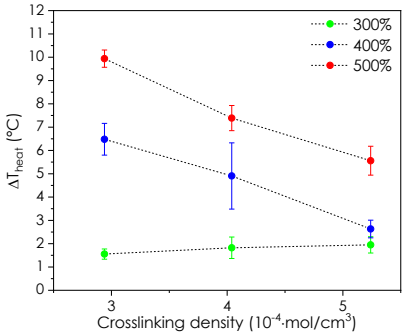
300%
400%
500%
ΔT_heat (°C)
Crosslinking density (10⁻⁴·mol/cm³)

(A)

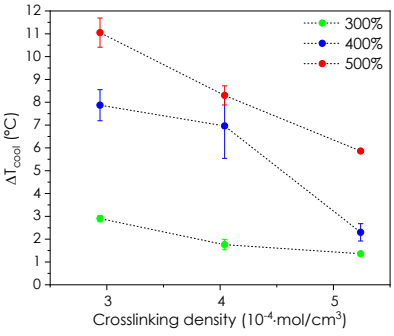
300%
400%
500%
ΔT_cool (°C)
Crosslinking density (10⁻⁴·mol/cm³)

(B)

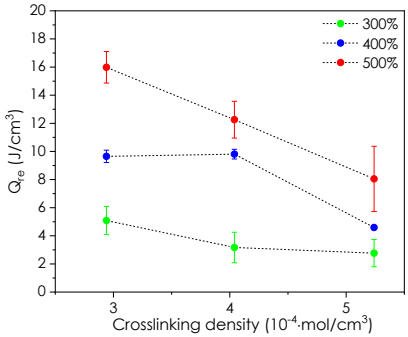
300%
400%
500%
Q_re (J/cm³)
Crosslinking density (10⁻⁴·mol/cm³)

(C)

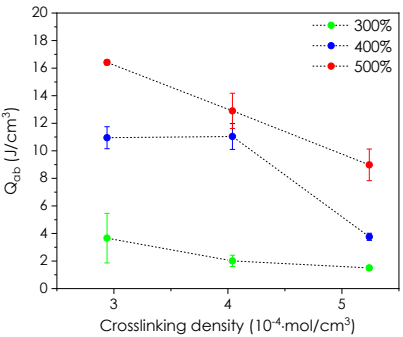
300%
400%
500%
Q_ab (J/cm³)
Crosslinking density (10⁻⁴·mol/cm³)

(D)

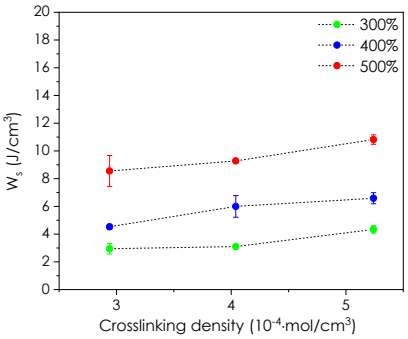
300%
400%
500%
W_s (J/cm³)
Crosslinking density (10⁻⁴·mol/cm³)

(E)

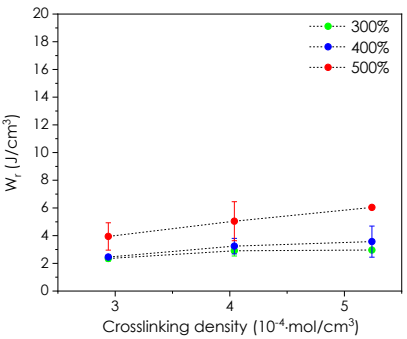
300%
400%
500%
W_r (J/cm³)
Crosslinking density (10⁻⁴·mol/cm³)

(F)

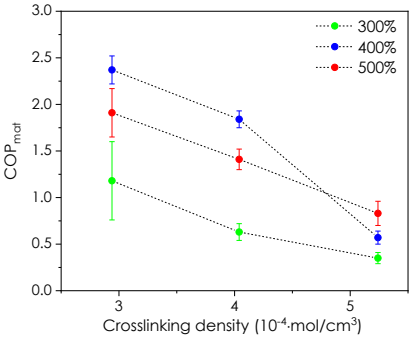


(G)

*Figure 4.17. Elastocaloric properties of the produced NR samples as a function of the maximum deformation applied and the crosslinking density. (A) Maximum $\Delta T_{heat}$, (B) maximum $\Delta T_{cool}$ (C) $Q_{re}$, (D) $Q_{ab}$, (E) mechanical energy at stretching per unit volume of material $W_s$, (F) mechanical energy at retraction per unit volume of material $W_r$, (G) $COP_{mat}$.*

Many of the observations made in the preliminary investigation with the pendulum testing machine are confirmed by the results obtained using the high-speed tensile testing setup. In line with the previous discussion, the deformation strongly affects the surface temperature evolution of the samples, as in all cases the increase in maximum strain results in a more significant temperature variation during both the stretching and retraction phases.

An additional aspect, not emerged with the preliminary setup, is the stress relaxation of the samples during the stretching phase. Stress relaxation in natural rubber is a multifactorial process where strain induced crystallization competes with viscoelastic phenomena, such as the reformation of entanglements and the breakage of physical bonds. SIC acts as a primary relaxation mechanism [140]. The phase transition from an amorphous to a crystalline state reduces the entropic tension within the network, leading to a significant decrease in stress while increasing the crystalline volume fraction. The energy associated with this stress drop is stored as latent heat, which is partly

recovered as cooling capacity during the retraction phase. On the contrary, the viscoelastic relaxation mechanisms promote an entropy increase through dissipative internal friction between macromolecules, which acts against the elastocaloric effect. Therefore, the higher is the contribution of SIC to stress relaxation, the higher would be the efficiency of the process. As shown in Figure 4.16B, 4.16D, and 4.16F, over a time scale of 250 s, the stress stabilizes for all samples and deformation levels. The maximum stress values ($\sigma_0$) and the percentages of stress relaxation (SR), calculated according to Equation (3.7), are reported in Table 4.15.

*Table 4.15. Maximum stress values ($\sigma_0$) and percentage of stress relaxation (SR) evaluated in a timescale of 250 s of the stretching phase.*

| | | Deformation level (%) | | |
|---|---|---|---|---|
| | **Sample** | **300%** | **400%** | **500%** |
| **$\sigma_0$ (MPa)** | NR_1.5S | 2.1 ± 0.1 | 2.8 ± 0.1 | 4.5 ± 0.2 |
| | NR_2.5S | 2.2 ± 0.2 | 3.7 ± 0.4 | 3.9 ± 0.1 |
| | NR_3.5S | 3.0 ± 0.1 | 3.6 ± 0.5 | 4.7 ± 0.4 |
| **SR (%)** | NR_1.5S | 15.3 ± 0.1 | 30.6 ± 2.0 | 28.1 ± 1.9 |
| | NR_2.5S | 10.7 ± 0.2 | 26.2 ± 0.5 | 26.7 ± 3.3 |
| | NR_3.5S | 18.6 ± 5.1 | 19.7 ± 7.1 | 29.8 ± 9.5 |

In agreement with the literature [141], stress relaxation increases with strain for all samples. This phenomenon is probably driven by the synergistic effect of adiabatic temperature increases, which accelerate viscoelastic phenomena, and the progressive evolution of crystallinity, as shown by XRD analysis. Among the samples, the results show that the least crosslinked one exhibits the highest SR values at 300% and 400%, whereas at 500% strain SR values are similar to those of NR_3.5. However, the dominance of one

mechanism over the others is difficult to understand from macroscopic data alone.

By comparing the temperature response of the samples in Figure 4.16A, 4.16C and 4.16E and Figure 4.17A and 4.17B, the crosslinking density is confirmed to influence the thermal response of NR. Moving from Figure 4.16A to Figure 4.16E, a decreasing trend in the temperature variation of the samples can be observed. This experimental observation could probably be the result of two contributions: the limit of chain extensibility and strain induced crystallization. As discussed in Sections 4.3.8 and Section 4.3.9, the samples exhibit different mechanical responses depending on the crosslinking density. With increasing degree of crosslinking, the chain length between crosslinks decreases, and the finite extensibility of the polymer chains is reached at lower deformation, resulting in an earlier onset of the strain-stiffening regime. During deformation, the reduction in configurational entropy, which governs the thermoelastic contribution to the temperature variation, is most significant during the initial orientation and approaches a plateau as the chains reach their stretching limit.

At 300% strain, all samples are still deforming within the plateau region. However, at 400% and 500%, strain, NR_3.5S, followed by NR_2.5S, enters the strain-stiffening regime meaning its polymer chains have largely exhausted their capacity for further orientation. In contrast, NR_1.5S continues to deform predominantly within the plateau region, where the polymeric chains retain a larger number of accessible conformations and continue to orient. Consequently, for these higher deformations, NR_1.5S is expected to experience the largest reversible entropy variation, followed by NR_2.5S and NR_3.5S. Therefore, the contribution of the thermoelastic effect to the temperature variation increases with decreasing crosslinking density. The second contribution concerns strain-induced crystallization. As reported in Section 4.3.9, by reducing crosslinking

density, the capability of the samples to crystallize under strain improves.

Thus, at a given deformation, the higher strain-induced crystallization phenomena and thermoelastic contribution make NR_1.5S the sample with the highest ΔT, during both the stretching and retraction phases. If the elastocaloric properties were compared under the same deformation mechanism, specifically with all samples deformed in the strain-stiffening regime, the properties of NR_1.5S would probably stand out even more. From Figure 4.17B, it is possible to notice that NR_1.5S shows a $\Delta T_{cool}$ of 2.9 °C at 300% and 11.0 °C at 500%. As it was observed also in the preliminary analysis, for a given deformation and crosslinking degree, $\Delta T_{cool}$ is similar to or even larger than $\Delta T_{heat}$ (Figure 4.17A and 4.17B) in almost all cases. The only exceptions are NR_2.5S deformed at 300% and NR_3.5S deformed at 300% and 500%, for which the temperature increase during stretching is larger than the temperature reduction during unloading. This is an interesting result since in studies reported in the literature that employ analogous tensile testing machines, $\Delta T_{heat}$ is very often larger than $\Delta T_{cool}$ [41], suggesting non-negligible dissipative phenomena such as macromolecular friction. Here, it is plausible that during the maintenance of the samples in traction, crystalline domains progressively develop. As the crystallization of these domains is not instantaneous, the heat generated during their formation may not have been considered in $\Delta T_{heat}$. Conversely, during unloading, if all crystalline domains, regardless of their formation time, melt, they could contribute to $\Delta T_{cool}$, potentially resulting in $\Delta T_{cool}$ values greater than $\Delta T_{heat}$. However, it is crucial to emphasize that this is a hypothesis and demands further experimental investigation.

Assuming that the percentage of crystallinity (χ) of the samples in the stretched state corresponds to that determined by XRD analysis (Table 4.12), the temperature decrease due to the melting of the crystalline domains ($\Delta T_{cool,SIC}$) was estimated. Specifically, given the

density and the $c_p$ of the samples, the temperature decrease was evaluated by using Equation (2.22). The specific melting enthalpy of NR was taken as 59.9 J/cm$^3$ [142]. The calculated $\Delta T_{cool,SIC}$ are reported in Table 4.16.

*Table 4.16. Temperature decrease assuming that the percentage of crystallinity of the stretched samples is that determined from the XRD analyses (see Table 4.12).*

| Sample | Deformation (%) | $\Delta T_{cool,SIC}$ (°C) |
|---|---|---|
| NR_1.5S | 300 | 3.9 |
| | 400 | 4.3 |
| | 500 | 4.6 |
| NR_2.5S | 300 | 3.0 |
| | 400 | 3.6 |
| | 500 | 4.3 |
| NR_3.5S | 300 | 2.9 |
| | 400 | 3.5 |
| | 500 | 3.7 |

As can be seen, the values obtained for NR_2.5S at 300% strain and NR_3.5S at 300% and 400% strain exceeds the $\Delta T_{cool}$ reported in Figure 4.17B. This divergence may be attributed to several factors. First, the degree of crystallinity derived from XRD analysis may be overestimated. Second, the sample may crystallize to a lesser extent under the testing conditions used for evaluating the elastocaloric effect. Finally, the presence of structural defects within the crystalline domains could lower the total heat absorbed during the phase transition. In contrast, in the other cases, the calculated $\Delta T_{cool,SIC}$ values are approximately half of the $\Delta T_{cool}$ values reported in Figure 4.17B. This suggests that SIC and the thermoelastic effect contribute

nearly equally to the overall elastocaloric response. Studies reported in the literature found that SIC is the primary contributor to the elastocaloric effect [43,45]. However, it should be noted that the crystallinity content was evaluated in a semi-quantitative manner, and therefore the values obtained may be subject to a certain degree of error.

Further analysis of Figure 4.16A, 4.16C and 4.16E shows that, also in this case, the thinning of the samples and the increase in the area of heat exchange during the stretching phase favours a more rapid heat transfer compared to the retraction phase. This is confirmed by the characteristic time of temperature dampening, determined both during heating (stretching phase) and cooling (retraction phase), reported in Table 4.17.

*Table 4.17. Characteristics time of temperature dampening ($\tau_c$) and heat transfer coefficient (h) calculated in the stretching and retraction phase of the NR samples.*

| | **Sample** | **Deformation level** | | |
|---|---|---|---|---|
| | | **300%** | **400%** | **500%** |
| $\tau_{c,s}$ (s) | NR_1.5S | 22.5 ± 0.5 | 22.3 ± 4.6 | 16.0 ± 2.9. |
| | NR_2.5S | 22.6 ± 2.2 | 21.0 ± 0.2 | 15.9 ± 1.7 |
| | NR_3.5S | 21.5 ± 1.1 | 20.3 ± 0.6 | 19.9 ± 5.7 |
| $\tau_{c,r}$ (s) | NR_1.5S | 60.6 ± 4.8 | 51.9 ± 5.5 | 55.7 ± 10.3 |
| | NR_2.5S | 44.1 ± 9.9 | 51.0 ± 6.6 | 58.5 ± 5.4 |
| | NR_3.5S | 52.5 ± 9.1 | 50.9 ± 4.3 | 56.6 ± 7.8 |
| $h_s$ (W/(m$^2$K)) | NR_1.5S | 29.5 ± 2.8 | 24.0 ± 4.2 | 29.5 ± 5.1 |
| | NR_2.5S | 30.3 ± 2.5 | 26.4 ± 1.5 | 30.0 ± 2.0 |
| | NR_3.5S | 31.3 ± 1.6 | 27.4 ± 1.1 | 23.4 ± 3.3 |
| $h_r$ (W/(m$^2$K)) | NR_1.5S | 16.0 ± 0.5 | 18.7 ± 3.1 | 18.2 ± 3.6 |
| | NR_2.5S | 22.6 ± 4.5 | 19.6 ± 2.5 | 16.6 ± 1.0 |
| | NR_3.5S | 19.8 ± 3.7 | 20.0 ± 2.1 | 17.6 ± 2.8 |

For a given degree of crosslinking, the $\tau_{c,s}$ tends to decrease with increasing deformation. This trend is expected as the thickness of the sample reduces and the area of heat exchange increases with increasing strain. Conversely, $\tau_{c,r}$ does not exhibit a clear correlation with deformation, yielding pretty similar values across the samples. Also this behavior is expected since, in the undeformed state, the sample present the same area of heat exchange and the $\tau_{c,r}$ should be the same. The minor discrepancies observed in $\tau_{c,r}$ may be attributed to fluctuations in environmental variables, such as ambient humidity or local air convection. The differences in $\tau_{c,s}$ and $\tau_{c,r}$ among the samples are probably due to variations in heat capacitance as well as, even in this case, fluctuations in environmental variables. Regarding the heat transfer coefficient, the values calculated in the stretching and retraction phases are quite similar across the different crosslinked samples for a given strain level and geometry. The minimal variations recorded are likely attributable to variations in the thermophysical properties of the surrounding air, as the experiments were conducted in a non-controlled environment. The values of heat transfer coefficient evaluated in the stretching phase range from 23.4 to 31.1 $W/(m^2 \cdot K)$, while those calculated in the retraction phase range from 16 to 22.6 $W/(m^2K)$. According to the literature, typical ranges of h are 3-20 $W/(m^2K)$ in conditions of natural convection, and 20-100 $W/(m^2K)$ in forced convection [139]. The rapid stretching of the samples might have triggered air movements, inducing a slight forced convection. Thus, it can be stated that the values obtained are in line with literature data. The heat transfer coefficient values are higher than those observed in the preliminary analysis. This difference may be attributed to the specimen's orientation during testing. A thin-sheet body experiences different convection regimes depending on whether it is positioned parallel or perpendicular to the ground. The vertical orientation promotes convective motion, resulting in higher heat transfer coefficients [143]. Using the pendulum testing machine, the sample was placed parallel to the floor, whereas in the tensile test, it

was positioned vertically, likely leading to the higher h values observed.

Going into details of the elastocaloric effect, Figure 4.17C and Figure 4.17D shows $Q_{re}$ and $Q_{ab}$ values of the samples as a function of deformation and degree of crosslinking. Both $Q_{re}$ and $Q_{ab}$ present the same trend: for a given crosslinking density, they increase with increasing deformation, whereas, if the deformation is fixed, they decrease with the degree of crosslinking. The least crosslinked sample releases and extracts the highest amount of thermal energy during the loading and unloading phase, respectively. In an ideal elastocaloric cycle, the heat released during the stretching phase should be approximately the same as the heat absorbed during the retraction phase, unless there are irreversible dissipative phenomena. The calculated $Q_{re}$ and $Q_{ab}$ are generally similar, with a few exceptions that can be ascribed either to irreversible losses or to approximations made in the computations. For instance, properties used as constants in the calculations (e.g., $c_p$, material density, volume, etc.) may actually vary with temperature and degree of deformation. Each assumption thus contributes to the final uncertainty, which propagates into the computed heat values. In addition, as the values are reported normalized by the volume of the sample, the difference between $Q_{re}$ and $Q_{ab}$ appears to be greater. The maximum difference registered between $Q_{re}$ and $Q_{ab}$ is lower than 1.5 J.

The elastocaloric effect of NR is studied in view of solid-state cooling applications. Therefore, the attention should be focused on the cooling capability of the materials. The most promising sample, i.e., NR_1.5S, absorbs approx. 16.4 J/cm$^3$ at a deformation of 500%. Studies in the literature that employ analogous tensile testing machines report values of heat extracted per refrigeration cycle of NR-based systems in the range 5–12 J/cm$^3$ [41,43], thus lower than the values obtained in this work. In the preliminary analysis, NR_1.5S was found to extract 19-20 J/cm$^3$ of thermal energy when tested at an impact velocity of 1.92 m/s. However, the deformation achieved in

such testing conditions was above 500%, a factor that could explain the higher $Q_{ab}$ registered.

The Coefficient of Performance (Figure 4.17F), evaluated by the ratio between the extracted thermal energy and the mechanical energy at stretching ($W_s$, Figure 4.17E), shows, once again, that NR_1.5S is the best formulation among the ones prepared, exhibiting a $COP_{mat}$ ranging from 1.8 to 2.4. The optimal compromise appears to be reached by deforming NR_1.5S at 400%. This not only allows for the highest $COP_{mat}$ value, but also ensures a safer operational condition, as it is farther from the strain at break values for this composition.

At this point in the discussion of the results, it was found interesting to calculate the conversion efficiencies from mechanical energy to heat energy following the approach of Yukiro et al. [22]. Specifically, the conversion efficiencies were calculated for the stretching phase ($\eta_s$) according to Equation (4.1):

$$\eta_s = \frac{Q_{re}}{W_s} \cdot 100 \qquad (4.1)$$

And for the retraction phase ($\eta_r$) according to Equation (4.2):

$$\eta_r = \frac{Q_{ab}}{W_r} \cdot 100 \qquad (4.2)$$

In Figure 4.18 the calculated conversion efficiencies are plotted as a function of maximum deformation and degree of crosslinking.

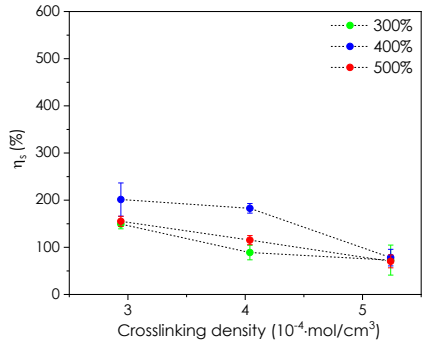


(A)

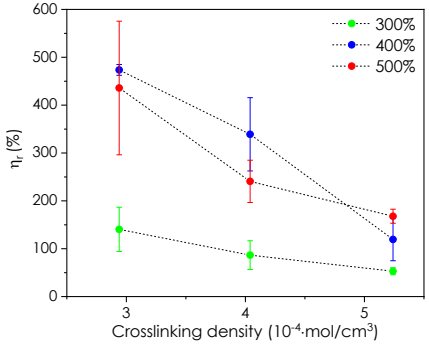


(B)

*Figure 4.18. Conversion efficiency at (A) stretching and (B) retraction phases of the prepared NR samples.*

The conversion efficiencies of the samples are, in almost all cases, greater than 100%, both in the stretching and retraction phases. Having η greater than 100 % in the stretching phase confirms that SIC occurred. Indeed, if the samples did not crystallize, the conversion efficiencies would be equal to a maximum of 100%. Values below 100%, specifically between 50 and 100%, have been obtained for NR_2.5S and NR_3.5S samples. The conversion efficiencies

determined in the retraction phase are generally greater than those determined in the stretching phase, as $W_r$ is lower than $W_s$. As for the $COP_{mat}$ values, NR_1.5S presents the highest $\eta_s$ and $\eta_r$ values and the deformation level of 400% is confirmed to promote the best conversion efficiencies.

In conclusion, it is worth highlighting that, from a practical perspective, the time required by the sample to return to room temperature, both during the stretching and retraction phases, proves to be rather long. The time of the entire elastocaloric cycle was set at 480 s to ensure the return of the materials to room temperature in each step and to wait the same time interval in the two phases. For the development of a solid-state cooling device, however, reducing the heat exchange time and increasing the cooling power are essential.

Starting from these considerations, the elastocaloric performance of NR under forced convection conditions was investigated by introducing a fan, having a power 2.5 W and positioned 50 cm from the specimens, capable of providing a heat transfer coefficient of approx. 45 $W/m^2K$ (value calculated according to the procedure described in Paragraph 3.2.12.2). The elastocaloric properties of the most promising NR formulation, NR_1.5S, were evaluated under these new conditions while keeping the cycle duration fixed at 480 s. Figure 4.19 shows the temperature variations of NR_1.5S deformed at 400% under natural and forced convection conditions, while Table 4.18 reports the $\tau_{c,s}$, $\tau_{c,r}$, $Q_{re}$ and $Q_{ab}$ of the sample under forced convection conditions.

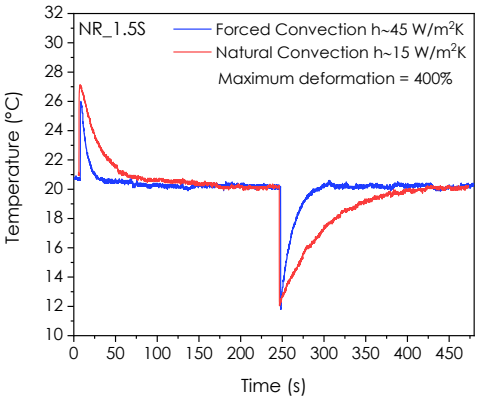


*Figure 4.19. Temperature variations of the surface of NR_1.5S deformed at 400% in conditions of natural convection (red curve) and forced convection (blue curve).*

*Table 4.18.Elastocaloric properties of NR_1.5S deformed at 400% strain in forced convection, for an elastocaloric cycle duration of 480 s.*

| **Sample** | **Elastocaloric cycle duration (s)** | **$\tau_{c,s}$ (s)** | **$\tau_{c,r}$ (s)** | **$\Delta T_{heat}$ (°C)** | **$\Delta T_{cool}$ (°C)** | **$Q_{re}$ (J/cm$^3$)** | **$Q_{ab}$ (J/cm$^3$)** |
|---|---|---|---|---|---|---|---|
| NR_1.5S | 480 | 8.1 | 13.6 | 5.3 | 8.3 | 8.4 | 12.5 |

As expected, operating under forced convection significantly reduces the time required for heat exchange with the surrounding environment. Compared to natural convection (Table 4.17), $\tau_{c,s}$ is reduced by more than half, while $\tau_{c,r}$ is reduced by more than one quarter. Regarding the elastocaloric properties, $\Delta T_{cool}$ and $Q_{ab}$ are comparable or even slightly higher than the corresponding values in natural convection (Figure 4.17B and Figure 4.17D), whereas $\Delta T_{heat}$ and $Q_{re}$ are marginally lower. It is possible that the infrared thermal imaging camera, due to its limited frame rate, fails to capture the maximum temperature increase in the initial stretching phase, leading to an underestimation of these parameters. Overall, no marked

differences were observed, indicating that the elastocaloric effect is not compromised by forced convection.

In light of these results, an elastocaloric cycle of 120 s is largely sufficient to complete heat transfer between the environment and the rubber. As reducing the stretching time might affect the extent of SIC of NR, the same NR_1.5S specimen was tested at 400% strain under forced convection conditions, with both stretching and retraction phases set to 60 s. The main elastocaloric properties were recalculated under these new conditions, and the obtained results are reported in Table 4.19

*Table 4.19. Elastocaloric properties of NR_1.5S deformed at 400% strain in forced convection, for an elastocaloric cycle duration of 120 s.*

| **Sample** | **Elastocaloric cycle duration (s)** | **$\tau_{c,s}$ (s)** | **$\tau_{c,r}$ (s)** | **$\Delta T_{heat}$ (°C)** | **$\Delta T_{cool}$ (°C)** | **$Q_{re}$ (J/cm$^3$)** | **$Q_{ab}$ (J/cm$^3$)** |
|---|---|---|---|---|---|---|---|
| NR_1.5S | 120 | 8.1 | 13.6 | 5.3 | 8.3 | 8.1 | 12.6 |

The values obtained are comparable to those reported in Table 4.18, suggesting that shortening the cycle time does not significantly affect SIC. Compared to the 480 s cycle imposed by natural convection, the adoption of forced convection shortens the cycle to 120 s, bringing the performance of NR a little bit closer to the timescales required for real cooling applications.

The elastocaloric performance of NR_1.5S deformed at 400% strain was then evaluated under forced convection in cyclic conditions. Specifically, the sample was subjected to 40 loading and unloading cycles. The most important elastocaloric properties and the percentage of stress relaxation, evaluated at the 1$^{st}$, 5$^{th}$, 10$^{th}$, 20$^{th}$, 30$^{th}$ and 40$^{th}$ cycles are shown in Figure 4.20. As the interest is focus on the cooling performance, $Q_{re}$ is not reported. A summary of the definitions of the elastocaloric parameters is provided in Table 4.20.

*Table 4.20. Summary of the definitions of the parameters determined in the elastocaloric tests.*

| Parameter | Meaning |
|---|---|
| $\Delta T_{heat}$ | Maximum temperature increase during the stretching phase |
| $\Delta T_{cool}$ | Maximum temperature reduction during the retraction phase |
| $Q_{ab}$ | Heat absorbed from the environment per unit volume of material during the stretching phase |
| $W_s$ | Mechanical energy at stretching |
| COP | Coefficient of performance, calculated as the ratio between $Q_{ab}$ and $W_s$ |

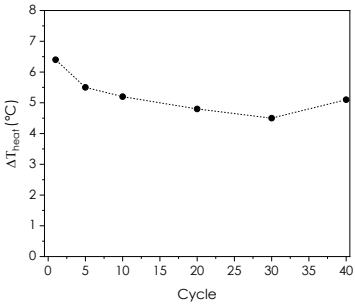


(A)

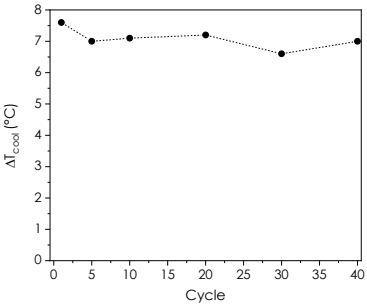


(B)

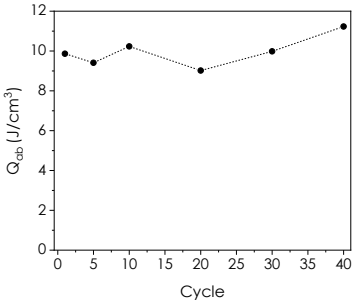


(C)

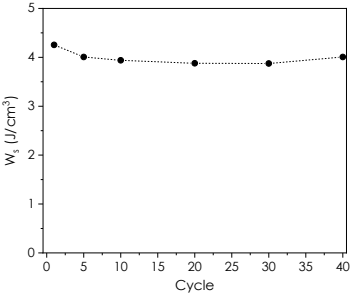


(D)

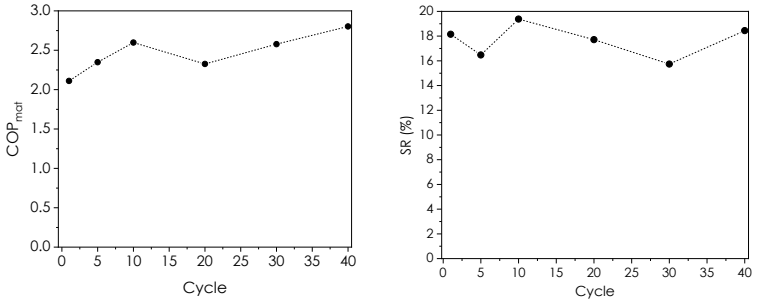


(E) (F)

*Figure 4.20. Elastocaloric properties of NR_1.5S deformed at 400% strain under forced convection and in cyclic conditions. (A) maximum $\Delta T_{heat}$, (B) maximum $\Delta T_{cool}$, (C) $Q_{ab}$, (D) $W_s$, (E) $COP_{mat}$ and (F) SR.*

The results evidence that the elastocaloric properties remain relatively stable up to 40 loading-unloading cycles. Compared to $\Delta T_{cool}$, $\Delta T_{heat}$ shows a more marked decreasing trend, starting from a value of 6.5 °C and stabilizing after the 5$^{th}$ cycle at values close to 5 °C. This phenomenon could be attributable to the Mullins effect, as $W_s$ is slightly reduced moving from the 1$^{st}$ to the 5$^{th}$ cycle. Although the sample was pre-stretched twice before testing, the Mullins effect likely still exerts a limited influence. This observation suggests that a higher number of pre-stretching cycles may be required prior to application to further mitigate the Mullins effect. Regarding the cooling capacity, $Q_{ab}$ remains almost stable within the range 9-11 J/cm$^3$, showing a slight increase from the first to the 40$^{th}$ cycle. The same can be observed for the $COP_{mat}$, which ranges between 2 and 3, and for SR values, which present values between 18% and 16%. The obtained values are comparable to the those obtained from a loading-unloading cycle. Overall, the results confirm that NR_1.5S maintains the cooling capacity under cyclic loading, highlighting once more its potential for elastocaloric applications.

In summary, the evaluation of the elastocaloric response of the NR samples by using the high-speed tensile testing system has led to the following conclusions:

- The crosslinking density is a key parameter affecting the elastocaloric effect: for a given deformation, $\Delta T_{heat}$, $\Delta T_{cool}$, $Q_{ab}$, $Q_{re}$ and COP increase with decreasing crosslinking density.
- The least crosslinked sample, NR_1.5S, demonstrates the most promising cooling performance, showing a heat extraction capacity of 16.4 J/cm$^3$ when deformed at 500% strain.
- The highest conversion efficiency between mechanical and thermal energy, as well as the highest $COP_{mat}$ values, are achieved at a deformation level of 400%.
- Working under forced convection conditions (h ~ 45 W/m$^2$K) does not compromise the elastocaloric performance. It shortens the time of the elastocaloric cycle, increasing the cooling power.
- The elastocaloric properties of NR_1.5S deformed at 400% strain under forced convection conditions remain relatively stable up to 40 loading-unloading cycles, with no reduction in the cooling capacity of the material as the number of cycles increases.

## *4.4 Conclusions*

In Chapter 4, the influence of the crosslinking density on the elastocaloric properties of NR has been investigated. Samples with varying degrees of crosslinking, 2.9, 4.0 and 5.2 $10^{-4}$·mol/cm$^3$, were produced by melt compounding and hot pressing and thermo-mechanically characterized. The assessment of the elastocaloric effect revealed that both the imposed deformation and the crosslinking density played a crucial role in the elastocaloric properties of NR. In particular, reducing the crosslinking degree and

increasing the deformation led to enhancing the capability of the material to extract thermal energy from the environment, primarily due to stronger contributions from strain-induced crystallization and thermoelasticity. The NR sample characterized by a crosslinking density of 2.9 $10^{-4}$·mol/$cm^3$ (the least crosslinked sample) was found capable of extracting 16.4 J/$cm^3$ of thermal energy in one single refrigeration cycle when stretched at 500%, exceeding values reported in comparable studies. The evaluation of the conversion efficiency parameters and the Coefficient of Performance of the materials ($COP_{mat}$) confirmed that the least crosslinked sample was the best performing formulation among the ones prepared, and evidenced that the highest conversion efficiency of mechanical to thermal energy was achieved at a deformation level of 400%. The $COP_{mat}$ determined for the best formulation ranged from 1.2 to 2.4. Furthermore, the elastocaloric properties of the most promising sample were also studied under cyclic conditions and proved stable up to 40 loading-unloading cycles.

The investigation of the Mullins effect of the prepared samples highlighted the need to pre-stretch the rubber (at least two times) before its applications, to ensure more reliable and consistent results, particularly in scenarios requiring significant deformations.

In conclusion, the results underscored the significance of rubber network structure, and in particular the crosslinking density, as one of the primary factors to be considered in enhancing the refrigeration potential of NR.

# 5 Effect of nanoclay addition on the elastocaloric properties of Natural Rubber

***Part of this chapter has been published in:***

M. Bianchi, L. Fambri, M. Bortolotti, A. Pegoretti and A. Dorigato

**"Elastocaloric performance of Natural Rubber: The role of nanoclay addition"**

*Macromolecules 2025, 30(14), 3035*
*https://doi.org/10.3390/molecules30143035*

## *5.1 Introduction*

NR has emerged as a promising elastocaloric material for solid-state cooling applications. However, its cooling efficiency remains lower than that of conventional vapour-compression systems. Improving the elastocaloric performance of NR is thus essential for developing solid-state cooling technologies that can compete with existing solutions.

In Chapter 4, it was demonstrated that reducing the crosslinking density significantly enhances the cooling capacity of NR. However, this improvement alone only partially brings the cooling performance of NR closer to that of current air conditioning systems. Therefore, it is important to identify other factors that could further enhance its cooling capacity. Several studies have brought to light that SIC is the major contributor to the elastocaloric effect of NR [41,45,144,145]. This means that the key to enhance its elastocaloric performance may be to increase the capability of rubber to crystallize under strain as much as possible. The role of layered silicates, specifically montmorillonite (MMT), in promoting and increasing the SIC of NR has been reported in the literature [80-82,146]. Carretero-Gonzales et al. found that the addition of 15 phr of nanoclays (both natural sodium

MMT and organically modified MMT) in crosslinked NR provided a more homogeneous distributed rubber network structure and induced an early onset as well as enhancement of crystallization under uniaxial deformation. The onset of SIC moved from 300% strain in the unfilled rubber to 120-140% strain in the filled NR [80,81]. In addition, they found that the strong orientation of the nanoclays along the stretching direction favoured a further orientation of the macromolecules, promoting the nucleation of crystalline domains under stretching. Nie et al. also observed that nanoclays (0.5 phr in the rubber formulation) changed the SIC behaviour of NR, as the crystallinity of the nanoclay-filled samples was higher than that of the unfilled rubber at the same strain level. This highlighted that the addition of nanoclays accelerated the strain-induced crystallization rate [146]. The research of Qu et al. revealed that the maximum degree of SIC of organo-modified MMT-filled NR was achieved for a nanoclay content equal to 5 wt%. At higher filler contents, the crystallinity under strain was reduced, probably due to a lower dispersion and exfoliation of organoclays in the rubber [82].

Although the incorporation of nanoclays has been found to significantly improve the SIC of NR, the effect of nanoclay addition on the elastocaloric performance of NR has never been investigated. Therefore, the focus of Chapter 5 is to explore whether the increased SIC promoted by nanoclays in NR could have a positive impact on its elastocaloric properties. Both natural and organo-modified MMT were thus melt-compounded at different concentrations (from 1 to 5 phr) in the optimized NR formulation identified in Chapter 4. The elastocaloric properties of the resulting nanocomposites were assessed and correlated to their morphological and thermo-mechanical behaviour.

## *5.2 Materials and Methods*

### 5.2.1 Materials

The materials used in this Section are listed in Table 5.1, along with the reference Section that provides the detailed description.

*Table 5.1 List of the materials used in this section of the PhD thesis.*

| Material | Section |
|---|---|
| Natural Rubber | 3.1.1 |
| Zinc Oxide | 3.1.2 |
| Sulphur | 3.1.2 |
| ZDBC | 3.1.2 |
| Stearic Acid | 3.1.2 |
| Toluene | 3.1.3 |
| Methanol | 3.1.3 |
| Acetone | 3.1.3 |
| Natural montmorillonite | 3.1.4 |
| Organomodified montmorillonite | 3.1.4 |

### 5.2.2 Sample preparation

As the incorporation of nanoclays has been shown to play a significant role in enhancing SIC of NR, the effect of nanoclay addition on the elastocaloric performance of NR was investigated. Both natural and organomodified MMT were melt-compounded at different concentrations into the NR formulation identified as optimal in Chapter 4. Nanoclay contents of 1, 3, and 5 phr were selected in order to promote SIC while minimizing excessive stiffening.

The formulation of the NR nanocomposites in parts per hundred rubber (phr) is reported in Table 5.2. The chosen nomenclature for the NR nanocomposites consists of the term NR followed by a number

indicating the nanoclay content in phr, and either the term MMT or O-MMT, which indicates the type of nanoclay. MMT refers to the natural montmorillonite, while O-MMT refers to the organomodified montmorillonite.

*Table 5.2. Composition in phr and nomenclature of the produced NR compounds (phr= parts per hundred rubber).*

| Sample | SMR 10 (phr) | Sulphur (phr) | ZnO (phr) | Stearic acid (phr) | ZDBC (phr) | MMT (phr) | O-MMT (phr) |
|---|---|---|---|---|---|---|---|
| NR | 100.0 | 1.5 | 5.0 | 2.0 | 0.7 | - | - |
| NR_1MMT | 100.0 | 1.5 | 5.0 | 2.0 | 0.7 | 1.0 | - |
| NR_3MMT | 100.0 | 1.5 | 5.0 | 2.0 | 0.7 | 3.0 | - |
| NR_5MMT | 100.0 | 1.5 | 5.0 | 2.0 | 0.7 | 5.0 | - |
| NR_1O-MMT | 100.0 | 1.5 | 5.0 | 2.0 | 0.7 | - | 1.0 |
| NR_3O-MMT | 100.0 | 1.5 | 5.0 | 2.0 | 0.7 | - | 3.0 |
| NR_5O-MMT | 100.0 | 1.5 | 5.0 | 2.0 | 0.7 | - | 5.0 |

The rubber compounds were prepared in accordance with ASTM 3182 standard, following the optimized process parameters reported in Chapter 4 . Initially, NR was masticated for 5 minutes in an internal mixer (Thermo Haake Rheomix 600), equipped with counter-rotating rotors, and operating at 50 °C and 60 rpm. The nanoclays, pre-dried in an oven at 60 °C for 48 hours, were subsequently added and mixed with the NR for 2 minutes. Zinc oxide, stearic acid, ZDBC and sulphur were then introduced and the resulting compound was further mixed and homogenized for two minutes. The vulcanization process was performed at a temperature of 120 °C and a pressure of 5 bar. The vulcanization time was selected based on the result of the rheological analysis described in Section 5.3.1. The vulcanization occurred in moulds having dimensions 110x110x1 $mm^3$ and 110x110x3 $mm^3$. Samples with a thickness of 1 mm were used for the

evaluation of the elastocaloric properties and for the determination of thermal properties by means of LFA analysis. The 3 mm-thick samples were produced to conduct the mechanical characterization.

## *5.3 Results and Discussion*

### 5.3.1 Rheological analysis

Rheological analysis was performed to explore the effect of nanoclay addition on the vulcanization characteristics of NR. Figure 5.1(A,B) shows the vulcanization curves at 120 °C of the various NR formulations, expressed as torque as a function of time, while Table 5.3 reports the most important results.

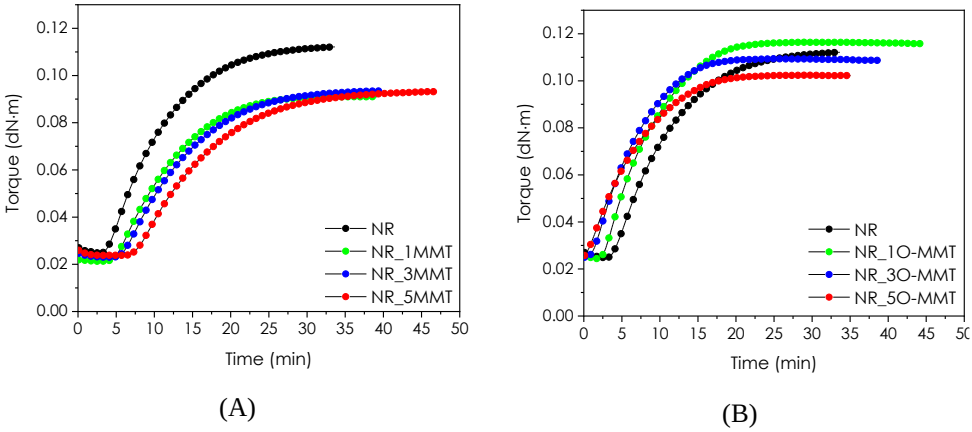


*Figure 5.1. Vulcanization curves of NR and (A) MMT-filled nanocomposites and (B) O-MMT-filled nanocomposites.*

*Table 5.3. Minimum torque ($T_{min}$), maximum torque ($T_{max}$) and optimum curing time ($t_{90\%}$) of neat NR and the prepared nanocomposites.*

| Sample | $T_{min}$ (dN·m) | $T_{max}$ (dN·m) | $t_{90\%}$ (min) |
|---|---|---|---|
| NR | 0.0251 | 0.1125 | 18 |
| NR_1MMT | 0.0210 | 0.0910 | 20 |
| NR_3MMT | 0.0230 | 0.0935 | 22 |
| NR_5MMT | 0.0239 | 0.0931 | 26 |
| NR_1O-MMT | 0.0244 | 0.1165 | 16 |
| NR_3O-MMT | 0.0250 | 0.1094 | 13 |
| NR_5O-MMT | 0.0258 | 0.1024 | 14 |

The incorporation of organoclays results in reduced scorch and vulcanization times, likely due to the amine groups present in the O-MMT structure, which act as additional vulcanizing agents, thereby accelerating the vulcanization kinetics [147]. For instance, the $t_{90\%}$ value decreases from 18 minutes for NR to 13 minutes for NR_3O-MMT. In contrast, natural nanoclays tend to retard the vulcanization process, as both scorch and curing times increase with higher MMT loadings. Specifically, an increment of up to 44% in $t_{90\%}$ is observed. Differences between the two series of nanocomposites are also observed in the maximum torque values. The addition of natural MMT leads to a decrease in $T_{max}$ compared with unfilled NR, whereas the incorporation of O-MMT results in $T_{max}$ values that are comparable to, or slightly higher than that of unfilled NR (as observed for the NR_1O-MMT formulation). These results suggest that the two types of nanoclays could exhibit different dispersion within the NR matrix. The higher $T_{max}$ observed for O-MMT nanocomposites could indicate a better interfacial interaction between the organoclay and rubber matrix, as well as a higher crosslink density of the rubber matrix.

### 5.3.2 Density measurements

The density values of the nanocomposites resulting from the application of Archimedes' principle are reported in Table 5.4.

*Table 5.4. Density of the unfilled NR and the relative nanocomposites.*

| Sample | Density ($g/cm^3$) |
|---|---|
| NR | 0.958 ± 0.006 |
| NR_1MMT | 0.960 ± 0.003 |
| NR_3MMT | 0.973 ± 0.001 |
| NR_5MMT | 0.981 ± 0.005 |
| NR_1O-MMT | 0.959 ± 0.001 |
| NR_3O-MMT | 0.966 ± 0.001 |
| NR_5O-MMT | 0.971 ± 0.003 |

The addition of nanoclays to NR promotes a slight density increase, which is more pronounced in the case of natural sodium MMT. This is a reasonable result, given that the density of the nanoclays, reported in Table 3.4, is higher than that of NR.

### 5.3.3 Evaluation of the crosslinking density

As the crosslinking density was found a parameter affecting the elastocaloric properties of NR (Chapter 4), the effect of nanoclay addition on the degree of crosslinking was investigated through swelling tests, and the results are reported in Table 5.5.

*Table 5.5. Crosslinking density of the unfilled NR and the relative nanocomposites obtained through swelling tests.*

| Sample | Crosslinking density ($10^{-4}$·mol/cm$^3$) |
|---|---|
| NR | 2.94 ± 0.21 |
| NR_1MMT | 3.02 ± 0.01 |
| NR_3MMT | 3.04 ± 0.09 |
| NR_5MMT | 2.94 ± 0.16 |
| NR_1O-MMT | 3.32 ± 0.02 |
| NR_3O-MMT | 3.73 ± 0.03 |
| NR_5O-MMT | 3.68 ± 0.04 |

As hypothesized from the results of the rheological analyses, the introduction of the organoclays induces a higher crosslinking degree. For instance, moving from unfilled NR to NR_3O-MMT, the crosslinking density increases from 2.94 $10^{-4}$·mol/cm$^3$ to 3.73 $10^{-4}$·mol/cm$^3$. This experimental evidence has been already reported in the literature and can be attributed, once again, to the amine groups present in the O-MMT structure, which can act as a vulcanizing agent and thus promote an increase in the crosslinking degree [147]. By contrast, the crosslinking density of MMT nanocomposites is comparable to that of NR. In Chapter 4, it was demonstrated that with increasing degree of crosslinking (in a range of crosslinking density comprised between 2.94 and 5.24 $10^{-4}$·mol/cm$^3$), the elastocaloric properties decrease. This aspect will be considered in the discussion of the elastocaloric properties of the samples.

### 5.3.4 X-Ray diffraction (XRD)

To investigate the dispersion of the nanoclays within the rubber matrix, XRD analysis was performed. The XRD diffraction patterns obtained on neat nanoclays, NR_5MMT and NR_5O-MMT

nanocomposites are reported in Figure 5.2(A,B), while Figure 5.2C shows the experimental fit of the basal peak, obtained by fitting the XRD patterns with a Pseudo-Voigt function without considering a structural model for simplicity.

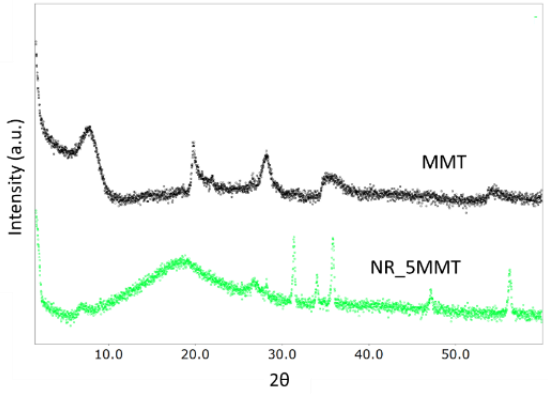


(A)

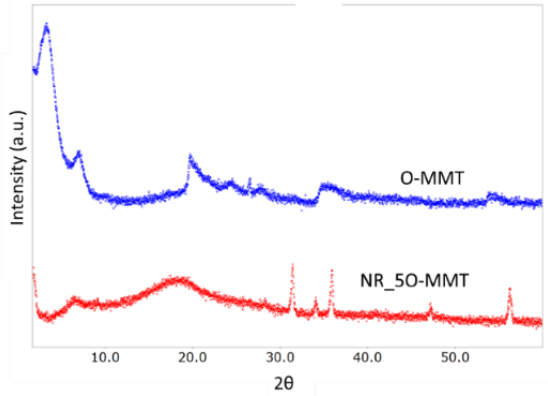


(B)

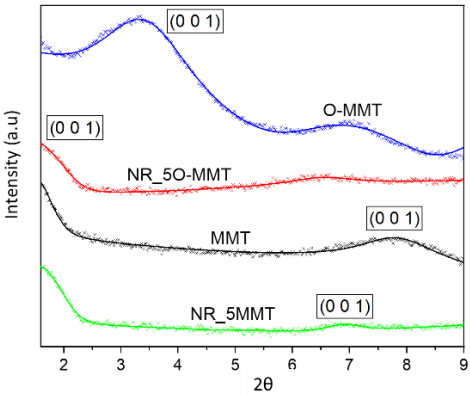


(C)

*Figure 5.2. Results of XRD analysis on neat nanoclay and the relative nanocomposites (nanoclay loading = 5 phr). High resolution XRD patterns of (A) neat MMT and NR_5MMT, (B) neat O-MMT and NR_5O-MMT samples, and (C) experimental fit of the basal peak performed with a Pseudo-Voigt function.*

The signal of the basal peak of neat natural nanoclay is localized at 2θ = 8° and slightly shifts to a lower 2θ value in the NR_5MMT sample. As regards the organoclays, the (001) reflection peak, observed at 2θ = 3°, significantly shifts towards lower 2θ values in the NR_5O-MMT nanocomposite. However, due to a probable overlap with the direct beam signal, it is difficult to detect it clearly. Given these challenges, the basal peak position for O-MMT in the NR_5O-MMT was assumed at 2θ = 1.6°, at the edge of the measurement range. Nonetheless, the true peak could lie at even lower 2θ values or might be absent in the case of complete organoclay exfoliation. The $d_{001}$ spacing values calculated using the Bragg's law are reported in Table 5.6.

*Table 5.6. Interlayer spacing for neat nanoclays and the produced nanocomposites calculated using the Bragg's law.*

| Sample | $d_{001}$ spacing [Å] |
|---|---|
| MMT | 11.4 |
| NR_5MMT | 12.7 |
| O-MMT | 26.1 |
| NR_5O-MMT | >51.7 |

As shown in Table 5.6, the interlamellar distances evaluated for the neat nanoclays are in good accordance with the values reported on the manufacturer data sheets (see Table 3.4). The interlayer spacing of the natural nanoclays sightly increases from 11.4 Å (for the neat MMT) to 12.7 Å in the NR_5MMT sample (i.e., an increase of 11.2%). The strong interlamellar interactions and the small initial $d_{001}$ spacing of MMT results in very limited intercalation in the NR matrix [78]. The situation is different for as concern the organoclays. The shared hydrophobic character of O-MMT and the NR matrix enhances their mutual compatibility, thereby promoting a strong intercalation (or exfoliation) of the organoclays, with $d_{001}$ spacing passing from 26.1 Å up to values higher than 51.7 Å.

### 5.3.5 Morphological analysis

SEM observations were also performed on the NR nanocomposites to investigate the nanoclay dispersion within the NR matrix. Representative FESEM micrographs of the cryofracture surface of NR_5MMT and NR_5O-MMT samples are presented in Figure 5.3(A–D). In particular, Figure 5.3(A,B) shows the morphological features of the NR_5MMT sample, while Figure 5.3 (C,D) of the NR_5O-MMT nanocomposite.

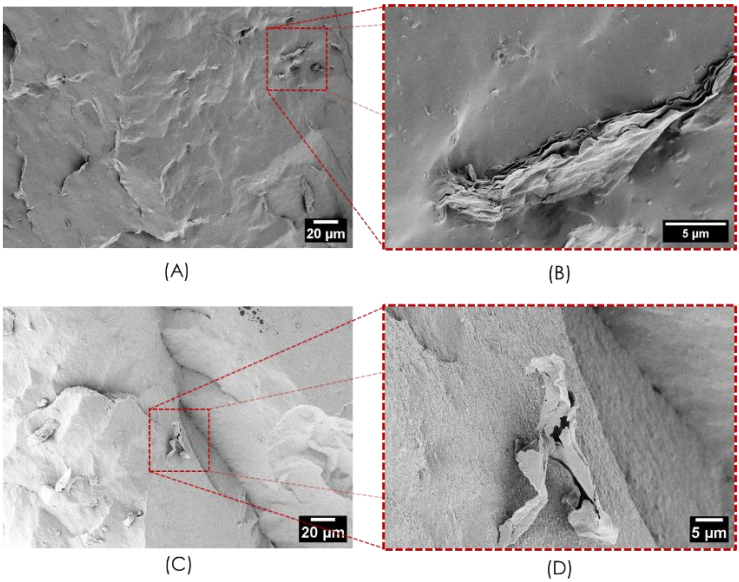


*Figure 5.3. FESEM micrographs at different magnifications of the cryofracture surface of the produced NR based nanocomposites. (A, B) NR_5MMT, (C, D) NR_5-OMMT.*

The organization of the nanoclay platelets in the rubber matrix plays a crucial role in their reinforcing effect. From Figure 5.3 (A-D) it is possible to appreciate that the use of natural sodium MMT leads to the production of a poorly intercalated nanocomposite. Indeed, the platelets are densely stacked and aggregated, indicating a poor affinity with the rubber matrix [148]. On the contrary, SEM micrographs of the NR_5OMMT sample reveal isolated nanoclay platelets in the matrix, suggesting the exfoliation of the organoclays and a good affinity with NR [148]. This outcome aligns with the results of both XRD and rheological analyses and suggests that in O-MMT nanocomposites the nanoclays could be strongly intercalated and/or partially exfoliated. The hydrophilic nature of MMT accounts for its poor compatibility with the hydrophobic NR matrix.

Conversely, the shared hydrophobic character of O-MMT and NR enhances their mutual compatibility, thereby promoting a finer nanofiller dispersion.

### 5.3.6 Differential Scanning Calorimetry (DSC)

DSC analysis was performed to determine whether the vulcanization of the nanocomposites was complete, and to evaluate the effect of the type and concentration of nanoclay on the glass transition temperature of NR. In Table 5.7, the $T_g$ of the samples determined in the 1st and 2nd heating scans are reported.

*Table 5.7. Glass transition temperature of the nanocomposites determined in the 1st and 2nd heating scan.*

| | **1st heating scan** | **2nd heating scan** |
|---|---|---|
| **Sample** | $T_g$ (°C) | $T_g$ (°C) |
| NR | -61.0 | -60.5 |
| NR_1MMT | -61.2 | -60.9 |
| NR_3MMT | -60.7 | -61.2 |
| NR_5MMT | -61.0 | -60.5 |
| NR_1O-MMT | -60.3 | -60.2 |
| NR_3O-MMT | -59.5 | -59.6 |
| NR_5O-MMT | -61.1 | -60.9 |

In all cases, no significant variation in $T_g$ is detected between the first and second heating scans, confirming that the vulcanization process was complete. The MMT-filled and O-MMT-filled samples show a glass transition temperature in the 1st heating scan ranging from -61.2 °C to -59.5 °C, which is comparable to that of unfilled NR (-61.0 °C). Therefore, it can be concluded that, at the explored loading levels, the addition of nanoclays does not significantly interfere with the polymer chain mobility.

### 5.3.7 Thermogravimetric analysis (TGA)

TGA analysis was performed to study the effect of the type and content of nanoclay on the thermal degradation of the produced NR nanocomposites. The thermogravimetric curves, along with their first derivative, of the nanocomposites and the neat nanoclays are shown in Figure 5.4(A-D), while Table 5.8 presents the most important results.

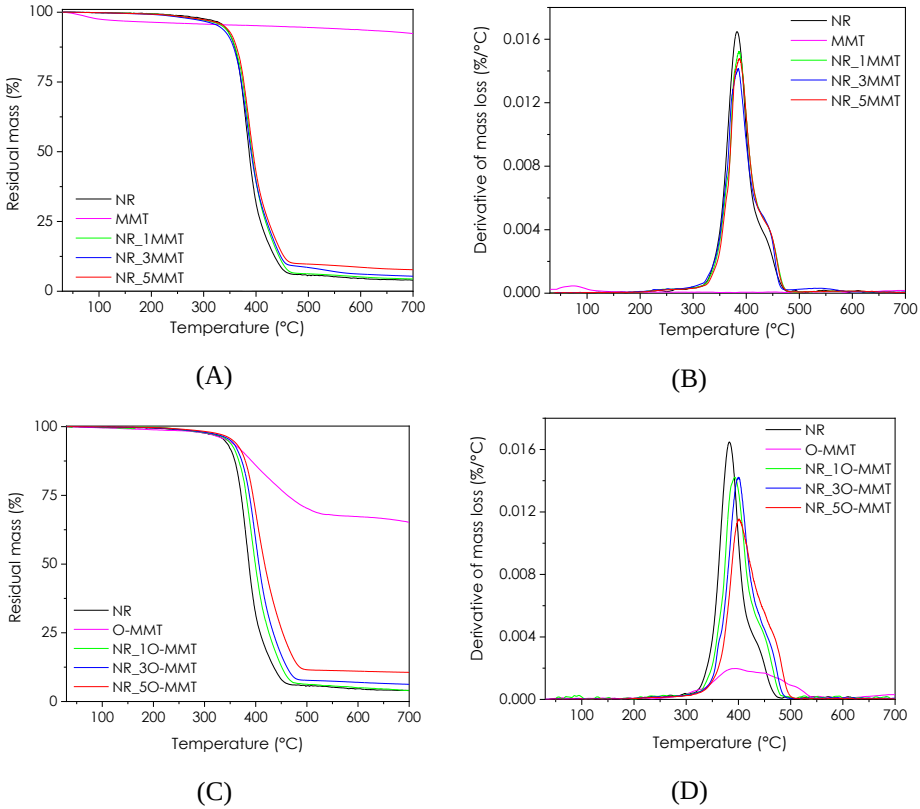


*Figure 5.4. (A,C) TGA curves and (B, D) DTGA curves of the nanoclays, NR and the produced nanocomposites. (A, B) Refer to MMT-filled nanocomposites, while (C,D) to O-MMT-filled nanocomposites.*

*Table 5.8. Results of the thermogravimetric analysis on the nanoclays, neat NR and the relative nanocomposites.*

| Sample | $T_{5\%}$ (°C) | $T_{peak}$ (°C) | $m_{700}$ (%) |
|---|---|---|---|
| NR | 339.0 | 382.8 | 4.0 |
| MMT | 432.8 | - | 92.6 |
| NR_1MMT | 335.7 | 386.4 | 4.4 |
| NR_3MMT | 328.7 | 385.0 | 5.4 |
| NR_5MMT | 339.2 | 387.0 | 7.7 |
| O-MMT | 344.7 | - | 65.1 |
| NR_1O-MMT | 345.3 | 393.0 | 4.1 |
| NR_3O-MMT | 350.5 | 400.2 | 6.3 |
| NR_5O-MMT | 355.2 | 401.2 | 10.6 |

Neat nanoclays exhibit, after being dried, different thermal decomposition behaviours. Natural MMT displays a weight loss of approximately 3% at temperatures below 100 °C, corresponding to the surface and interlayer-absorbed water. Above 100 °C, the bound and structural water are removed [137], and the total weight loss at 700 °C is about 7.4%. Regarding the organoclays, the absorbed water content is lower than that of MMT and the decomposition begins at approx. 200-250 °C, occurring in a single broad step, attributable to the thermal degradation of the organic modifier. The total weight loss of O-MMT at 700 °C is about 34.9% [149,150].

The thermal degradation of NR is not significantly affected by the addition of MMT. The thermogravimetric curves of the NR/MMT samples nearly overlap with that of unfilled NR, and, by analysing the values of $T_{5\%}$ it can be seen that values close to or even lower than those of NR are registered. As regards the temperature corresponding to the maximum degradation rate, only a slight increase is observed in the filled samples compared to NR, and this improvement remains

limited. These results confirm the polymer chains are not intercalated into the galleries of the silicate [150]. By contrast, NR/O-MMT nanocomposites display enhanced thermal stability compared with unfilled NR. As clearly shown in Figure 5.4(C,D), the thermogravimetric curves of O-MMT-filled samples are shifted to higher temperatures with respect to NR. Both $T_{5\%}$ and $T_d$ increase progressively with organoclay content in the rubber matrix. For example, $T_d$ of NR_5O-MMT is 401.2 °C, which is 18.4 °C higher than that of unfilled NR. The better dispersion of the organoclay nanolayers within the rubber matrix compared to the natural nanoclay, have probably prevented out-diffusion of the volatile decomposition products, increasing the thermal stability of NR [150,151]. For both types of nanocomposites, the residual mass increases with increasing nanoclay content in the formulation.

### 5.3.8 Laser Flash Analysis (LFA)

The specific heat capacity, thermal diffusivity and thermal conductivity values of the unfilled NR and the relative nanocomposites, obtained from LFA, are reported in Table 5.9.

*Table 5.9. Specific heat capacity, thermal conductivity and thermal diffusivity at 20 °C of neat NR and the relative nanocomposites from LFA.*

| Sample | $c_p$ (J/g·K) | α ($mm^2/s$) | λ (W/m·K) |
|---|---|---|---|
| NR | 1.70 ± 0.05 | 0.081 ± 0.001 | 0.132 ± 0.003 |
| NR_1MMT | 1.87 ± 0.08 | 0.085 ± 0.001 | 0.153 ± 0.006 |
| NR_3MMT | 1.82 ± 0.03 | 0.086 ± 0.001 | 0.151 ± 0.002 |
| NR_5MMT | 1.75 ± 0.03 | 0.088 ± 0.001 | 0.150 ± 0.003 |
| NR_1O-MMT | 1.82 ± 0.05 | 0.081 ± 0.002 | 0.141 ± 0.001 |
| NR_3O-MMT | 1.82 ± 0.04 | 0.081 ± 0.001 | 0.144 ± 0.002 |
| NR_5O-MMT | 1.75 ± 0.02 | 0.084 ± 0.001 | 0.142 ± 0.004 |

Regardless of the type and amount of nanoclays, the prepared nanocomposites do not show significant differences in thermal properties. Compared to the unfilled NR, the nanofilled samples exhibit a very slight increase in specific heat capacity and thermal conductivity. This is probably due to the presence of nanoclays which are characterized by a higher thermal conductivity (~0.7 W/m·K) with respect to the NR matrix [152]. Since the thermal properties of the NR nanocomposites are comparable, any difference in their elastocaloric performances among the samples cannot be attributed to their different thermal behaviour and heat transfer capability.

### 5.3.9 Shore A hardness measurements

Table 5.10 reports the results of the Shore A hardness test on the neat NR and the prepared nanocomposites.

*Table 5.10. Shore A hardness measurements for the unfilled rubber and the nanocomposites.*

| Samples | Shore A hardness |
|---|---|
| NR | 38.0 ± 0.8 |
| NR_1MMT | 40.4 ± 0.5 |
| NR_3MMT | 40.7 ± 1.0 |
| NR_5MMT | 41.6 ± 0.4 |
| NR_1O-MMT | 42.0 ± 0.2 |
| NR_3O-MMT | 45.9 ± 0.2 |
| NR_5O-MMT | 48.0 ± 0.5 |

Shore A hardness increases with nanoclay addition, in proportion to the nanofiller concentration, and the effect is more pronounced for O-MMT-filled samples. The maximum increase observed is 9.5% for MMT-filled nanocomposites and 26.3% for O-MMT-filled samples.

This difference can be attributed to the higher crosslinking density promoted by the organoclays, as well as to their improved dispersion within the rubber matrix [153].

### 5.3.10 Quasi-static tensile tests

Figure 5.5(A,B) shows the stress-strain behaviour of the unfilled NR and the relative nanocomposites. Specifically, the representative stress-strain curves of NR/MMT samples are reported in Figure 5.5A, while in Figure 5.5B the stress-strain plots of NR/O-MMT samples are shown. The most important results of the quasi-static tensile tests are reported in Table 5.11.

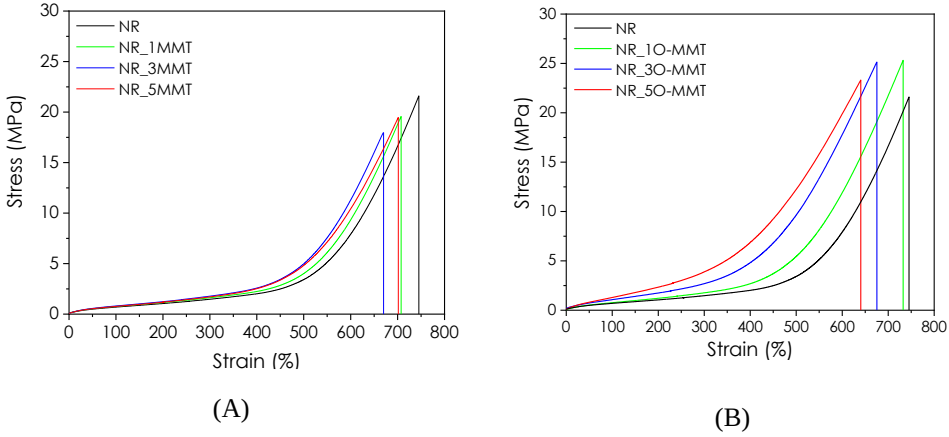


*Figure 5.5. Representative stress-strain curves from quasi-static tensile tests on (A) NR and NR/MMT nanocomposites, (B) NR and NR/O-MMT nanocomposites.*

*Table 5.11. Results of quasi-static tensile tests on the unfilled NR and the prepared nanocomposites.*

| Sample | $E_{100\text{-}200}$ (MPa) | $\sigma_{200\%}$ (MPa) | $\sigma_{400\%}$ (MPa) | $\sigma_b$ (MPa) | $\varepsilon_b$ (mm/mm) | $E_b$ (J/cm$^3$) |
|---|---|---|---|---|---|---|
| NR | 0.35 ± 0.08 | 1.08 ± 0.13 | 2.10 ± 0.23 | 21.28 ± 3.73 | 730 ± 14 | 32.2 ± 6.4 |
| NR_1MMT | 0.37 ± 0.02 | 1.12 ± 0.04 | 2.11 ± 0.15 | 19.45 ± 4.97 | 701 ± 58 | 28.5 ± 9.9 |
| NR_3MMT | 0.42 ± 0.04 | 1.22 ± 0.10 | 2.48 ± 0.29 | 19.55 ± 3.05 | 686 ± 32 | 29.2 ± 6.8 |
| NR_5MMT | 0.42 ± 0.06 | 1.20 ± 0.03 | 2.56 ± 0.07 | 18.96 ± 3.34 | 698 ± 30 | 30.2 ± 6.1 |
| NR_1O-MMT | 0.44 ± 0.02 | 1.19 ± 0.07 | 2.62 ± 0.33 | 26.08 ± 2.94 | 754 ± 41 | 44.7 ± 12.1 |
| NR_3O-MMT | 0.57 ± 0.09 | 1.54 ± 0.19 | 4.22 ± 0.46 | 25.39 ± 0.58 | 653 ± 34 | 42.6 ± 3.3 |
| NR_5O-MMT | 0.77 ± 0.20 | 1.91 ± 0.33 | 5.36 ± 0.94 | 20.05 ± 3.55 | 630 ± 72 | 35.6 ± 10.9 |

By comparing Figure 5.5A and Figure 5.5B, the effect of nanoclay type and content on the mechanical properties of the nanocomposites is evident. Focusing at first on the mechanical behaviour of NR/MMT samples, the stress-strain curves of the nanocomposites overlap with that of the unfilled NR up to a strain of approx. 300%. This observation is also confirmed by the $E_{100\text{-}200}$ and $\sigma_{200\%}$ values reported in Table 5.11, which show no significant difference among these samples. At strain levels above 300%, the stress-strain curves show a slight stiffening in the NR/MMT nanocomposites with respect to neat NR. For example, NR_5MMT exhibits a $\sigma_{400\%}$ value of 2.56 MPa, +22% than neat NR. Overall, the addition of MMT has promoted a slight decrease in strain and stress at break, and specific tensile energy to break. The most significant reduction in $E_b$ is registered in NR_1MMT (-11% than neat NR), while for $\sigma_b$ in NR_5MMT (-11% than neat NR). Given the obtained results and the considerations drawn from the morphological analysis, it can be concluded that the poor intercalation of the rubber into the nanoclay galleries and the

limited filler/NR interaction (due to the hydrophilic nature of the natural nanoclays and the hydrophobic nature of the NR matrix) led to a limited reinforcement.

A different behavior is observed in the case of NR/O-MMT samples. At the same filler loading, a stronger reinforcement effect is achieved compared to NR/MMT nanocomposites. The mechanical response of the nanocomposites diverges from that of neat NR from the outset, with increases in the elastic modulus as well as in $\sigma_{200\%}$, and $\sigma_{400\%}$ as the nanoclay content increases. For example, NR_5O-MMT exhibits an elastic modulus of 0.77 MPa and a $\sigma_{400\%}$ of 5.36 MPa (+120% and +155% than neat NR, respectively). The tensile strength of NR improves with the addition of 1 and 3 phr of O-MMT, whereas at 5 phr it becomes comparable to that of unfilled NR, likely due to aggregation phenomena occurring at filler contents above 3 phr. A similar trend is observed for the specific energy to break. The improved mechanical properties with respect to NR MMT filled-nanocomposites can be explained on the basis of XRD and SEM analysis, which showed the intercalation/exfoliation of O-MMT in the NR matrix. The higher crosslinking density found in O-MMT/NR samples with respect to the neat NR (Table 5.5) could also be in part responsible for the stiffening of these nanocomposites, and also for the slight $\sigma_b$ decrease observed at elevated O-MMT amounts.

For the evaluation of the elastocaloric effect, the samples were deformed to 400% strain, as in Chapter 4 it was demonstrated that this deformation level is the best performing. As reported in Table 5.11, the stress required to reach this level of deformation in all the NR nanocomposite samples ($\sigma_{400\%}$) is below 6 MPa. It can therefore be concluded that, even with the addition of nanoclays, the value of $\sigma_{400\%}$ remains comparable to the stress levels required to compress refrigerant gases in current air conditioners (1–8 MPa) [135].

### 5.3.11 Evaluation of strain induced crystallization

XRD analyses were performed on NR_5MMT and NR_5O-MMT samples in the stretched state at 400% (the level of deformation used to investigate elastocaloric properties) to evaluate the effect of nanoclay addition on the extent of SIC of the samples. The diffraction patterns obtained for neat NR and the nanocomposites deformed at a strain of 400% are shown in Figure 5.6, while the crystallinity content and the average crystallite size calculated are reported in Table 5.12.

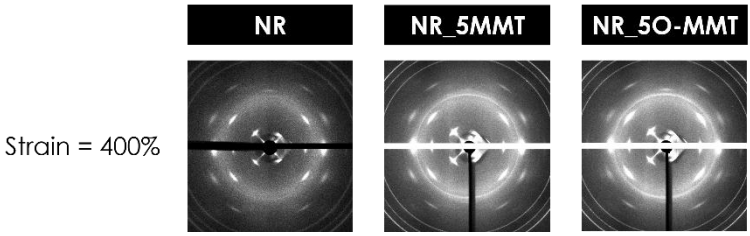


*Figure 5.6. Diffraction patterns of neat NR and NR_5MMT and NR_5O-MMT nanocomposites deformed at 400% strain.*

*Table 5.12. Average crystallite size and crystallinity obtained from XRD measurements on neat NR, NR_5MMT and NR_5O-MMT, deformed at a strain of 400%.*

| Sample | Deformation (%) | Average Crystallite Size (Å) | Crystallinity (%) |
|---|---|---|---|
| **NR** | 400 | 91.6 | 11.8 |
| **NR_5MMT** | 400 | 71.3 | 11.4 |
| **NR_5O-MMT** | 400 | 78.9 | 13.0 |

The diffraction patterns of both nanocomposites exhibit additional reflection rings compared to neat NR, which are attributed to the presence of nanoclays in the rubber formulations. The calculated

crystallinity indicates that the addition of organoclay enhances the ability of NR to crystallize under strain. Specifically, the NR_5O-MMT sample exhibits a crystallinity of 13.0%, compared to 11.8% for neat NR, i.e., an increase of approximately 10%. In contrast, the NR_5MMT sample shows a similar, though slightly lower, degree of SIC relative to neat NR (11.4%). The O-MMT exfoliation and the improved polymer–filler interactions probably have promoted a further molecular alignment under deformation, favouring SIC. In agreement with the findings of Carretero et al. [80,81], good interfacial adhesion between the filler and the NR matrix, as observed in O-MMT-filled nanocomposites, enhances the extent of SIC. However, differently to the results obtained in this work, Carretero et al. observed an increase in SIC (approx. 50%) even in nanocomposites filled with 15 phr of natural nanoclays, corresponding to approximately one-third of the increase reported for NR filled with 15 phr of organoclays. The higher nanofiller content in their study likely contributed to the improved crystallization behaviour under strain. Moreover, the incorporation of the fillers leads to a reduction in the average crystallite size, with the NR_5MMT sample showing the smallest value of 71.3 Å. This experimental evidence is in agreement with the findings of Yuko Ikeda et al. [154], who observed a reduction in the crystallite size in the NR samples filled with carbon black and calcium carbonate, compared to unfilled NR.

In conclusion, the higher crystallinity content found in the O-MMT-filled sample suggests that these nanocomposites could exhibit a more pronounced elastocaloric effect. Based on the measured difference in crystallinity, an increase in $\Delta T_{cool}$, attributed solely to SIC, of approximately 0.6 °C would be expected in NR_5O-MMT sample.

### 5.3.12 Evaluation of the Mullins effect

The incorporation of nanofillers has been widely reported to intensify the Mullins effect in NR [84,85]. From a practical standpoint, a more pronounced Mullins effect in the produced nanocomposites could require additional pre-stretching cycles compared to unfilled NR to reach a stable mechanical response. To determine whether the addition of nanoclay at the concentrations under investigation intensified this stress-softening phenomenon, the cyclic behaviour of the nanocomposites was investigated and benchmarked against that of unfilled NR. This evaluation is particularly important, as an unmitigated Mullins effect could compromise the assessment of elastocaloric performance and ultimately lower the energy conversion capability of the samples. Figure 5.7(A-F) shows the stress-strain response of the NR nanocomposites under cyclic tensile loading when a maximum strain level of 400% is applied. In particular, Figure 5.7 (A-C) illustrates the mechanical behaviour of NR/MMT samples, while Figure 5.7 (D-F) of NR/O-MMT nanocomposites. The stress at the maximum deformation per each cycle (peak stress) and the energy dissipated in the $1^{st}$, $2^{nd}$, $5^{th}$ and $10^{th}$ cycles are reported in Figure 5.8(A,B) and Figure 5.8 (C,D), respectively, while the residual deformation at the end of the $10^{th}$ cycle is reported in Figure 5.9.

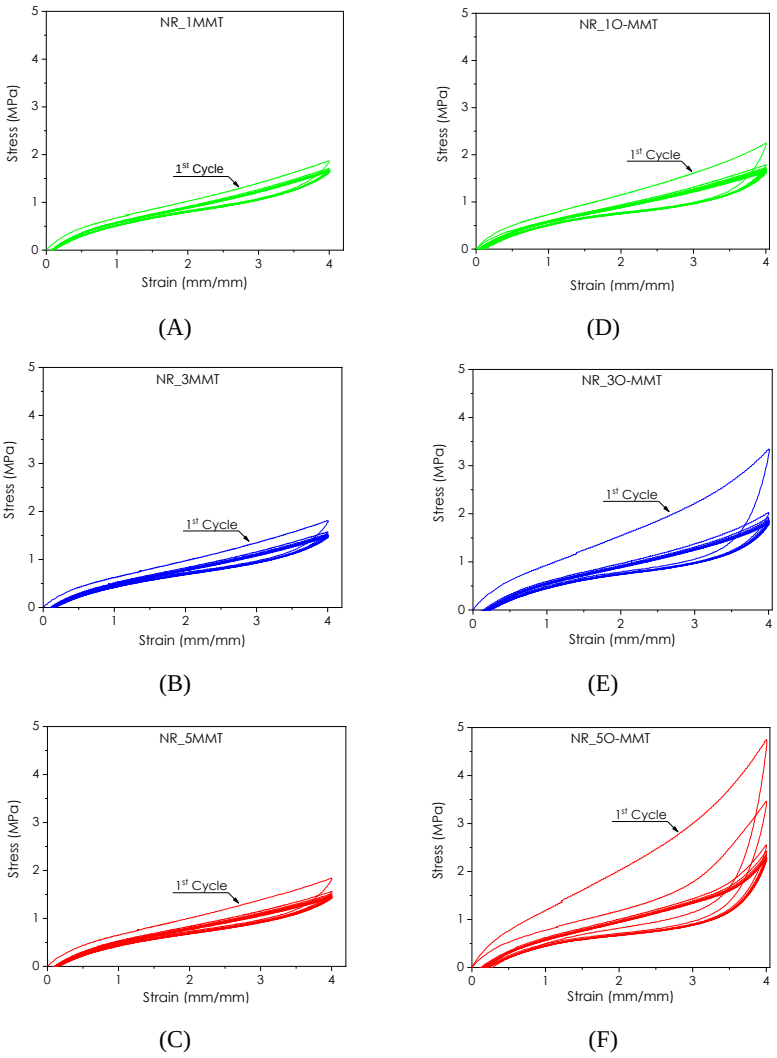


*Figure 5.7. Stress-strain curves of the NR based nanocomposites subjected to uniaxial cyclic tension (maximum strain level = 400%). (A) NR_1MMT, (B) NR_3MMT, (C) NR_5MMT, (D) NR_1O-MMT, (E) NR_3O-MMT, (F) NR_5O-MMT. The first cycle is evidenced in all the graphs.*

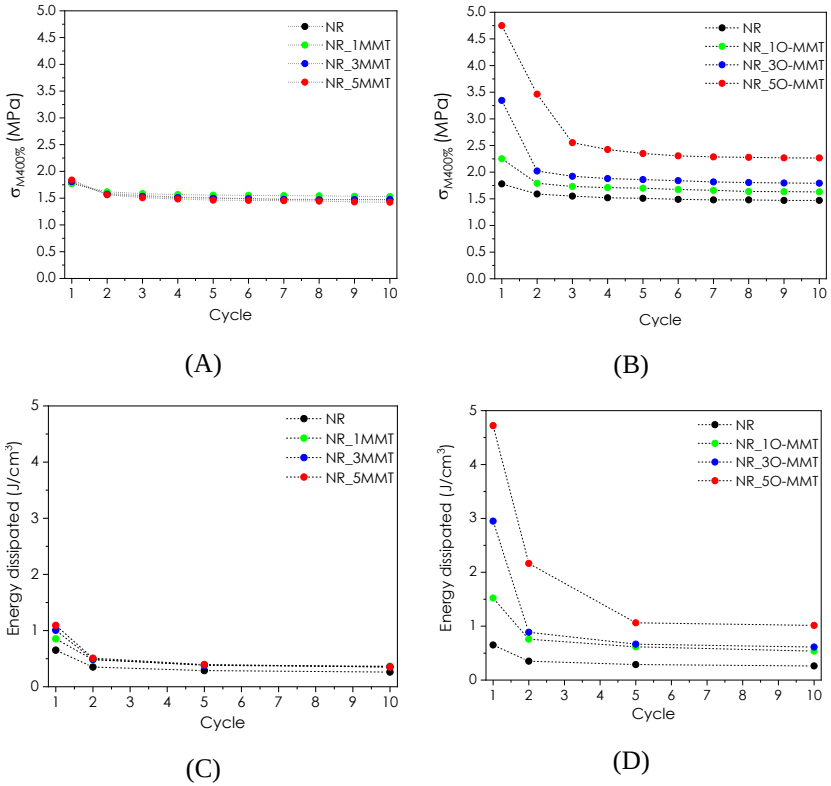


*Figure 5.8. Results from the uniaxial cyclic tension tests on the neat NR and the relative nanocomposites. (A, B) Maximum stress at 400% and (C, D) specific energy dissipated as a function of cycle number. (A, C) refer to NR/MMT samples, while (B, D) to NR/O-MMT samples.*

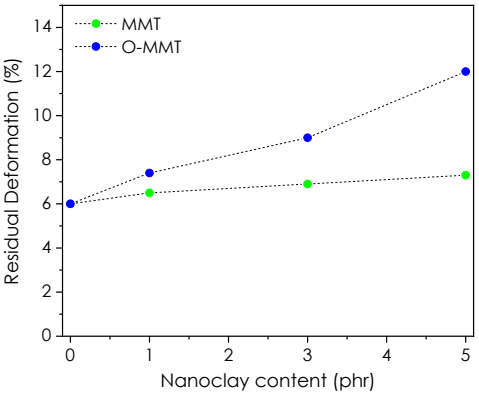


*Figure 5.9. Residual deformation after ten loading-unloading cycles as a function of type and concentration of nanoclays in the prepared NR nanocomposites.*

For the NR/MMT nanocomposites, the mechanical response stabilizes after the first loading–unloading cycle. The filler content exerts only a minor influence on the Mullins effect, and the overall stress-softening behaviour remains comparable to that of unfilled NR. The residual deformation is about 6–7%, essentially the same as that observed for the unfilled rubber. In contrast, the NR/O-MMT nanocomposites exhibit a more pronounced Mullins effect, as shown by the larger hysteresis in the first cycle and the more pronounced drop in peak stress ($\sigma_{M400\%}$) between the initial and subsequent cycles. For instance, NR_5O-MMT dissipates 4.8 J/cm³ in the first loading–unloading cycle, approximately five times the value measured for NR_5MMT (1.1 J/cm³). Moreover, increasing the organoclay content further accentuates both the stress softening and the residual deformation, which reaches 12% at 5 phr O-MMT, about twice the value measured for unfilled NR. It is interesting to observe that after the first cycles, the hysteresis loop increases with filler concentration, a feature not observed for the NR/MMT series. This experimental evidence could be attributed to an increase in internal friction between macromolecules and filler and, according to the results reported by

Le Cam [138], to a more pronounced SIC with increasing filler content.

Among the theories advanced to explain the Mullins effect (Section 2.3.8), there are some regarding molecules slipping. Particularly, some authors have proposed that, during the first extension, the macromolecules slip over the filler surface, and new physical bonds are instantaneously created along the chains. The new bonds would be of the same physical nature as the original ones but would appear at different places along the polymeric chain, causing the softening of rubber. Considering this, the different behaviour found in the two series of nanocomposites can be attributed again to the different dispersion and interactions the fillers have with the NR matrix. The hydrophilic nature of MMT causes this filler to weakly interact with the NR chains, and, consequently, the nanocomposites exhibit a Mullins effect comparable to the unfilled rubber. Instead, the hydrophobic tails of the organoclays allow a more intense interaction with the NR matrix, promoting the formation of a higher density of physical bonds between the filler and NR macromolecules. In addition, the elevated dispersion (or exfoliation) of O-MMT within the NR observed in the SEM micrographs (see Figure 5.3C and Figure 5.3D) greatly increases the surface area of interaction between the clays and the rubber. The rapture and reformation of the O-MMT-rubber physical bonds during the first cycle could explain the greater Mullins effect observed in organoclay-filled nanocomposites.

Based on the results obtained, the nanocomposites were pre-stretched three times prior to evaluating their elastocaloric performance, i.e., one additional cycle compared with unfilled NR.

### 5.3.13 Evaluation of the elastocaloric effect

The elastocaloric properties of the samples were investigated using the high-speed tensile testing machine STEP Lab XUD05 (STEP Lab S.r.l., Resana TV, Italy) and following the procedure described in Section 3.2.12. All the experimental parameters were selected on the basis of the results reported in Chapter 4. Specifically, the tests were performed by deforming the samples to 400% strain at a crosshead speed of 0.5 m/s. Heat exchange between the rubber and the environment occurred through forced convection using a small fan (power = 2.5 W) positioned 50 cm from the samples, which provided a heat transfer coefficient of approx. 45 $W/m^2K$. The duration of each elastocaloric cycle was 120 seconds, with the stretching and retraction phases set at 60 seconds each.

Figure 5.10A and 5.10C show the temperature variation of the surface of the neat NR and the relative nanocomposites during the stretching and retraction phases as a function of time, while Figure 5.10B and 5.10D report the stress sustained by the samples as a function of time in the stretching and subsequent holding phase. The percentage of stress relaxation is shown in Table 5.13, while in Figure 5.11(A-G) the most important results of the elastocaloric tests on the neat NR and the relative nanocomposites are reported.

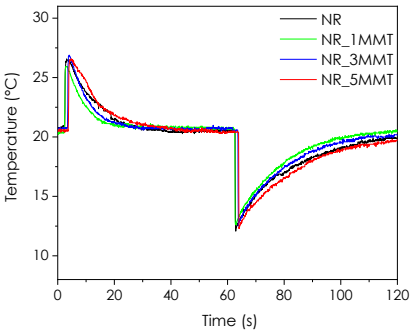


(A)

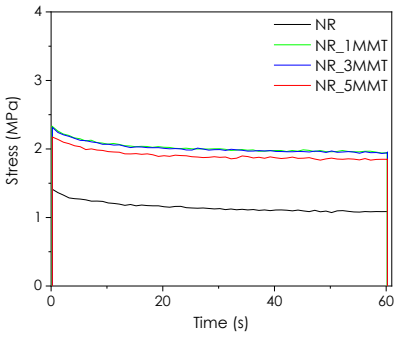


(B)

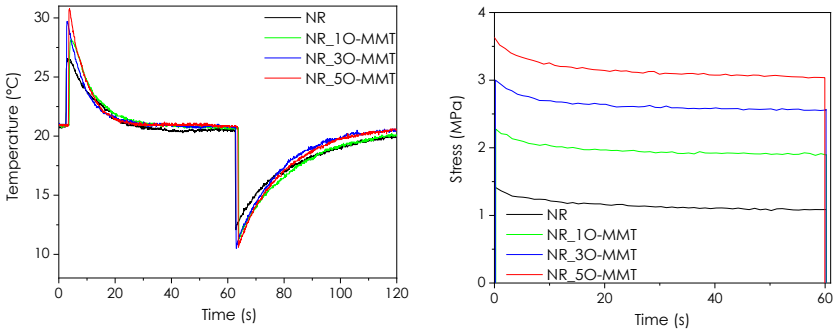


(C) (D)

*Figure 5.10. (A, C) Temperature variation of the surface of the samples as a function of time, (B, D) stress variation in the stretching and subsequent holding step as a function of time. (A, B) refer to MMT nanocomposites, (C, D) refer to O-MMT nanocomposites.*

*Table 5.13. Percentage of stress relaxation (SR) evaluated over the time scale of the stretching phase from elastocaloric tests on neat NR and the relative nanocomposites.*

| Sample | SR (%) |
|---|---|
| NR | 22.2 ± 1.3 |
| NR_1MMT | 20.0 ± 4.7 |
| NR_3MMT | 18.8 ± 4.3 |
| NR_5MMT | 17.4 ± 3.7 |
| NR_1O-MMT | 18.2 ± 2.1 |
| NR_3O-MMT | 16.4 ± 2.2 |
| NR_5O-MMT | 16.2 ± 0.4 |

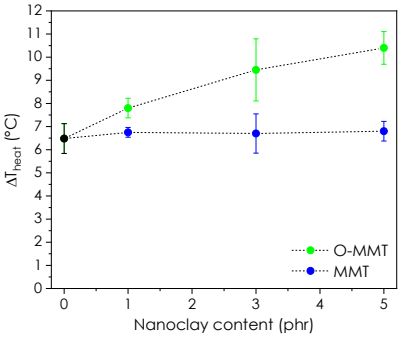
ΔT_heat (°C)
Nanoclay content (phr)
O-MMT
MMT

(A)

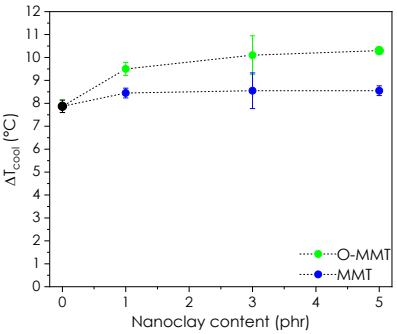
ΔT_cool (°C)
Nanoclay content (phr)
O-MMT
MMT

(B)

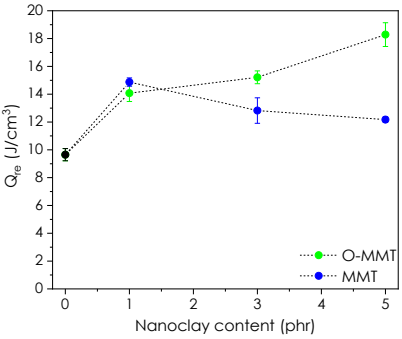
Q_re (J/cm³)
Nanoclay content (phr)
O-MMT
MMT

(C)

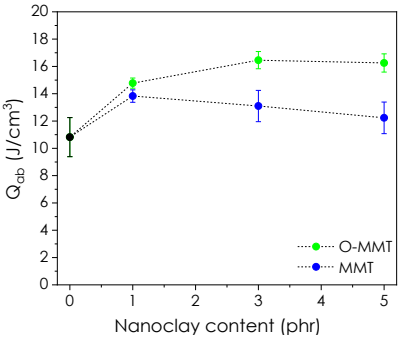
Q_ab (J/cm³)
Nanoclay content (phr)
O-MMT
MMT

(D)

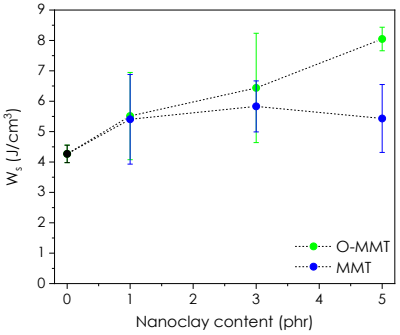
W_s (J/cm³)
Nanoclay content (phr)
O-MMT
MMT

(E)

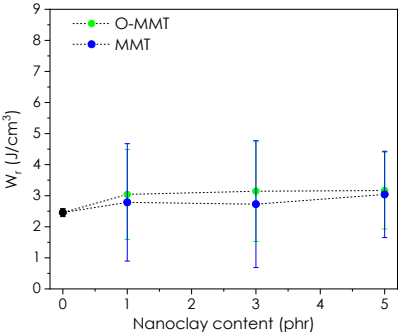
W_r (J/cm³)
Nanoclay content (phr)
O-MMT
MMT

(F)

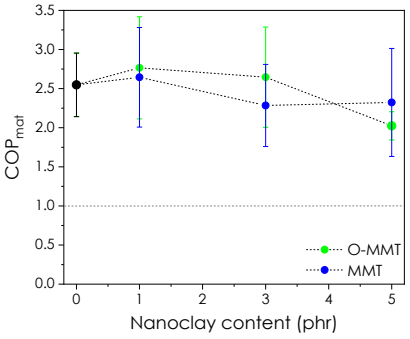


(G)

*Figure 5.11. Results of the elastocaloric tests on the neat NR and the relative nanocomposites. (A) Maximum $\Delta T_{heat}$, (B) maximum $\Delta T_{cool}$, (C) $Q_{re}$, (D) $Q_{ab}$, (E) $W_s$ per unit volume of material, (F) $W_r$ per unit volume of material, (G) $COP_{mat}$.*

Two main considerations emerge from the analysis of the obtained results. The type of nanoclay influences not only the mechanical properties of the nanocomposites, as discussed in Section 5.3.10, but also their elastocaloric performance. Higher values of $\Delta T_{heat}$ and $\Delta T_{cool}$ have been registered in O-MMT nanocomposites with respect to unfilled NR and MMT/NR samples, especially at elevated organoclay amounts. For example, NR_5O-MMT shows a $\Delta T_{heat}$ of 10.4 °C and a $\Delta T_{cool}$ of 10.3 °C, +63% and +32% than neat NR, respectively. On the other hand, natural sodium nanoclay seems to have a very limited positive effect on the cooling capacity of NR.

By comparing $\Delta T_{heat}$ and $\Delta T_{cool}$ values (Figure 5.11A and 5.11B), it can be appreciated that, for both the unfilled rubber and NR/MMT samples, the absolute values of $\Delta T_{cool}$ are slightly greater, by approx. 1.5-2.0 °C, than those of $\Delta T_{heat}$, while for the NR/O-MMT nanocomposites the temperature changes recorded during stretching and retraction phases are similar, particularly at higher filler loadings. This can be explained by recalling the mechanisms contributing to the rubber temperature change. The mechanisms involved and their role

in the temperature variations are summarized in Table 5.14. The up arrows indicate that the mechanism promotes the heating of the sample, while the down arrows indicate the mechanism promotes the cooling of the rubber.

*Table 5.14. Mechanisms involved in the temperature variations of the samples during the stretching and retraction phase.*

| Mechanism | Stretching phase | Retraction phase |
|---|---|---|
| Thermoelastic effect | ↑ | ↓ |
| SIC | ↑ | \ |
| Internal friction macromolecules-macromolecules and macromolecules-nanoclays | ↑ | ↑ |
| Melting of the crystallites | \ | ↓ |

The addition of nanoclay to NR increases the internal friction, as interactions are no longer limited to NR macromolecules but also occurred between polymer–filler as well as between filler particles. Consequently, internal friction contributes more to heat dissipation both during the loading and unloading phase with respect to the unfilled NR. During the stretching phase the temperature increase ($\Delta T_{heat}$), results from the combined effects of the thermoelastic response, SIC, and internal friction. Among these mechanisms, SIC evolves while the samples are maintained in the stretched state, with the greatest part of crystallites developing in the first milliseconds after the stretching [45]. Consequently, only a part of the heat generated during their formation contributes to $\Delta T_{heat}$. When the sample is unloaded, the melting of the crystallites and the thermoelastic effect positively contribute to the $\Delta T_{cool}$, while the frictional heat is a mechanism that plays havoc with the cooling of the rubber, reducing $\Delta T_{cool}$ and the cooling effect. If the friction is almost negligible, it is reasonable that $\Delta T_{cool}$ is higher than $\Delta T_{heat}$ since,

during unloading, all crystalline domains, regardless of their formation time, melt, thus fully contributing to $\Delta T_{cool}$. If internal fiction is not negligible, $\Delta T_{cool}$ lower or equal to $\Delta T_{heat}$ is expected. The higher contribution of internal friction found in NR/O-MMT samples with respect to MMT nanocomposites is another evidence of the better dispersion of O-MMT within the NR matrix.

Going into details of the elastocaloric effect, Figure 5.11C and 5.11D show the $Q_{re}$ and $Q_{ab}$ values of the samples. For a given type of clay and clay content, the values of $Q_{re}$ and $Q_{ab}$ are generally higher than those measured for NR and are similar to each other, with the exception of the NR_5OMMT sample. For this nanocomposite, $Q_{re}$ is notably higher compared to $Q_{ab}$, suggesting the presence of significant dissipative phenomena. Both types of nanocomposites, at 1 phr of filler, release and absorb approximately the same amount of thermal energy. However, at higher filler loadings, the O-MMT nanocomposites exhibit significantly greater $Q_{re}$ and $Q_{ab}$ compared to MMT-filled samples. Focusing on the cooling capacity, in one single loading-unloading cycle, NR_3O-MMT and NR_5O-MMT samples are capable of extracting more than 16 J/cm$^3$ of heat from the surrounding environment, compared to 11 J/cm$^3$ of the unfilled NR (i.e., an increase of 45%). These findings highlight that the selection of a proper nanofiller is fundamental for enhancing the elastocaloric properties of NR. In particular, the affinity and compatibility between the rubber and the filler play a key role in the elastocaloric performances. As reported in Table 5.5, the crosslinking density of NR/O-MMT nanocomposites was found to be higher compared to unfilled NR and NR/MMT samples. In Chapter 4, it was demonstrated that an increased degree of crosslinking leads to a decrease in the cooling capacity of NR. This suggests that the presence of O-MMT in the NR matrix largely overcompensates for the negative impact caused by the higher crosslinking density.

The enhanced cooling capacity observed in the NR/O-MMT samples is undoubtedly attributable to their greater ability to crystallise under

strain compared to neat NR and the NR/MMT samples, as seen in Paragraph 5.3.11. In addition to this, other phenomena may have contributed to the improved elastocaloric performance. For example, the O-MMT could contribute to a more homogeneous rubber network structure, as documented in the literature [80]. A more uniform macromolecular structure, characterized by a more consistent chain length and crosslinking density, allows for greater conformational changes during stretching, resulting in a larger entropy change between the undeformed and stretched states [155]. Moreover, the observed improvement may also stem from a strain amplification effect induced by the nanoclays, promoting a higher thermoelastic effect. This mechanism could also explain why elastocaloric properties of the NR/MMT samples are slightly higher than those of neat NR, since no significant differences in terms of SIC were found between these samples. Further investigation is necessary to validate these hypotheses.

Although organoclay-filled NR samples exhibit higher $Q_{ab}$, no significant differences are observed in $COP_{mat}$ (Figure 5.11G) between the two series of NR nanocomposite, and the $COP_{mat}$ is found to range between 2 and 3. This is attributed to the greater work of deformation required for the NR/O-MMT samples (Figure 5.11E) with respect to MMT nanocomposites. For example, the work of deformation of NR_5-OMMT is 8.0 J/cm$^3$, compared to 4.3 J/cm$^3$ of neat NR and 5.4 J/cm$^3$ of NR_5MMT sample. The higher $W_s$ values observed in O-MMT nanocomposites are due to the stiffening effect provided by the better nanofiller dispersion and the higher polymer/filler interaction.

As regards the stress relaxation behaviour of the samples, the SR values obtained for the nanocomposites (Table 5.13), ranging between 16% and 20%, are slightly lower than those measured for unfilled NR (22%). For both nanocomposites, a clear reduction in SR with increasing nanoclay content can be observed. For the same filler content, the MMT samples show marginally higher SR values,

although the difference is limited. The higher $\Delta T_{heat}$ values registered for O-MMT-filled samples would be expected to promote greater SR than in unfilled NR and MMT nanocomposites. However, this effect is likely counterbalanced by a stabilization of the mechanical response induced by the organoclays.

In light of the obtained results, the NR_3O-MMT formulation appears to be the most promising as it provides an enhanced cooling capacity compared to NR, while exhibiting lower heat dissipation due to internal friction relative to NR_5O-MMT. For this reason, the cyclic elastocaloric properties of this sample were further investigated in order to evaluate its performance under repeated loading–unloading conditions. Specifically, the sample underwent 40 loading-unloading cycles. The most important elastocaloric properties and the SR values, evaluated at the $1^{st}$, $5^{th}$, $10^{th}$, $20^{th}$, $30^{th}$ and $40^{th}$ cycles, are shown in Figure 5.12(A-F). As the interest is focused on the cooling performance, $Q_{re}$ is not reported here.

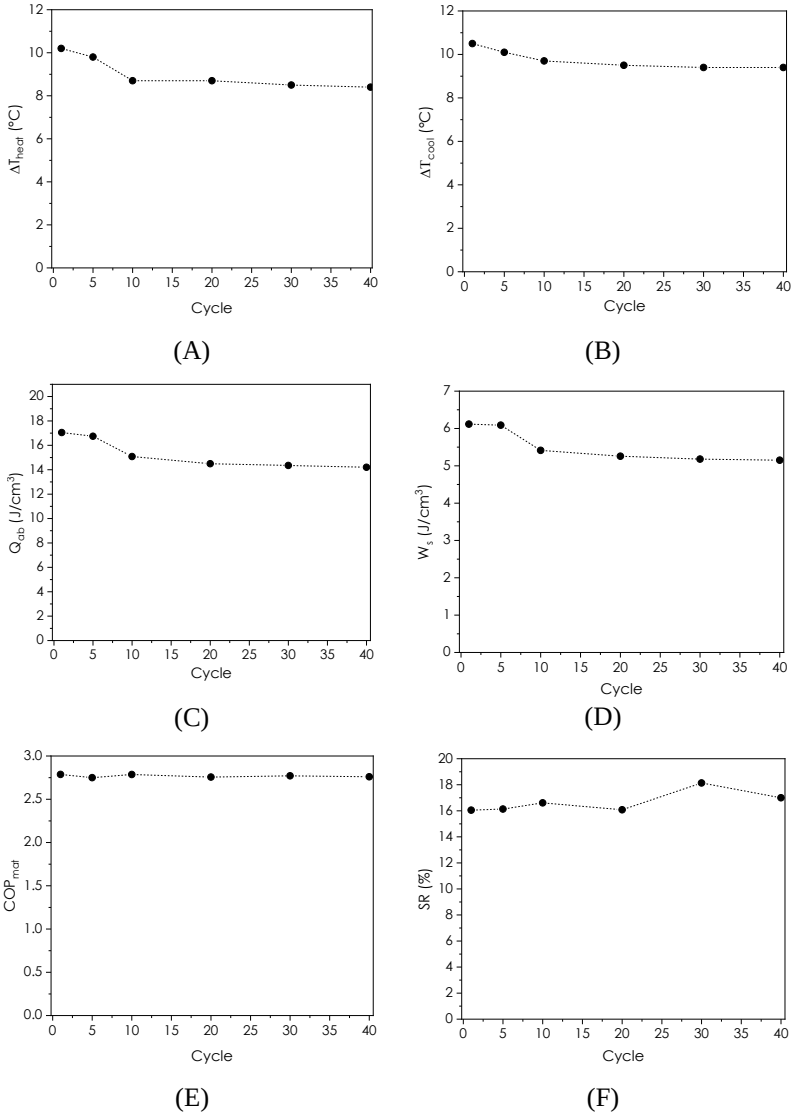


*Figure 5.12. Elastocaloric properties of NR_3O-MMT sample under cyclic conditions. (A) $\Delta T_{heat}$, (B) $\Delta T_{cool}$, (C) $Q_{ab}$, (D) $W_s$,(E) $COP_{mat}$ and (F) SR.*

Overall, the elastocaloric properties of NR_3O-MMT remain relatively stable up to 40 loading-unloading cycles. A slight decrease in the values of $\Delta T_{heat}$, $\Delta T_{cool}$, $Q_{ab}$ and $W_s$ is observed between the first and the tenth cycle, after which they stabilize. Specifically, $\Delta T_{heat}$ decreases from 10.2 °C to 8.7 °C at the $10^{th}$ cycle, while $\Delta T_{cool}$ decreases from 10.5 °C to 9.7 °C. Regarding $Q_{ab}$, it stabilizes after the tenth cycle at 15.1 J/cm$^3$. As discussed in Chapter 4, this settiling-in phase is probably linked to the Mullins effect and could be limited or eliminated by pre-stretching the samples a higher number of times. Across all cycles, the $COP_{mat}$ remains approximately 2.7, as both $Q_{ab}$ and $W_s$ follow the same trend over the cycles. Additionally, the percentage of stress relaxation remains constant at values of about 16% which is a positive indication that the mechanical behaviour of the samples is stable over 40 cycles.

In conclusion, the enhanced cooling capacity of NR, achieved through the addition of organoclays, is also maintained under cyclic conditions, highlighting that this approach to improving the elastocaloric performance of NR is promising and could be extended to other fillers as well.

## *5.4 Conclusions*

In Chapter 5, the influence of nanoclay addition, both natural (MMT) and organo-modified (O-MMT), on the elastocaloric performance of NR was investigated. XRD and SEM analyses revealed a good degree of intercalation/exfoliation of the organomodified nanoclays within the NR matrix, whereas natural MMT exhibited a strongly aggregated morphology. These morphological features translated into a more pronounced mechanical stiffening and reinforcement, associated to a more evident Mullins effect in NR/O-MMT nanocomposites.

Despite the slight increase in crosslinking density of NR induced by the presence of O-MMT which tended to reduce the elastocaloric efficiency in unfilled NR, the NR/O-MMT samples displayed a

remarkable enhancement in elastocaloric performance. In particular, organoclay-filled NR nanocomposites demonstrated up to a ~45% increase in the heat extracted per refrigeration cycle with respect to unfilled NR. More specifically, the heat absorbed from the environment increased from 11 J/cm$^3$ (in the case of unfilled NR) to 16 J/cm$^3$ (with a O-MMT amount of 5 phr). This improvement was ascribed to a synergistic combination of enhanced strain-induced crystallization confirmed by XRD analysis, improved macromolecular structural homogeneity, and potential strain amplification effects promoted by the organoclays. In contrast, the incorporation of natural MMT yielded only marginal improvements in both mechanical and elastocaloric properties, primarily due to poor dispersion and limited nanofiller-matrix interaction. Despite the better cooling capacity of NR/O-MMT samples, the $COP_{mat}$ was found to be comparable in the two series of nanocomposites and ranging between 2 and 3. This was due to the greater work of deformation found in O-MMT nanocomposites, ascribed to their higher stiffness. Among the O-MMT filled samples, the formulation containing 3 phr of organoclay was found to be the best performing. Investigating the elastocaloric properties of this formulation under cyclic conditions revealed stability up to 40 cycles.

Overall, these findings highlighted that the selection of a proper nanofiller could play a fundamental role in enhancing the elastocaloric properties of NR. In particular, the compatibility between the rubber and the filler resulted in playing a key role on their mechanical and cooling performance. Further efforts will be devoted in the future to investigate if the better cooling capacity of NR/O-MMT samples could be attributed to a higher crystallinity developed in these systems during stretching with respect to NR/MMT samples. In addition, the effect of filler functionalization on the elastocaloric performance of NR will also be deepened.

# 6 General conclusions

## *6.1 Concluding remarks*

The aim of this work was to investigate the influence of rubber network structure and rubber formulation on the elastocaloric properties of natural rubber (NR) based systems. Specifically, the effect of (i) crosslinking density and (ii) the addition of nanofillers on the cooling capacity was deeply analysed. This study was driven by the need to enhance the cooling capacity of NR in order to develop sustainable solid-state cooling technologies capable of competing with the current refrigeration systems based on compression of refrigerant with elevated environmental impact.

In the first part of the work, presented in Chapter 4, the effect of crosslinking density on the elastocaloric performance of NR was investigated. Samples with varying degrees of crosslinking were produced and thermo-mechanically characterized. The results showed that the crosslinking density played a crucial role in the elastocaloric properties of NR. Specifically, reducing the crosslinking degree enhanced the cooling capacity of the material for the same deformation, due to a greater contribution from strain-induced crystallization and the thermoelastic effect. The least crosslinked sample was found to be capable of extracting 16.4 J/cm$^3$ of thermal energy in a single refrigeration cycle when stretched at 500%, exceeding values reported in comparable studies. The evaluation of the Coefficient of Performance ($COP_{mat}$) confirmed the least crosslinked sample as the best formulation, exhibiting a $COP_{mat}$ value ranging up to 2.4, and evidenced that the highest conversion efficiency between mechanical and thermal energy was achieved at 400% deformation. The elastocaloric properties of the most promising NR formulation were also studied under cyclic conditions, proving to be stable up to 40 loading-unloading cycles.

In the second part of the work, presented in Chapter 5, the potential to further enhance the cooling capacity of the most promising NR formulation identified in Chapter 4 was investigated. Since in the literature the incorporation of nanoclays was shown to significantly improve the SIC behaviour of NR, the effect of adding nanoclays, both natural (MMT) and organomodified (O-MMT), on the elastocaloric performance of NR was systematically evaluated. The results evidenced that filler-rubber compatibility played a crucial role in the cooling performance. Indeed, the better dispersion of the organo-modified nanoclays within the NR matrix promoted not only a better mechanical behaviour (in terms of stiffness and strength), but also a significantly enhanced cooling performance with respect to MMT nanofilled systems. In particular, organoclay-filled NR nanocomposites demonstrated up to a ~45% increase in the heat extracted per refrigeration cycle with respect to unfilled NR when deformed at 400% strain. More specifically, the heat absorbed from the environment increased from 11 J/cm$^3$ (in the case of unfilled NR) to 16 J/cm$^3$ (with an O-MMT amount of 5 phr). This improvement was ascribed to a synergistic combination of enhanced strain-induced crystallization confirmed by XRD analysis, improved macromolecular structural homogeneity, and potential strain amplification effects promoted by the organoclays. In contrast, the incorporation of natural MMT yielded only marginal improvements in the elastocaloric properties, primarily due to poor dispersion and limited nanofiller-matrix interaction. Despite the better cooling capacity of NR/O-MMT samples, the $COP_{mat}$ was found to be comparable in the two series of nanocomposites and ranged between 2 and 3. This was due to the greater work of deformation found in O-MMT nanocomposites, ascribed to their higher stiffness. The elastocaloric properties of O-MMT nanocomposites were also studied under cyclic conditions and found to be stable up to 40 loading and unloading cycles. This demonstrated that the addition of nanoclay did not affect the stability of the elastocaloric capability of the prepared nanocomposites.

In conclusion, this work demonstrated that the rubber network structure and the rubber formulation represent the starting point for future research aimed at maximizing the cooling performance of NR-based systems, given their strong influence on the elastocaloric behaviour.

## *6.2 Future Developments*

At the end of this PhD work, it is worthwhile to provide some recommendations for future research directions in this field.

In light of the results obtained, it would be of great interest to evaluate the effect of adding other nanofillers, such as Carbon Nanotubes (CNTs), graphene, hexagonal boron nitride (h-BN), etc., on the elastocaloric performance of NR-based systems. Such studies could clarify whether, in addition to filler–matrix compatibility, the shape of the nanofillers also influences SIC and thermoelasticity. Another aspect to explore could concern the dispersion and orientation of these fillers within the NR matrix, and the impact these factors could have on the ability of NR to crystallize under strain.

A fundamental aspect that remains largely unexplored is fatigue resistance of elastocaloric polymers. This aspect, which was not addressed in the present work and is rarely discussed in the literature on elastocaloric elastomers, is essential for practical applications. In a solid-state cooling device, the material must withstand thousands of loading–unloading cycles. Therefore, even before ensuring high elastocaloric performance, the material must exhibit adequate fatigue resistance. Although natural rubber is known for its excellent fatigue properties, these are typically evaluated at strain amplitudes much lower than those used to study the elastocaloric effect. It is plausible to hypothesize that the large strain amplitudes employed in this work could significantly reduce the fatigue resistance of NR. Future research should therefore focus on quantifying this potential deterioration and identifying strategies to mitigate it. One possible

approach could be to operate with a pre-strained material (for example at 250% strain) and working at lower deformation amplitudes, for example between 250% and 450%.

In addition to fatigue resistance, it will also be necessary to evaluate the stability of the elastocaloric performance over a much larger number of cycles, since the 40 cycles tested in this work can only be considered a preliminary indication of cyclic stability.

Finally, the development of a cooling prototype will be a crucial step to demonstrate the effectiveness of NR-based systems in generating a real refrigeration cycle, enabling the evaluation of their long-term stability, cooling capacity, energy efficiency, and operational reliability. The main challenges in designing the prototype will be to ensure separation between the two functional regions of the system, i.e., the zone in which the elastocaloric materials are mechanically deformed and heat up, and the zone in which they cool down, and to select an appropriate mechanical system capable of delivering the required deformation to the elastocaloric material. Additionally, robust safety mechanisms must be integrated to guarantee automatic shutdown in the event of malfunction or hazardous operating conditions. Minimising environmental impact through careful material selection will constitute a key priority, complemented by the adoption of a design-for-disassembly approach that enables complete dismantling at the end of the system's service life. Economic considerations will also play a critical role, as the total cost of the prototype must remain competitive with that of conventional air-conditioning systems of comparable capacity. Successfully addressing these challenges will be crucial for advancing NR-based technologies from laboratory research to practical solid-state refrigeration applications.

As a step toward practical implementation, an initial attempt was made at the end of this PhD work to develop a laboratory-scale prototype of a NR-based elastocaloric cooling system. However, due

to its preliminary nature, this activity was not included in the thesis. The principle of the prototype is schematized in Figure 6.1, while a more detailed design of the 3D-printed prototype is shown in Figure 6.2 The device consists of a wheel and an eccentrically positioned hub, which is free to rotate and does not come into direct contact with the wheel [156]. Rubber bands connect the hub to the wheel.

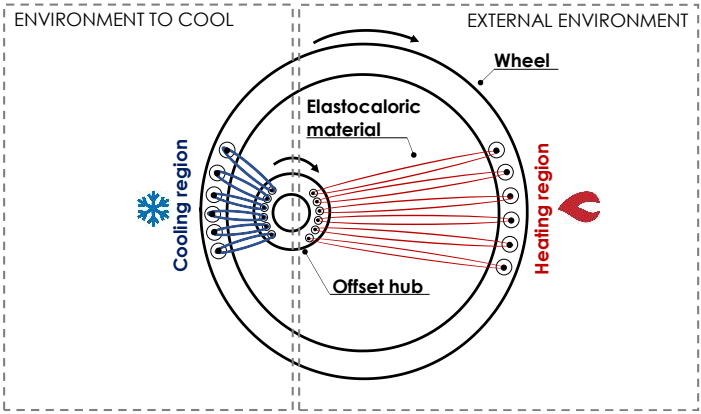


*Figure 6.1. Scheme of the developed prototype.*

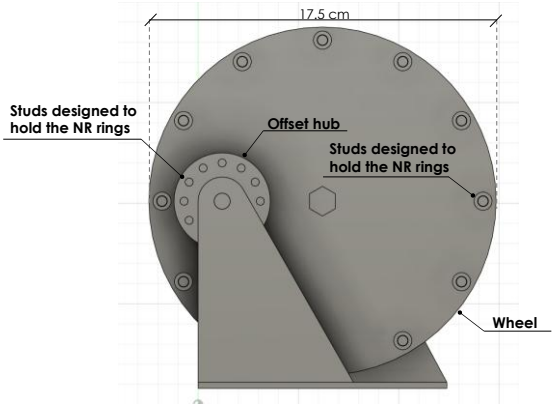


(A)

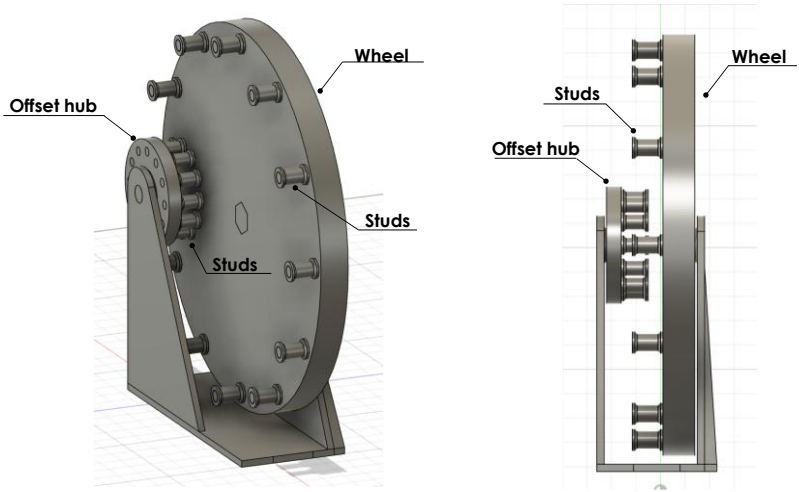


*Figure 6.2(A-C). 3D printed prototype of the NR-based elastocaloric cooling system. (A) Frontal view, (B) diagonal view and (C) lateral view.*

When the wheel rotates around the hub, the offset between the hub and the wheel centre causes a nonuniform deformation of the rubber bands: approximately half of the bands are stretched, while the remaining bands experience reduced stretching or are in the undeformed state. While the wheel rotates, the contracting rubber bands exert a tangential force on the hub, generating a torque that induces its rotation. As a result, the rubber bands continuously cycle between stretched and undeformed states as the wheel rotates. In the region where the rubber bands are stretched, the material heats up. Conversely, in the region where the bands contract and return to the undeformed state, the material cools down. By spatially separating these two regions, i.e., placing the heating region in contact with the external environment and the cooling region in contact with the environment to cool, a solid-state cooling prototype could be

developed. The challenging aspect, which will require more attention, would be the separation of the two regions.

Preliminary tests were conducted using rubber rings with a thickness of 0.8 mm connected to the stubs of the wheel and the hub. The prototype was designed to impose a maximum deformation of the rubber rings of 400%. Infrared thermal images of the prototype during operation are reported in Figure 6.3. As the wheel rotates, it is evident that approximately half of the rubber rings undergo stretching and heat up, while the remaining rubber rings return to the undeformed state and cool down.

This preliminary prototype will require further development and optimization. Nevertheless, it may serve as a useful starting point for future investigations.

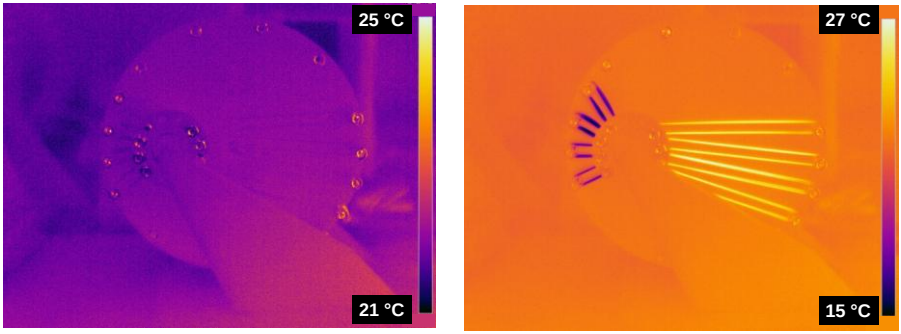


(A) (B)

*Figure 6.3(A,B). Infrared thermal images of the prototype at rest and during operation. (A) Prototype at rest, with rubber bands in thermal equilibrium with the environment. (B) Prototype during operation: half of the rubber bands stretch and heat up while the other half return to the undeformed state and cool down.*

# 7 Side activities

During the PhD, complementary research activities were carried out to broaden expertise in the field of materials engineering. These activities included:

- The production and investigation of the microstructural, thermomechanical and shape memory properties of biodegradable blends based on poly(lactic acid) (PLA) and poly(butylene adipate terephthalate) (PBAT). This activity began during the research fellow and proceeded during the first year of the PhD.
- Contribution to the thermo-mechanical characterization of a biocompatible scaffold, in the framework of a collaboration with the University of Palermo (UniPa). The scaffold, consisting of an electrospun PLLA network combined with a polyamidoamine hydrogel (AGMA1), was developed at UniPa for applications in peripheral nerve regeneration.
- Participation in the PRIN 2022 “Towards a new generation of eco-sustainable multifunctional textiles (GENTEXT)” project, which involved contributions to the development and thermo-mechanical characterization of multifunctional compounds based on polylactic acid (PLA), polybutylene succinate (PBS), and poli-β-idrossibutirrato (PHB), aimed at potential applications in the textile industry.

The following section will present the main side activity, namely the production and characterization of PLA/PBAT blends. Given their complementary characteristics and overlapping application fields, blending stiff PLA with flexible PBAT represents a valuable technical approach for developing eco-sustainable packaging with tuneable properties. Nevertheless, limited information is available on the thermo-mechanical properties of these blends, particularly regarding the effect of PBAT addition on the shape-memory

behaviour of PLA. The present work therefore has concerned the production and investigation of the microstructural, thermo-mechanical, and shape-memory properties of PLA/PBAT blends prepared by melt compounding.

## *7.1 Evaluation of the Physical and Shape Memory Properties of Fully Biodegradable Poly (lactic acid) (PLA)/Poly (butylene adipate terephthalate) (PBAT) Blends*

***Part of this chapter has been published in:***

M. Bianchi, A. Dorigato, M. Morreale and A. Pegoretti

**"Evaluation of the Physical and Shape Memory Properties of Fully Biodegradable Poly(lactic acid) (PLA)/Poly(butylene adipate terephthalate) (PBAT) Blends"**

*Polymers 2023, 15(4), 881*

*https://doi.org/10.3390/polym15040881*

### 7.1.1 Introduction

In recent years, the increasing difficulties of plastic disposal have raised concerns worldwide. Most of the plastic waste ends up in landfills, oceans, soil and water, representing thus serious hazards for plants, animals and humans. According to recent statistics, every year up to 12.7 million tons of plastic enter the oceans, causing the death of several seabirds and aquatic animals. The severity of this problem will exponentially increase with the increase in global non-biodegradable plastic consumption [157-159]. Plastic waste is estimated to triple by 2060, as claimed by the latest forecast by the Organisation for Economic Co-operation and Development (OECD) Global Plastic Outlook, rising from 353 million tons of waste in 2019 to 1014 million tons in the next decades [160]. Therefore, measures and solutions must be taken to avoid irreversible consequences on ecosystems and human beings.

Biodegradable polymers (BPs) have attracted significant scientific and industrial interest as promising candidates for addressing these challenges [157]. Polylactic acid (PLA) in particular has gained attention due to its origin from renewable sources, its good mechanical performance, ease processability, commercial availability, and relatively low environmental footprint [161-164]. PLA is currently used in several disposable packaging applications and further distinguished by its thermo-responsive shape memory behaviour, which renders it attractive for advanced uses such as active and intelligent packaging [163,164]. Nonetheless, the intrinsic brittleness and limited toughness of PLA restrict its applicability in demanding sectors.

One possible solution to enhance the performance of PLA while maintaining biodegradability is through blending with other polymers possessing complementary characteristics. Poly(butylene adipate-co-terephthalate) (PBAT) is a fully biodegradable aliphatic–aromatic copolyester characterized by high flexibility, elasticity, and thermal stability [165,166]. However, its stiffness and strength are rather poor. Owing to the complementary nature of PLA and PBAT, blending these two polymers is a promising strategy to obtain eco-sustainable materials with tuneable thermo-mechanical and functional properties. Previous investigations have demonstrated that the incorporation of PBAT into PLA matrices can significantly improve elongation at break, impact resistance, and melt processability, while maintaining an acceptable modulus and tensile strength [167-170]. However, the literature still lacks systematic studies focusing on the thermo-mechanical properties of PLA/PBAT blends, and no investigations have reported on the influence of PBAT addition on the shape memory behaviour of PLA.

This work aims to investigate the thermo-mechanical and shape memory properties of fully biodegradable PLA/PBAT blends produced by melt compounding and hot pressing. Particular emphasis has been placed on the role of blend composition in determining

processability and functional performance. The outcomes of this study are expected to provide novel insights into the development of eco-friendly polymeric systems for advanced packaging applications, combining biodegradability with intelligent material functionalities.

### 7.1.2 Experimental Part

#### *7.1.2.1 Materials*

The PLA used in this work was an Ingeo™ 2500HP supplied by NatureWorks® LLC (Minnetonka, MN, USA) in pellets form. According to the producer's technical datasheet, it was characterized by a specific gravity of 1.24 g/cm$^3$, a melt flow index (MFI) of 8 g/10 min (210 °C, 2.16 kg) and a melting temperature of 165-180 °C. Polymer granules of PBAT Technipol® Bio 1160 were purchased from Sipol Spa (Mortara, PV). According to the supplier datasheet, its specific gravity was 1.23 g/cm$^3$, the MFI was 20 g/10 min (160 °C, 2.16 kg) and the melting temperature was about 115 °C.

#### *7.1.2.2 Sample Preparation*

PLA/PBAT blends at different relative ratios were prepared by melt compounding in an internal mixer (Thermo Haake® Rheomix 600), equipped with counter-rotating rotors. The compounding temperature was kept at 180 °C while the mixing time was 10 minutes. The rotor speed was set at 60 rpm. Prior to processing, PLA and PBAT pellets were dried at 50 °C overnight to remove moisture. After compounding, the blends were hot-pressed in a hydraulic press for 10 minutes at a pressure of 7 bar and a temperature of 180 °C, followed by water cooling. The processing temperature was selected after preliminary trials, and viscosimetric measurements on both virgin and processed samples (not reported for the sake of brevity) demonstrated that the molecular weight of the constituents was retained after melt compounding and hot-pressing operations. In this way, square sheets with in-plane dimensions of 150x150 mm$^2$ and a thickness of 1 mm were prepared. The composition (in wt% and vv%) of the prepared samples along with their codes is reported in Table 7.1. The final

number in the code refers to the PBAT weight concentration in the blend.

*Table 7.1. List of the prepared samples and their nominal composition.*

| Sample | PLA content (wt%/vv%) | PBAT content (wt%/vv%) |
|---|---|---|
| PLA | 100.0/100.0 | - |
| PLA_PBAT_15 | 85.0/84.9 | 15.0/15.1 |
| PLA_PBAT_30 | 70.0/69.8 | 30.0/30.2 |
| PLA_PBAT_45 | 55.0/54.8 | 45.0/45.2 |
| PLA_PBAT_60 | 40.0/39.8 | 60.0/60.2 |
| PLA_PBAT_75 | 25.0/24.8 | 75.0/75.2 |
| PBAT | - | 100.0/100.0 |

### *7.1.2.3 Experimental techniques*

*Rheological analysis*

In order to investigate the effect of the blend composition on the viscosity at the molten state, dynamic rheological tests were carried out through a DHR-2 rheometer (TA In-strument, New Castle, DE, USA) by using a plate-plate configuration and setting a gap distance of 1 mm. Disc samples (diameter 25 mm, thickness 1 mm) were selected for the measurements. The tests were conducted at 180 °C in frequency sweep mode, applying a maximum shear strain of 1%. In this way, the trends of the complex viscosity (η*), storage modulus (G') and loss modulus (G'') were evaluated in an angular frequency range 0.1–1000 rad/s. One specimen was tested for each formulation.

*Microstructural characterization*

In order to investigate the dispersion of the two constituents in the blends, optical microscope micrographs were acquired on polished

samples, by using an upright incident-light optical CH-9435 Heerbrugg microscope.

The interfacial adhesion between the PLA and PBAT phases was investigated by means of a field emission scanning electron microscope (FESEM) AG-SUPRA 40 (Carl Zeiss, Ober-Kochen, Germany), operating at an accelerating voltage of 2.5 kV. The samples were soaked in liquid nitrogen for 1 h and then cryofractured. The fracture surface was analysed after Pd/Pt sputtering to provide enhanced electrical conductivity.

*Thermal characterization*

Thermogravimetric analysis (TGA) was performed in order to investigate the degradation resistance of the produced blends, by using a Mettler TG50 thermo-balance (Mettler-Toledo GmbH, Schwerzenbach, Switzerland). Samples with a mass of 20 mg were tested at a heating rate of 10 °C/min from 25 °C up to 700 °C under a nitrogen flow of 10 mL/min. One specimen for each composition was tested. The temperature associated with a mass loss of 5% ($T_{5\%}$) and the residual mass at 700 °C ($m_{700}$) were evaluated. In addition, from the first derivative of the thermogravimetric curve (DTG), the temperatures corresponding to the maximum mass loss rate of PLA ($T_{peak1}$) and PBAT ($T_{peak2}$) were determined.

Differential scanning calorimetry (DSC) tests were performed on the prepared blends by means of a Mettler DSC30 calorimeter (Mettler Toledo GmbH, Schwerzenbach, Switzerland). Specimens with a mass of 10 mg were subjected to the following thermal ramps: (I) first heating scan from -80 °C to 200 °C at 10 °C/min, (II) cooling scan from 200 °C to -80 °C at 10 °C/min, (III) final heating scan from -80 °C to 200 °C at 10 °C/min. One specimen was tested for each composition. Nitrogen was used as the purge gas at a flow of 100 mL/min. DSC analysis allowed the determination of the glass transition temperature ($T_g$), the melting and cold crystallization

temperatures ($T_m$, $T_{cc}$) and specific enthalpy values ($\Delta H_m$, $\Delta H_{cc}$) of the blend constituents. Moreover, the PLA and PBAT crystallinity degree ($\chi_c$) was calculated according to Equation (7.1):

$$\chi_c\,(\%) = 100 \cdot \frac{\Delta H_m - \Delta H_{cc}}{\Delta H_m^0 \cdot w} \qquad (7.7.1)$$

where $\Delta H_{cc}$ is the cold crystallization enthalpy, $\Delta H_m^0$ is the theoretical melting enthalpy of fully crystalline polymer and $w$ is the weight fraction of the polymer phase in the blend. $\Delta H_m^0$ was taken as 93 J/g for fully crystalline PLA and 114 J/g for fully crystalline PBAT [168,171].

*Mechanical characterization*

Dynamic-mechanical analysis was carried out through a DMA Q800 (TA instrument, New Castle, USA) machine, to investigate the dependence of the storage modulus (E') and loss modulus (E'') of the produced blends on temperature. The tests were performed on rectangular specimens (gauge length 10 mm, width 5 mm, thickness 1 mm) at a frequency of 1 Hz, with a strain amplitude of 0.05 %, and with a heating ramp from 25 °C to 130 °C at 3 °C/min. One specimen was tested for each composition. In this way, the values of the storage modulus at 25 °C ($E'_{25}$) and at 85 °C ($E'_{85}$) were determined to evaluate the storage modulus drop below and above the glass transition temperature of PLA. One specimen was tested for each composition.

Tensile properties under quasi-static conditions were measured by means of an Instron 5969 (Instron Corporation, Norwood, MA, US) tensile testing machine, equipped with a load cell of 10 kN and operating at a crosshead speed of 5 mm/min. The tests were performed on ISO 527 type 1BA specimens at 25 °C. The elastic modulus (E) was measured as a secant value between two strain levels (0.1 and 0.2 mm/mm) in the linear stress-strain region. Moreover, the

tensile stress at break ($\sigma_b$) and the strain at break ($\varepsilon_b$) were determined. Five specimens were tested for each composition.

*Evaluation of the shape memory behaviour*

The investigation of the shape memory behaviour of the prepared PLA/PBAT blends was performed on prismatic rectangular specimens (width 5 mm, thickness 1 mm, length 20 mm) by means of a DMA Q800 (TA instrument, New Castle, USA) apparatus, operating in single cantilever mode. Since at 25 °C and 85 °C the PLA phase in the blends is respectively in the glassy and in the rubbery state, these temperatures were selected for exploring the shape memory performance of the samples. The tests were carried out according to the thermo-mechanical cycle typically employed for shape memory polymers (SMPs) [172], consisting of a programming step, followed by a recovery step. More specifically, the specimens were subjected to the following thermo-mechanical history: (I) heating of the specimen and equilibrium at 85 °C, (II) application of a ramp force of 1 N/min, (III) drive-off of the motor when a displacement ($d_{imp}$) of 8000 µm was achieved, (IV) cooling and equilibrium of the sample at 25 °C, (VII) isothermal step for 5 minutes, (V) drive-on of the motor and application of a constant load equal to 0.001 N to monitor continuously the sample displacement as a function of the temperature, (VII) equilibrium at 85 °C, (VIII) isothermal for 30 minutes at 85 °C. One specimen was tested for each composition. The graphical representation and the schematization of the thermo-mechanical cycle is illustrated in Figure 7.1(A,B). In Figure 7.1B, $d_{imp}$ is the programmed displacement at step (III), $d_{fix}$ is the effectively fixed displacement at step (V) and $d_{30}$ is the displacement reached by the movable clamp at the end of the recovery process at step (VIII).

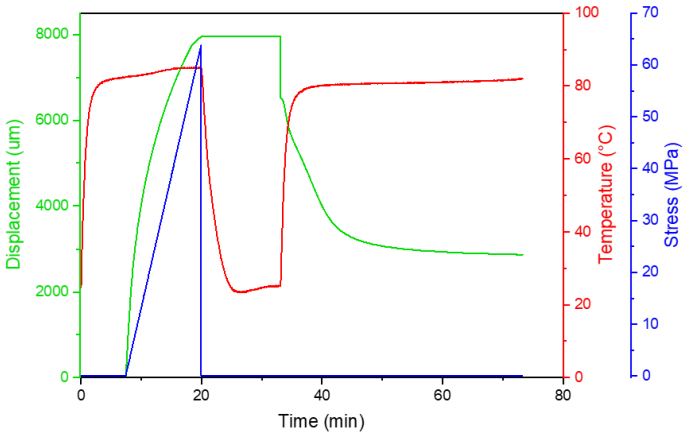


(A)

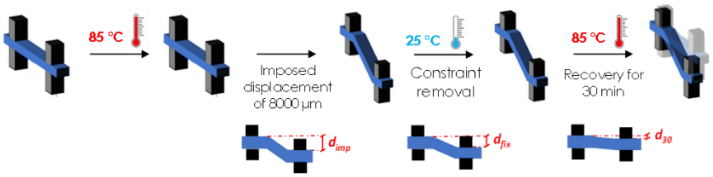


(B)

*Figure 7.1. (A) Graphical representation and (B) schematization of the thermo-mechanical cycle adopted to investigate the shape memory behaviour of the PLA/PBAT blends.*

The strain fixity (SF) and strain recovery (SR) parameters were then determined, in order to describe the shape memory performance of the PLA/PBAT blends. For each specimen, the SF and SR were respectively calculated according to Equation (7.2) and (7.3):

$$SF(\%) = \frac{d_{fix}}{d_{imp}} . 100 \qquad (7.2)$$

$$SR(\%) = \frac{d_{imp} - d_{30}}{d_{imp}} . 100 \qquad (7.3)$$

### 7.1.3 Results and discussion

*Rheological analysis*

Dynamic rheological tests were carried out to investigate the effect of the blend composition on the rheological properties at the processing temperature (180 °C), in order to obtain information about the processability of these materials. Figure 7.2(A-C) shows the results of the dynamic rheological tests performed on neat PLA, neat PBAT and all the prepared blends in terms of dynamic moduli (G', G") and complex viscosity (η*).

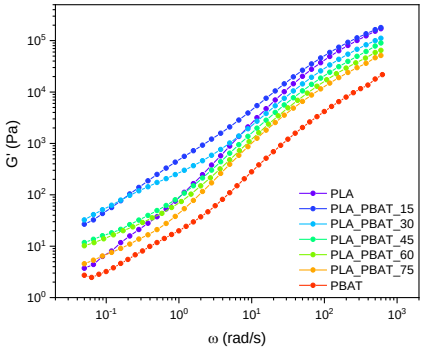


(A)

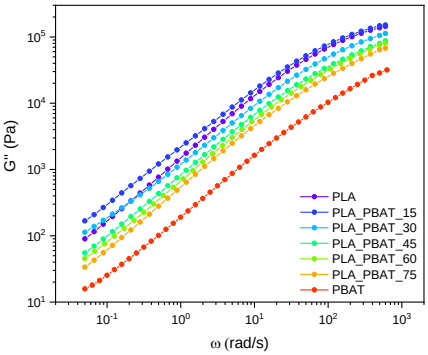


(B)

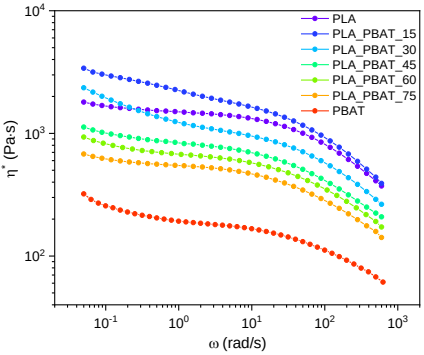


(C)

*Figure 7.2. Results of the dynamic rheological tests at 180 °C on the neat matrices and on the prepared blends. Trends of (A) storage modulus, (B) loss modulus, (C) complex viscosity as a function of the angular frequency.*

Figure 7.2(A-C) shows, respectively, the storage and loss modulus of the PLA/PBAT blends as a function of the frequency. All the samples exhibit a similar trend of the G' in the high-frequency range, while differences can be seen at lower frequencies. The G' of all blends in the low-frequency range was higher than that of neat PLA and neat PBAT, suggesting that the two polymers are probably immiscible [173]. Furthermore, significant differences in the slopes of the curves appear at low frequencies, i.e., with the appearance of a shoulder in the PLA_PBAT_15 blend. This behaviour is very likely to be due to a droplet/matrix morphology [174-177] and it substantially disappears at higher compositions. This could be attributed to the formation of more complex morphologies showing slow relaxation dynamics [175-177] and will be further investigated and discussed in the following morphological characterization section.

Comparing the loss and the storage modulus values, it can be observed that the G'' is greater than the G'. This, combined with their overall trends, suggests that a liquid-like rheological behaviour prevails over a solid-like one for all of the investigated blends.

Furthermore, the frequency dependence of the G'' is almost the same for all the samples in the entire frequency range. Finally, when increasing the PBAT content in the blends, both the G' and G'' decrease.

The complex viscosity of the neat PLA and PBAT (Figure 7.2C) is similar to the values reported in the literature, highlighting the negligible thermal degradation these materials undergo during the production process [178]. On a general level, all the samples exhibited a shear thinning behaviour, more pronounced in the high-frequency range. The η * of PLA is approximately one order of magnitude higher than that of PBAT, as shown in Figure 7.2C. Therefore, this suggests that it is much easier for PBAT to disperse within the PLA matrix, once processed at the molten state. With the increasing PBAT concentration, the complex viscosity of the blends decreases, except for that of PLA_PBAT_15 and PLA_PBAT_30 in the low-frequency regime, attributable to yield stress, likely to be due to resistance to the flow of the PBAT domains in the PLA matrix.

*Microstructural characterization*

The optical microscope images of the prepared blends are shown in Figure 7.3(A-E).

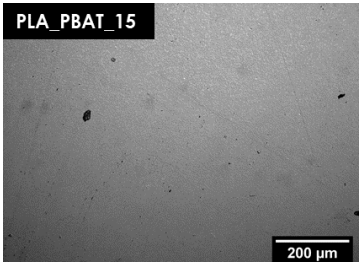


(A)

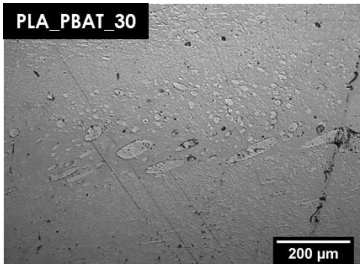


(B)

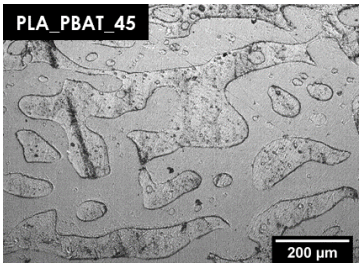


(C)

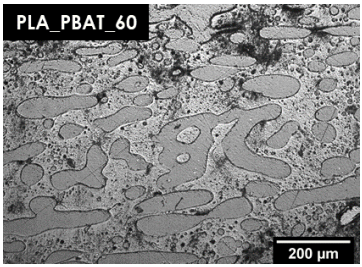


(D)

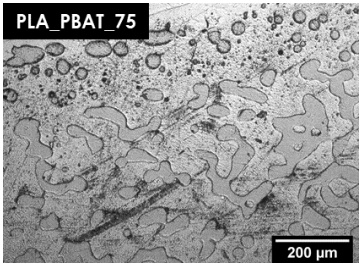


(E)

*Figure 7.3. Optical microscope images of the prepared PLA/PBAT blends. (A) PLA_PBAT_15, (B) PLA_PBAT_30, (C) PLA_PBAT_45, (D) PLA_PBAT_60, (E) PLA_PBAT_75.*

The bright field micrographs shown in Figure 7.3(A-E) provide interesting information about the microstructural features of the produced PLA/PBAT blends. Firstly, it is possible to notice that PLA and PBAT are immiscible since all the analysed compositions show an evident phase separation, which is consistent with the observation reported in other studies on these systems [167,179]. Secondly, depending on the PLA/PBAT ratio, the two phases exhibit either a sea-island morphology (Figure 7.3(A,B,E), i.e., a discrete domain (regularly or irregularly shaped) embedded in the surrounding matrix, or an almost co-continuous structure (Figure 7.3(C,D)), i.e., large interconnected domains with irregular shapes. Focusing at first on blends with low PBAT contents, PLA_PBAT_15 (Figure 7.3A)

presents a fine structure with small and spherical PBAT domains evenly dispersed in the PLA matrix. After a statistical analysis of the domain size distribution, it is possible to conclude that the size of PBAT domains increases with the PBAT concentration, from 3.6 ± 0.7 μm for the PLA_PBAT_15 blend up to 11.9 ± 8.9 μm for the PLA_PBAT_30 sample. Moreover, in the PLA_PBAT_30 blend (Figure 7.3B), there is the coexistence of small and large PBAT droplets, with either spherical or irregularly elongated shapes. The formation of these small PBAT domains in the PLA matrix could be responsible for the high complex viscosity values evidenced in the low-frequency range in the PLA_PBAT_15 and PLA_PBAT_30 samples (see Figure 7.2C). The dispersed PBAT phase probably hindered the mobility of the PLA chains, inducing a viscosity increase. A significant change in morphology is observable in the PLA_PBAT_45 blend (Figure 7.3C). This sample exhibits an almost co-continuous morphology, with a 3D network of large and elongated PBAT domains in the PLA matrix. Moreover, it is interesting to observe that small PLA droplets are immersed in some PBAT domains. This experimental evidence suggests that PLA/PBAT is a polymer blend characterized by high viscosity, since double-emulsion structures are generally present in blends with this feature [180]. As it can be seen in Figure 7.3D, PLA_PBAT_60 also presents a co-continuous morphology. However, differently to PLA_PBAT_45, PBAT is the primary constituent in this case, highlighting that in the PBAT concentration interval between 45 wt% and 60 wt%, the phase inversion occurred. Future works will aim at identifying the exact composition associated to this inversion. By a more detailed analysis of the blend containing 60 wt% of PBAT, it is possible to observe that PLA domain size and shape are broadly distributed, since small PLA droplets are present in the PBAT matrix together with the coarser domains. Finally, by further increasing the PBAT content in the blends up to 75 wt% (Figure 7.3E), the size of the PLA domains, as well as the statistical dispersion of their size distribution, decreases. Their elongated shape probably derives from the coalescence of

smaller domains. In conclusion, it is interesting to point out that, on a general level, when PBAT is in the dispersed phase of the blend, its domains are smaller than those formed by PLA when PBAT is the primary constituent. In fact, as it has been evidenced by rheological measurements, PBAT presents a significantly lower viscosity, which favours its breakup in the PLA matrix.

SEM observations were also performed on these blends in order to obtain further information about the interfacial adhesion conditions. The micrographs of the cryofracture surface of the prepared blends are presented in Figure 7.4(A-G).

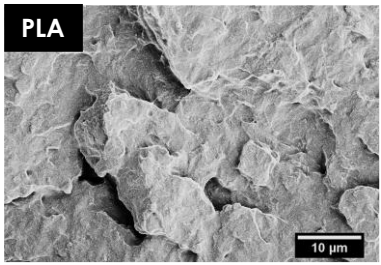


(A)

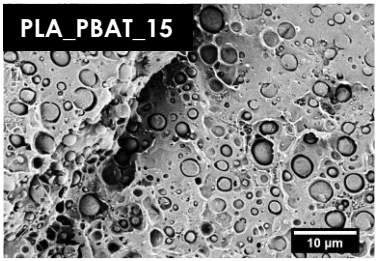


(B)

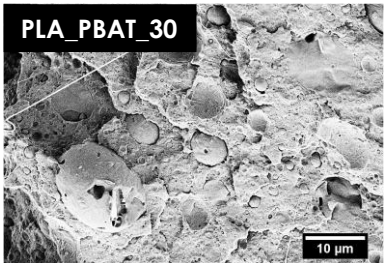


(C)

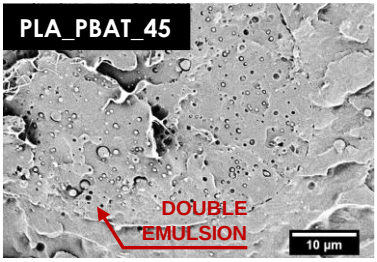


(D)

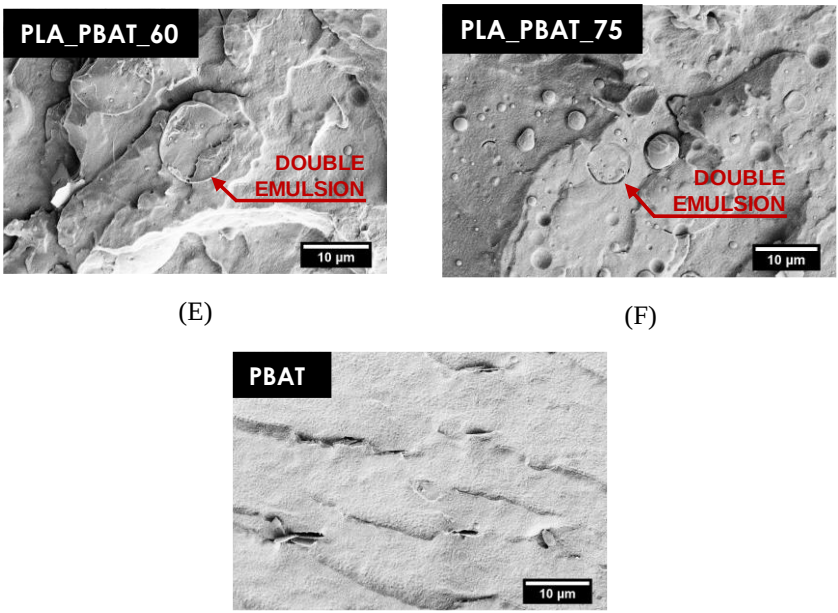


*Figure 7.4. SEM micrographs of the cryofracture surface of neat PLA, neat PBAT and the prepared blends: (A) PLA, (B) PLA_PBAT_15, (C) PLA_PBAT_30, (D) PLA_PBAT_45, (E) PLA_PBAT_60, (F) PLA_PBAT_75, (G) PBAT.*

Neat PLA and PBAT (Figure 7.4(A,G)) present a different cryofracture surface appearance, which helps in identifying the two components in the blends (Figure 7.4(B–F)). In particular, the cryofracture surface of PLA appears rough (Figure 7.4A), while that of PBAT is smoother (Figure 7.4G). The micrographs of the blends reported in Figure 7.4(B–F) show that the interfacial adhesion between PLA and PBAT is rather poor, since voids are clearly visible at the interface. The neat separation between the two phases and the presence of detachment phenomena, mostly visible in the PLA_PBAT_15 and PLA_PBAT_45 samples (Figure 7.4(B, D)), are

evidence of the immiscibility and the poor compatibility of these two polymers. In future works, the interfacial adhesion needs to be improved by using suitable compatibilizers. The SEM images reveal the presence of very small domains in the order of 1–5 μm (of PLA in the PLA_PBAT_15 and PLA_PBAT_30 samples, and of PBAT in the PLA_PBAT_60 and PLA_PBAT_75 samples) dispersed in the major phase, which has not been possible to observe in the optical micrographs. This confirms the broad domain size distribution already detected in Figure 7.3(A,B) and Figure 7.4(D,E). Furthermore, as indicated by the red arrows in Figure 7.4(D–G), double-emulsion structures can be detected at this magnification level.

*Thermal characterization*

Thermogravimetric tests were performed in order to investigate the thermal degradation behaviour of the prepared blends and to explore the influence of blend composition on their degradation resistance. The thermogravimetric curves of the prepared samples along with the corresponding derivative curves are presented in Figure 7.5(A,B), while the most significant results are reported in Table 7.2.

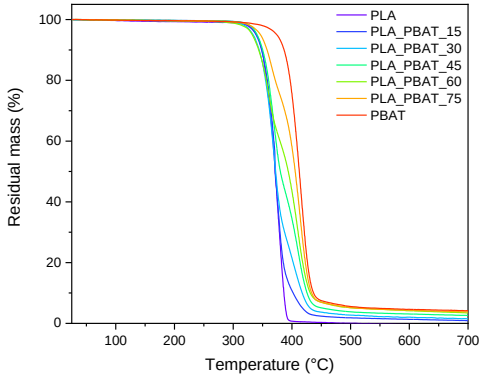


(A)

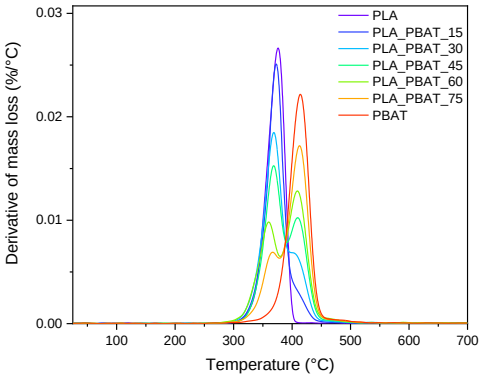


(B)

*Figure 7.5. TGA tests on neat PLA, neat PBAT and their blends. Trends of (A) residual mass and (B) mass loss derivative as a function of temperature.*

*Table 7.2. Results of the TGA tests on neat PLA, neat PBAT and their blends.*

| Sample | $T_{5\%}$ (°C) | $T_{peak1}$ (°C) | $T_{peak2}$ (°C) | $m_{700}$ (%) |
|---|---|---|---|---|
| **PLA** | 339.7 | 376.1 | - | 0.0 |
| **PLA_PBAT_15** | 341.2 | 372.6 | - | 0.9 |
| **PLA_PBAT_30** | 341.8 | 368.8 | 406.0 | 1.5 |
| **PLA_PBAT_45** | 343.7 | 368.5 | 409.9 | 2.6 |
| **PLA_PBAT_60** | 345.3 | 360.0 | 409.4 | 3.4 |
| **PLA_PBAT_75** | 346.5 | 366.4 | 412.6 | 3.8 |
| **PBAT** | 374.3 | - | 414.4 | 4.2 |

As it is possible to observe from Figure 7.5(A,B), the thermal degradation of neat polymers occurs in one single step. PLA and PBAT start degrading at temperatures close to 340 °C and 370 °C, respectively, and show maximum degradation rates at 376 and 414 °C, as reported in Table 7.2. The higher degradation resistance of PBAT is probably attributable to the presence of benzene rings in its molecular structure [181]. A plateau in the TGA curves above 400 °C

for PLA and above 450 °C for PBAT can be noticed, highlighting that no significant mass loss in the nitrogen atmosphere occurs at higher temperatures. As for the residue at 700 °C ($m_{700}$), PLA completely degrades without leaving any solid residue, while PBAT presents an $m_{700}$ value of 4.2%. This indicates that partial coking and carbonization occurs for PBAT. Consequently, it is possible to observe that the residual mass increases proportionally to the PBAT amount in the samples.

The decomposition process of all the PLA/PBAT blends takes place in two different steps, associated with the thermal degradation of the PLA and PBAT phases. This is further evidence of the immiscibility of these polymers. With the increasing PBAT concentration, the thermal stability of the blends slightly increases. Indeed, as it can be seen from Table 7.2, the temperature corresponding to a 5% weight loss ($T_{5\%}$) shifts to higher temperatures, moving from the PLA_PBAT_15 to PLA_PBAT_75 sample.

In order to investigate the thermal properties of the PLA/PBAT blends, DSC analysis has been carried out. The DSC thermograms collected in the first and second heating scans of the neat PLA, neat PBAT and PLA/PBAT blends are shown in Figure 7.6(A,B), while the most significant results are reported in Table 7.3. The DSC tests collected in the cooling scan did not provide noteworthy results and were therefore not reported for the sake of brevity.

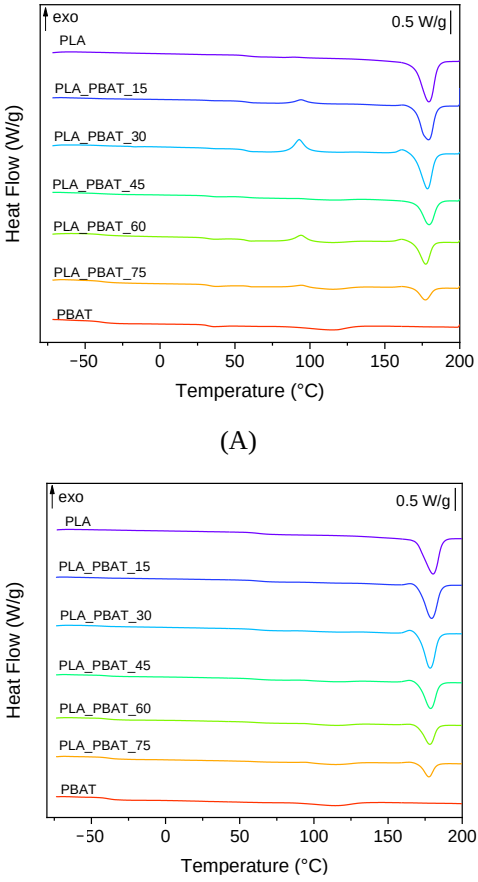


*Figure 7.6. DSC thermograms of neat PLA, neat PBAT and PLA/PBAT blends. (A) First heating scan, (B) second heating scan.*

*Table 7.3. Results of the DSC tests on neat PLA, neat PBAT and PLA/PBAT blends (first and second heating scan).*

| Sample | $T_{gPBAT}$ (°C) | $T_{gPLA}$ (°C) | $T_{ccPLA}$ (°C) | $\Delta H_{ccPLA}$ (J/g) | $T_{mPBAT}$ (°C) | $\Delta H_{mPBAT}$ (J/g) | $T_{mPLA}$ (°C) | $\Delta H_{mPLA}$ (J/g) | $\chi_{PLA}$ (%) | $\chi_{PBAT}$ (%) |
|---|---|---|---|---|---|---|---|---|---|---|
| 1st heating | | | | | | | | | | |
| PLA | - | 57.6 | - | | - | | 178.0 | 58.3 | 62.2 | - |
| PLA_PBAT_15 | | 58.9 | 93.3 | 20.3 | | | | 48.6 | 35.8 | |
| PLA_PBAT_30 | -36.9 | 56.5 | 93.0 | 15.2 | | | 177.1 | 39.8 | 37.7 | |
| PLA_PBAT_45 | -39.1 | 57.3 | - | - | 114.1 | 2.7 | 178.5 | 32.1 | 62.7 | 6.3 |
| PLA_PBAT_60 | -39.6 | 56.5 | 93.8 | 6.9 | 115.2 | 3.3 | 176.5 | 22.2 | 41.2 | 4.9 |
| PLA_PBAT_75 | -39.1 | 58.5 | 93.7 | 1.8 | 114.7 | 5.9 | 176.1 | 13.0 | 47.9 | 6.9 |
| PBAT | -39.7 | - | - | - | 113.7 | 11.9 | - | - | - | 10.4 |
| 2nd heating | | | | | | | | | | |
| PLA | - | 62.4 | - | - | - | - | 179.1 | 54.5 | 58.6 | - |
| PLA_PBAT_15 | -44.1 | 61.4 | - | - | | | 178.0 | 43.0 | 54.4 | |
| PLA_PBAT_30 | -41.9 | 61.2 | - | - | | | 177.3 | 38.6 | 59.3 | |
| PLA_PBAT_45 | -39.5 | 59.2 | - | - | 114.0 | 3.2 | 177.6 | 31.4 | 61.5 | 6.3 |
| PLA_PBAT_60 | -39.9 | 59.0 | - | - | 114.0 | 4.7 | 177.4 | 22.1 | 59.4 | 6.9 |
| PLA_PBAT_75 | -38.5 | 59.1 | - | - | 113.4 | 6.3 | 176.5 | 14.0 | 56.6 | 7.5 |
| PBAT | -39.0 | - | - | - | 114.2 | 11.2 | - | - | - | 9.8 |

By analysing the results, it is possible to observe that the DSC traces of neat PLA and PBAT present the typical profile of semicrystalline materials. In the first heating scan, the melting point of neat PLA is 178.0 °C, while the glass transition temperature is 57.6 °C. The crystallinity degree of neat PLA is very high (62.1%) and no cold crystallization peaks are observable, probably because the preliminary drying promoted the crystallization of the material. As it is possible to observe from Figure 7.6A, the endothermic peak of PLA is preceded by a small exothermic peak. According to the literature, this signal corresponds to the reorganization of the α'-crystal of PLA into α-crystals [182]. The α-phase is an ordered structure produced at a high crystallization temperature, while the α'-phase is a metastable disordered phase that develops at low temperatures. Above 150 °C, the α'-crystals become unstable and the phase transformation into α-crystals takes place. In regards to PBAT, it shows a $T_g$ at −39.7 °C and a weak and broad endothermic melting peak at 113.7 °C, indicating its low crystallization rate and limited crystallinity degree (10.4%).

Focusing on the first heating DSC scan of the PLA/PBAT blends, it is interesting to observe that the $T_m$ and $T_g$ values of the PLA and PBAT phases in the blends correspond to those detected for neat polymers, and are thus unaltered by the addition of another phase in the blends. This experimental evidence, together with the well-distinct melting phenomena of the two constituents, confirms that the PLA and PBAT phases are immiscible. In the PLA_PBAT_15 sample, the weak signals associated with the glass transition and melting of the PBAT phase do not permit the determination of the $T_g$ and $T_m$ for this polymer. In all the blends except for PLA_PBAT_45, an exothermic peak at a temperature close to 93 °C is noted, attributable to the cold-crystallization of PLA macromolecules, which, after the glass transition, acquire sufficient energy to rearrange and crystallize. The crystallinity degree of PLA is significantly reduced in the blends, especially in the PLA_PBAT_15 and

PLA_PBAT_30 samples. This suggests that the PLA crystallization process of PLA is hindered by the presence of a second phase in the blend. On the other hand, the peculiar morphology of the PLA_PBAT_45 blend, characterized by the presence of large PBAT domains, has probably favoured the crystallization of PLA. Indeed, the crystallization degree of this sample is 62.7%, comparable of that of neat PLA. The crystallization rate of PBAT is also impaired by the presence of PLA in the blends, since the $\chi_{PBAT}$ in the blends is lower than that of the neat PBAT.

In the second heating scan, the cold crystallization peak of PLA disappears. This confirms that water cooling after hot pressing partially hindered the crystallization of PLA within the blends. In comparison to the first heating stage, the crystallization degree of both PLA and PBAT is higher in almost all the samples, close to the values of the neat constituents. Finally, no significant differences in the $T_m$ and $T_g$ of PLA and PBAT determined by the first and second heating scan can be detected.

#### *7.1.3.1 Mechanical characterization*

This work, as explained above, aims to evaluate the shape memory performance of PLA/PBAT blends using the glass transition of PLA as the switching temperature. In order to identify the temperature range in which the shape memory behaviour of the prepared materials should be evaluated, a DMA analysis was carried out. The trends of the storage modulus and loss modulus as a function of temperature are presented in Figure 7.7(A, B), while the results of the DMA tests on the prepared samples are reported in Table 7.4.

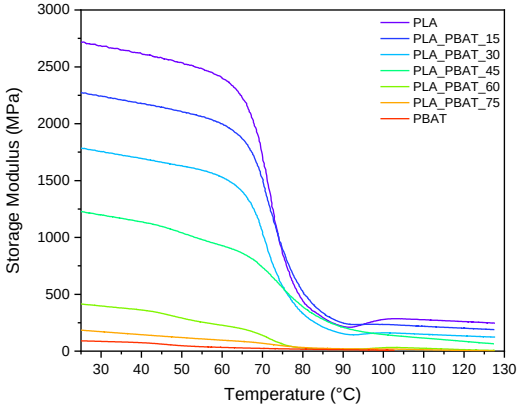


(A)

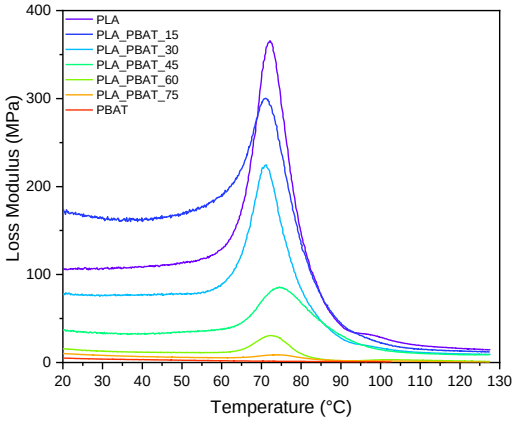


(B)

*Figure 7.7. Storage modulus (a) and loss modulus (b) from DMA on neat PLA, neat PBAT and PLA/PBAT blends.*

*Table 7.4. Results of the DMA tests on the prepared blends.*

| Sample | Storage modulus at 25 °C (MPa) | Storage modulus at 85 °C (MPa) |
|---|---|---|
| **PLA** | 2725.0 | 278.1 |
| **PLA_PBAT_15** | 2279.3 | 336.5 |
| **PLA_PBAT_30** | 1775.0 | 208.4 |
| **PLA_PBAT_45** | 1221.6 | 276.9 |
| **PLA_PBAT_60** | 420.2 | 19.5 |
| **PLA_PBAT_75** | 188.2 | 24.5 |
| **PBAT** | 87.9 | 15.3 |

As is visible from Figure 7.7(A,B), the glass transition temperature of PLA ranges between 55 °C and 85 °C. The intensity of the loss modulus peak, associated with this transition, progressively decreases and broadens with the increasing PBAT concentration in the blends, while the corresponding peak remains for all the samples close to a temperature of 70–80 °C. The storage modulus of the blends decreases significantly in the range of 65–80 °C and the drop becomes more pronounced with the increasing PLA content in the samples. Above 90 °C, the cold crystallization of PLA occurs and the modulus rises because of the presence of newly formed crystals. This is particularly evident for the PLA, PLA_PBAT_15, PLA_PBAT_30 and PLA_PBAT_60 samples. It is important to underline that the DSC thermograms of the neat PLA do not reveal any cold crystallization peaks. It can be hypothesized that the lower heating rate used and the orientation of the PLA macromolecules in the stress direction obtained in the DMA tests have probably promoted the cold crystallization of the neat PLA.

Since at 25 °C and at 85 °C the PLA phases in the blends are, respectively, in the glassy and rubbery states, these temperatures were selected for exploring the shape memory performance of the samples. More specifically, 85 °C was chosen as the temperature at which the

samples were deformed to the temporary shape. On the other hand, 25 °C was chosen as the temperature at which the deformed samples were cooled down to fix the temporary shape. To avoid any interference with the cold crystallization phenomenon of PLA, temperatures higher than 85 °C were not considered to explore the shape memory behaviour. The storage moduli of the samples at 25 °C and at 85 °C are reported in Table 7.4. By passing from 25 to 85 °C, all the blends experience a storage modulus drop of about one order of magnitude. However, it is possible to notice that the higher the PLA content in the sample, the higher the E' difference at the two considered temperatures. Since the greater the drop in the storage modulus, the better the shape memory performances of the material, higher shape memory effects are expected in blends with low PBAT contents.

Quasi-static tensile tests were carried out in order to investigate the influence of the PLA/PBAT relative ratio on the mechanical properties of the blends. The representative stress–strain curves of the neat PLA, neat PBAT and of PLA/PBAT blends are shown in Figure 7.8, while the main results are reported in Table 7.5.

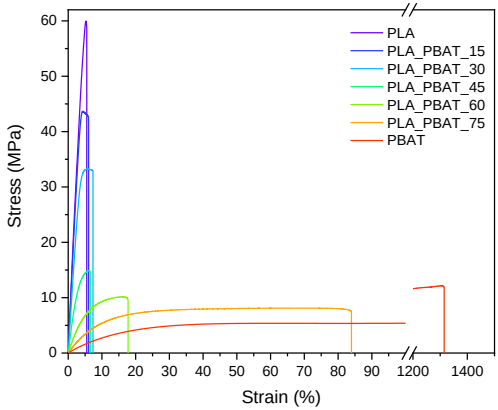


*Figure 7.8. Representative stress–strain curves from quasi-static tensile tests on neat PLA, neat PBAT and PLA/PBAT blends.*

*Table 7.5. Results of quasi-static tensile test at 25 °C on neat PLA, neat PBAT and PLA/PBAT blends.*

| Sample | E (MPa) | $\sigma_b$ (MPa) | $\varepsilon_b$ (mm/mm) |
|---|---|---|---|
| **PLA** | 4119.4 ± 673.3 | 59.2 ± 2.4 | 0.058 ± 0.007 |
| **PLA_PBAT_15** | 3030.9 ± 219.2 | 42.2 ± 0.7 | 0.060 ± 0.003 |
| **PLA_PBAT_30** | 2295.4 ± 66.2 | 32.3 ± 1.1 | 0.079 ± 0.013 |
| **PLA_PBAT_45** | 1694.3 ± 78.2 | 11.8 ± 3.4 | 0.055 ± 0.014 |
| **PLA_PBAT_60** | 221.9 ± 17.9 | 9.2 ± 0.3 | 0.203 ± 0.029 |
| **PLA_PBAT_75** | 87.7 ± 17.9 | 7.7 ± 0.6 | 0.838 ± 0.122 |
| **PBAT** | 87.7 ± 2.0 | 10.7 ± 1.2 | 12.378 ± 1.361 |

Neat PLA is characterized by an average tensile strength of 59.2 MPa, a Young's modulus of 4119.4 MPa and a strain at break of 5.8%. On the other hand, neat PBAT presents a much lower tensile strength (10.7 MPa) and elastic modulus (87.7 MPa), but a significantly greater strain at break (1237.8%). As it can be seen from Table 7.5, the addition of PBAT to PLA leads to a general decrease in stiffness and strength, while the elongation at break remains almost comparable to that of PLA up to a PBAT concentration of 45 wt%. This means that as long as PLA is the matrix constituent of the blend, negligible toughening effects can be obtained, probably due to the low interfacial adhesion between the two phases and the intrinsic, relative brittleness of PLA. The limited interfacial adhesion also explains the considerable $\sigma_b$ drop with limited PBAT contents. A significant increase in blend ductility is noticed for PBAT contents higher than 60 wt%, i.e., when phase inversion has occurred and PBAT becomes the major constituent. In particular, PLA_PBAT_60 and PLA_PBAT_75 are characterized by a strain at break 3.5 and 14.4 times higher than that of neat PLA, respectively. However, it is interesting to note that, even though PBAT constitutes the matrix of these blends, $\varepsilon_b$ is decisively lower than that of neat PBAT. The

presence of large PLA domains and, once again, the low adhesion between the two phases are probably responsible for this result. Regarding the elastic modulus and tensile strength, the prepared blends exhibit high values of E and $\sigma_b$ up to a PBAT content of 30 wt%, while experiencing a drop for higher PBAT concentrations. Once more, this can be explained by recalling the blend morphology. As it was observed in Figure 7.3(A, B), in the PLA_PBAT_15 and PLA_PBAT_30 samples, the PBAT phase is evenly dispersed in the PLA matrix, and the dimensions of the domains are smaller compared to those of the other samples. Moving to the PLA_PBAT_30 to PLA_PBAT_45 sample, the morphology completely changes. Large and irregularly shaped PBAT domains appear, and the interfacial area increases, causing a reduction in blend stiffness and strength. In the future, it will be interesting to enhance the interfacial adhesion between the two phases by using suitable compatibilizers. In conclusion, it is possible to say that when PBAT is added to the PLA matrix as a dispersed component, the tensile strength and elastic modulus decrease but the elongation at break remains the same. In contrast, when PBAT is the major constituent, i.e., PLA is the dispersed component, the stiffness and strength increase with the increasing PLA content, but the elongation at break is significantly reduced.

The elastic modulus of the blends was theoretically predicted by using three models, i.e., the Series, Parallel and Equivalent Box models. More specifically, the Series and Parallel models were used to predict the upper and lower boundaries of blend stiffness [183], according to the expressions reported in Equation (7.4) and (7.5), respectively.

$$E_b = E_{PLA} \cdot V_{PLA} + E_{PBAT} \cdot V_{PBAT} \quad (7.4)$$

$$E_b = \frac{E_{PLA} \cdot E_{PBAT}}{(V_{PLA} \cdot E_{PBAT} + V_{PBAT} \cdot E_{PLA})} \quad (7.5)$$

where $E_b$ is the elastic modulus of the blend, $E_{PLA}$ and $E_{PBAT}$ are the elastic moduli of neat PLA and PBAT, respectively, while $V_{PLA}$ and $V_{PBAT}$ are the volume fractions of PLA and PBAT in the samples. The Parallel model assumes that the continuous phase consists of the higher modulus polymer and therefore represents the upper boundary. On the other hand, the lower boundary is represented by the Series model, which assumes that the lower modulus component is the continuous phase. The Equivalent Box model (EBM) combined with the phase continuity percolation approach was also used to predict the modulus of these polymer blends [183]. The EBM operates with partly parallel (subscript p) and partly series (subscript s) couplings of two components. It is a two-parameter model in that of the four volume fractions, only two are independent variables. The volume fractions of the constituents are correlated as reported in Equation (7.6) and (7.7):

$$V_{PLA} = (V_{PLAp} + V_{PLAs}) \quad (7.6)$$

$$V_{PBAT} = (V_{PBATp} + V_{PBATs}) \quad (7.7)$$

where $V_{PLA} + V_{PBAT} = V_{PLAs} + V_{PLAp} + V_{PBATs} + V_{PBATp} = 1$. The tensile modulus of the blend ($E_b$) is given as reported in Equation (7.8)

$$E_b = E_p \cdot V_p + E_s \cdot V_s = E_{PLA} \cdot V_{PLAp} + E_{PBAT} \cdot V_{PBATp} + \frac{V_s^2}{\frac{V_{PLAs}}{E_{PLA}} + \frac{V_{PBATs}}{E_{PBAT}}} \quad (7.8)$$

where $E_p$ and $E_s$ are, respectively, the elastic moduli of the parallel and series branch of the system, $V_p$ is the sum of $V_{PLAp}$ and $V_{PBATp}$, and $V_s$ is the sum of $V_{PLAs}$ and $V_{PBATs}$. Using the universal formula provided by percolation theory for the elastic modulus of binary systems, Kolarik et al. derived equations for the determination of the volume fractions in parallel, as reported in Equations (7.9) and (7.10):

$$V_{PLAp} = \left(\frac{V_{PLA} - V_{PLAcr}}{1 - V_{PLAcr}}\right)^{T} \quad (7.9)$$

$$V_{PBATp} = \left(\frac{V_{PBAT} - V_{PBATcr}}{1 - V_{PBATcr}}\right)^{T} \quad (7.10)$$

where $V_{PLAcr}$ and $V_{PBATcr}$ are the critical volume fractions at which the component PLA and PBAT become partially continuous and T is the critical exponent. The best fit of the experimental results was obtained with $V_{PLAcr} = V_{PBATcr} = 0.1$ and T = 1.6.

The experimental and theoretical values of the elastic modulus of the prepared blends as a function of the volume fraction of PBAT are shown in Figure 7.9.

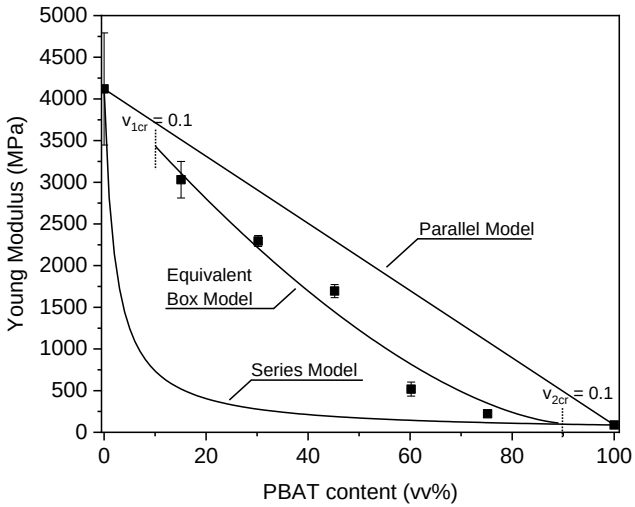


*Figure 7.9. Experimental and theoretical values of the elastic modulus of the produced blends as a function of the PBAT content.*

All the elastic modulus values fall into the range between the Parallel and Series models, suggesting that PLA and PBAT are partially compatible, even though they are not miscible. It is interesting to

notice that the experimental results are in good agreement with the theoretical predictions based on the Equivalent Box model. Finally, the elastic modulus of the PLA_PBAT_75 sample predicted by the Series model practically coincides with the experimental value. This indicates that for this composition, PBAT is the continuous phase with PLA dispersed within it.

*Evaluation of the shape memory behaviour*

Testing the shape memory properties of polymers using a DMA apparatus in single cantilever mode is quite useful when one needs to compare the shape memory performance of materials showing different elongation at break values. Table 7.6 shows the strain fixity and strain recovery parameters of the neat PLA, neat PBAT and PLA/PBAT blends, together with the corresponding maximum applied strain in the tests.

*Table 7.6. Strain fixity and strain recovery parameters of neat PLA, neat PBAT and PLA/PBAT blends.*

| Sample | Applied strain (%) | SF (%) | SR (%) |
|---|---|---|---|
| **PLA** | 7.2 | 83.8 | 56.9 |
| **PLA_PBAT_15** | 7.5 | 81.9 | 63.5 |
| **PLA_PBAT_30** | 7.6 | 77.3 | 73.6 |
| **PLA_PBAT_45** | 7.5 | 73.1 | 64.3 |
| **PLA_PBAT_60** | 7.8 | 80.2 | 54.7 |
| **PLA_PBAT_75** | 8.1 | 91.4 | 14.3 |
| **PBAT** | 10.0 | 91.3 | 8.7 |

As expected, neat PLA is characterized by a good strain fixity capability, reaching an SF value of 83.8%. It is worth noting that the strain recovery of neat PLA is quite limited, considering the values reported in the literature. Only slightly more than half of the imposed deformation (56.7%) is recovered during the recovery step. This

experimental result can probably be attributed to its high crystallinity degree. However, to confirm this hypothesis, future works will need to focus on varying the processing conditions to obtain a PLA with lower crystallinity and investigating its shape memory properties. In regards to neat PBAT, an excellent strain fixability (SF value of 91.3%) and negligible recovery capabilities (SR value of 8.7%) have been found. Due to the absence of a transition temperature in the explored temperature range, neat PBAT cannot exhibit a shape memory behaviour. Consequently, the excellent strain fixability is to be attributed to viscous flow and not to true elastic shape memory behaviour.

With the addition of PBAT, the shape memory performance of PLA undergoes a particular trend. As can be seen from Table 7.6, while the fixing capability tends to slightly decrease up to a PBAT concentration of 45% and then to increase again for higher PBAT amounts, the strain recovery parameter exhibits almost the opposite trend. It increases up to a PBAT content of 30 wt% and then decreases. The higher SR parameters of PLA_PBAT_15 and PLA_PBAT_30 compared to neat PLA could be probably related to the lower crystallinity degree of PLA in these blends, as evidenced by the DSC analyses. The samples constituted by a PBAT matrix (PLA_PBAT_60 and PLA_PBAT_75) fix the deformation well but show inferior recovery capabilities. In particular, in the PLA_PBAT_75 blend, the SR is almost complementary to the SF parameter, indicating that just a very small deformation is recovered during the recovery step. The higher fixability and the lower recovery capabilities of these blends are probably attributable to two aspects. The first is related to the fact that PBAT does not present a transition temperature in the explored temperature range, as previously discussed. Therefore, neat PBAT cannot exhibit a shape memory behaviour and the excellent strain fixability of the PBAT-rich blends is to be attributed to viscous flow and creep of the PBAT matrix. The second aspect is related to the poor adhesion between the PLA and

PBAT phases, which probably causes a non-optimal stress transfer between the two constituents. A scheme illustrating this aspect is reported in Figure 7.10(A,B). Although the proposed scheme is a simplification as it assumes purely tensile conditions, while the samples were indeed subjected to a combination of flexural and shear stresses, it serves to illustrate the impact of the poor interfacial adhesion between PLA and PBAT on the shape memory properties. The focus on the tensile component is justified as it represents the most critical stress state for promoting debonding phenomena. PLA provides at the same time both the transition temperature that guarantees the fixability of the temporary shape and the retractive forces that allow the material to recover the original permanent shape. In more detail, the net points, or the crystalline domains, determine the permanent shape of the polymer. The glassy area, instead, acts as a molecular switch and is responsible for the fixability of the temporary shape. Consequently, the PLA domains should act as a spring in the PBAT matrix and guarantee recovery to the initial condition. However, the poor adhesion between the phases does not allow a good transfer of these retractive forces from the PLA domains to the PBAT matrix and, as a result, the blend exhibits poor recovery capabilities (Figure 7.10B). To confirm this hypothesis, it will be useful in future works to perform the same shape memory tests on compatibilized blends. Furthermore, the difference in SR parameters among PLA_PBAT_60 and PLA_PBAT_75 (54.7% and 14.3%, respectively) is probably due to the morphologies these blends show. Both PLA_PBAT_60 and PLA_PBAT_75 are high-PBAT-content blends; however, while PLA_PBAT_60 presents a co-continuous structure, PLA_PBAT_75 exhibits a sea-island morphology (Figure 7.3(D,E)). The elongated and interconnected PLA domains in PLA_PBAT_60 probably promote a higher recovery capability with respect to that of PLA_PBAT_75. It has already been mentioned that only PLA presents a shape memory behaviour, and only PLA can provide the retractive forces to allow the blend to return to the original conditions. Consequently, the presence of larger PLA domains in the

blend is beneficial from the point of view of the recovery performances.

The best compromise between shape fixability and recovery capability was obtained in the PLA_PBAT_30 sample, for which SF and SR values of 77.3% and 73.6% were obtained, respectively. However, it should be noticed that the compositions exhibiting the more interesting shape memory properties do not coincide with the blends showing a significant improvement in PLA ductility. Once again, the addition of a proper compatibilizer could give a satisfactory answer to this issue.

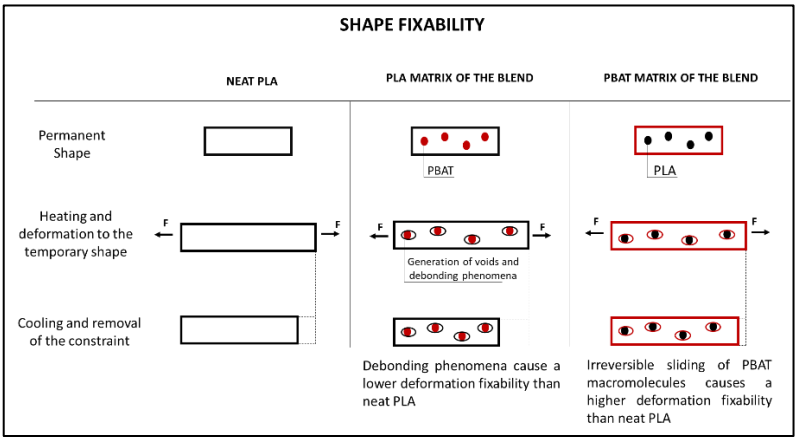


(A)

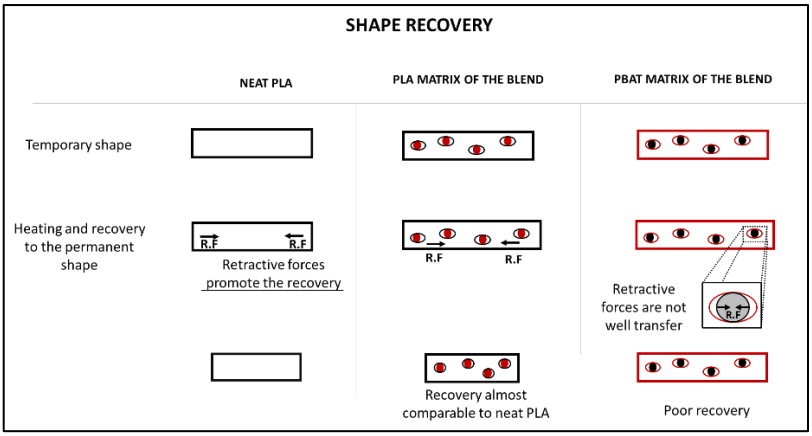


(B)

*Figure 7.10. Schematization of the proposed mechanism for the shape memory behaviour of the produced blends. Modelization of (a) strain fixity and (b) strain recovery behaviour. The scheme is a simplification as it assumes purely tensile conditions. However, it serves to illustrate the impact of the poor interfacial adhesion between PLA and PBAT on the shape memory properties.*

### 7.1.4 Conclusions

The present work investigated the microstructural, thermomechanical and shape memory properties of biodegradable PLA/PBAT blends produced by melt compounding at different relative amounts. Rheological measurements, optical microscopy and SEM micrographs evidenced the immiscibility and the low interfacial adhesion between the PLA and PBAT phases. Depending on the PLA/PBAT ratio, the two constituents exhibited either a sea-island morphology or an almost co-continuous structure, and it was shown that phase inversion occurred in a PBAT concentration interval between 45 wt% and 60 wt%. The immiscibility of these blends was also confirmed by a DSC analysis, as the glass transition temperatures of PLA and PBAT corresponded to the values of neat polymers and

were unaffected by the blend composition. The TGA analysis revealed that the addition of PBAT slightly improved the thermal stability of PLA, probably because of the presence of rigid benzene rings in the molecular structure of PBAT.

Tensile tests evidenced that the stiffness and strength of the blends decreased with the increasing PBAT concentration, while the elongation at break remained comparable to that of neat PLA (5.8%) up to a PBAT content of 45 wt%. A significant increment in blend ductility was registered only for higher PBAT concentrations (elongation at break up to 83.8% with a PBAT amount of 75 wt%).

The shape memory performance of PLA was impaired by the addition of PBAT. In particular, a reduction in the strain recovery parameter was registered with the increasing PBAT content, probably due to the low adhesion between the constituents. The best compromise between shape fixability and recovery capability was obtained with a PBAT content of 30 wt% and SF and SR values of 77.3% and 73.6%, respectively.

These results constitute a basis for future research on innovative multifunctional biodegradable polymer blends with promising applications in the packaging field and suggest that their properties could be enhanced by applying suitable compatibilizers. Future works should focus on the selection of the most appropriate compatibilizer, the effect of blend compatibilization on the physical and shape memory properties of these systems and a deep investigation of the gas permeability of the blends.

# 8 References


1. Alamgir, W.; Shan, H. The Multifaceted Consequences of Climate Change on Human Health. *Life and Science* **2023**, *4*, 2.

2. Russo, S.; Sillmann, J.; Sterl, A. Humid heat waves at different warming levels. *Scientific Reports* **2017**, *7*, 7477.

3. Baldwin, J.W.; Dessy, J.B.; Vecchi, G.A.; Oppenheimer, M. Temporally Compound Heat Wave Events and Global Warming: An Emerging Hazard. *Earth's Future* **2019**, *7*, 411.

4. Li, S.; Chen, Y.; Wei, W.; Fang, G.; Duan, W. The increase in extreme precipitation and its proportion over global land. *Journal of Hydrology* **2024**, *628*, 130456.

5. Bianchi, M.; Fambri, L.; Fredi, G.; Pegoretti, A.; Dorigato, A. Elastocaloric Performance of Natural Rubber in Solid State Cooling: Evaluation of the Effect of Crosslinking Density. *Applied Sciences* **2024**, *14*, 10525.

6. Prabakaran, R.; Lal, D.M.; Kim, S.C. A state of art review on future low global warming potential refrigerants and performance augmentation methods for vapour compression based mobile air conditioning system. *Journal of Thermal Analysis and Calorimetry* **2023**, *148*, 417.

7. Davis, L.W.; Gertler, P.J. Contribution of air conditioning adoption to future energy use under global warming. *Proceedings of the National Academy of Sciences* **2015**, *112*, 5962.

8. Mañosa, L.; Planes, A. Solid-state cooling by stress: A perspective. *Applied Physics Letters* **2020**, *116*, 050501.

9. Li, L.; He, S.; Xiao, F.; Zeng, Y.; Liu, Y.; Zhou, Y.; Cai, X.; Jin, X. Cooling innovations: Elastocaloric shape memory alloys, manufacturing, simulation, and refrigerator. *Progress in Materials Science* **2025**, *153*, 101477.

10. Mevada, H.; Liu, B.; Gao, L.; Hwang, Y.; Takeuchi, I.; Radermacher, R. Elastocaloric cooling: A pathway towards future cooling technology. *International Journal of Refrigeration* **2024**, *162*, 86.

11. Bianchi, M.; Fambri, L.; Bortolotti, M.; Pegoretti, A.; Dorigato, A. Elastocaloric Performance of Natural Rubber: The Role of Nanoclay Addition. *Molecules* **2025**, *30*, 3035.

12. Birol, D.F. The Future of Cooling. Opportunities for energy-efficient air conditioners. *International Energy Agency* **2018**.

13. McLinden, M.O.; Seeton, C.J.; Pearson, A. New refrigerants and system configurations for vapor-compression refrigeration. *Science* **2020**, *370*, 791.

14. Process Solution Inc. How Does a Compression Refrigeration System Work? Available online: https://processsolutions.com/how-does-a-compression-refrigeration-system-work/ (accessed on 1/07/2025).

15. Ritchie, H. Air conditioning causes around 3% of greenhouse gas emissions. How will this change in the future? *Online at OurWorldinData.org* 2024.

16. Sion, M. Elastocaloric Heat Pump Proof of Concept for Near Room Temperature Refrigeration Using Natural Rubber. PhD thesis, Université de Tohoku, 2025.

17. Steven Brown, J.; Domanski, P.A. Review of alternative cooling technologies. *Applied Thermal Engineering* **2014**, *64*, 252.

18. Sakamoto, S.-i.; Watanabe, Y. The experimental studies of thermoacoustic cooler. *Ultrasonics* **2004**, *42*, 53.

19. Cazorla, C. Novel mechanocaloric materials for solid-state cooling applications. *Applied Physics Reviews* **2019**, *6*, 041316.

20. Chauhan, A.; Patel, S.; Vaish, R.; Bowen, C.R. A review and analysis of the elasto-caloric effect for solidstate

refrigeration devices: Challenges and opportunities. *MRS Energy & Sustainability* **2015**, *2*, 16.

21. Bruederlin, F.; Bumke, L.; Chluba, C.; Ossmer, H.; Quandt, E.; Kohl, M. Elastocaloric Cooling on the Miniature Scale: A Review on Materials and Device Engineering. *Energy Technology* **2018**, *6*, 1588.

22. Yukihiro, Y. Effet élastocalorique dans le caoutchouc naturel et le terpolymère : mécanismes responsables de la variation de température et bilan énergétique sous déformation. PhD thesis, Universitè de Lion, 2022.

23. Bonacina, C.; Cavallini, A.; Mattarolo, L. *Trasmissione del Calore*; cleup editore: Padova, 1989; pp. 116.

24. Imamura, W.; Paixão, L.S.; Usuda, É.O.; Gama, S.; Lopes, É.S.N. i-Caloric Effects: a proposal for normalization. *arXiv preprint* **2018**.

25. Kim, J.-Y. Caloric effects in ferroic materials. PhD Thesis, Department of Materials Science & Metallurgy, University of Cambridge, 2021.

26. Lyubina, J. Magnetocaloric materials for energy efficient cooling. *Journal of Physics D: Applied Physics* **2017**, *50*, 053002.

27. Nguyen, T.-A.; Kakuta, N.; Uchida, K.-i.; Nagano, H. Near-infrared imaging of heat transfer behavior between gadolinium and fluid during magnetization/demagnetization process of magnetocaloric effect. *Journal of Applied Physics* **2024**, *135*, 193904.

28. Fraunhofer, I.P.M. Magnetocaloric materials & systems. Available online: https://www.ipm.fraunhofer.de/en/bu/gas-and-process-technology/expertise/caloric-systems/magnetocaloric-systems.html (accessed on 1/07/2025).

29. Cheng, P.; Zhang, G.; Li, Z.; Yang, B.; Zhang, Z.; Wang, D.; Du, Y. Combining magnetocaloric and elastocaloric effects to achieve a broad refrigeration temperature region in

Ni43Mn41Co5Sn11 alloy. *Journal of Magnetism and Magnetic Materials* **2022**, *550*, 169082.

30. Torelló, A.; Defay, E. Electrocaloric Coolers: A Review. *Advanced Electronic Materials* **2022**, *8*, 2101031.

31. Fraunhofer, I.P.M. Electrocaloric materials & systems. Available online: https://www.ipm.fraunhofer.de/en/bu/gas-and-process-technology/expertise/caloric-systems/electrocaloric-systems.html (accessed on 1/07/2025).

32. Fraunhofer, I.P.M. Elastocaloric materials & systems. Available online: https://www.ipm.fraunhofer.de/en/bu/gas-and-process-technology/expertise/caloric-systems/elastocaloric-systems.html (accessed on 1/07/2025).

33. Borzacchiello, A.; Cirillo, L.; Greco, A.; Masselli, C. A comparison between different materials with elastocaloric effect for a rotary cooling prototype. *Applied Thermal Engineering* **2023**, *235*, 121344.

34. Xie, Z.; Sebald, G.; Guyomar, D. Comparison of elastocaloric effect of natural rubber with other caloric effects on different-scale cooling application cases. *Applied Thermal Engineering* **2017**, *111*, 914.

35. Cirillo, L.; Greco, A.; Masselli, C. Cooling through barocaloric effect: A review of the state of the art up to 2022. *Thermal Science and Engineering Progress* **2022**, *33*, 101380.

36. Carvalho, A.M.G.; Imamura, W.; Usuda, E.O.; Bom, N.M. Giant room-temperature barocaloric effects in PDMS rubber at low pressures. *European Polymer Journal* **2018**, *99*, 212.

37. Gottschall, T.; Kuz'min, M.D.; Skokov, K.P.; Skourski, Y.; Fries, M.; Gutfleisch, O.; Zavareh, M.G.; Schlagel, D.L.; Mudryk, Y.; Pecharsky, V.; et al. Magnetocaloric effect of gadolinium in high magnetic fields. *Physical Review B* **2019**, *99*, 134429.

38. Qiu, Y.; Wu, H.; Wang, J.; Lou, J.; Zhang, Z.; Liu, A.; Kitamura, T.; Chai, G. Giant electrocaloric effect in ferroelectric ultrathin films at room temperature mediated by flexoelectric effect and work function. *Journal of Applied Physics* **2017**, *122*.

39. Neese, B.; Chu, B.; Lu, S.-G.; Wang, Y.; Furman, E.; Zhang, Q.M. Large Electrocaloric Effect in Ferroelectric Polymers Near Room Temperature. **2008**, *321*, 821.

40. Yin, R.; Hou, Y.; Lv, X.; Li, J.; Zhong, R.; Su, Y.; Qiao, L.; Che, R.; Zhu, L.; Liu, C.; et al. Optimizing electrocaloric effect of PbSc0.5Ta0.5O3 ceramics near/below room temperature by ordering degree modulation. *Journal of Advanced Ceramics* **2025**, *14*, 9221088.

41. Bennacer, R.; Liu, B.; Yang, M.; Chen, A. Refrigeration performance and the elastocaloric effect in natural and synthetic rubbers. *Applied Thermal Engineering* **2022**, *204*, 117938.

42. Candau, N.; Fernandes, J.P.C.; Vasmer, E.; Maspoch, M.L. Cellulose nanocrystals as nucleating agents for the strain induced crystallization in natural rubber. *Soft Matter* **2022**, *18*, 8663.

43. Candau, N.; Vives, E.; Fernández, A.I.; Maspoch, M.L. Elastocaloric effect in vulcanized natural rubber and natural/wastes rubber blends. *Polymer* **2021**, *236*, 124309.

44. Candau, N.; Zimny, A.; Vives, E.; Maspoch, M.L. Elastocaloric Waste/Natural Rubber Materials with Various Crosslink Densities. *Polymers* **2023**, *15*, 2566.

45. Haissoune, H.; Chenal, J.-M.; Chazeau, L.; Sebald, G.; Morfin, I.; Lebrun, L.; Dalmas, F.; Coativy, G. Elastocaloric effect: Impact of heat transfer on strain-induced crystallization kinetics of natural rubber. *Polymer* **2022**, *263*, 125506.

46. Ebewele, R.O. *Polymer Science and Technology*, 1st ed.; CRC Press: 2000.

47. Charrier, J.-M. *Polymeric Materials and Processing*, 1st ed.; Oxford University Press: 1991; p. 656.

48. Bin Samsuri, A. Degradation of Natural Rubber and Synthetic Elastomers. In *Shreir's Corrosion*; Elsevier: 2010; pp. 2407.

49. Tomičić-Pupek, K.; Srpak, I.; Havaš, L.; Srpak, D. Algorithm for Customizing the Material Selection Process for Application in Power Engineering. *Energies* **2020**, *13*, 6458.

50. Market Analysis Report. *Elastomers Market Size, Share & Trends Analysis Report By Type (Thermoplastics, Thermosets), By End Use (Automotive, Medical, Consumer Goods, Industrial), By Region, And Segment Forecasts, 2025 - 2030*; GVR-2-68038-786-5; p. 100.

51. Jansen, J. Comparing Thermoplastic Elastomers and Thermoset Rubber: Each class of material is well suited for its range of applications, but there are key differences. *Plastics Engineering* **2016**, *72*, 36.

52. Bianchi, M. Evaluation of the shape memory behaviour of EPDM/paraffin foams. Master thesis, Univeristy of Trento, 2021.

53. Shanks, R.A.; Kong, I. General Purpose Elastomers: Structure, Chemistry, Physics and Performance. In *Advances in Elastomers I*, Visakh, P.M., Thomas, S., Chandra, A.K., Mathew, A.P., Eds.; Springer Berlin Heidelberg: Berlin, Heidelberg, 2013; Volume 11, pp. 11.

54. Valentini, L.; Manchado, M.A.L. *High-Performance Elastomeric Materials Reinforced by Nano-Carbons*; Elsevier: 2020.

55. Erman, B.; Mark, J.E.; Roland, C.M. *The science and technology of rubber*, 4th edition ed.; Elsevier Academic Press: Amsterdam Boston, 2013.

56. John, B. *Plastic Materials*, 7th ed.; Butterworth-Heinemann: 1999; p. 920.

57. Sapkota, J. Influence of clay modification on curing kinetcs of natural rubber nanocomposites. Master's thesis, Tampere University of Technology, 2011.

58. Karen, G.B. The Manufacturing Process Of Rubber. Available online: https://www.sciencing.com/manufacturing-process-rubber-5206099/ (accessed on 12/07/2025).

59. Crawford, R. *Plastics and Rubber: engineering design and applications*, 1st ed.; Mechanical engineering publications ltd: 1985.

60. Sperling, L.H. *Introduction to physical polymer science*, 4th ed.; Wiley: Hoboken, N.J, 2006; p. 845.

61. Datta, R.N. *Rubber curing systems*; iSmithers Rapra Publishing: 2002; Volume 12.

62. Amiruddin, M.A.A.; Sarkawi, S.S. A rheological characteristics and kinetic study for sulphur accelerated vulcanisation of epoxidized natural rubber. *Journal of Rubber Research* **2023**, *26*, 363.

63. Bhowmick, A.K.; Hall, M.M.; Benarey, H.A. *Rubber Products Manufacturing Technology*, 1st edition ed.; Routledge: New York, 1994.

64. Nocil, L. Vulcanization & Accelerators. Available online: https://www.nocil.com/ (accessed on 15/06/2025).

65. Gonzales, L.; Rodriguez, A.; Valentin, J.L. Conventional and Efficient Crosslinking of Natural Rubber Effect of Heterogeneities on the Physical Properties. **2005**, 638.

66. Magni, D. Mechanical characterization of fibres-reinforced elastomers: a study on continuous glass fibres-Sylgard 184 composite. Master thesis, Politecnico di Milano, 2021.

67. Treolar, L.R.G. *The physics of rubber elasticity*, 3rd ed.; Oxford university press: New York, 2005.

68. Tibbitt, M.W. Lecture 11: Rubber elasticity. **2019**.

69. Glaser, Z.R.; Eirich, F.R. Thermal behavior of elastomers at high rates of tensile straining. *Journal of Polymer Science Part C: Polymer Symposia* **1970**, *31*, 275.

70. Larrañaga, A.; Lizundia, E. Strain-Induced Crystallization. In *Crystallization in Multiphase Polymer Systems*; Elsevier: 2018; pp. 471.

71. Toki, S.; Sics, I.; Ran, S.; Liu, L.; Hsiao, B.S. Molecular orientation and structural development in vulcanized polyisoprene rubbers during uniaxial deformation by in situ synchrotron X-ray diffraction. *Polymer* **2003**, *44*, 6003.

72. Diani, J.; Fayolle, B.; Gilormini, P. A review on the Mullins effect. *European Polymer Journal* **2009**, *45*, 601.

73. Nie, Y.; Gu, Z.; Wei, Y.; Hao, T.; Zhou, Z. Features of strain-induced crystallization of natural rubber revealed by experiments and simulations. *Polymer Journal* **2017**, *49*, 309.

74. Dantas De Oliveira, A.; Augusto Gonçalves Beatrice, C. Polymer Nanocomposites with Different Types of Nanofiller. In *Nanocomposites - Recent Evolutions*, Sivasankaran, S., Ed.; IntechOpen: 2019.

75. Dorigato, A.; Morandi, S.; Pegoretti, A. Effect of nanoclay addition on the fiber/matrix adhesion in epoxy/glass composites. *Journal of Composite Materials* **2012**, *46*, 1439.

76. Dorigato, A.; Pegoretti, A.; Penati, A. Effect of the polymer—filler interaction on the thermo-mechanical response of polyurethane-clay nanocomposites from blocked prepolymer. *Journal of Reinforced Plastics and Composites* **2011**, *30*, 325.

77. Dorigato, A.; Pegoretti, A.; Quaresimin, M. Thermo-mechanical characterization of epoxy/clay nanocomposites as matrices for carbon/nanoclay/epoxy laminates. *Materials Science and Engineering: A* **2011**, *528*, 6324.

78. Pegoretti, A.; Dorigato, A.; Brugnara, M.; Penati, A. Contact angle measurements as a tool to investigate the filler–matrix

interactions in polyurethane–clay nanocomposites from blocked prepolymer. *European Polymer Journal* **2008**, *44*, 1662.

79. Pegoretti, A.; Dorigato, A.; Penati, A. Tensile mechanical response of polyethylene – clay nanocomposites. *Express Polymer Letters* **2007**, *1*, 123.

80. Carretero-González, J.; Retsos, H.; Verdejo, R.; Toki, S.; Hsiao, B.S.; Giannelis, E.P.; López-Manchado, M.A. Effect of Nanoclay on Natural Rubber Microstructure. *Macromolecules* **2008**, *41*, 6763.

81. Carretero-Gonzalez, J.; Verdejo, R.; Toki, S.; Hsiao, B.S.; Giannelis, E.P.; López-Manchado, M.A. Real-Time Crystallization of Organoclay Nanoparticle Filled Natural Rubber under Stretching. *Macromolecules* **2008**, *41*, 2295.

82. Qu, L.; Huang, G.; Liu, Z.; Zhang, P.; Weng, G.; Nie, Y. Remarkable reinforcement of natural rubber by deformation-induced crystallization in the presence of organophilic montmorillonite. *Acta Materialia* **2009**, *57*, 5053.

83. Denora, I.; Marano, C. Stretch-induced softening in filled elastomers: A review on Mullins effect related anisotropy and thermally induced recovery. *Polymer Testing* **2024**, *133*, 108399.

84. Qian, M.; Zou, B.; Chen, Z.; Huang, W.; Wang, X.; Tang, B.; Liu, Q.; Zhu, Y. The Influence of Filler Size and Crosslinking Degree of Polymers on Mullins Effect in Filled NR/BR Composites. *Polymers* **2021**, *13*, 2284.

85. Fu, W.; Wang, L.; Huang, J.; Liu, C.; Peng, W.; Xiao, H.; Li, S. Mechanical Properties and Mullins Effect in Natural Rubber Reinforced by Grafted Carbon Black. *Advances in Polymer Technology* **2019**, *2019*, 1.

86. Dorfmann, A.; Ogden, R.W. A constitutive model for the Mullins effect with permanent set in particle-reinforced rubber. *International Journal of Solids and Structures* **2004**, *41*, 1855.

87. Blanchard, A.F.; Parkinson, D. Breakage of carbon-rubber networks by applied stress. *Industrial & Engineering Chemistry Research* **1952**, *44*, 799.

88. Houwink, R. Slipping of molecules during the deformation of reinforced rubber. *Rubber Chemistry and Technology* **1956**, *29*, 888.

89. Kraus, G.; Childers, C.W.; Rollman, K.W. Stress softening in carbon black reinforced vulcanizates. Strain rate and temperature effects. **1966**, *10*, 229.

90. Hanson, D.E.; Hawley, M.; Houlton, R.; Chitanvis, K.; Rae, P.; Orler, E.B. Stress softening experiments in silica-filled polydimethylsiloxane provide insight into a mechanism for the Mullins effect. **2005**, *46*, 10989.

91. Cavallerogomma. Natural rubber: how it is produced and main uses. Available online: https://cavallerogomma.it/en/natural-rubber-how-it-is-produced-and-main-uses/ (accessed on 10/07/2025).

92. Kitjanon, J.; Khuntawee, W.; Sutthibutpong, T.; Boonnoy, P.; Phongphanphanee, S.; Wong-ekkabut, J. Transferability of Polymer Chain Properties between Coarse-Grained and Atomistic Models of Natural Rubber Molecule Validated by Molecular Dynamics Simulations. *Journal of Physics: Conference Series* **2017**, *901*, 012096.

93. AidEnvironment. *Natural Rubber. Production & Consumption*; Pilot report 3; 2024.

94. Davies, B. Natural rubber — Its engineering characteristics. *Materials & Design* **1986**, *7*, 68.

95. Ali, M.F.B. Investigating the opportunities to improve smallholder rubber production through the development of an integrated decision support system: A Malaysian case study. PhD Thesis, The University of Queensland, 2021.

96. RubberWorld. Global rubber production faces continued challenges in 2025. Available online:

https://rubberworld.com/global-rubber-production-faces-continued-challenges-in-2025/ (accessed on 11/07/2025).

97. Moonart, U.; Utara, S. Effect of surface treatments and filler loading on the properties of hemp fiber/natural rubber composites. *Cellulose* **2019**, *26*, 7271.

98. Natural Rubber. In *Polymer Science: A Comprehensive Reference*; Elsevier: 2012; pp. 281.

99. Weber&Schaer. Price Development Chart. Available online: https://www.weber-schaer.com/en/products/natural-rubber-latex/price-charts/ (accessed on 10/07/2025).

100. Rohlwing, K. Natural rubber prices are rising. Available online: https://www.fleetowner.com/emissions-efficiency/article/21152253/natural-rubber-prices-are-rising (accessed on 10/07/2025).

101. Santoso, A.B. Analysis: Natural rubber demand in danger. Available online: https://www.thejakartapost.com/paper/2020/07/07/analysis-natural-rubber-demand-in-danger.html (accessed on 12/06/2025).

102. Gabrielle, N. Adverse weather curbs Thai, Chinese rubber output, lifting prices to 13-year high. Available online: https://www.reuters.com/markets/commodities/adverse-weather-curbs-thai-chinese-rubber-output-lifting-prices-13-year-high-2024-10-16/ (accessed on 12/06/2025).

103. RubberWorld. Global rubber shortfall looms in 2025 on stagnant output. Available online: https://rubberworld.com/global-rubber-shortfall-looms-in-2025-on-stagnant-output/ (accessed on 11/07/2025).

104. Omar, M.F.; Ali, F.; Jami, M.S.; Azmi, A.S.; Ahmad, F.; Marzuki, M.Z.; Muniyandi, S.K.; Zainudin, Z.; Kim, M.P. A Comprehensive Review of Natural Rubber Composites: Properties, Compounding Aspects, and Renewable Practices with Natural Fibre Reinforcement. *Journal of Renewable Materials* **2025**, *13*, 497.

105. Weber&Schaer. Flexibility is our raw material. Available online: https://www.weber-schaer.com/en/ (accessed on 10/07/2025).

106. Molecular Structure of Natural Rubber and Its Characteristics Based on Recent Evidence. In *Biotechnology - Molecular Studies and Novel Applications for Improved Quality of Human Life*; InTech: 2012.

107. Biochemical composition of Hevea brasiliensis latex: A focus on the protein, lipid, carbohydrate and mineral contents. In *Advances in Botanical Research*; Elsevier: 2020; pp. 201.

108. Feltex Co, L.T.D. Skim block and crepe. Available online: https://www.feltex.co.th/HTML/skimblock.php (accessed on 12/07/2025).

109. Indiamart. Sheet Pale Latex Crepe (PLC) rubber. Available online: https://www.indiamart.com/proddetail/pale-latex-crepe-plc-rubber-23184390548.html (accessed on 12/07/2025).

110. Agriculture.Institute. Different Marketable Forms of Natural Rubber: Latex, RSS, Crepe, and TSR. Available online: https://agriculture.institute/post-harvest-mgt-value-addition/marketable-forms-of-natural-rubber/#:~:text=Pale%20crepe:%20Produced%20from%20high,often%20preferred%20for%20specific%20applications. (accessed on 15/07/2025).

111. Agriculture.Institute. Processing and Grading of Technically Specified Rubber (TSR). Available online: https://agriculture.institute/post-harvest-mgt-value-addition/processing-grading-technically-specified-rubber/ (accessed on 15/07/2025).

112. Gent, A.N. Rubber. *Encyclopedia Britannica* **2023**.

113. Weber&Schaer. Quality and quantity. Passion and experties. Available online: https://www.weber-schaer.com/en/products/natural-rubber-latex/ (accessed on 10/07/2025).

114. Mark, J.E. *Polymer data handbook*, 1st ed.; Oxford University Press: 1998.

115. Vishnu, S.; Prabu, B.; Pugazhvadivu, M. Strategies to improve the mechanical performance of elastomers using ternary blends: A review. *Hybrid Advances* **2023**, *3*, 100062.

116. Xie, Z.; Sebald, G.; Guyomar, D. Temperature dependence of the elastocaloric effect in natural rubber. *Physics Letters A* **2017**, *381*, 2112.

117. Coativy, G.; Haissoune, H.; Seveyrat, L.; Sebald, G.; Chazeau, L.; Chenal, J.-M.; Lebrun, L. Elastocaloric properties of thermoplastic polyurethane. *Applied Physics Letters* **2020**, *117*.

118. Sion, M.; Jay, J.; Coativy, G.; Komiya, A.; Sebald, G. Natural rubber based elastocaloric solid-state refrigeration device: design and performances of a single stage system. *Journal of Physics: Energy* **2024**, *6*, 025003.

119. Lanxess, R. Zinkoxyd aktiv-Technical Data Sheet. Available online: https://lanxess.com/ (accessed on 10/06/2025).

120. Carlo Erba reagents. Toluene-product sheet. Available online: https://www.carloerbareagents.com/cerstorefront/cer-it/p/225800DD14150/0000000000000386002/downloadVariant (accessed on 1/06/2025).

121. Carlo Erba reagents. Acetone-product sheet. Available online: https://www.carloerbareagents.com/cerstorefront/cer-it/p/002100DD14150/0000000000000508200/downloadVariant (accessed on 1/06/2025).

122. Carlo Erba reagents. Mathanol-Product Sheet. Available online: https://www.carloerbareagents.com/cerstorefront/cer-exp/p/111500BB08550/downloadProduct (accessed on 1/06/2025).

123. Byk. CLOISITE-20 A. Available online: https://www.byk.com/en/products/additive-guide/cloisite-20-a (accessed on 1/06/2025).

124. ASTM D5289. Standard Test Method for Rubber Property—Vulcanization Using Rotorless Cure Meters. **2019**.

125. ASTM D792. Density and Specific Gravity (Relative Density) of Plastics by Displacement. **2020**.

126. ASTM D6814. Determination of Percent Devulcanization of Crumb Rubber Based on Crosslink Density. **2018**.

127. Takahashi, Y.; Kumano, T. Crystal Structure of Natural Rubber. *Macromolecules* **2004**, *37*, 4860.

128. ASTM E1461. Standard Test Method for Thermal Diffusivity by the Flash Method. **2022**.

129. ASTM D2240. Standard Test Method for Rubber Property—Durometer Hardness. **2010**.

130. ASTM D412. Vulcanized Rubber and Thermoplastic Elastomers— Tension. **2021**.

131. Ucar, H.; Basdogan, I. Dynamic characterization and modeling of rubber shock absorbers: A comprehensive case study. *Journal of Low Frequency Noise, Vibration and Active Control* **2018**, *37*, 509.

132. Huneau, B. Strain-induced crystallization of natural rubber: a review of x-ray diffraction investigations. *Rubber Chemistry and Technology* **2011**, *84*, 425.

133. Zhao, F.; Bi, W.; Zhao, S. Influence of Crosslink Density on Mechanical Properties of Natural Rubber Vulcanizates. *Journal of Macromolecular Science, Part B* **2011**, *50*, 1460.

134. Boyce, M.C.; Arruda, E.M. Constitutive Models of Rubber Elasticity: A Review. *Rubber Chemistry and Technology* **2000**, *73*, 504.

135. Van Wijk, M. Diagnosi pressione e temperatura aria condizionata. Available online: https://www.mvwautotechniek.nl/it/diagnose-airconditioning-druk-en-temperatuur/ (accessed on 15/06/2025).

136. Trabelsi, S.; Albouy, P.A.; Rault, J. Crystallization and Melting Processes in Vulcanized Stretched Natural Rubber. *Macromolecules* **2003**, *36*, 7624.

137. Tosaka, M. Strain-Induced Crystallization of Crosslinked Natural Rubber As Revealed by X-ray Diffraction Using Synchrotron Radiation. *Polymer Journal* **2007**, *39*, 1207.

138. Le Cam, J.B. Energy storage due to strain-induced crystallization in natural rubber: The physical origin of the mechanical hysteresis. *Polymer* **2017**, *127*, 166.

139. Bird, R.B. *Transport Phenomena*, Revised Second Edition ed.; Wiley: 2007.

140. Tosaka, M.; Kawakami, D.; Senoo, K.; Kohjiya, S.; Ikeda, Y.; Toki, S.; Hsiao, B.S. Crystallization and Stress Relaxation in Highly Stretched Samples of Natural Rubber and Its Synthetic Analogue. *Macromolecules* **2006**, *39*, 5100.

141. Fernandes, V.A.; De Focatiis, D.S.A. The role of deformation history on stress relaxation and stress memory of filled rubber. *Polymer Testing* **2014**, *40*, 124.

142. Le Cam, J.-B. Measuring Strain-Induced Crystallinity in Rubbers from IR Thermography. In *Residual Stress, Thermomechanics & Infrared Imaging, Hybrid Techniques and Inverse Problems, Volume 7*, 1 ed.; River Publishers: New York, 2025; pp. 57.

143. Ernst Rudolf Georg Eckert, E.E.S. *Studies on Heat Transfer in Laminar Free Convection with the Zehnder-Mach Interferometer*, 5747 ed.; United States, Air Force, Air Materiel Command, 1948.

144. Le Cam, J.B.; Albouy, P.A.; Charlès, S. Comparison between x-ray diffraction and quantitative surface calorimetry based on infrared thermography to evaluate strain-induced crystallinity in natural rubber. *Review of Scientific Instruments* **2020**, *91*, 044902.

145. Mitchell, J.C.; Meier, D.J. Rapid stress-induced crystallization in natural rubber. *Journal of Polymer Science Part A-2: Polymer Physics* **1968**, *6*, 1689.

146. Nie, Y.; Huang, G.; Qu, L.; Wang, X.; Weng, G.; Wu, J. New insights into thermodynamic description of strain-induced crystallization of peroxide cross-linked natural rubber filled with clay by tube model. *Polymer* **2011**, *52*, 3234.

147. Vishvanathperumal, S.; Gopalakannan, S. Effects of the Nanoclay and Crosslinking Systems on the Mechanical Properties of Ethylene-propylene-diene Monomer/styrene Butadiene Rubber Blends Nanocomposite. *Silicon* **2019**, *11*, 117.

148. Kathuria, A.; Zhang, S. Sustainable and Repulpable Barrier Coatings for Fiber-Based Materials for Food Packaging: A Review. *Frontiers in Materials* **2022**, *9*, 929501.

149. Cervantes-Uc, J.M.; Cauich-Rodríguez, J.V.; Vázquez-Torres, H.; Garfias-Mesías, L.F.; Paul, D.R. Thermal degradation of commercially available organoclays studied by TGA–FTIR. *Thermochimica Acta* **2007**, *457*, 92.

150. López-Manchado, M.; Herrero, B.; Arroyo, M. Preparation and characterization of organoclay nanocomposites based on natural rubber. *Polymer International* **2003**, *52*, 1070.

151. Carli, L.N.; Roncato, C.R.; Zanchet, A.; Mauler, R.S.; Giovanela, M.; Brandalise, R.N.; Crespo, J.S. Characterization of natural rubber nanocomposites filled with organoclay as a substitute for silica obtained by the conventional two-roll mill method. *Applied Clay Science* **2011**, *52*, 56.

152. Pusch, R. *Is montmorillonite-rich clay of MX-80 type the ideal buffer for isolation of HLW?*; Technical Report TR-99-33; 1999.

153. Sookyung, U.; Nakason, C.; Thaijaroen, W.; Vennemann, N. Influence of modifying agents of organoclay on properties of nanocomposites based on natural rubber. *Polymer Testing* **2014**, *33*, 48.

154. Poompradub, S.; Tosaka, M.; Kohjiya, S.; Ikeda, Y.; Toki, S.; Sics, I.; Hsiao, B.S. Mechanism of strain-induced crystallization in filled and unfilled natural rubber vulcanizates. *Journal of Applied Physics* **2005**, *97*, 103529.

155. Zhang, S.; Yang, Q.; Li, C.; Fu, Y.; Zhang, H.; Ye, Z.; Zhou, X.; Li, Q.; Wang, T.; Wang, S.; et al. Solid-state cooling by elastocaloric polymer with uniform chain-lengths. *Nature Communications* **2022**, *13*, 9.

156. Science, A. A refrigerator that works by stretching rubber bands. Available online: https://www.youtube.com/watch?v=lfmrvxB154w (accessed on 10/03/2025).

157. Shen, M.; Song, B.; Zeng, G.; Zhang, Y.; Huang, W.; Wen, X.; Tang, W. Are biodegradable plastics a promising solution to solve the global plastic pollution? *Environmental Pollution* **2020**, *263*, 114469.

158. Nanda, S.; Patra, B.R.; Patel, R.; Bakos, J.; Dalai, A.K. Innovations in applications and prospects of bioplastics and biopolymers: a review. *Environmental Chemistry Letters* **2022**, *20*, 379.

159. Luckachan, G.E.; Pillai, C.K.S. Biodegradable Polymers- A Review on Recent Trends and Emerging Perspectives. *Journal of Polymers and the Environment* **2011**, *19*, 637.

160. Fleck, A. Plastic waste: Here's what it could look like by 2060. Available online: https://www.weforum.org/stories/2022/07/recycling-efforts-not-enough-to-solve-plastic-waste-problem/ (accessed on 1/10/2022).

161. Pang, X.; Zhuang, X.; Tang, Z.; Chen, X. Polylactic acid (PLA): Research, development and industrialization. *Biotechnology Journal* **2010**, *5*, 1125.

162. Bax, B.; Müssig, J. Impact and tensile properties of PLA/Cordenka and PLA/flax composites. *Composites Science and Technology* **2008**, *68*, 1601.

163. Leonés, A.; Sonseca, A.; López, D.; Fiori, S.; Peponi, L. Shape memory effect on electrospun PLA-based fibers tailoring their thermal response. *European Polymer Journal* **2019**, *117*, 217.

164. Arrieta, M.; Samper, M.; Aldas, M.; López, J. On the Use of PLA-PHB Blends for Sustainable Food Packaging Applications. *Materials* **2017**, *10*, 1008.

165. Ferreira, F.V.; Cividanes, L.S.; Gouveia, R.F.; Lona, L.M.F. An overview on properties and applications of poly(butylene adipate-co -terephthalate)–PBAT based composites. *Polymer Engineering & Science* **2019**, *59*.

166. Jian, J.; Xiangbin, Z.; Xianbo, H. An overview on synthesis, properties and applications of poly(butylene-adipate-co-terephthalate)–PBAT. *Advanced Industrial and Engineering Polymer Research* **2020**, *3*, 19.

167. Al-Itry, R.; Lamnawar, K.; Maazouz, A. Rheological, morphological, and interfacial properties of compatibilized PLA/PBAT blends. *Rheologica Acta* **2014**, *53*, 501.

168. Ludwiczak, J.; Frąckowiak, S.; Leluk, K. Study of Thermal, Mechanical and Barrier Properties of Biodegradable PLA/PBAT Films with Highly Oriented MMT. *Materials* **2021**, *14*, 7189.

169. Nofar, M.; Maani, A.; Sojoudi, H.; Heuzey, M.C.; Carreau, P.J. Interfacial and rheological properties of PLA/PBAT and PLA/PBSA blends and their morphological stability under shear flow. *Journal of Rheology* **2015**, *59*, 317.

170. Sarul, D.S.; Arslan, D.; Vatansever, E.; Kahraman, Y.; Durmus, A.; Salehiyan, R.; Nofar, M. Preparation and

characterization of PLA/PBAT/CNC blend nanocomposites. *Colloid and Polymer Science* **2021**, *299*, 987.

171. Botta, L.; Titone, V.; Mistretta, M.C.; La Mantia, F.P.; Modica, A.; Bruno, M.; Sottile, F.; Lopresti, F. PBAT Based Composites Reinforced with Microcrystalline Cellulose Obtained from Softwood Almond Shells. *Polymers* **2021**, *13*, 2643.

172. Hemjyoti, K. *Shape memory polymers*, 1st ed.; De Gruyter: 2018.

173. Nofar, M.; Salehiyan, R.; Sinha Ray, S. Rheology of poly (lactic acid)-based systems. *Polymer Reviews* **2019**, *59*, 465.

174. Palierne, J.F. Linear rheology of viscoelastic emulsions with interfacial tension. *Rheologica Acta* **1990**, *29*, 204.

175. Casamento, F.; D'Anna, A.; Arrigo, R.; Frache, A. Rheological behavior and morphology of poly(lactic acid)/low-density polyethylene blends based on virgin and recycled polymers: Compatibilization with natural surfactants. *Journal of Applied Polymer Science* **2021**, *138*, 50590.

176. Castro, M.; Carrot, C.; Prochazka, F. Experimental and theoretical description of low frequency viscoelastic behaviour in immiscible polymer blends. *Polymer* **2004**, *45*, 4095.

177. D'Anna, A.; Arrigo, R.; Frache, A. PLA/PHB Blends: Biocompatibilizer Effects. *Polymers* **2019**, *11*, 1416.

178. Arias, A.; Sojoudiasli, H.; Heuzey, M.-C.; Huneault, M.A.; Wood-Adams, P. Rheological study of crystallization behavior of polylactide and its flax fiber composites. *Journal of Polymer Research* **2017**, *24*, 46.

179. Su, S.; Duhme, M.; Kopitzky, R. Uncompatibilized PBAT/PLA Blends: Manufacturability, Miscibility and Properties. *Materials* **2020**, *13*, 4897.

180. Qiao, Z.; Wang, Z.; Zhang, C.; Yuan, S.; Zhu, Y.; Wang, J.; Wang, S. PVAM–PIP/PS Composite Membrane with High

Performance for CO2 /N2 Separation. *AIChE Journal* **2013**, *59*, 215.

181. Liu, B.; Guan, T.; Wu, G.; Fu, Y.; Weng, Y. Biodegradation Behavior of Degradable Mulch with Poly (Butylene Adipate-co-Terephthalate) (PBAT) and Poly (Butylene Succinate) (PBS) in Simulation Marine Environment. *Polymers* **2022**, *14*, 1515.

182. Di Lorenzo, M.L.; Androsch, R. Influence of α′-/α-crystal polymorphism on properties of poly(lactic acid). *Polymer International* **2019**, *68*, 320.

183. Kolarik, J. Simultaneous Prediction f the Modulus and Yield Strenght of Bianry Polymer Blends.Tensile moduli of co-continuous polymer blends. **1996**, *36*, 2518.

# Scientific production

(Updated to November 30th 2025)

**From Master's thesis work**

- Bianchi, M.; Valentini, F.; Fredi, G.; Dorigato, A.; Pegoretti, A. Thermo-Mechanical Behavior of Novel EPDM Foams Containing a Phase Change Material for Thermal Energy Storage Applications. *Polymers*, **2022**, 14, 4058.
- Bianchi, M.; Valentini, F.; Fredi, G.; Dorigato, A.; Pegoretti, A. Shape memory behaviour of novel EPDM/paraffin foams. *Polymer Engineering and Science*, **2023**, 63(5), 1633.

**From PhD's thesis work**

- Bianchi, M.; Fambri, L.; Fredi, G.; Dorigato, A.; Pegoretti, A. Elastocaloric Performance of Natural Rubber in Solid State Cooling: Evaluation of the Effect of Crosslinking Density. *Applied Sciences*, **2024**, 14(22), 10525.

- Bianchi, M.; Fambri, L.; Dorigato, A.; Pegoretti, A. Elastocaloric Performance of Natural Rubber: The Role of Nanoclay Addition. *Molecules*, **2025**, 30(14), 3035.

**From side activities**

- Bianchi, M.; Pegoretti, A.; Fredi. G. An overview of poly(vinyl alcohol) and poly(vinyl pyrrolidone) in pharmaceutical additive manufacturing. *Journal of Vinyl and Additive Technology*, **2023**, 29(2), 223.
- Bianchi, M.; Dorigato, A.; Morreale, M.; Pegoretti, A. Evaluation of the physical and shape memory properties of fully biodegradable poly(lactic acid) (PLA) / poly(butylene adipate terephthalate) (PBAT) blends. *Polymers*, **2023**, 15(4), 881.
- Scirè, S.; Bianchi, M.; Pensabene, M.; Dorigato, A.; Mauro, N. A robust, biocompatible scaffold for peripheral nerve regeneration:integration of PLLA nanofibers with a RGD-like poly(amidoamine) hydrogel. *European Polymer Journal*, **2025**, 235, 114097.

# Awards

(Updated to November 30th 2025)

**Milan Polymers Days (MIPOL) 2023 – Best Poster Award –** "Effect of crosslinking density on the elastocaloric properties of Natural Rubber". 7th-9th June 2023, Milan (Italy).

# Participation to Congress and Schools

(Updated to 30th November 2025)

**National congress contribution**

- Bianchi M, Valentini F, Fredi G, Dorigato A, Pegoretti A. "**Evaluation of the shape memory behavior of novel epdm/paraffin foams**". Interuniversity Consortium of Materials Science and Technology (INSTM), 23rd-26th January 2022, Sestriere (Italy).
- Bianchi M, Valentini F, Fredi G, Dorigato A, Pegoretti A. "**Multifunctional Ethylene Propylene Diene Monomer (EPDM)/paraffin foams coupling shape memory behaviour and Thermal Energy Storage (TES) properties**". Associazione Italiana di Scienza e Tecnologia delle Macromolecole (AIM), 4th-7th September 2022, Trento (Italy).
- Bianchi M, Valentini F, Fredi G, Dorigato A, Pegoretti A. "**Multifunctional EPDM/Paraffin foams coupling shape memory behavior and TES properties**". INSTM, 22nd-25th January 2023, Bressanone (Italy).
- Bianchi M, Fambri L, Pegoretti A, Dorigato A. "**Effect of crosslinking density on the elastocaloric properties of Natural Rubber**". Milan Polymers Days (MIPOL), 7th-9th June 2023, Milan (Italy).
- Bianchi M, Fambri L, Pegoretti A, Dorigato A. "**Effect of crosslinking density on the elastocaloric properties of Natural Rubber**". Time of Polymer (TOP) conference, 11th-15th June 2023, Ischia (Italy).
- Bianchi M, Fambri L, Pegoretti A, Dorigato A. "**Effect of crosslinking density on the elastocaloric properties of Natural Rubber"**. Macrogiovani (AIM), 12th-13th June 2024, Rimini (Italy).
- Bianchi M, Fambri L, Pegoretti A, Dorigato A. "**Solid-state cooling by Natural Rubber: effect of crosslinking density on the elastocaloric performance**". TOP conference, 4th-8th June 2025, Ischia (Italy).

**International congress contribution**

- Bianchi M, Valentini F, Fredi G, Dorigato A, Pegoretti A. "**Multifunctional Ethylene Propylene Diene Monomer (EPDM)/paraffin foams coupling shape memory behaviour and Thermal Energy Storage (TES) properties**". European Polymer Federation (EPF) conference, 26th June-1st July 2022, Prague.
- Bianchi M, Valentini F, Fredi G, Dorigato A, Pegoretti **A. "Mutifunctional EPDM/paraffin foams coupling thermal management and shape memory properties".** International Conference on Composite Materials (ICCM), 30thJuly-4th August 2023, Belfast.
- Bianchi M, Fambri L, Pegoretti A, Dorigato A. **"Solid-state cooling by Natural Rubber. Evaluation of the effect of crosslinking density on the elastocaloric performance".** Polymers for a safe and sustainable future conference, 28th-31st May 2024, Athens.
- Bianchi M, Fambri L, Pegoretti A, Dorigato A. "**Solid-state cooling by Natural Rubber. Evaluation of the effect of crosslinking density on the elastocaloric performance**". German Rubber Conference DKT, 1st-4th July 2024, Nuremberg.
- Bianchi M, Fambri L, Pegoretti A, Dorigato A. "**The role of nanoclay addition on the elastocaloric performance of Natural Rubber**". International Conference on Natural Fibers (ICNF), 16th-18th June 2025, Lisbon.
- Bianchi M, Fambri L, Pegoretti A, Dorigato A. "**The role of nanoclay addition on the elastocaloric performance of Natural Rubber**". EPF conference, 22nd-27th June 2025, Groningen.

**Summer schools**

- 21th AIMAT School "I Materiali nella Transizione Energetica". AIMAT, July 13-16th 2022, Ischia (Italy).

- 22th AIMAT School “Intelligenza Materiale: dagli Smart Materials all’Intelligenza Artificiale”. AIMAT, July 14-17th 2024, Ischia.

## Teaching activities

- Tutoring activities (from 2022 to 2025) of the Master’s course: “*Polymeric and Composite Materials*” taught by Prof. Luca Fambri and Prof. Alessandro Pegoretti.
- Tutoring activities (from 2023 to 2025) of the Bachelor’s course: “*Laboratorio di Tecnologie delle materie plastiche*”, taught by Prof. Andrea Dorigato.